

Experimental and computational study of dielectric barrier discharges for environmental applications

Proefschrift voorgelegd tot het behalen van de graad van doctor in de Wetenschappen aan de Universiteit Antwerpen te verdedigen door

Robby Aerts



Promotor
Prof. dr. Annemie Bogaerts

Faculteit Wetenschappen
Departement Chemie
Antwerpen 2014

 Universiteit
Antwerpen

Experimental and computational study of dielectric barrier discharges for environmental applications

Experimentele en computationele studie van diëlektrische barrière ontladingen voor milieutoepassingen

Proefschrift voorgelegd tot het behalen
van de graad van doctor in de wetenschappen
aan de Universiteit Antwerpen
te verdedigen door

Robby Aerts

Promotor: Prof. Dr. Annemie Bogaerts
Antwerpen, 2014

Contents

CONTENTS	I
ACKNOWLEDGMENT	V
LIST OF FIGURES	VII
LIST OF TABLES	XIII
CHAPTER 1: BACKGROUND	3
1.1 INTRODUCTION	4
1.2 TYPE OF POLLUTION	5
1.2.1 <i>Global climate change and the greenhouse effect</i>	5
1.2.2 <i>Ozone depletion</i>	8
1.2.3 <i>Air pollution</i>	8
1.2.4 <i>Acid rain</i>	9
1.3 TYPE OF POLLUTANTS	9
1.3.1 <i>Acid gas</i>	10
1.3.2 <i>Greenhouse Gases (GHGs)</i>	11
1.3.3 <i>Volatile Organic Compounds (VOCs)</i>	12
1.4 THE ENERGY CHALLENGE	13
1.5 POLITICAL EFFORTS	15
1.6 REFERENCES	19
CHAPTER 2: PLASMA TECHNOLOGY FOR ENVIRONMENTAL APPLICATIONS	21
2.1 INTRODUCTION	22
2.1.1 <i>Time-scales in NTP plasmas</i>	23
2.1.2 <i>Plasma chemistry</i>	25
2.2 NON-THERMAL PLASMAS FOR ENVIRONMENTAL APPLICATIONS	27
2.2.1 <i>Dielectric Barrier Discharge (DBD)</i>	27
2.2.2 <i>Corona discharge</i>	29
2.2.3 <i>Gliding arc discharges</i>	30
2.2.4 <i>Microwave discharges</i>	32
2.2.5 <i>Packed bed reactor</i>	33
2.3 APPLICATIONS INVESTIGATED IN THIS PHD DISSERTATION	35
2.3.1 <i>Flue gas treatment</i>	35
2.3.2 <i>CO₂ splitting</i>	37
2.4 AIM OF THIS PHD DISSERTATION.....	41
2.5 REFERENCES	43
CHAPTER 3: DESCRIPTION OF THE MODEL AND THE EXPERIMENTS	49

3.1	MODEL.....	50
3.1.1	<i>Physical description of the model.....</i>	50
3.1.2	<i>Power deposition in a DBD plasma</i>	53
3.2	EXPERIMENTAL SET-UP	56
3.2.1	<i>Description of the DBD reactor.....</i>	56
3.2.2	<i>Gas chromatographic analysis</i>	57
3.2.3	<i>Electrical diagnostics.....</i>	59
3.2.4	<i>Discharge power.....</i>	60
3.3	REFERENCES	65
CHAPTER 4: SINGLE PULSE SIMULATIONS FOR ETHYLENE DESTRUCTION IN DBDS		69
4.1	INTRODUCTION	70
4.2	DESCRIPTION OF THE CHEMISTRY AND THE EXPERIMENT	70
4.2.1	<i>Description of the chemical model.....</i>	70
4.2.2	<i>Description of the validation experiments.....</i>	72
4.3	RESULTS AND DISCUSSION.....	73
4.3.1	<i>Validation of the model.....</i>	73
4.3.2	<i>Effect of concentration</i>	76
4.3.3	<i>Effect of specific energy deposition</i>	78
4.3.4	<i>Contribution of the important destruction reactions</i>	80
4.4	CONCLUSION	84
4.5	REFERENCES	85
CHAPTER 5: REAL TIME SCALE SIMULATIONS FOR ETHYLENE DESTRUCTION IN DBDS		87
5.1	INTRODUCTION	88
5.2	DESCRIPTION OF THE MODEL AND THE CHEMISTRY.....	89
5.2.1	<i>Description of the chemical model.....</i>	89
5.2.2	<i>Description of the validation experiments.....</i>	89
5.3	RESULTS AND DISCUSSION	90
5.3.1	<i>Description of the power deposition</i>	90
5.3.2	<i>Effect of SED on the ethylene destruction process</i>	93
5.3.3	<i>Identification of the destruction pathway.....</i>	96
5.3.4	<i>Effect of the air humidity on the ethylene destruction process.....</i>	100
5.3.5	<i>Production of O₃, NO₂, HNO₂, HNO₃ and N₂O.....</i>	105
5.4	CONCLUSION	108
5.5	REFERENCES	109
CHAPTER 6: SINGLE PULSE SIMULATIONS FOR CO₂ SPLITTING IN DBDS.....		113
6.1	INTRODUCTION	114
6.2	DESCRIPTION OF THE MODEL AND THE CHEMISTRY.....	115
6.3	RESULTS AND DISCUSSION	120
6.3.1	<i>Validation of the model.....</i>	120
6.3.2	<i>Description of the power deposition in the model</i>	121

6.3.3	<i>Energy transfer from electrons to different channels of CO₂ excitation, ionization and dissociation</i>	123
6.3.4	<i>Importance of electron impact reactions</i>	125
6.3.5	<i>Behavior of vibrationally excited CO₂ molecules</i>	127
6.3.6	<i>Behavior of neutrals in the plasma</i>	133
6.3.7	<i>Behavior of ions in the plasma</i>	136
6.3.8	<i>Contribution of the various plasma species to the CO₂ splitting</i>	139
6.4	CONCLUSIONS.....	147
6.5	REFERENCES.....	150
CHAPTER 7: REAL TIME SCALE SIMULATIONS AND EXPERIMENTAL STUDY FOR CO₂ SPLITTING IN DBDS		153
7.1	INTRODUCTION.....	154
7.2	DESCRIPTION OF THE CHEMISTRY AND THE EXPERIMENTS.....	155
7.2.1	<i>Description of the chemical model</i>	155
7.2.2	<i>Description of the validation experiments</i>	156
7.3	RESULTS AND DISCUSSION.....	158
7.3.1	<i>Experimental parameter screening</i>	158
7.3.2	<i>Modelling the plasma chemistry of CO₂ splitting</i>	169
7.3.3	<i>Theoretical energy cost versus actual energy cost</i>	179
7.3.4	<i>Feasibility of CO₂ splitting by DBDs, and benchmarking with other techniques</i> 181	
7.4	CONCLUSIONS.....	190
7.5	REFERENCES.....	194
CHAPTER 8: IN-SITU CHEMICAL TRAPPING OF OXYGEN IN CO₂ SPLITTING		197
8.1	INTRODUCTION.....	198
8.2	DESCRIPTION OF THE MODEL AND THE CHEMISTRY.....	200
8.2.1	<i>Description of the chemical model</i>	200
8.2.2	<i>Description of the validation experiments</i>	200
8.3	RESULTS AND DISCUSSION.....	201
8.3.1	<i>Modelling the oxygen trapping upon addition of H₂ and CH₄</i>	201
8.3.2	<i>Experimental proof for oxygen trapping upon CH₄ addition</i>	205
8.3.3	<i>Liquids produced: Study of the carbon balance based on the calculations</i> ..	207
8.3.4	<i>Energy-efficiency study of the chemical trapping of O₂</i>	209
8.4	CONCLUSION.....	213
8.5	REFERENCES.....	216
CHAPTER 9: GENERAL CONCLUSIONS AND CRITICAL ASSESSMENT		219
SUMMARY		221
SAMENVATTING		225

LIST OF PUBLICATIONS	231
LIST OF CONFERENCE CONTRIBUTIONS	233
APPENDIX I.....	235
APPENDIX II.....	245

Acknowledgment

This work would not have been possible without the help and the encouragements of others. First I would like to thank prof. Annemie Bogaerts for giving me the opportunity to do this PhD and for making critical remarks together with the useful scientific discussions. There was always time to help me in your busy schedule.

At the start of my research dr. Tom Martens was very kind to help me with the basics of Fortran and plasma modelling. Also later on, I always appreciated his advice. I would also want to thank dr. Ming Mao who helped me a lot with the basics of the global_kin model and the physical interpretation of my research. Furthermore, I am very grateful to have Péter Simon sitting next to me. He is the person who always finds a solution for every numerical and physical problem. Péter I thank you a lot for all your advice.

For technical help I always could count on Luc Van't Dack to assist me in finding the right materials by digging in old laboratories. Also for more practical problems, Luc was there to help me.

For all support with financial and administrative issues I always could rely on the help of Nelly Suijkerbuijk and Ingrid Swenters. Thank you for your help with those complicated papers.

During my research I could always count on validation results from the University of Manchester by Prof. Christopher Whitehead and dr. Xin Tu. I also want to thank the people from VITO,

especially dr. Sabine Paulussen and ing. Erwin van Hoof, for their experimental expertise.

Furthermore, the group Applied Physics at the University of Ghent deserves a word of gratitude. Thank you, Prof. Rino Morent and Arne Vandenbroucke, for the helpful collaboration. My research could not be possible without the first version of `global_kin`; therefore many thanks to Prof. Mark Kushner and his co-workers.

I also want to acknowledge the people from the mechanical workshop which could literally make everything possible. Gilles, Lucien and Eddy, thank you so much.

The PLASMANT colleagues at the University of Antwerp are all great people and colleagues. Wouter, we started our work together at PLASMANT and you were a great support to me and my work.

Finally I want to thank my family. Especially my parents Dirk and Inge, they were always interested in my work. But, the person who deserves most gratitude is my wife Kathlyn. She was my biggest fan on which I could always rely. Thank you so much.

List of Figures

Figure 1-1: Production of primary energy sources (left graph) together with a detailed graph (right graph) of the renewable energy (% of total, based on tons of oil equivalent)^[18]. 15

Figure 2-1: Time-scale of elementary processes in non-thermal plasma processes^[6] 24

Figure 2-2: Several DBD configurations^[7]. (a), (b) and (c) are different configurations for planar DBDs, (d) is an end-on-view of a cylindrical DBD and (e) is a surface DBD or more commonly known as a plasma actuator..... 28

Figure 2-3: Schematic diagram of a corona discharge reactor in a point-to-plate configuration. 30

Figure 2-4: Schematic diagram of a gliding arc configuration: (A) reagent gas breakdown; (B) equilibrium heating phase; (C) non-equilibrium reaction phase^[11]. 31

Figure 2-5: Schematic diagram of a microwave discharge. 32

Figure 2-6: Packed bed DBD configurations^[12]: parallel plate (a) and cylindrical (b). 34

Figure 3-1: Typical current-voltage waveforms for a filamentary DBD. 53

Figure 3-2: Schematic overview of the modelling methodology. 55

Figure 3-3: Schematic diagram of the experimental setup for the experiments with CO₂, in front view and top view (left) as well as a picture of the set-up (right). 57

Figure 3-4: Schematic diagram of the circuit used for measuring the discharge power of a DBD reactor^[9]. 60

Figure 3-5: Comparison between DBD modes: The top graphs represent the filamentary mode and the bottom graphs represent the homogeneous mode^[14] 62

Figure 3-6: Lissajous plots three different discharge gaps of a DBD, at a plasma power of ± 35 W, with a quartz dielectric (A)^[13] 64

Figure 4-1: The top graph presents a comparison between the simulations and the experiments for the removal efficiency as a function of the specific energy density (SED) at 13700 ppm, 8700 ppm and 3500 ppm ethylene in dry air at a gas temperature of 300 K. The bottom graph presents a comparison of the ethylene and NO densities between our simulations and simulations adopted from literature in Niessen *et al.*^[34] and Shin *et al.*^[33], for the same conditions. The left y-axis is for the comparison with the data of Niessen *et al.*, whereas the comparison with the data of Shin *et al.* corresponds to the right y-axis. 75

Figure 4-2: Calculated relative contributions of radicals, metastables and electrons to the destruction of ethylene, as a function of the ethylene concentration in dry air at a SED of 600 mJ/cm³. 77

Figure 4-3: Calculated relative contribution of radicals, metastables and electrons to the destruction of ethylene, as a function of the SED in a dry air mixture containing 500 ppm ethylene..... 79

Figure 4-4: Calculated relative contributions of the most important destruction reactions during the current pulse and the afterglow region, together with the corresponding total values (i.e., relative contributions of total destruction either during the pulse or afterglow, i.e., no. 5 and 11, respectively), for an ethylene concentration of 100 ppm and a SED of 600 mJ/cm³. 80

Figure 5-1: Measured voltage (left y-axis) and current (right y-axis) as a function of time, for a specific energy deposition (SED) of 1.2 J/cm³ (a) and 2.4 J/cm³ W (b), in the case of 3500 ppm C₂H₄ in dry air. The red circles indicate that the number of microdischarge pulses increases as a function of SED (or power)..... 91

Figure 5-2: Electron density, both calculated from the model and estimated from the experiment, as a function of the specific energy deposition (SED) (left y-axis), as well as the total number of microdischarge pulses assumed in the simulations for a residence time of 0.684 s (right y-axis), for 3500 ppm C₂H₄ in dry air. 93

Figure 5-3: Comparison between calculated (solid lines) and measured (dashed lines) removal efficiency (RE) (a), and selectivities towards CO and CO₂, i.e., S_{CO} (b) and S_{CO₂} (c), at different concentrations of C₂H₄ in dry air, and as a function of the SED. 95

- Figure 5-4: Ethylene destruction pathway in dry and humid air, as elucidated by the model. The thickness of the arrows indicates the importance of the various reaction paths. The pathway is more or less similar in both dry and humid air, except for some extra destruction path through OH radicals in humid air, as indicated by the dashed arrow in the figure. 97
- Figure 5-5: Comparison between calculated (solid lines) and measured (dashed lines) RE (red; circle), S_{CO} (black; triangle) and S_{CO_2} (blue; square), as a function of the relative air humidity, for an energy deposition of 1.8 J/cm^3 at 8700 ppm C_2H_4 in air. 101
- Figure 5-6: Calculated concentrations of H_2O (left axis), CH_2O and C_2H_2 (right axis), formed as by-products in C_2H_4 destruction, as a function of time during 10 consecutive microdischarge pulses, in the case of humid air with 20% RH (dashed lines) and dry air (solid lines), for a total energy deposition of 1.8 J/cm^3 at 8700 ppm C_2H_4 in air..... 102
- Figure 6-1: Calculated fractional densities of CO_2 conversion products, at 30 Torr, 400 K and a power input of 1.5 kW/cm^2 , obtained in this work, in comparison with the results from Cenian and coworkers^[29]. 121
- Figure 6-2: Calculated electron temperature (dashed green line; right y-axis) and electron density (solid red line; left y-axis) as a function of time during a single-pulse discharge and its afterglow. The applied power pulse is indicated by the solid black line (not shown on y-axis)..... 123
- Figure 6-3: Fractions of electron energy transferred to different channels of excitation as well as ionization and dissociation of CO_2 , as a function of the reduced electric field (E/n), as calculated from the corresponding cross sections of the electron impact reactions. The E/n region characteristic for DBDs is indicated by "DBD region". The electron impact dissociation reaction of CO_2 through electron impact excitation, followed by dissociation, is mentioned in the figure as "dissociation". The sum of electron impact electronic excitation reactions of CO_2 which form excited levels without dissociation are mentioned as "Electronic excitation" 124
- Figure 6-4: Rates of the different electron impact reactions with ground state CO_2 (solid lines) and vibrationally excited CO_2 (dashed lines) as a function of time during and after one discharge pulse of 30 ns..... 126

Figure 6-5: Densities of the vibrationally excited CO₂ species (left y-axis) and the ground state CO₂ density (right y-axis), as a function of time, during and after one discharge pulse of 30 ns (a), as well as for five consecutive discharge pulses of 30 ns with an interpulse period of 1 μs (b). 129

Figure 6-6: Net formation of vibrationally excited CO₂ (i.e., the sum of all levels) integrated over the time of one (30 ns) pulse and its afterglow (a), and fall back ratio of vibrationally excited CO₂ (i.e., the fraction of vibrational CO₂ that has decayed back to the ground state) (b), for a wide range of interpulse times. 132

Figure 6-7: Densities of the important neutral species as a function of time, during and after one discharge pulse of 30 ns (a), as well as for five consecutive discharge pulses of 30 ns with an interpulse period of 1 μs (b). 135

Figure 6-8: Densities of the ions as a function of time, during and after one discharge pulse of 30 ns (a), as well as for five consecutive discharge pulses of 30 ns with an interpulse period of 1 μs (b). Note that in (b) only those ions are shown that do not disappear immediately after pulse termination. The other ions are only characterized by a peak at each pulse, as can be derived from (a). 138

Figure 6-9: Rates for CO₂ loss (a) and formation (b) by the most important ion and neutral reactions, as a function of time during and after one discharge pulse of 30 ns. 140

Figure 7-1: Pictures of the DBD plasma at a frequency of 6 kHz (A) and 75 kHz (B), illustrating the difference in filamentary character. 159

Figure 7-2: Effect of the dielectric on the conversion (black curves, left axis) and energy efficiency (red curves, right axis), as a function of the SEI. The calculation of the error bars is based on the uncertainties of the power, the flow rate and the GC measurements. The error bars of the conversion in the y-direction are smaller than 1% and therefore not visible. 161

Figure 7-3: Effect of the discharge gap on the conversion (Figure A) and energy efficiency (Figure B), as a function of the SEI. The calculation of the error bars is based on the uncertainties of the power, the flow rate and the GC measurements. The error-bars of the conversion in the y-direction are smaller than 1% and therefore not visible. 162

- Figure 7-4: Lissajous plots for the three different discharge gaps, at a plasma power of ± 35 W, with a quartz dielectric (A), and schematic diagram of the Lissajous plot, explaining all the quantities that can be deduced from it (see text) (B). 163**
- Figure 7-5: Comparison of the electric current waveforms for the three different discharge gaps at a plasma power of ± 35 W, with a quartz dielectric, illustrating the reduced streamer formation for the gap of 3.3 mm..... 165**
- Figure 7-6: Effect of the gas flow rate (or residence time) and plasma power on the conversion (Figure A) and energy efficiency (Figure B), plotted as a function of the SEI, using alumina dielectrics. The corresponding values of plasma power, resulting in certain SEI values at the fixed gas flow rates of 50 and 100 ml/min (black and blue curves), as well as the corresponding values of the residence time, resulting in certain SEI values at a fixed plasma power of ± 40 W (red curve), are also shown in Figure A. The calculation of the error bars is based on the uncertainties of the power, the flow rate and the GC measurements. For the sake of clarity, the error bars are only presented for the energy efficiency. The green circle in Figure A indicates the conditions plotted in Figure 8 below..... 168**
- Figure 7-7: Comparison of the voltage and electric current waveforms for three different combinations of plasma power and gas flow rate (or residence time), yielding a similar SEI (cf. the green circle indicated in Figure 7 above). 169**
- Figure 7-8: Comparison of the calculated and measured values for the conversion, as a function of the SEI. Note that the power density, and hence the SEI, used in the model is multiplied by a factor 7, to account for the lower volume occupied by the streamers (see text). The calculation of the error bars is based on the uncertainties of the power, the flow rate and the GC measurements. The error-bars in the y-direction are smaller than 1% and therefore not visible. 171**
- Figure 7-9: Comparison of the conversion, calculated with the simplified model and the full model from Chapter Chapter 6:, as a function of SEI in the model..... 172**
- Figure 7-10: Reaction scheme, illustrating the chemistry of CO_2 splitting and further reactions, as predicted by the reduced model. 176**
- Figure 7-11: Calculated molecule densities as a function of residence time (A), and densities of all plasma species included in the simplified model, as a function of time during 5 consecutive microdischarge filaments (B), for a SEI of 129 J/cm^3 ... 178**

Figure 7-12: Energy cost (black curves; left axis) and energy efficiency (red curves; right axis), as calculated from the electrical power (“actual”; dashed lines) and from the plasma power (“theoretical”; solid lines), as a function of the SEI, using alumina dielectrics and a constant flow rate of 50ml/min.....	180
Figure 7-13: Modifications to a simple DBD reactor, as reported in literature, yielding a higher CO₂ conversion and energy efficiency. Both the reported maximum values of conversion and energy efficiency are plotted, as well as the relative changes compared to the same setup without the modification. See text for more explanation. The dashed green line indicates no change compared to the standard setup.....	186
Figure 8-1: Calculated O-based selectivity of the reaction products as a function of H₂ fraction added to the CO₂ plasma.	202
Figure 8-2: Calculated O-based selectivity of the reaction products, as a function of CH₄ fraction added to the CO₂ plasma.	203
Figure 8-3: Calculated fractions of the various components in the gas mixture after plasma treatment, for pure CO₂ and for different fractions of H₂ and CH₄ added to the CO₂ plasma. Note that the remaining fraction (up to 100%) corresponds to unreacted CO₂.....	204
Figure 8-4: Measured normalized area of each product obtained by GC analysis, after plasma treatment of CO₂ with various admixtures of CH₄. Note: the 0% CH₄ point for CO is not displayed, since a split-peak method was used for the calibration of the CO and CH₄ peaks. Furthermore, we were not able to measure the CH₃OH concentration in our setup.....	206
Figure 8-5: Calculated fractions in the carbon balance of the various components in the gas mixture after plasma treatment, as obtained from the model, for pure CO₂ and for different fractions of CH₄ added to the CO₂ plasma.....	208

List of Tables

Table 1-1: Composition of the atmosphere ^[10]	6
Table 1-2: GWP based on 20 years together with the lifetime for some substances ^[11]	7
Table 1-3: Typical VOCs and their health effects.	13
Table 2-1: The main plasma processes. A and B represent atoms and M stands for a temporary collision partner ^[1]	26
Table 2-2: List of plasma systems used for the treatment of flue gases, with an indication on their characteristic electron and gas temperature as well as the actual treatment ^[17]	36
Table 4-1: A comparison of the energy efficiency, in ppm/(mJ/cm ³), between different pollutants, as adopted from literature and our own work (for C ₂ H ₄). The efficiency is calculated by dividing the converted concentration of the pollutant by the specific energy deposition.	76
Table 5-1: Calculated concentrations of O ₃ , NO ₂ , N ₂ O and HNO ₂ formed as by-products in the destruction of 3500 ppm C ₂ H ₄ in dry air, for different values of SED. The measured values of the NO ₂ and N ₂ O concentrations are also indicated between brackets.....	105
Table 6-1: Overview of the ground-state species included in the model.	115
Table 6-2: Overview of excited species included in the model.....	116
Table 6-3: Overview of the time-integrated net rates of the different reaction types contributing to the loss of ground state CO ₂ , during a pulse of 30 ns, an afterglow of 0.1 s, and the sum of both, as well as the net overall contributions (in %) for the actual dissociation of the CO ₂ ground state molecules. ^a	142
Table 6-4: Overview of the time-integrated net rates of the different reaction types contributing to the loss of vibrationally excited CO ₂ , during a pulse of 30 ns, an afterglow of 0.1s, and the sum of both, as well as the net overall contributions (in %) for the actual dissociation of the vibrationally excited CO ₂ molecules. ^a	145

Table 7-1: Reactions included in the reduced chemistry model, as well as the corresponding rate coefficients and the references where these data are adopted from. The rate coefficients are in units of $\text{cm}^3 \text{s}^{-1}$ for the two-body reactions, and in $\text{cm}^6 \text{s}^{-1}$ for the three-body reactions..... 174

Table 7-2: Benchmark of our results, in terms of maximum conversion, energy efficiency and the corresponding gas flow rates in both cases, with data from literature for other plasma types and classical thermal splitting, all carried out at atmospheric pressure..... 182

Table 7-3: Summary of the experimental parameter screening, illustrating their effect on the CO_2 conversion and energy efficiency. 191

Table 8-1: Calculated values of CO_2 conversion, specific energy deposition for CO_2 conversion (SED_{CO_2}) and CH_4 conversion (SED_{CH_4}) as well as the energy cost for producing 1 mole of CO (E_{CO}) in the case of pure CO_2 splitting, as well as when adding 3% H_2 or 2% CH_4 as trapping gases. 211

Table 8-2: Energy cost of different CO_2 separation systems, as well as the obtained CO_2 purity^[4]. 212

PART I:

GENERAL BACKGROUND

Chapter 1:

Background

In this chapter, the climate change and the different types of air pollution as well as their impact on the environment are discussed. Furthermore, the related energy challenge which mankind will be facing is introduced. Finally, at the end of the chapter the political efforts on the international and European level are reviewed.

1.1 Introduction

Nowadays, environmental awareness is a fact in our globalized world. Moreover, environmental protection is becoming an issue of growing concern. The industrialization has led to the emission of various kinds of chemicals that danger both human and ecological life^[1]. Since the end of World War II, governments have become aware that legislation of emissions needs to become more strict and severe in order to ensure the protection of our environment for generations to come. The first international examples are international treaties like the Kyoto protocol (1997) and the protocol of Gothenburg (1999). The sources for these kind of emissions are exhausts of mobile (e.g. cars) and stationary sources (e.g. industrial plants) which are polluting the air with a variety of harmful substances that threat human and ecological life^[2]. Next to NO_x, SO_x and H₂S, volatile organic compounds (VOCs) are a large and important group of pollutants. Moreover, another type of pollution can be distinguished, which can be assigned to the increasing amounts of greenhouse gases, such as carbon dioxide (CO₂).

It is well known that human activity is changing the composition of the earth's atmosphere to include increasing amounts of greenhouse gases^[3]. The burning of fossil fuels, the world's dominant source of energy, is the main cause for CO₂ emissions, which have dramatically increased since the industrial revolution. The remaining CO₂ trapped in the earth's atmosphere contributes to the global warming trend, which has been documented over the last century to show an increase in global temperature of about 1-2°C^[4,5]. Although this is only a small difference in temperature; the consequences for earth's physical and biological systems cannot be underestimated.

1.2 Type of pollution

1.2.1 Global climate change and the greenhouse effect

Climate change is the environmental challenge of the 21st century^[6]. It is considered as any significant change to the factors that make up climate, such as temperature, precipitation and wind over, periods of time lasting decades or longer.

Greenhouse gases (GHGs) affect climate change by trapping heat in the atmosphere. In principle, the earth absorbs, reflects and radiates heat from the sun. However if GHGs are present, they will first allow UV radiation from the sun to pass through the atmosphere unimpeded to reach the earth's surface. As some of this energy will be absorbed into the surface, infrared radiation (IR) is reradiated back into the atmosphere, where it becomes absorbed by the GHGs. These GHGs are IR sensitive, i.e. they have bonds, which can absorb some IR radiation by their degrees of freedom. Furthermore, they will also enhance the infrared (IR) radiation emitted by the GHGs at colder temperatures and higher altitudes. In the end, not all of the radiation can escape and this causes a general heating of the atmosphere known as the greenhouse effect^[7]. It should be realized that without the warming effects of the atmosphere, the average temperature on earth would be -15 °C instead of +15 °C^[8]. Nevertheless, an artificial increasing concentration of GHGs by human activities will cause the temperature to increase even more.

GHG's are not always produced by human activity, some of them are naturally occurring, such as water vapor and carbon dioxide, making the greenhouse effect a naturally occurring phenomenon^[9]. General speaking, water vapor is the most common GHG, although it is not anthropogenic in origin. Looking at the composition of the atmosphere in **Table 1-1** we can

distinguish GHGs from biological and industrial sources; moreover, some GHGs can react in the atmosphere by photochemical reactions.

Table 1-1: Composition of the atmosphere^[10].

species	relative abundance (parts per billion by volume)	source	comment
N ₂	7.81×10^8	biologic	long lived
O ₂	2.01×10^8	biologic	long lived
H ₂ O	$10^6 - 10^7$	physical	long lived
Ar	9.34×10^6	radiogenic	permanent
CO ₂	3.5×10^5	biologic, industrial	variable, increasing
Ne	1.8×10^4	interior	permanent
He	5.2×10^3	radiogenic	escaping
CH ₄	1.6×10^3	biologic	variable, increasing
Kr	1.0×10^3	interior	permanent
H ₂	5.0×10^2	biologic, photochemical	variable
N ₂ O	3.0×10^2	biologic, industrial	increasing
CO	1.0×10^2	photochemical, industrial	variable, increasing
SO ₂	$<10^2$	industrial, photochemical	variable
O ₃	$<10^2$	photochemical	variable
Xe	9×10^1	interior	permanent
NO, NO ₂ , NO _x	variable	industrial, biologic	— *
CH ₃ Cl	6.0×10^{-1}	biologic	short lived
CCl ₂ F ₂	2.9×10^{-1}	industrial	increasing
CCl ₃ F	1.7×10^{-1}	industrial	increasing
CCl ₄	1.2×10^{-1}	industrial	increasing
CH ₃ CCl ₃	9.8×10^{-2}	industrial	increasing
CF ₄	7.0×10^{-2}	industrial	increasing
CH ₃ Br	1.0×10^{-2}	biologic, industrial	possibly increasing

*Relatively short lived, with an average lifetime of roughly one month.

To evaluate how big the global warming effect of one substance can be, the global warming potential (GWP) can be used. **Table 1-2** gives an overview of the GWP for some substances or a group of substances.

Table 1-2: GWP based on 20 years together with the lifetime for some substances^[11].

Substance	Lifetime (years)	GWP (20years)
Carbon dioxide	-	1
Methane	12.4	85
Nitrous oxide	121	264
Chlorofluorocarbons	45-1020	5860-10900
Fully Fluorinated Species	Days - 50000	<1 - 17500

The table shows that the global warming can be influenced drastically by human activity, especially by the emission of fluorinated substances, but also by the increasing emission of CO₂, N₂O and CH₄.

The Intergovernmental Panel on Climate Change (IPCC) concluded in 2013 that warming of the climate is now considered unequivocal^[11]. This conclusion is based on a number of observations going from an increasing ocean acidification, and a global temperature rising to changes in global average sea level, as well as precipitation and storms. They concluded that the combined globally averaged land and ocean surface temperatures show a warming of 0.85°C, over the period from 1880 to 2012. Moreover, the total increase between the average of the period 1850–1900 and the average of the period 2003–2012 is 0.78°C. The global sea level rose by 0.19 m, which can be attributed to glacier mass loss and the ocean thermal expansion from warming. Based on different scenarios, the IPCC predicts that the global surface temperature change for the end of the 21st century is likely to exceed 1.5°C relative to the period 1850 to 1900. It is certain that drastic changes in our way of living, combined with new technologies, are becoming a necessity for our existence.

1.2.2 Ozone depletion

Ozone is a substance that has a paradox on earth between harmful and vital to life, depending of the height in the atmosphere. About 90% of ozone in the atmosphere is located in the stratosphere (10-50km), where it protects life on earth from the sun's harmful radiation, while at the bottom of the troposphere (0-10 km) ozone contributes to harmful smog^[12]. Most of the ozone is concentrated in the so-called ozone layer at the bottom of the stratosphere. This layer of ozone protects the earth from ultraviolet (UV) radiation from the sun.

It is in this part that ozone depletion is taking place due to chemical destruction of the ozone layer beyond natural reactions^[12]. At this level the ozone concentration is maintained by the destruction, formation and accumulation of ozone through catalytic cycles involving hydrogen, nitrogen, bromine, chlorine and iodine oxides^[12]. These anthropogenic pollutants react with ozone in such a way that the ozone concentration in the ozone layer keeps decreasing.

1.2.3 Air pollution

Air pollution is nowadays a general term for pollution induced by vehicular emissions from petrol and diesel engines, but historically air pollution arises from the high levels of smoke and sulphur dioxide from combustion of sulphur containing fossil fuels. At this moment air pollution is seen as a mixture of various pollutants including carbon dioxide, NO_x, particulate matter and VOCs^[10]. Furthermore, ozone is also formed from photochemical reactions resulting from the reactions between sunlight and NO_x or VOCs.

1.2.4 Acid rain

Acid rain refers to a mixture of wet and dry deposition from the atmosphere containing higher than normal amounts of nitric and sulfuric acids. Although precipitation is naturally acidic due to carbon dioxide in the atmosphere, the acidity has increased in recent years due to anthropogenic pollutants^[10].

These pollutants result from both natural sources, such as volcanoes and decaying vegetation, and man-made sources, primarily emissions of sulfur dioxide (SO₂) and nitrogen oxides (NO_x) which are released from power plants and other fossil fuel burning processes. These gases react in the atmosphere with water, oxygen, and other chemicals to form various acidic compounds. Once formed, the acids can be transported over long distances by wind before they are deposited as precipitation. As a result, the higher acidity can cause long term damage to terrestrial ecosystems, including forests and freshwater lakes, and the wildlife within.

1.3 Type of pollutants

There are many types of air and gaseous pollutants and therefore Chang et al.^[13] divided them in several groups:

- Particulate matter (PM)
- Acid gases: SO_x, NO_x, HCl
- Greenhouse gases: CO_x, CH₄, N_xO_y, perfluorocarbons (PFCs)
- Volatile organic compounds (VOCs): toluene, benzene, trichloroethylene, dichloromethane (DCM), trichloroethane, formic acid, methanol, xylene, ethylene

- Ozone depleting substances (ODS): carbon tetrachloride, chlorofluorocarbons (CFCs) such as freons and halons, hazardous air pollutants (HAPs)
- Toxic gases: mercury, dioxanes
- Radioactive gases: isotopes of carbon, iodine, cesium, radon

In the discussion below the most important pollutants that can be abated by plasma technology will be introduced.

1.3.1 Acid gas

Oxides of nitrogen (N_xO_y) in the atmosphere have been shown to be detrimental to human health and the environment^[14,15]. Additionally, nitrogen oxides can react in the air to produce smog as well as other toxic substances such as ozone and peroxyacetyl nitrate (PAN). As a result, a severe emission legislation is introduced by the European Union.

NO_x is made up of the sum of nitrogen oxide (NO) and nitrogen dioxide (NO_2). In urban areas, anthropogenic emissions of NO_x contribute to high levels of ozone that are harmful to human health and plants. Ozone is formed from photochemical reactions resulting from the reaction of sunlight with NO_x . Adverse effects of NO_x to human health include the irritation of lungs and the potential of lowering resistance to respiratory infections. Furthermore, NO_x contributes to the formation of acid rain.

Sulphur dioxide is another acidic gas, which when combined with water vapor in the atmosphere, produces acid rain, as mentioned in Section 1.2.4. Its main source can be found from power stations that burn fossil fuels. It adversely affects people suffering chronic lung diseases as for example asthma^[10].

1.3.2 Greenhouse Gases (GHGs)

Carbon dioxide is probably the most well-known greenhouse gas, although without CO₂, life as we know it would not exist. It plays a vital role in photosynthesis by plants, releasing oxygen into the environment. The prior natural sources of CO₂ are plants as well, but also volcanic eruptions, peat fires and oceans. In contrast, the anthropogenic emissions are emitted through the burning of fossil fuels, transport use, deforestation and putrefying organic matter^[10].

Another greenhouse gas is nitrous oxide, also known as laughing gas, due to the euphoric effects of inhaling it. The gas is rather scarce in the atmosphere but it has a rather long lifetime which makes it a perfect greenhouse gas. It has a GWP of 310 times that of CO₂, making it much more effective than CO₂. Consequently, the cumulative effect of emissions of N₂O will be much greater than those of CO₂. N₂O is released at the earth's surface mainly through biological sources but also through anthropogenic activity. Industrial processes and artificial nitrogen fertilizers are well-known anthropogenic sources and make up to 50 -75% of the total emissions^[10].

Ozone is widely used to purify drinking water, eliminating odors, sterilizing equipment and treat sewage commercially. Although ozone can be categorized as a GHG (absorbs and emits IR radiation, see also section 1.2.1), the short lifetime of ozone (hours-days) precludes a meaningful calculation of the global warming potential^[11]. However, ground level ozone is a pollutant that causes irritation of the airway to the lungs^[10]. High levels of ozone are usually found during spells of hot, still weather in summertime because sunlight provides the energy which is needed to initiate ozone formation.

Methane is known from natural gas and has the highest abundance of all hydrocarbons in the atmosphere and a long lifetime. It stays in the atmosphere between 9 and 15 years and has a GWP of 21^[10]. Human sources of CH₄ include natural gas and petroleum systems, coal mining, combustion, landfill sites, waste water treatment and certain industrial processes^[10]. The rapid growth of the world population and its increasing demands for energy, food, shelter, water and other basic needs, caused a concentration increase of 145% since pre-industrial times^[10].

1.3.3 Volatile Organic Compounds (VOCs)

VOCs are a group of organic compounds which have a partial vapor pressure of at least 0.1 mbar under normal conditions^[16]. The impact on the environment depends of the concentration and its reactivity with other substances.

Depending on their chemical structure and concentration, they can cause various effects such as the creation of photochemical smog, secondary aerosols and tropospheric ozone^[17]. They also have an effect on the deterioration of the stratospheric ozone layer and thus also on global warming. Some of them are toxic and cause odor nuisance while others have carcinogenic effects, proving their adverse effects on human health^[2]. **Table 1-3** provides an overview of typical VOCs that have been studied for removal with non-thermal plasma (NTP) along with their related health effects.

Table 1-3: Typical VOCs and their health effects.

VOC	Effect
Acetone	Carcinogen
Ethlyne	Anesthetic illness
Formaldehyde	Sore throat, dizziness, headache
Dicloroethane	Paralysis of nerve center
Trichloroethylene	Liver and kidney diseases, skin irritation
Benzene	carcinogen
Toluene	Headache, dizziness
Xylene	Headache, dizziness
Styrene	Probable carcinogen

1.4 The energy challenge

The world's primary source of energy is derived from fossil fuels, a non-renewable energy source formed from the remains of animals and plants buried millions of years ago. There is no fast or easy way to replenish the supply of fossil fuels once they are used up, given the extended length of time needed to create them. Oil, coal, and natural gas are the three primary forms in which fossil fuels are produced and they account for 21%, 36%, and 25% of energy consumption, respectively^[7]. The question of whether the earth's natural energy supply will be enough to overcome our high dependency on fossil fuels combined with increasing global energy demand is getting more critical.

In 2008 the global average energy consumption was 16.8 TW, which is the basis for "the Terawatt challenge". The challenge will be to provide the same amount of energy on a sustainable way. At this moment, 80% of the global average energy consumption is produced by fossil fuels, which are no sustainable feed stocks for producing energy due to their environmental issues as discussed in section 1.2. Furthermore, it is certain that our main supply of fossil fuels will come to its end. The remaining 20% can be addressed to hydropower (1.5%), burning of biomass (9.5%), renewable

resources (1.7%, see below for more details) and nuclear energy (7.3%). Globally the fraction of energy by renewable resources is around 0.29 TW but this amount will possibly increase, if the prices of fossil fuels will increase even more^[18]. Moreover, we find that growing industries like China and India demand more energy and thus, also more renewable energy sources. To concede in this increasing supply, not only an increase in the production of energy by renewable sources is needed, but more importantly the energy efficiency of the processes involved should be increased^[19].

Renewable energy sources have a greater appeal because they can regenerate and be sustained nearly infinitely. The most commonly used renewable energy sources are biomass, hydropower, geothermal, wind, and solar energy. Biomass, an organic material made from plant and animal waste, can be converted to fuels and methane gas, or it can be burned directly to produce energy in the form of heat and steam. Hydropower is among others the process where water is forced to spin blades of a turbine, producing electricity in a generator. Water and steam heated from processes in the earth's core can be brought to the surface for heating purposes and electricity in the form of geothermal energy. Wind turbines collect the kinetic energy of the wind to produce electricity. Solar energy can be converted into electrical energy through the use of photovoltaic devices and solar thermal/electric power plants can create heat and electricity.

In Europe, 22.3% of the energy production is renewable and 23.5% of this renewable energy is consumed to produce electricity. The remainder of the renewable energy is used for the production of heat and steam for industrial and residential purposes as well as for transportation^[18]. **Figure 1-1** shows the production of primary energy in 2012 together with different forms of renewable energy.

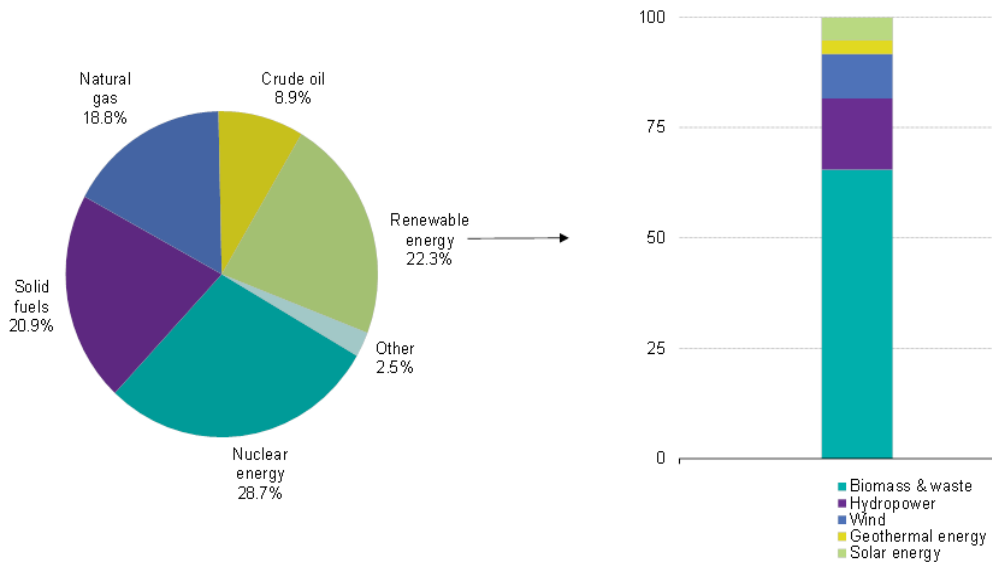


Figure 1-1: Production of primary energy sources (left graph) together with a detailed graph (right graph) of the renewable energy (% of total, based on tons of oil equivalent)^[18].

1.5 Political efforts

Since World War II, governments have become aware that emission legislation needs to become increasingly severe in order to ensure the protection of our environment for generations to come. International treaties like the Kyoto protocol (1997) and the protocol of Gothenburg (1999) are important examples.

On November 27 2001 the guideline 2001/81/EG regarding emissions maxima for air pollutants was published. This National Emission Ceilings (NEC) guideline imposes the members of the European Union certain ceiling emissions for NO_x, SO₂, VOC's and NH₃. Furthermore, the members were obligated to create a program which suggests how they can fulfill the guidelines. The European commission evaluates for each member the absolute

emissions year after year together with the predictions for next year^[20].

The basis for the guideline were the following^[20]:

- A reduction by half of the surface where critical acidification can be found.
- 67% reduction of the ozone surplus above the ceiling value for public health.
- 33% reduction of the ozone surplus above the ceiling value for vegetation.

On January 2007 the European Commission presented a series of proposals setting targets of greenhouse gas reduction. The EU would commit itself to reducing emissions of developed countries by 30% (compared to the 1990 levels) by 2020 in international negotiations. In addition, the Commission planned to reduce its domestic emissions by at least 20% by 2020^[21]. This proposal is part of the Energy & Climate Package adopted by the European Union. This package sets ambitious energy and climate targets, the 3x20 objectives: 20% emissions reduction, 20% increase of renewable energy and 20% increase in energy efficiency by 2020^[21].

The climate and energy package comprises four pieces of complementary legislation which are intended to deliver on the 20-20-20 targets: The first one is the reforming of the EU Emissions Trading System (EU ETS). The EU ETS is described as the key tool for reducing industrial greenhouse gas emissions most cost-effectively.

Secondly, the package deals with national targets for non-EU ETS emissions such as emissions from housing, agriculture, waste and transport (excluding aviation). Around 60% of the EUs total emissions come from sectors outside the EU ETS.

In a third piece, Member States are obligated to take binding national targets for raising the share of renewable energy in their energy consumption by 2020. These national targets will enable the EU as a whole to reach its 20% renewable energy target for 2020 as well as a 10% share of renewable energy in the transport sector. Furthermore, the targets will also help to reduce greenhouse gas emissions and the EUs dependence on imported energy.

The fourth piece of the climate and energy package is creating a legal framework for the environmentally safe use of carbon capture and storage technologies (CCS). CCS involves capturing the carbon dioxide emitted by industrial processes and storing it in underground geological formations where it does not contribute to global warming^[21,22].

Finally on March 8 2011, the EC adapted the original package because it didn't address the energy efficiency target directly. This is being done through the "Energy Efficiency Plan" and the "Energy Efficiency Directive" for saving more energy through concrete measures. The set of measures proposed aims at creating substantial benefits for households, businesses and public authorities. It should improve the EUs industrial competitiveness with a potential for the creation of up to 2 million jobs^[22].

We can conclude that some political efforts are made in recent years; however, the plan proposed by the European Union is

ambitious and does need efforts from technology point of view but also from ourselves.

1.6 References

- [1] P. S. Monks, C. Granier, S. Fuzzi, A. Stohl, M. L. Williams, H. Akimoto, M. Amann, A. Baklanov, U. Baltensperger, I. Bey, et al., *Atmos. Environ.* **2009**, *43*, 5268–5350.
- [2] A. M. Vandenbroucke, R. Morent, N. De Geyter, C. Leys, *J. Hazard. Mater.* **2011**, *195*, 30–54.
- [3] A. J. Hunt, E. H. K. Sin, R. Marriott, J. H. Clark, *ChemSusChem* **2010**, *3*, 306–22.
- [4] P. M. Cox, R. a Betts, C. D. Jones, S. a Spall, I. J. Totterdell, *Nature* **2000**, *408*, 184–7.
- [5] G. P. Peters, R. M. Andrew, T. Boden, J. G. Canadell, P. Ciais, C. Le Quéré, G. Marland, M. R. Raupach, C. Wilson, *Nat. Clim. Chang.* **2012**, *3*, 4–6.
- [6] M. T. and H. L. M. Solomon, S., D. Qin, M. Manning, Z. Chen, M. Marquis, K.B. Averyt, *Climate Change 2007: The Physical Science Basis*, Cambridge, **2007**.
- [7] L. F. Spencer, PhD Dissertation, The Study of CO₂ Conversion in a Microwave Plasma / Catalyst System, The University of Michigan, **2012**.
- [8] J. G. Calvert, *The Chemistry of the Atmosphere: Its Impact on Global Change*, Blackwell Science, **1994**.
- [9] M. Manning, A. Reisinger, *Philos. Trans. A. Math. Phys. Eng. Sci.* **2011**, *369*, 1891–905.
- [10] A. M. Harling, PhD Dissertation, Non-Thermal Plasma Systems for the Destruction of Gaseous Pollutants, The University of Manchester, **2006**.
- [11] V. B. and P. M. M. Stocker, T.F., D. Qin, G.-K. Plattner, M. Tignor, S.K. Allen, J. Boschung, A. Nauels, Y. Xia, *IPCC, 2013: Climate Change 2013: The Physical Science Basis. Contribution of Working Group I to the Fifth Assessment Report of the Intergovernmental Panel on Climate Change*, Cambridge University Press, Cambridge (UK) and New York (US), **2013**.
- [12] H. B. Singh, D. A. Salstein, *Composition, Chemistry, and Climate of the Atmosphere. 2: Mean Properties of the Atmosphere*, New York, NY, United States, **1994**.
- [13] J.-S. Chang, *Sci. Technol. Adv. Mater.* **2001**, *2*, 571–576.
- [14] A. Harling, J. Whitehead, *technology* **2007**, 1355–1358.

- [15] R. Dorai, PhD Dissertation, Modeling of Plasma Remediation of NO_x Using Global Kinetic Models Accounting for Hydrocarbons, University of Illinois, **2000**.
- [16] Europese Gemeenschap, *Publ. van Eur. Gem.* **1999**, 27.
- [17] J. R. Odum, T. P. W. Jungkamp, R. J. Griffin, H. J. L. Forstner, R. C. Flagan, J. H. Seinfeld, *Environ. Sci. Technol.* **1997**, 31, 1890–1897.
- [18] Eurostat, "Production of primary energy, EU-28, 2012," can be found under http://epp.eurostat.ec.europa.eu/statistics_explained/index.php/Renewable_energy_statistics, **2014**.
- [19] N. S. Lewis, *MRS Bull.* **2011**, 32, 808–820.
- [20] European Commision, "NEC Guideline," **2001**.
- [21] Commission to the European Council, *Limiting Global Climate Change to 2 Degrees Celsius – The Way Ahead for 2020 and beyond*, Brussels, **2007**.
- [22] The European Commission, "The 2020 climate and energy package," can be found under http://ec.europa.eu/clima/policies/package/index_en.htm, **2014**.

Chapter 2:

Plasma technology for environmental applications

In this chapter, a general introduction is given about plasma technology, together with a presentation of the important time-scales in plasmas, followed by a discussion of the general plasma chemistry. In part 2 an overview of non-thermal plasmas for environmental applications is given. In part 3 the environmental applications that are investigated in this PhD dissertation are explained. Finally, the aim of this PhD dissertation will be discussed in part 4.

2.1 Introduction

Plasma is the fourth state of matter, which can be considered as a partially ionized “gas”. Thus, any gas can potentially become plasma once energy is applied to create a significant density of electrons and ions. A plasma exists of negatively charged species (electrons and negative ions), positive ions, radicals, molecules, atoms, excited states and photons. The charged species are considered to be balanced in the bulk of the plasma, giving plasmas the characteristic of quasi-neutrality. Indeed, despite the existence of charged particles, plasmas as a whole are considered neutral.

Different types of plasmas can be distinguished based on their temperature, density and dimensions. Plasmas that occur naturally in the environment, including solar ares, the earth's ionosphere, the aurora borealis, and lightning, are defined as natural plasmas. Laboratory plasmas can be generated in a diverse range of conditions and can be used for many applications and therefore, two groups are distinguished, i.e. high temperature plasmas, known from nuclear fusion, and low temperature plasmas, also defined as gas discharges. These gas discharges can be either thermal or non-thermal, depending on the conditions and the energy applied. Thermal plasmas are characterized by the fact that all plasma species are in thermal equilibrium, with temperatures in the order of a few 10000K. These plasmas are currently used for welding, cutting and waste treatment^[1,2]. In contrast, non-equilibrium or non-thermal plasmas (NTPs), the temperature of the electrons (or the average energy) is much higher than that of the other plasma species.

A NTP typically consists of electrons which are accelerated by an electric field, gaining a typical temperature in the range of 10,000 to 250,000 K (1-25 eV), while the gas molecules remain at

relative low temperatures^[1,2]. In principle most of the energy is transferred to the electrons and thus to the electron induced chemistry, which makes NTPs an attractive alternative for conventional air cleaning techniques^[3,4]. NTPs are characterized by a potentially low energy consumption and high flexibility; however, they suffer from a limited energy density^[1].

Some processes like greenhouse gas conversion require plasmas which have a high electron temperature as well as a high electron density but are still in local non-equilibrium. This can be realized by another sub-group of plasmas, i.e. so-called warm plasmas^[1,5]. These discharges are somewhere between thermal and non-thermal discharges. Literature showed optimal values for the conversion of carbon dioxide in these discharges. In principle warm plasmas represent a discharge which is in non-equilibrium and at higher temperatures. Moreover, in some specific cases, like in CO₂, this effect increases the concentration of vibrationally excited species.

In this work we will focus only on the use of NTPs for the destruction of VOCs as well as for the conversion of carbon dioxide.

2.1.1 Time-scales in NTP plasmas

NTPs consist of many species (i.e. molecules, atoms, radicals, ions, electrons, excited species and photons) but more important is the fact that these species react at different time-scales. In general, the plasma chemistry can be divided into a primary process and a secondary process, as schematically shown in **Figure 2-1**.

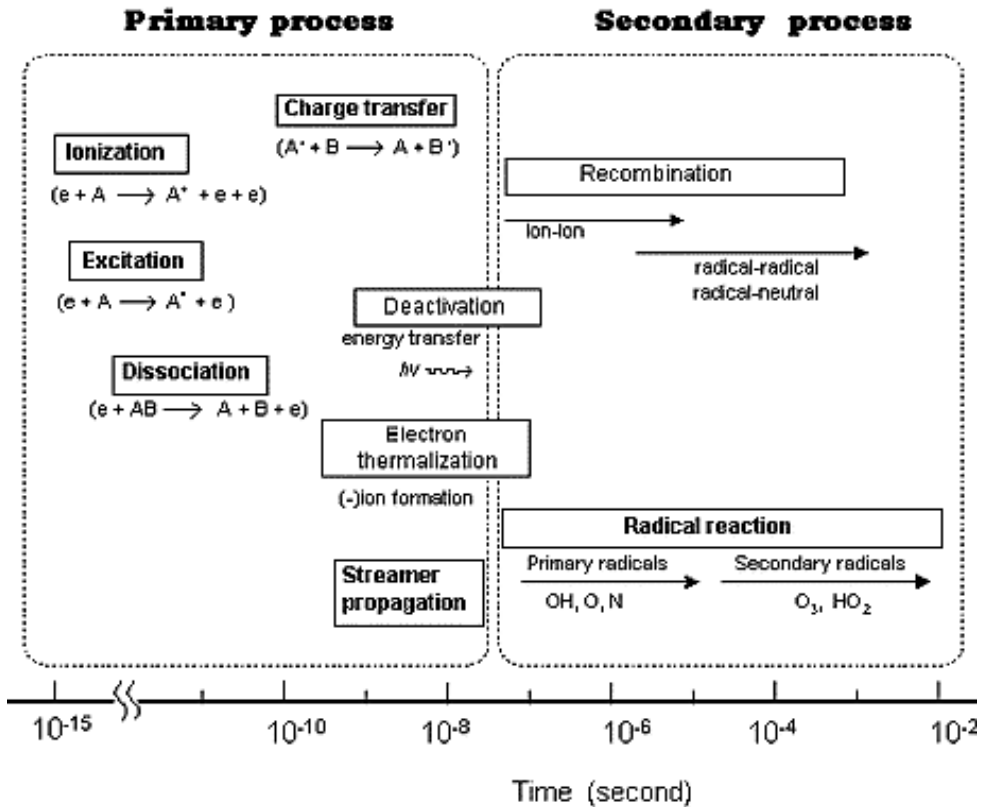


Figure 2-1: Time-scale of elementary processes in non-thermal plasma processes^[6].

The primary process plays the role to generate active species, especially radicals and ions. This process includes ionization, excitation, dissociation and charge transfer. The typical timescale for the primary processes is around a couple of nanoseconds. The secondary process is the process where chemical reactions between the primary species, i.e. electrons, radicals, excited molecules and ions, can be found. This process is usually completed within approximately 10⁻² s.

2.1.2 Plasma chemistry

The most widely used method for the formation of non-thermal plasma is by the application of an external electric field between two electrodes surrounding a volume of gas. The plasma can be operated either at low pressures or at atmospheric pressure and above.

Every discharge has its typical gas breakdown voltage (V_b) which is defined as the minimum voltage required to breakdown a gas resulting in a plasma (or discharge). This V_b is dependent on the gas and the reactor configuration, i.e. the pressure and the distance between the electrodes^[1]. When a voltage is applied, free electrons, which exist to some extent in a gas volume as a result of an interaction with cosmic radiation, will become accelerated. If the voltage comes close to the breakdown voltage, the current flow will increase drastically due to an intensive avalanche of electrons in the discharge gap between the electrodes. These high energy electrons will collide with gas molecules giving rise to the primary process as discussed in section 2.1.1. A more detailed description of these processes is listed in **Table 2-1**.

Table 2-1: The main plasma processes. A and B represent atoms and M stands for a temporary collision partner^[1].

Electron/Molecular Reactions	
Excitation	$e^- + A_2 \rightarrow A_2^* + e^-$
Dissociation	$e^- + A_2 \rightarrow 2 A + e^-$
Attachment	$e^- + A_2 \rightarrow A_2^-$
Dissociative attachment	$e^- + A_2 \rightarrow A^- + A$
Ionization	$e^- + A_2 \rightarrow A_2^+ + 2 e^-$
Dissociative ionization	$e^- + A_2 \rightarrow A^+ + A + e^-$
Recombination	$e^- + A_2^+ \rightarrow A_2$
Detachment	$e^- + A_2^- \rightarrow A_2 + 2 e^-$
Atomic/Molecular Reactions	
Penning dissociation	$M + A_2 \rightarrow 2 A + M$
Penning ionization	$M^* + A_2 \rightarrow A_2^+ + M + e^-$
Charge transfer	$A^{+/-} + B \rightarrow B^{+/-} + A$
Ion recombination	$A^- + B^+ \rightarrow AB$
Neutral recombination	$A + B + M \rightarrow AB + M$
Decomposition	
Electronic	$e^- + AB \rightarrow A + B + e^-$
Atomic	$A^* + B_2 \rightarrow AB + B$
Synthesis	
Electronic	$e^- + A \rightarrow A^* + e^-, A^* + B \rightarrow AB$
Atomic	$A + B \rightarrow AB$

The electrons are much lighter than their other collision partners and therefore only a small portion of the energy is transferred at each collision. In most non-thermal plasmas for gas processing, the plasma is only weakly ionized. The degree of ionization in the plasma can be defined as the ratio of the density of charged particles to the density of neutral species; this is generally in the range of 10^{-7} – 10^{-14} [1].

In an electronically excited gas molecule or atom, an electron exists in a high energy orbital further from the nucleus, whilst an electron “hole” exists in the lower energy orbital that it was originally excited from. This excited state can be metastable,

characterized by a rather long lifetime, or it can spontaneously return to its more stable ground state or another lower level. When this de-excitation to a lower energy orbital occurs, the excess energy is released in the form of a photon. Furthermore, the plasma can exhibit a visible glow if the energies of the emitted photons are in the visible region of the electromagnetic spectrum.

In plasma processing of gases, each of the plasma species may have different roles. Electrons, being the first to receive energy from the electric field, distribute this energy through collisions, generating the first reactive species (see section 2.1.1). By vibrational excitation some energy can be transferred into gas heating, which can also accelerate some chemical reactions in the plasma. Because the electrons generate reactive species, like ions and radicals, certain reactions can occur, which normally would require high energy, when following thermal reaction pathways. Eventually, the goal is to control the complex chemical processes in plasma by selecting the appropriate gases, plasma type and operating conditions for the required application.

2.2 Non-thermal plasmas for environmental applications

In this section an overview of different NTPs used for environmental applications is presented.

2.2.1 Dielectric Barrier Discharge (DBD)

The DBD was first developed in 1857 by Ernst Werner Von Siemens for use in ozone production and was originally called the silent discharge^[6]. The DBD is a high pressure, non-thermal, low temperature plasma. The configuration of a DBD is similar to an

arc with two electrodes and an air gap, but a DBD has the addition of a high breakdown voltage material placed in between the electrodes to prevent arcing, often a dielectric. In practice, one electrode is grounded and the other is attached to a high frequency (60 Hz - 100 kHz) and high voltage power source (0 - 50 kV) which can be accomplished in a variety of possible configurations, as seen in **Figure 2-2**^[7].

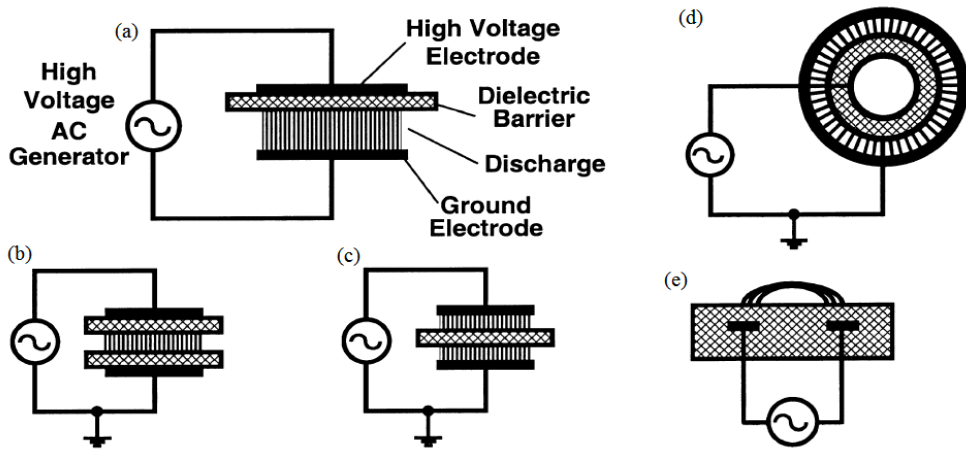


Figure 2-2: Several DBD configurations^[7]. (a), (b) and (c) are different configurations for planar DBDs, (d) is an end-on-view of a cylindrical DBD and (e) is a surface DBD or more commonly known as a plasma actuator.

When a voltage greater than the breakdown voltage is applied to a DBD reactor, short-living microdischarges will be generated in the discharge gap. It can be deemed that the plasma is enclosed in the volume surrounded by these microdischarges. The microdischarges are distributed randomly in time and space and are approximately cylindrical. The typical radius and duration of microdischarges are 100 μm and 1-100 ns, respectively^[1].

A microdischarge will be generated when the local electron density at a certain location in the discharge gap reaches a critical

value. The charges transferred by an individual microdischarge would accumulate on the dielectric surface, resulting in the reduction of the applied electric field. Subsequently, the microdischarges would extinguish when the electric field is reduced to an extent that the electron attachment prevails over ionization. The next microdischarge at the same location can only take place when the local electron density is raised to the critical value again. Therefore, the dielectric (such as quartz, ceramic,...) has two functions: limiting the charge transferred by an individual microdischarge and spreading the microdischarge over the electrode surface^[1,8]. Indeed, such a dielectric will prevent the transition of the microdischarge to an arc discharge and it will increase the homogeneity (spreading on the surface), so that the probability of the collisions between electrons and background gas molecules increases. This discharge will be investigated in this PhD dissertation.

2.2.2 Corona discharge

Corona gas discharges are low energy electric discharges with a non-thermal ionization that takes place in the vicinity of an electrode of sufficiently low radius of curvature, at atmospheric conditions. They typically have an extremely non-uniform electric field distribution caused by the sharp edge or sharp point of its electrode(s). Corona plasmas are self-sustained and no external energy, other than that of the electric field, is needed to sustain the gas ionization processes^[9]. Moreover, they can operate both in positive as negative polarity.

Depending on the relative polarity of the electrodes, different forms of the discharge can be distinguished. For a typical point-to-plate electrode configuration, a positive corona is formed at a pointed anode, whilst a negative corona is formed at a pointed cathode. In a positive corona, the initial breakdown of the gas produces a burst pulse, which is limited to the area immediately surrounding the electrode. As the discharge is space-charge

limited, an increase in voltage creates additional charged species, leading to the formation of streamers. These streamers extend into the inter-electrode gap and can be observed at a given time. In this mode, the corona occupies a relatively large active volume and has a low temperature of $\sim 27\text{ }^{\circ}\text{C}$ which is beneficial for gas processing^[10].

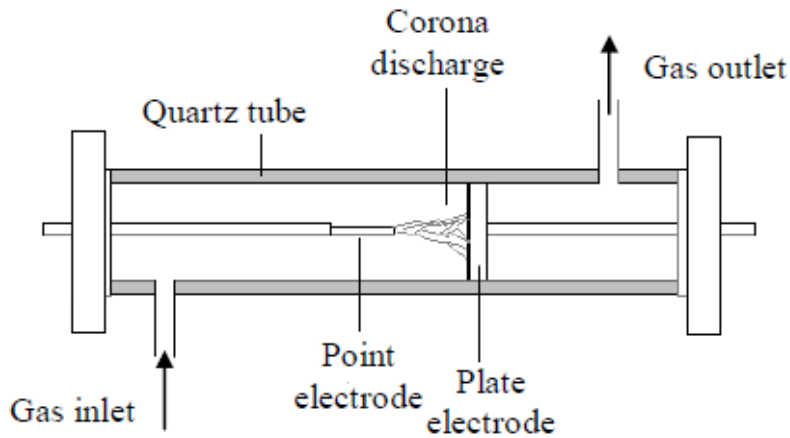


Figure 2-3: Schematic diagram of a corona discharge reactor in a point-to-plate configuration.

2.2.3 Gliding arc discharges

A classical "gliding arc" is a so-called auto-oscillating periodic discharge between at least two diverging electrodes, with the gas flowing in the direction of the diverging electrodes. When a voltage is applied between the electrodes an arc discharge is formed at the smallest inter-electrode gap. Subsequently this arc moves with the gas flow along the electrodes to the exit nozzle. The arc grows with an increasing inter-electrode gap until it extinguishes. At that same moment a new arc will be formed again at the smallest inter-electrode distance to start a new cycle.

The gliding arc plasma can be operated in the thermal and non-thermal regime depending of the applied power and flow. Furthermore, the arc can be operated in the transition regime which is an evolving arc starting in the thermal regime going to the non-thermal regime. This regime combines the benefits of both regimes, making the discharge energy-efficient^[1]. A schematic figure and a picture of a classical gliding arc are presented in **Figure 2-4**.

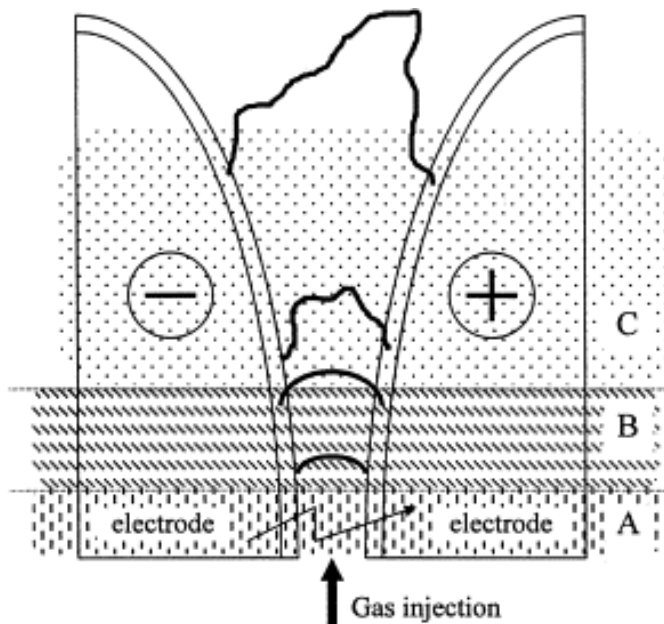


Figure 2-4: Schematic diagram of a gliding arc configuration: (A) reagent gas break-down; (B) equilibrium heating phase; (C) non-equilibrium reaction phase^[11].

2.2.4 Microwave discharges

In a microwave discharge the energy coming from electromagnetic waves in the microwave range is transferred to the plasma. This energy coupling can be performed by many ways, but the most typical one is the coupling with waveguides^[1]. In this configuration a dielectric tube is placed orthogonal on the electromagnetic waves. The plasma is then controlled and ignited in the quartz tube. Furthermore, a tangential gas flow is used to stabilize the plasma.

Normally, at pressures around 100 torr, non-equilibrium conditions can be generated with the microwave plasma which results in an electron temperature around 1 eV and a gas temperature below 1000 K^[1]. In general, the energy-efficiency of the microwave discharges, at least for CO₂ conversion, decreases with increasing pressure, which makes the pressure one of challenges for industrial application. **Figure 2-5** shows a schematic diagram of a typical microwave discharge configuration used for gas processing.

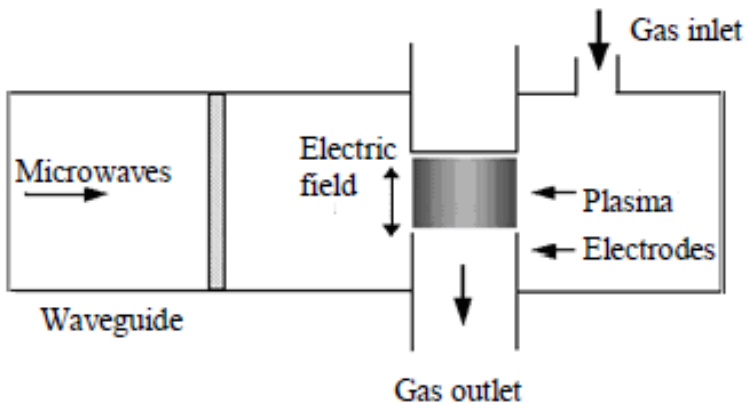


Figure 2-5: Schematic diagram of a microwave discharge.

2.2.5 Packed bed reactor

A packed-bed reactor is actually a special modification of the DBD reactor (see section 2.2.1). For this modification the gap between two parallel electrodes is packed with dielectric pellets, such as barium titanate beads (BaTiO_3) or glass beads. One of the most important properties of these materials is their high dielectric constant, which can vary between 4 for glass up to 20000 for BaTiO_3 . Some typical configurations are presented in **Figure 2-6**. In (a) a parallel plate configuration is used while (b) presents a cylindrical configuration.

The dielectric pellets can concentrate the electrostatic lines of flux leading to enhanced electric fields at the contact points between the beads. As there are many contact points, the average electric field can be enhanced and in turn also the average energy of the electrons. This enhancement can increase the electric field with a factor of 10 to 250 depending on the dielectric constant, curvature and contact angle of the packing material^[12]. Furthermore, a lower voltage can be used to ignite the discharge because of the reduced gap distance inside the reactor.

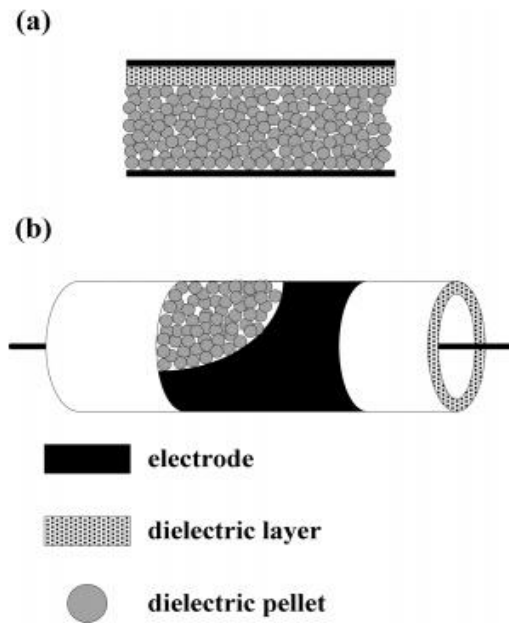


Figure 2-6: Packed bed DBD configurations^[12]: parallel plate (a) and cylindrical (b).

2.3 Applications investigated in this PhD dissertation

In the previous section (section 2.2), a general overview of the principle and the configuration is given, for a variety of plasmas used for environmental purposes. In this section, we will focus more on the actual application by discussion two major applications in gas processing. The first section will cover flue gas treatment, while the second covers the splitting of carbon dioxide.

2.3.1 Flue gas treatment

Currently, there is significant interest for the development of non-equilibrium plasma methods for gas purification and abatement. The most common discharge types for this application, reported in literature are DBDs, corona discharges and packed bed surface discharges^[13-16]. These methods are based on the formation of a high concentration of chemically active species (i.e., O₃, O and N₂ metastable molecules) in the polluted gas stream using non-equilibrium low-temperature plasma, without appreciable heating of the treated gas flow. Those generated chemically active species will react with the pollutants and decompose them into less toxic end products (such as CO₂, CO, ...)^[4].

Table 2-2 gives an overview of the different plasma systems used for flue gas treatment, together with an indication on their characteristic electron and gas temperature (high/medium/low). Indeed several treatments are possible with plasma systems; however, it must be clear that the destruction of ozone depleting substances (ODS) and VOCs cover most of the plasma systems. For this reason, the aim of this dissertation will be to investigate the abatement/destruction of VOCs.

Table 2-2: List of plasma systems used for the treatment of flue gases, with an indication on their characteristic electron and gas temperature as well as the actual treatment^[17].

	Electron temperature	Gas temperature	Treatment flue gases
Electron beam	Extremely high	Low	Acid gases, VOC
Dielectric Barrier discharge	Medium	Low	Oxidation of VOC or acid gases
Packed bed reactor	High	Low	PFC, oxidation of VOC
Pulsed corona	Medium	Low	VOC
Pulsed power	High	Medium	Acid gases
Flow stabilized corona	Locally high	Low	Acid gases, VOC, toxic gases
RF discharge	Medium	High	ODS/VOC
Microwave discharge	Medium	Medium	ODS/VOC

The use of DBDs for the control of gaseous pollutants was addressed by several researchers, with first publications in the beginning of the 90's^[18–23]. Nowadays, more and more papers are published for the plasma abatement of VOCs by a DBD, presenting advanced reactor configurations, including packed bed reactors (see section 2.2.5), the combination of plasma with catalyst in so-called plasma catalysis, and even micro plasma reactors with and without catalyst^[24–26]. Each of these configurations demonstrated an improvement in terms of removal and energy efficiency; however, the total performance gap between plasma technology and the conventional destruction technology is still too small to be a competitive alternative.

In this dissertation we have chosen to investigate the abatement of ethylene (C₂H₄) in a DBD as a case study, but we expect that the results could also be used as a guideline for other hydrocarbons or VOCs. Indeed, ethylene is a well-known and widely investigated hydrocarbon in plasma catalysis, photocatalysis and combustion science^[14,27–32]. It is an odorless and colorless gas which exists in nature and is generated by human

activities, such as engine exhausts, petrochemical derivative and in thermal power plants^[33]. Moreover, it is used in the food industry to ripen tomatoes, bananas, pears, and a few other fruits postharvest^[34]. It is harmful for mankind, causing anesthetic illness and contributes to photochemical smog^[35]. More details of this application, and on the model investigation itself, can be found in **PART II (Chapter 4 and Chapter 5)**.

2.3.2 CO₂ splitting

In recent years, there is a growing interest in the conversion of CO₂ into value-added chemicals or new fuels by means of plasma technology^[1,2,36–85]. This includes both pure CO₂ splitting into CO and O₂^[1,36–58], as well as the reaction with CH₄ (i.e., so-called dry reforming)^[2,59–78], H₂^[79,80] or H₂O^[82–85], yielding syngas and other useful products, such as methanol, formaldehyde and formic acid. Different types of plasmas have been applied for this purpose, but most research is carried out with dielectric barrier discharges (DBD)^[36–45,50,51,59–75,78,79], microwave plasmas^[52,54,57,76,83,84] and gliding arc discharges^[56,58,77].

At the same time, the large scale adoption of renewable energy sources poses a challenge regarding efficient storage and easy transport of the electricity produced (i.e., during peak moments on the grid). The most efficient solution appears to be chemical storage in fuels^[86]. Since fuels offer a much higher gravimetric and volumetric energy storage capacity, they have much higher energy densities than electrical storage techniques and they match the existing worldwide liquid fuel infrastructure^[86,87]. As such, the current transition to renewable energy sources does not only give plasma processes a clean electricity source, but because of the high operation flexibility, plasmas can be turned on and off quickly, making it a suitable technology for storing intermittent sustainable energy in a chemical form.

To overcome the inert character of CO₂, gas discharges can be very useful, as the electrons can activate the molecules. More specifically, the vibrational excitations can stimulate the dissociation and the electronic excitations can stimulate ionization. Indeed, to have an efficient splitting, it is important that energy is transferred to where it is needed.

In a molecule there are four major channels into which energy can be transferred: the vibrational, electronic, rotational and translational (kinetic) channels. Each of these channels has different chemical pathways for dissociation with a different energy efficiency. For example, by exciting the vibrational states of CO₂ with a microwave discharge, an energy efficiency of up to 90% was achieved^[1].

To obtain a better view on the energy transfer in CO₂ dissociation, the molecular states and their CO₂ dissociation pathways are described below:

- 1) Vibrational state: meaning that the energy is transferred to bending and stretching modes of the chemical bonds. By transferring this energy to the vibrational state a certain stress will be induced in the C-O bonds, which eventually causes them to break directly. Furthermore, the transferred energy will lower the reaction activation barriers with other species (see also **Chapter 6**). Fridman suggested that the asymmetric stretch mode is the most efficient mode for dissociation of CO₂^[1].
- 2) Electronic state: meaning that the energy is transferred to electrons in higher energy levels. In this case, high energy electrons will induce electron impact dissociation reactions and recombination reactions that directly dissociate CO₂.

- 3) Rotational state: this is when the energy is transferred to the rotation of the molecule around its axis. However, this mode does not initiate any dissociation pathways for CO₂.
- 4) Translational (kinetic energy): is the energy transferred to the motion of the molecules. Although high energy collisions can cause CO₂ dissociation (by mode conversion to other molecular states), it is not considered as an important dissociation pathway.

Rotational and translational excitation are inefficient pathways for CO₂ dissociation. Rotational excitation does not have a direct pathway for molecular dissociation and must be mode-converted to the other three energy states to be useful for dissociation. Increasing the kinetic energy of molecules for the purpose of dissociation requires accelerating heavy particles to high speeds at low pressure and having them collide with another. This is inefficient because the kinetic energy is easily transferred to other energy states, and the process requires very low pressures for efficient ion/neutral particle acceleration.

The most efficient CO₂ dissociation pathway transfers all of its energy into vibrational excitation, while keeping translational, electronic and rotational energies at a minimum^[36,88]. Indeed, the bending and stretching of molecular bonds caused by vibrational energy takes the most direct path to dissociation. Furthermore, assuming that the bending and stretching of molecular bonds is not enough to break CO₂ bonds, the stress on the molecular bonds lowers the activation barrier for chemical reactions (see also **Chapter 6**).

However, when not all energy is transferred to vibrational excitation, such as in DBDs, electronic excitation is the next best dissociative process. Electronic excitation will induce dissociation

pathways of CO₂, such as dissociative attachment, direct electron impact dissociation, and dissociative ionization (see section 2.1.2 and **Chapter 6**).

As mentioned in the beginning of this section, in order to use CO₂ as a feedstock gas, it can be split into O₂ and CO, which is a valuable feedstock gas for the chemical industry. Although the atomic and molecular plasma chemistry can be very complex (as discussed above and in section 2.1.2), the splitting of CO₂ can be summarized as follows:



Thermodynamically, this reaction requires 283 kJ/mol or 2.94 eV/molecule at 400K and atmospheric pressure.

In this dissertation, the focus will be on splitting of CO₂ in a DBD, because it has a very simple design, which is beneficial for up-scaling, when moving to real applications. This was demonstrated already many years ago for the large scale production of ozone^[1,81]. Moreover, it operates at atmospheric pressure, which is again most suitable for practical applications. Finally, it can easily be combined with a packing (of simple dielectric beads and/or catalytic material) (see also section 2.2.5)^[37,50,59,61,67–71], which opens perspectives for the selective production of targeted compounds. More details of this application, as well as of the model investigation itself, can be found in **PART III (Chapter 6, Chapter 7 and Chapter 8)**.

2.4 Aim of this PhD dissertation

The aim of this PhD dissertation is to obtain more insight into the complex chemistry of the applications discussed in the previous sections (sections 2.3.1 and 2.3.2), by using computer simulations. Furthermore, a verification of the simulations is also performed by a series of validation experiments. Both the model and the validation experiments will be outlined in the next chapter (**Chapter 3**).

In **Chapter 4** we aim to investigate the influence of electrons, metastable nitrogen and radicals on the initial destruction process of ethylene in dry air. We use a kinetic model to predict the influence of different ethylene concentrations at different values of specific energy deposition (SED).

In **Chapter 5** we aim to investigate not only the initial destruction but the complete destruction process of ethylene in humid air for a series of parameters, i.e. SED, concentration, humidity. The goal of this chapter is to give conclusions about the energy efficiency and the environmental impact of ethylene destruction by a DBD.

Chapter 6 aims to get information about the initial splitting of CO₂ in a pulsed plasma system, such as a DBD. Furthermore, we investigate the contribution of the vibrational and electronic excitation states, as well as all other plasma species. Also, the effect of accumulation is investigated by simulating a series of pulses.

In **Chapter 7** the model described in **Chapter 6** will be extended to cover real time scales, and a detailed experimental study will be carried out. In this chapter we aim to investigate the energy

efficiency and the conversion for a series of parameters (dielectrics, gap, flow and power) to obtain an idea of the maximum efficiency of CO₂ splitting in DBDs. Furthermore, we aim to present a simple chemical model to predict the conversion in DBDs.

Finally, in **Chapter 8** we aim to investigate the trapping of oxygen by adding a hydrogen source (CH₄ and H₂), which can enhance the chemical conversion into water. The reason of this study is that, if oxygen can be trapped, the separation of the products of CO₂ splitting is expected to be more simple and cheaper.

2.5 References

- [1] A. Fridman, *Plasma Chemistry*, Cambridge University Press, New York, **2008**.
- [2] X. Tao, M. Bai, X. Li, H. Long, S. Shang, Y. Yin, X. Dai, *Prog. Energy Combust. Sci.* **2011**, *37*, 113–124.
- [3] A. M. Vandembroucke, R. Morent, N. De Geyter, C. Leys, *J. Hazard. Mater.* **2011**, *195*, 30–54.
- [4] H. L. Chen, H. M. Lee, S. H. Chen, M. B. Chang, S. J. Yu, S. N. Li, *Environ. Sci. Technol.* **2009**, *43*, 2216–27.
- [5] A. Gutsol, A. Rabinovich, A. Fridman, *J. Phys. D. Appl. Phys.* **2011**, *44*, 274001.
- [6] W. Siemens, *Ann. der Phys. und Chemie* **1857**, *178*, 66–122.
- [7] U. Kogelschatz, B. Eliasson, W. Egli, *Pure Appl. Chem.* **1999**, *71*, DOI 10.1351/pac199971101819.
- [8] U. Kogelschatz, B. Eliasson, W. Egli, *Le J. Phys. IV* **1997**, *07*, C4–47–C4–66.
- [9] E. Rajch, a. Jaworek, a. T. Sobczyk, a. Krupa, *Czechoslov. J. Phys.* **2006**, *56*, B803–B808.
- [10] H. J. Gallon, PhD Dissertation, Dry Reforming of Methane Using, University of Manchester, **2010**.
- [11] A. Fridman, S. Nester, L. A. Kennedy, A. Saveliev, O. Mutaf-Yardimci, *Prog. Energy Combust. Sci.* **1999**, *25*, 211–231.
- [12] H. Chen, H. Lee, S. Chen, Y. Chao, M. Chang, *Appl. Catal. B Environ.* **2008**, *85*, 1–9.
- [13] L. Xia, L. Huang, X. Shu, R. Zhang, W. Dong, H. Hou, *J. Hazard. Mater.* **2008**, *152*, 113–9.
- [14] S. Chavadej, K. Saktrakool, P. Rangsunvigit, L. Lobban, T. Sreethawong, *Chem. Eng. J.* **2007**, *132*, 345–353.
- [15] H.-X. Ding, A.-M. Zhu, X.-F. Yang, C.-H. Li, Y. Xu, *J. Phys. D. Appl. Phys.* **2005**, *38*, 4160–4167.
- [16] Y. Sun, A. Chmielewski, in *Org. Pollut. Ten Years After Stock. Conv. - Environ. Anal. Updat.*, **2012**.
- [17] J.-S. Chang, *Sci. Technol. Adv. Mater.* **2001**, *2*, 571–576.
- [18] B. Eliasson, U. Kogelschatz, *IEEE Trans. Plasma Sci.* **1991**, *19*, 309–323.
- [19] B. Eliasson, W. Egli, U. Kogelschatz, *Pure Appl. Chem.* **1994**, *66*, 1275–1286.
- [20] I. Traus, H. Suhr, *Plasma Chem. Plasma Process.* **1992**, *12*, 275–285.

- [21] I. Sardja, S. K. Dhali, *Appl. Phys. Lett.* **1990**, *56*, 21.
- [22] S. K. Dhali, I. Sardja, *J. Appl. Phys.* **1991**, *69*, 6319.
- [23] M. B. Chang, M. J. Kushner, M. J. Rood, *J. Environ. Eng.* **1993**, *119*, 414–423.
- [24] K. Urashima, K. G. Kostov, Y. Okayasa, T. Iwaizumi, K. Yoshimura, T. Kato, *IEEE Trans. Ind. Appl.* **2001**, *37*, 1456–1463.
- [25] H.-H. Kim, Y.-H. Lee, A. Ogata, S. Futamura, *Catal. Commun.* **2003**, *4*, 347–351.
- [26] A.-A. H. Mohamed, R. H. Stark, J. H. Yuan, K. H. Schoenbach, *IEEE Trans. Plasma Sci.* **2005**, *33*, 1416–1425.
- [27] R. K. Janev, D. Reiter, *ChemInform* **2003**, *34*, DOI 10.1002/chin.200325274.
- [28] Y. Xu, L. Jia, M. Ge, L. Du, G. Wang, D. Wang, *Chinese Sci. Bull.* **2006**, *51*, 2839–2843.
- [29] A.-M. Zhu, Q. Sun, J.-H. Niu, Y. Xu, Z.-M. Song, *Plasma Chem. Plasma Process.* **2005**, *25*, 371–386.
- [30] L. Cloutman, *A Selected Library of Transport Coefficients for Combustion and Plasma Physics Applications*, Livermore, **2000**.
- [31] M. Hussain, S. Bensaid, F. Geobaldo, G. Saracco, N. Russo, *Ind. Eng. Chem. Res.* **2011**, *50*, 2536–2543.
- [32] K. Francke, *Catal. Today* **2000**, *59*, 411–416.
- [33] A. M. Harling, D. J. Glover, J. C. Whitehead, K. Zhang, *Environ. Sci. Technol.* **2008**, *42*, 4546–50.
- [34] S. P. Burg, E. A. Burg, *Plant Physiol.* **1962**, *37*, 179–89.
- [35] J. Li, C. Ma, X. Xu, J. Yu, Z. Hao, S. Qiao, *Environ. Sci. Technol.* **2008**, *42*, 8947–51.
- [36] S. Paulussen, B. Verheyde, X. Tu, C. De Bie, T. Martens, D. Petrovic, A. Bogaerts, B. Sels, *Plasma Sources Sci. Technol.* **2010**, *19*, 034015.
- [37] Q. Yu, M. Kong, T. Liu, J. Fei, X. Zheng, *Plasma Chem. Plasma Process.* **2011**, *32*, 153–163.
- [38] Y. Tagawa, S. Mori, M. Suzuki, I. Yamanaka, T. Obara, J. Ryu, Y. Kato, *Kagaku Kogaku Ronbushu* **2011**, *37*, 114–119.
- [39] J. Wang, G. Xia, A. Huang, S. L. Suib, Y. Hayashi, H. Matsumoto, **1999**, *159*, 152–159.
- [40] R. Li, *Solid State Ionics* **2004**, *172*, 235–238.

- [41] R. Li, Q. Tang, S. Yin, T. Sato, *Fuel Process. Technol.* **2006**, *87*, 617–622.
- [42] R. Li, Q. Tang, S. Yin, T. Sato, *J. Phys. D. Appl. Phys.* **2007**, *40*, 5187–5191.
- [43] R. Li, Q. Tang, S. Yin, T. Sato, *Appl. Phys. Lett.* **2007**, *90*, 131502.
- [44] S. Wang, Y. Zhang, X. Liu, X. Wang, *Plasma Chem. Plasma Process.* **2012**, *32*, 979–989.
- [45] G. Zheng, J. Jiang, Y. Wu, R. Zhang, H. Hou, *Plasma Chem. Plasma Process.* **2003**, *23*, 59–68.
- [46] T. Nunnally, K. Gutsol, A. Rabinovich, A. Fridman, A. Gutsol, A. Kemoun, *J. Phys. D. Appl. Phys.* **2011**, *44*, 274009.
- [47] S. L. Suib, S. L. Brock, M. Marquez, J. Luo, H. Matsumoto, Y. Hayashi, *J. Phys. Chem. B* **1998**, *102*, 9661–9666.
- [48] S. L. Brock, T. Shimojo, M. Marquez, C. Marun, S. L. Suib, H. Matsumoto, Y. Hayashi, *J. Catal.* **1999**, *184*, 123–133.
- [49] L. F. Spencer, A. D. Gallimore, *Plasma Chem. Plasma Process.* **2010**, *31*, 79–89.
- [50] K. Jogan, A. Mizuno, T. Yamamoto, J.-S. Chang, *IEEE Trans. Ind. Appl.* **1993**, *29*, 876–881.
- [51] R. Aerts, T. Martens, A. Bogaerts, *J. Phys. Chem. C* **2012**, *116*, 23257–23273.
- [52] L. Maya, *J. Vac. Sci. Technol. A Vacuum, Surfaces, Film.* **2000**, *18*, 285.
- [53] M. Tsuji, T. Tanoue, K. Nakano, Y. Nishimura, *Chem. Lett.* **2001**, *30*, 22–23.
- [54] A. Vesel, M. Mozetic, A. Drenik, M. Balat-Pichelin, *Chem. Phys.* **2011**, *382*, 127–131.
- [55] A. P. H. Goede, W. A. Bongers, M. G. Graswinckel, R. M. C. van de Sanden, L. Martina, K. Jochen, A. Schulz, W. Mathias, *3rd Eur. Energy Conf. Budapest* **2013**.
- [56] A. Indarto, J. Choi, H. Lee, H. K. Song, *Environ. Eng. Sci.* **2006**, *23*, 1033–1043.
- [57] L. F. Spencer, A. D. Gallimore, *Plasma Sources Sci. Technol.* **2013**, *22*, 015019.
- [58] A. Indarto, D. R. Yang, J.-W. Choi, H. Lee, H. K. Song, *J. Hazard. Mater.* **2007**, *146*, 309–15.
- [59] K. Zhang, B. Eliasson, U. Kogelschatz, *Ind. Eng. Chem. Res.* **2002**, *41*, 1462–1468.
- [60] S. L. Yao, M. Okumoto, A. Nakayama, E. Suzuki, *Energy & Fuels* **2001**, *15*, 1295–1299.

- [61] M. Kraus, B. Eliasson, U. Kogelschatz, A. Wokaun, *Phys. Chem. Chem. Phys.* **2001**, *3*, 294–300.
- [62] B.-B. Hwang, Y.-K. Yeo, B.-K. Na, *Korean J. Chem. Eng.* **2003**, *20*, 631–634.
- [63] Y. Zhang, Y. Li, Y. Wang, C. Liu, B. Eliasson, *Fuel Process. Technol.* **2003**, *83*, 101–109.
- [64] Q. Wang, B.-H. Yan, Y. Jin, Y. Cheng, *Plasma Chem. Plasma Process.* **2009**, *29*, 217–228.
- [65] Q. Wang, H. Shi, B. Yan, Y. Jin, Y. Cheng, *Int. J. Hydrogen Energy* **2011**, *36*, 8301–8306.
- [66] J. Sentek, K. Krawczyk, M. Młotek, M. Kalczywska, T. Kroker, T. Kolb, A. Schenk, K.-H. Gericke, K. Schmidt-Szałowski, *Appl. Catal. B Environ.* **2010**, *94*, 19–26.
- [67] I. Istadi, N. Amin, *Chem. Eng. Sci.* **2007**, *62*, 6568–6581.
- [68] Q. Wang, B.-H. Yan, Y. Jin, Y. Cheng, *Energy & Fuels* **2009**, *23*, 4196–4201.
- [69] H. J. Gallon, H. Kim, X. Tu, J. C. Whitehead, *Energy* **2011**, *39*, 2176–2177.
- [70] H. J. Gallon, X. Tu, J. C. Whitehead, *Plasma Process. Polym.* **2012**, *9*, 90–97.
- [71] X. Tu, H. J. Gallon, M. V Twigg, P. A. Gorry, J. C. Whitehead, *J. Phys. D. Appl. Phys.* **2011**, *44*, 274007.
- [72] N. R. Pinhao, A. Janeco, J. B. Branco, *Plasma Chem. Plasma Process.* **2011**, *31*, 427–439.
- [73] G. Scarduelli, G. Guella, D. Ascenzi, P. Tosi, *Plasma Process. Polym.* **2011**, *8*, 25–31.
- [74] C. De Bie, T. Martens, J. van Dijk, S. Paulussen, B. Verheyde, S. Corthals, A. Bogaerts, *Plasma Sources Sci. Technol.* **2011**, *20*, 024008.
- [75] R. Snoeckx, R. Aerts, X. Tu, A. Bogaerts, *J. Phys. Chem. C* **2013**, *117*, 4957–4970.
- [76] B. Fidalgo, a Dominguez, J. Pis, J. Menendez, *Int. J. Hydrogen Energy* **2008**, *33*, 4337–4344.
- [77] Z. Bo, J. Yan, X. Li, Y. Chi, K. Cen, *Int. J. Hydrogen Energy* **2008**, *33*, 5545–5553.
- [78] H. K. Song, H. Lee, J.-W. Choi, B. Na, *Plasma Chem. Plasma Process.* **2004**, *24*, 57–72.
- [79] B. Eliasson, U. Kogelschatz, B. Xue, L.-M. Zhou, *Ind. Eng. Chem. Res.* **1998**, *37*, 3350–3357.
- [80] M. Kano, G. Satoh, S. Iizuka, *Plasma Chem. Plasma Process.* **2011**, *32*, 177–185.

- [81] U. Kogelschatz, *Plasma Chem. Plasma Process.* **2003**, *23*, 1–46.
- [82] S. Futamura, H. Kabashima, *Carbon Dioxide Utilization for Global Sustainability, Proceedings of 7th the International Conference on Carbon Dioxide Utilization*, Elsevier, **2004**.
- [83] T. Ihara, M. Kiboku, Y. Iriyama, *Bull. Chem. Soc. Jpn.* **1994**, *67*, 312–314.
- [84] T. Ihara, T. Ouro, T. Ochiai, M. Kiboku, Y. Iriyama, *Bull. Chem. Soc. Jpn.* **1996**, *69*, 241–244.
- [85] A. Gutsol, A. Rabinovich, A. Fridman, *J. Phys. D. Appl. Phys.* **2011**, *44*, 274001.
- [86] Z. Jiang, T. Xiao, V. L. Kuznetsov, P. P. Edwards, *Philos. Trans. A. Math. Phys. Eng. Sci.* **2010**, *368*, 3343–64.
- [87] M. Mikkelsen, M. Jørgensen, F. C. Krebs, *Energy Environ. Sci.* **2010**, *3*, 43.
- [88] V. Givotov, A. Fridman, M. Krotov, E. Krasheninnikov, B. Patrushev, V. Rusanov, G. Sholin, *Int. J. Hydrogen Energy* **1981**, *6*, 441–449.

Chapter 3:

Description of the model and the experiments

In this chapter, the model used for the numerical investigation is discussed, starting with the physical background, followed by the approximations used for the power deposition. The second section describes the experiments performed in this dissertation, together with the applied diagnostic tools.

3.1 Model

3.1.1 Physical description of the model

The simulations in this work are performed using the numerical model Global_kin developed by Dorai and Kushner^[1,2]. We used two basic modules of this model: the Boltzmann equation module and a zero-dimensional plasma chemistry module.

First, a reaction mechanism is defined (see “Description of the Chemistry” in **Chapter 4 and Chapter 6**). Next, the Boltzmann equation module calculates the values of the reaction rate coefficients for the electron impact reactions, based on the collision cross sections, and depending on the electron energy. Subsequently, look-up tables with these rate coefficients as a function of electron energy (or electron temperature) are created. These coefficients will then be used as input in the chemistry module to calculate the source terms for the electron impact gas phase reactions, leading to production and loss of the various plasma species. The rate coefficients for the other gas phase reactions, i.e., between heavy plasma species, are adopted from literature. Hence, the time-evolution in number density of the various plasma species is calculated from:

$$\frac{dn_i}{dt} = \sum_j [(a_{ij}^R - a_{ij}^L) k_j \prod_l n_l^{L_l}] \quad (\text{E3-1})$$

where n_i is the density of species i , a_{ij}^R and a_{ij}^L are the right-hand side and left-hand side stoichiometric coefficients of species i in reaction j , k_j is the reaction rate coefficient and $n_l^{L_l}$ is the density of the l^{th} species in the left-hand side of reaction j . Note that no

transport is included in this chemistry module. Indeed, the plasma reactor is considered as a batch reactor, with a uniform concentration of species over the entire reactor volume.

The electron induced reactions depend on electron temperature, which changes, on one hand, due to Joule heating from the applied power, and on the other hand, due to the energy lost in collisions. The electron temperature is calculated from:

$$\frac{d}{dt} \left(\frac{3}{2} n_e k_B T_e \right) = \vec{j} \cdot \vec{E} - \sum_i \frac{3}{2} n_e \nu_{mi} \left(\frac{2m_e}{M_i} \right) k_B (T_e - T_i) + \sum_l n_e k_l N_l \Delta \varepsilon_l \quad (\text{E3-2})$$

where n_e is the electron density, k_B is Boltzmann's constant, T_e is the electron temperature, \vec{j} and \vec{E} are the current density and the electric field in the discharge, ν_{mi} is the electron momentum transfer collision frequency with species i , m_e is the electron mass and M_i and T_i are the mass and temperature of species i . Finally, k_l is the reaction rate coefficient for the l^{th} electron impact process, N_l is the density of the gas phase collision partner and $\Delta \varepsilon_l$ is the corresponding change in the electron energy (hence negative for energy loss). To summarize, the first term expresses the Joule heating, whereas the second and third terms represent the energy loss due to elastic and inelastic collisions, respectively. Since the model is zero-dimensional, the product of current density with electric field is not used here to calculate the Joule heating, but instead, the ratio of the applied power to the plasma volume is used, which is equivalent.

The chemistry module is called every time step, but the Boltzmann module is only called when the background gas

density has changed significantly. In the next chapters the Boltzmann code is called at the middle of each pulse. Indeed, it is not necessary to call this Boltzmann module in every time step. More details on the model can be found in the papers by Dorai and Kushner^[1,2].

In this work the Global_kin model was extended with a reaction analysis module so that automatically an overview is printed of all absolute contributions of the relevant reactions to the production and loss of every species. For the absolute contributions, equation (E3-1) is used. Next to the absolute contributions, also the relative contributions of the relevant reactions to the production and loss of a species are calculated from:

$$\gamma_{ij} = \left((a_{ij}^R - a_{ij}^L) k_j \prod_l n_l^L \right) / \left(\frac{dn_i}{dt} \right)_{prod/loss} \quad (\text{E3-3})$$

where γ_{ij} is the relative contribution of reaction j to the production or loss of species i , which is always evaluated versus the total dn_{ij}/dt production or loss. All the other parameters have the same meaning as in equation (E3-1). It should be mentioned that gas heating was not calculated explicitly in the model, but a fixed gas temperature of 300 or 400K was assumed, depending on the application. We know from experiments that the bulk gas temperature does not rise significantly, i.e., the gas at the outlet is still more or less at room temperature. However, there could be some local heating during one single micro-discharge. For this reason, we investigated the influence on the chemistry, and it does not influence the electron impact reactions, which are found to be the most important reactions during the micro-discharge pulse (see below).

3.1.2 Power deposition in a DBD plasma

DBDs mostly operate in filamentary mode, which can be observed by the many short peaks in the electrical current waveform as shown in **Figure 3-1**. These filaments (streamers) are spread in volume and time, making it very difficult to model in a typical (continuum) plasma model.

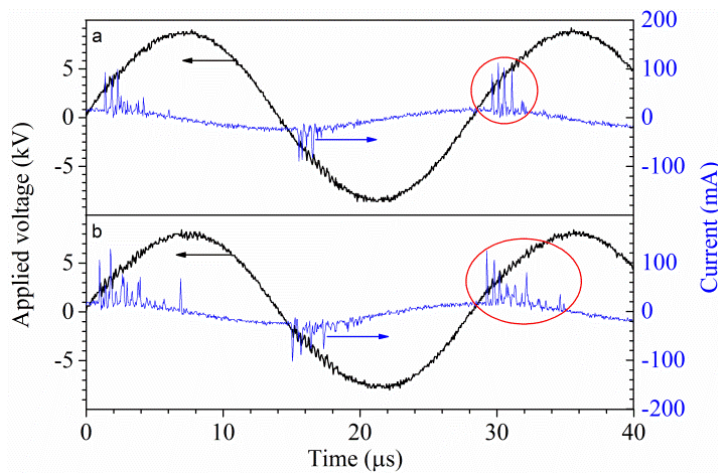


Figure 3-1: Typical current-voltage waveforms for a filamentary DBD.

By using a zero-dimensional kinetic model, this problem can be overcome as follows. The power deposition is defined as a pulse of 1-100 ns, which corresponds to the typical lifetime of such a filament^[3]. The maximum power deposition in this pulse is chosen to obtain typical values for electron temperature and electron density, as reported in literature^[4]. By simulating a number of these consecutive discharge pulses, the filamentary behavior of the DBD can be mimicked.

Although in reality, a large number of filaments occur per half cycle (see **Figure 3-1**), an individual gas molecule will not pass all these filaments, as they are spread in volume. The exact

number of filaments that a typical molecule will pass when flowing through the reactor is not known. Therefore, the model is fitted to the experiment in four steps.

In the first step, an individual pulse is simulated with a certain specific energy input (SEI) for the expected electron temperature and electron density which can be found in literature. In a second step, the SEI from the experiment is evaluated and fitted by repeating the individual pulse at a certain frequency until the SEI in the model is the same as in the experiment. In the last step, the accumulation effects are studied; this step is crucial for large power depositions like in greenhouse gas conversion. In this step, the accumulation of the plasma species to unphysically high densities in subsequent pulses is investigated, which would influence the conversion. If unphysically high densities are observed, the frequency of the pulses should probably be lowered.

Finally, each model consists of a number of repeating pulses, followed by a number of afterglows, simulated for a certain frequency with the same residence time and energy input as in the experiment. However, for the models with greenhouse gas conversion, a correction factor is necessary for the SEI. Indeed, the actual plasma volume (i.e., sum of the filament volumes) is typically much smaller than the total volume of the plasma reactor. Therefore, the specific energy input in the model needs to be typically a factor 10-100 higher, depending on the gas, the reactor geometry and the power under study (i.e., filamentary character or not), to account for this smaller volume^[5,6]. As a result, a correction factor needs to be used for the simulations with high powers, (i.e. many pulses (± 1000)) which are typically used in greenhouse gas conversion. A schematic overview of the modelling methodology is shown in **Figure 3-2**.

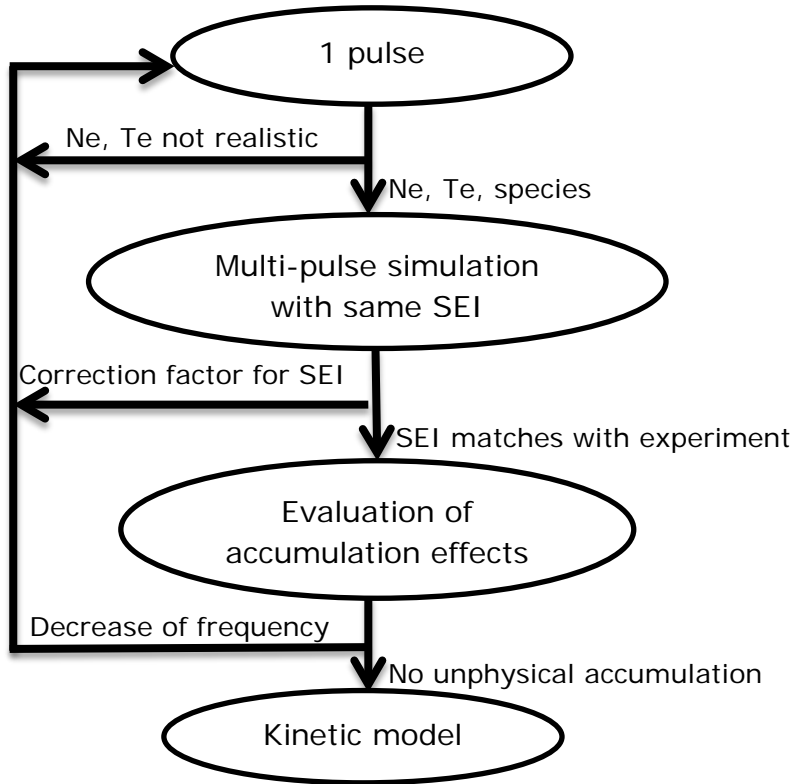


Figure 3-2: Schematic overview of the modelling methodology.

3.2 Experimental set-up

As already indicated in section 2.4, the modelling work goes side by side with validation experiments. The experiments on CO₂ presented in this PhD thesis (**Part III**) were performed at PLASMANT, whereas the experiments for the destruction of ethylene (**Part II**), were performed at the University of Manchester. As the latter experiments were obtained through our collaboration, the experimental set-up used in these experiments will be discussed briefly in **Chapter 4 and Chapter 5**. The experiments for the CO₂ splitting (**Part III**), are performed at PLASMANT in a home-made DBD reactor (**Chapter 7 and Chapter 8**). Therefore, in the next section we will give a detailed description of this reactor and diagnostic tools used in this PhD dissertation.

3.2.1 Description of the DBD reactor

A schematic picture of the experimental setup, both in front view and top view, is shown in **Figure 3-3**. The plasma reactor is a tubular DBD reactor, consisting of a dielectric tube and two concentric cylindrical electrodes. The inner electrode is a stainless steel rod, which is grounded. Several diameters for the inner electrode are used, i.e., 10, 12 and 13 mm, in order to vary the discharge gap (see below). The outer electrode is a nickel foil, connected to a high voltage power supply, and placed around the dielectric tube. The latter has an inner diameter of 16.54 mm and an outer diameter of 22 mm. Two types of dielectrics, i.e., alumina and quartz, are used. The length of the total reactor, including inner electrode and dielectric tube is 200 mm, but the length of the nickel mesh electrode was only 90 mm, and the latter defines the length of the discharge plasma.

The CO₂ gas flow to the plasma reactor is regulated by mass flow controllers (EL-flow of Bronkhorst), and can be adjusted between 10 and 1000 ml/min. The DBD reactor is powered by an AC high-voltage power supply (AFS), providing a maximum peak-to-peak voltage of 40 kV and a variable frequency of 1-90 kHz.

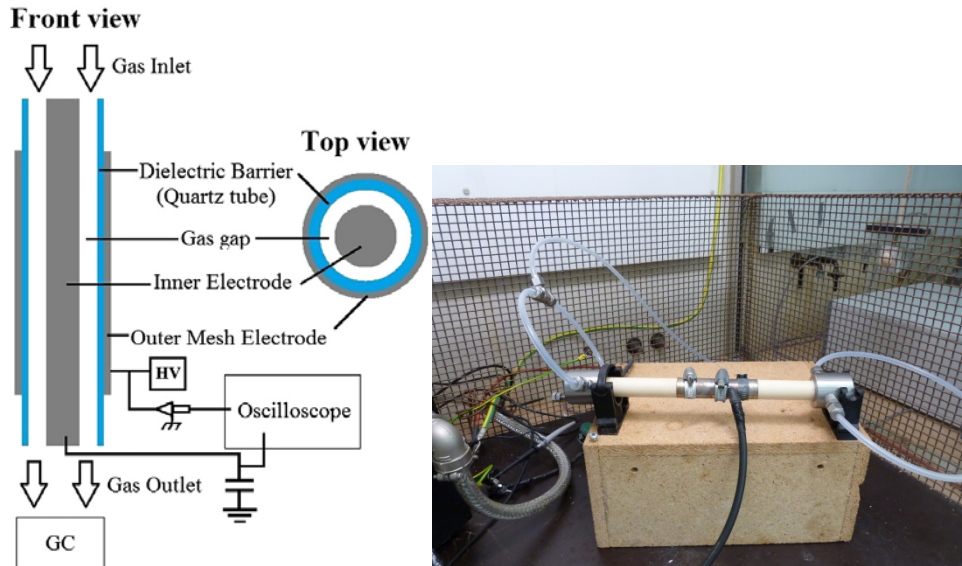


Figure 3-3: Schematic diagram of the experimental setup for the experiments with CO₂, in front view and top view (left) as well as a picture of the set-up (right).

3.2.2 Gas chromatographic analysis

The feed and product gas streams in the experiment were analyzed by gas chromatography (GC). In general, chromatography refers to the chemical separation of mixtures into pure substances and can be used for both gases and liquids.

Chromatography requires a “mobile phase” (containing the mixture to be separated) and a “stationary phase” through which the mobile phase can be eluted. The most common mobile phases are inert gases like argon and helium, but more recently also

nitrogen is used, which is much cheaper compared to noble gases. This gas flows through a column which represents the stationary phase. This stationary phase is in most cases a liquid or solid coating depending on the required separation. Nowadays, most columns are capillary columns which are much smaller compared to packed columns, making the separation faster and better^[7]. By injecting a sample into the column, different gas species pass through the column at different rates, depending on the strength of electrostatic interactions with the walls of the column. In consequence, the gas mixture becomes separated into individual components that reach the end of the column and are detected at different times.

By measuring the retention time of each species in the column, the component gases can be identified by comparison with chromatograms for known standards. In general, the retention times are affected by the type of column, the gas concentration, pressure as well as temperature; therefore, a selection of the appropriate column materials and operating conditions is critical for the resolution of the gas mixture^[7]. A signal is produced by each specific component as it reaches the detector, which results in a peak on the chromatogram at a residence time that is characteristic for that gas. Finally, the relation between the peak area and the gas concentration allows a quantitative measurement.

In this work the feed and product gases are analyzed by a three-channel compact-gas chromatograph (CGC) (Interscience), equipped with two thermal conductivity detectors (TCD) and a flame ionization detector (FID). The first TCD channel contains a Molecular Sieve 5A column for the segregation of the molecular gases, O₂, N₂ and CO, while the second TCD channel is equipped with a Rt-QBOND column for the measurement of CO₂ and C₁-C₂ hydrocarbons. The FID is equipped with a Rtx-5 column for the measurement of C₁ to C₁₀ containing compounds.

A critical remark should be made when performing inline GC analysis on plasma gas processing. When using an external calibration method, the quantities of the gas components are defined as a function of the molar flow rate of each species. However, the latter changes during the conversion, mainly due to chemical reactions and possibly also due to deposition at the reactor walls. Pinhão and co-workers estimated an expansion (contraction) factor for mixtures of He/CH₄/CO₂ between 0.98 and 1.12^[8].

The introduction of noble gases in the gas mixture would allow for an internal calibration, which takes this variation in molar flow rate into account. However, we are interested in the CO₂ conversion without the influence of a noble gas as internal standard. Therefore, in this work, external standards are used, but to account for this expansion effect, we correct, for each specific conversion, for the change in volume due to the change in total number of moles. More specifically, for the reaction under study (CO₂ → CO + 0.5 O₂), this means e.g., at 10% conversion, that the gas mixture contains 90 vol% CO₂, 10 vol% CO and 5 vol% O₂, which amounts to a total of 105 vol%. So we multiply by 105% to correct for this change in volume. Of course, this assumes that no other products than CO and O₂ are formed. These are indeed the only products detected on the GC.

3.2.3 Electrical diagnostics

One other important diagnostic part is the electrical diagnostics of the plasma. The current is recorded by a Rogowski-type current monitor (Pearson 4100), while a high voltage probe (Tektronix P6015A) is used to measure the applied voltage. Furthermore, to obtain the charge generated in the discharge, the voltage on the external capacitor (10 nF) is measured. Finally, all the electrical signals are sampled by a four-channel digital oscilloscope

(PicoScope 6402A). These signals can be used to calculate the discharge power of the discharge itself.

3.2.4 Discharge power

In principle there are two possible methods for determination of the discharge power in a plasma reactor. Although more methods can be distinguished due to a different mathematical processing, the fundamental basics can be reduced to two methods. These methods require the measuring of the high voltage applied to the discharge (U) and the current passing through the discharge (i). The latter can be deduced from the voltage across a resistor (R) or the voltage across a capacitor (C). **Figure 3-4** shows a simple circuit used for measuring the discharge power, which is adaptable to both methods of power determination by the means of a switch.

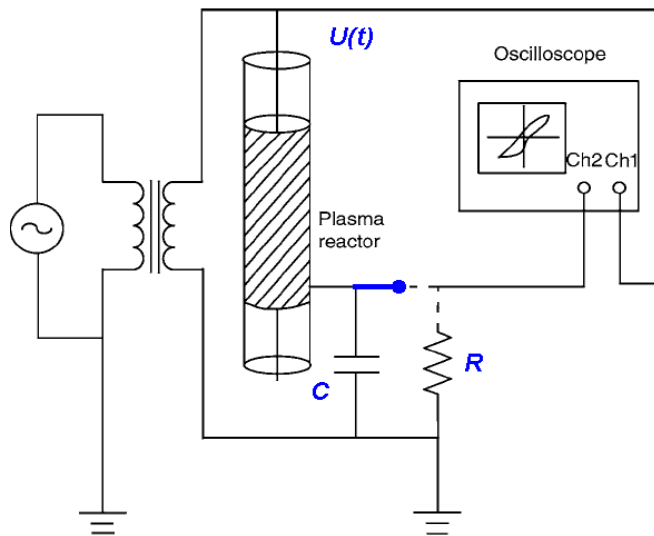


Figure 3-4: Schematic diagram of the circuit used for measuring the discharge power of a DBD reactor^[9].

The first method, i.e. the so-called **current method**, is the most straightforward method. Following the formalism of Feng and Castle^[10] the instantaneous power $p(t)$ of the discharge is given by:

$$p(t) = U(t) * i(t) \quad (\text{E3-4})$$

where $U(t)$ is the high voltage (HV) on the reactor and $i(t)$ is the current flowing through the reactor (and resistor R). The current $i(t)$ is simply found from:

$$i(t) = \frac{V_R(t)}{R} \quad (\text{E3-5})$$

where $V_R(t)$ is the voltage across a resistor R . The average power over a single cycle of the high voltage, period T , is given by

$$P = \frac{1}{T} \int_{t_0-T/2}^{t_0+T/2} p dt = \frac{1}{T} \int_{t_0-T/2}^{t_0+T/2} U(t) * i(t) dt = \frac{1}{T} \int_{t_0-T/2}^{t_0+T/2} \frac{U(t) * V_R(t)}{R} dt \quad (\text{E3-6})$$

where t_0 is the center of the cycle.

However, the main problem with this method occurs when DBDs operate in the filamentary mode. Indeed, DBDs can operate in a homogeneous mode with only one current peak during each half period, or in a filamentary mode with many current peaks, as shown below in **Figure 3-5**. If the plasma operates in the filamentary mode, many microdischarges are formed, representing short (2-100 ns) current pulses in the waveform. To capture all these data, an oscilloscope with a very high bandwidth is necessary and even then the overlap of current pulses makes the use of the current method very difficult to perform accurately^[11].

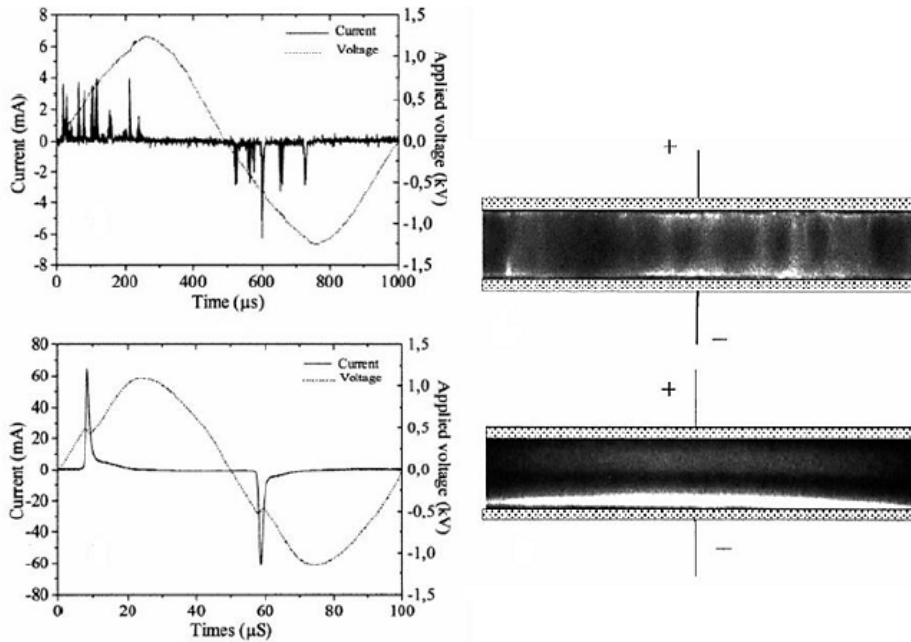


Figure 3-5: Comparison between DBD modes: The top graphs represent the filamentary mode and the bottom graphs represent the homogeneous mode^[14].

Manley^[12] introduced an alternative way to record the current pulses, with the so-called **Lissajous Method**. He replaced the probe resistor R by a probe capacitor C . The capacitor accumulates a charge from the current flowing through the reactor and this can be determined by measuring the voltage on the capacitor V_c .

$$q(t) = C * V_c(t) \tag{E3-7}$$

The capacitor stores the charges and therefore, no charges are lost by an inaccurate oscilloscope bandwidth or overlapping peaks. The energy per cycle, W , can be found from (E3-6) by multiplying by T .

$$W = \int_{t_0-T/2}^{t_0+T/2} U(t) * i(t) dt \quad (\text{E3-8})$$

The current flowing through the measuring capacitor, C , is given by:

$$i(t) = \frac{dq}{dt} = \frac{C * dV_c}{dt} \quad (\text{E3-9})$$

Therefore, the energy per cycle becomes:

$$W = \int_{t_0-T/2}^{t_0+T/2} U(t) * C * V_c(t) dt = \int_{t_0-T/2}^{t_0+T/2} U(t) * dq(t) \quad (\text{E3-10})$$

By recording $U(t)$ and $q(t)$ as a series of n regularly sampled points over one cycle, we can approximate (E3-10) by a summation, using trapezoidal integration, as:

$$W \approx \sum_{k=1}^n \left(\frac{U_{k+1} + U_k}{2} \right) (q_{k+1} - q_k) \quad (\text{E3-11})$$

Finally, the plasma power can be found by multiplying the energy per cycle. So, if the voltage U has a frequency, f , where $f = 1/T$, we have:

$$P = f * W = f * \sum_{k=1}^n \left(\frac{U_{k+1} + U_k}{2} \right) (q_{k+1} - q_k) \quad (\text{E3-12})$$

Furthermore, the plasma power is represented by the area of the U - q Lissajous figure, with the voltage $U(t)$ on the x-axis and the charge $q(t)$ on the y-axis, as shown in **Figure 3-6**.

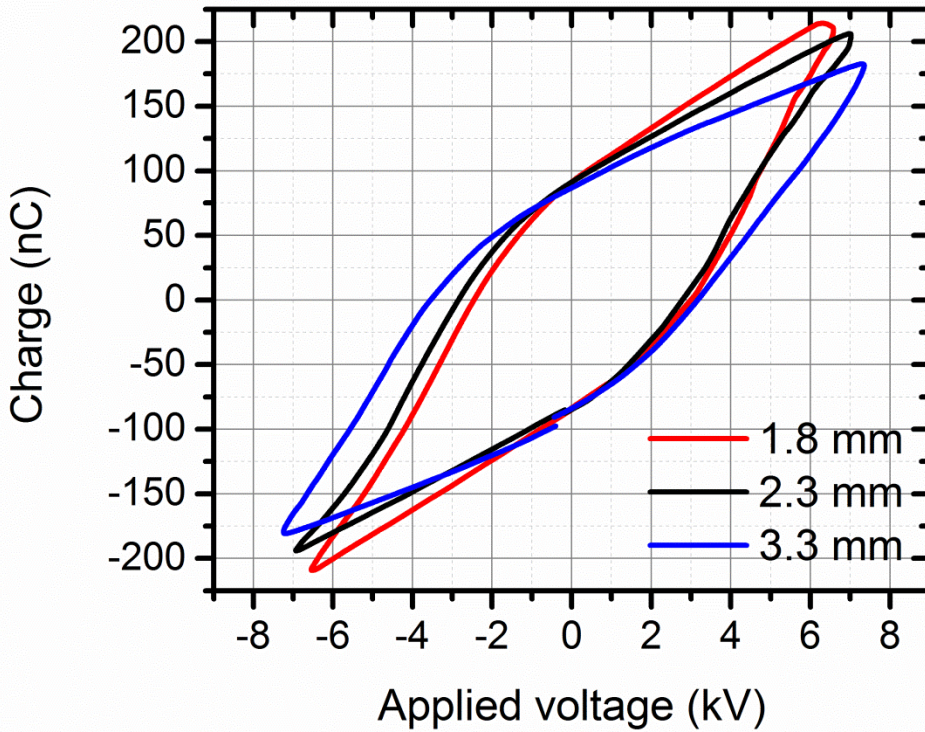


Figure 3-6: Lissajous plots three different discharge gaps of a DBD, at a plasma power of ± 35 W, with a quartz dielectric^[13].

3.3 References

- [1] R. Dorai, Modeling of Atmospheric Pressure Plasma Processing of Gases and Surfaces, University of Illinois at Urbana-Champaign, **2002**.
- [2] R. Dorai, M. J. Kushner, K. Hassouni, *J. Appl. Phys.* **2000**, *88*, 6060.
- [3] A. Fridman, *Plasma Chemistry*, Cambridge University Press, New York, **2008**.
- [4] A. Fridman, S. Nester, L. A. Kennedy, A. Saveliev, O. Mutaf-Yardimci, *Prog. Energy Combust. Sci.* **1999**, *25*, 211–231.
- [5] O. Motret, C. Hibert, S. Pellerin, J. M. Pouvesle, *J. Phys. D. Appl. Phys.* **2000**, *33*, 1493–1498.
- [6] O. Motret, S. Pellerin, M. Nikravech, V. Massereau, J. M. Pouvesle, **1997**, *17*.
- [7] D. A. Skoog, D. M. West, F. J. Holler, Stanley R. Crouch, *Fundamentals of Analytical Chemistry*, Thomson Learning, Belmont, **2004**.
- [8] N. R. Pinhao, A. Janeco, J. B. Branco, *Plasma Chem. Plasma Process.* **2011**, *31*, 427–439.
- [9] H. J. Gallon, PhD Dissertation, Dry Reforming of Methane Using, University of Manchester, **2010**.
- [10] R. Feng, G. S. P. Castle, S. Jayaram, *IEEE Trans. Ind. Appl.* **1998**, *34*, 563–570.
- [11] H.-E. Wagner, R. Brandenburg, K. V. Kozlov, A. Sonnenfeld, P. Michel, J. F. Behnke, *Vacuum* **2003**, *71*, 417–436.
- [12] T. C. Manley, *Trans. Electrochem. Soc.* **1943**, *84*, 83.
- [13] U. Kogelschatz, *Plasma Chem. Plasma Process.* **2003**, *23*, 1–46.
- [14] A. Bogaerts, *Plasmatechnologie (Cursus)*, Universiteit Antwerpen, Wilrijk, **2014**.

PART II:

STUDY OF

ETHYLENE DESTRUCTION

Chapter 4:

Single pulse simulations for ethylene destruction in DBDs

In this chapter, we describe the simulation results for one pulse, for ethylene destruction in a DBD. Indeed, the initiation of the destruction process of VOCs with low temperature plasmas is still not well understood. It is stated in literature to be dominated by electrons, radicals and metastable species. Yet, the specific contribution of these species and the influence of the specific energy deposition and/or VOC concentration have never been investigated. Here, a kinetic model is presented for the destruction of ethylene in low temperature plasmas, that allows to calculate the relative importance of all plasma species and their related reactions. Modifying the ethylene concentration and/or the specific energy deposition had a major impact on the relative importance of the radicals (i.e., mainly O atoms) and the metastable nitrogen (i.e., more specifically $N_2(A^3\Sigma^+_u)$) in the destruction process. The results show that the direct destruction by electron impact reactions for ethylene can be neglected; however, the influence of $N_2(A^3\Sigma^+_u)$ can certainly not be neglected.

Aerts, R., Tu, X., De Bie, C., Whitehead, J. C., & Bogaerts, A. (2012). An Investigation into the Dominant Reactions for Ethylene Destruction in Non-Thermal Atmospheric Plasmas. *Plasma Processes and Polymers*, 9(10), 994–1000. doi:10.1002/ppap.201100168

4.1 Introduction

A crucial step in the destruction process of VOCs is the initiation step, where the reactions with the VOC itself occur. This process is in most cases not well known and therefore many authors suggest different types of dominant reactions. Some authors suggest direct electron impact dissociation as one of the dominant destruction reactions, but also dissociation reactions induced by metastables and radicals are believed to be dominant destruction mechanisms^[1-9]. As far as we know, no comparative investigation has been carried out before to support these assumptions. For this reason, we will use a kinetic model to calculate the contributions of the most important species and reactions to the initiation of the ethylene destruction.

4.2 Description of the chemistry and the experiment

4.2.1 Description of the chemical model

The physical description of the model is already described in **Chapter 3**. Therefore, in this section only the chemistry will be described. The complete destruction process of ethylene in dry air (79% N₂ and 21% O₂), is modelled with a chemistry which contains 545 reactions and 103 species (see Appendix I).

To identify the important reactions, a brief summary of the mechanism for the destruction of ethylene is presented here. Most of the initial destruction of ethylene is caused by reactions with O atoms to form products like CH₂, CH₃ and CHO radicals but also stable molecules, such as formaldehyde. Formaldehyde is also mentioned as one of the major by-products in other papers

involving ethylene destruction by plasma^[10,11]; on its turn it will react with OH radicals to form CHO radicals, which finally react further to form CO and CO₂. Our simulations predict that the CHO radicals are the controlling reactants for the selectivity of CO and CO₂, together with the oxidation of CO to CO₂ by O atoms. An alternative destruction pathway is the destruction by reaction with nitrogen metastable molecules to C₂H₂ and to C₂H₃ radicals. These species will then react with O atoms or molecular oxygen to form formaldehyde, which reacts further to CO and CO₂ as discussed above. One other possible mechanism, but less likely, is the direct destruction by electron impact dissociation reactions, which can also produce C₂H₂ and C₂H₃ radicals.

The metastable molecules represent both the N₂(A³Σ⁺_u) and N₂(A¹Σ⁻_u) species, whereas the radicals playing a role in the ethylene destruction, include O atoms, OH and CH₃ radicals, and H atoms.

A DBD is typically characterized by many current pulses (or streamers); however, the exact number of pulses each molecule passes per time is not known and modelling streamer formation is beyond the scope of this study. In literature, two different energy deposition systems are typically assumed in zero dimensional plasma modeling of DBDs. The first one assumes a uniform processing of the gas as it passes through the reactor. During each half-cycle, the micro-discharge current pulses create active species which then will initiate or continue the chemistry^[12,13]. This method does not only describe a current pulse and an afterglow but also accumulation effects of certain radicals as a function of time, which is also the case in realistic DBDs. The second method describes only one current pulse and therefore neglects the accumulation by repetition of the pulses^[14].

In this Chapter, the second method was applied, to focus on the initiation process during one pulse. However, in the next Chapter, the real-time simulation of ethylene destruction, including many consecutive pulses, will be described. As our main interest lies here in the detailed chemistry of one current pulse to indicate the effect of short living species, such as metastables and electrons, on the initiation step, the results for one current pulse of 200 ns with a rise and fall time of 10 ns are shown only, followed by an afterglow of almost 1 ms at a gas temperature of 300 K. The electron density is calculated to be in the order of 10^{12} cm^{-3} at a specific energy deposition of 5 mJ/cm^3 and 10^{15} cm^{-3} at a SED of 2500 mJ/cm^3 , which is in reasonable agreement with literature^[14,15]. However, simulations were also performed with a multi-pulsed energy deposition of 10 ns pulses and a frequency of 7.35 Hz. This simulation indicated only a slight increase in removal efficiency by 1% caused by accumulation of O atoms. Other accumulating species like ozone and NO_x were also found in higher densities compared to one pulse but did not influence the removal efficiency.

4.2.2 Description of the validation experiments

The validation experiments of this model were performed at the University of Manchester. The experimental setup used is a cylindrical DBD reactor consisting of two coaxial fused quartz tubes, both of which are covered by a stainless steel mesh electrode. A more detailed description of the reactor can be found in Tu et al. without a catalyst inside the reactor and a gap of 3 mm instead of 4.5 mm^[16]. The reactor volume is 11.4 cm^3 and the experiments are carried out at a constant flow rate of 1 slm at 300 K, which corresponds to a residence time of 0.684s. The gases are analyzed by a two-channel micro-gas chromatography (Agilent 3000A) equipped with two thermal conductivity detectors (TCD). The first channel contains a Molecular Sieve 5A column for the separation of H₂, CO and CH₄, while the second channel is

equipped with a Poraplot Q column for the measurement of CO₂ and C₂–C₄ hydrocarbons. The gas chromatograph is calibrated for a wide range of concentrations for each gaseous component using reference gas mixtures (Agilent Universal Gas Mixture) and other calibrated gas mixtures. All the electrical signals are sampled by a four-channel digital oscilloscope (Agilent DSO6014A, 2 GHz). To measure the discharge power, an online real-time measurement based on LABVIEW is used for calculation of the Q–U Lissajous figures.

4.3 Results and Discussion

4.3.1 Validation of the model

In order to validate the model, simulations and experiments were performed for concentrations of 3500 ppm, 8700 ppm and 13700 ppm ethylene in dry air as a function of the SED. The upper graph in **Figure 4-1** presents the removal efficiency from the experiment and the simulations for the three different concentrations mentioned above. The removal efficiency (RE) is defined as:

$$\text{Removal efficiency (\%)} = \text{RE (\%)} = \frac{C_2H_4_{inlet} - C_2H_4_{outlet}}{C_2H_4_{inlet}} \quad (\text{E4-1})$$

The figure shows a reasonable agreement between the simulations and the experiment for the different values of SED and ethylene concentration. An almost complete destruction is reached at 2500 mJ/cm³ for 3500 and 8700 ppm ethylene; the highest concentration of 13700 ppm requires a slightly higher SED for complete destruction, i.e., around 2750 mJ/cm³. It should be mentioned that a stable plasma could not be obtained experimentally at lower values of SED and therefore the ethylene

concentration was chosen here to be higher than commonly used concentrations in VOC treatment (which are typically below 1000 ppm). However, for the validation of the model at lower values of concentration and SED, a comparison with results adopted from literature in NO_x abatement has been presented in the bottom graph of **Figure 4-1**. The bottom graph presents the density of ethylene and NO, as obtained by our simulations compared with the work of Niessen et al.^[13], who investigated the influence of 2000 ppm C₂H₄, 430 ppm NO and 70 ppm NO₂ in a 77/13/10 N₂/O₂/H₂O air mixture. A reasonable agreement for the density of C₂H₄ and NO is obtained, even at lower values of SED as compared to our own experiments. The bottom graph also presents results of Shin et al.^[11] who investigated the influence of 500 ppm ethylene and 500 ppm NO in a gas mixture containing 90/10 N₂/O₂ and also in this case a reasonable agreement is reached.

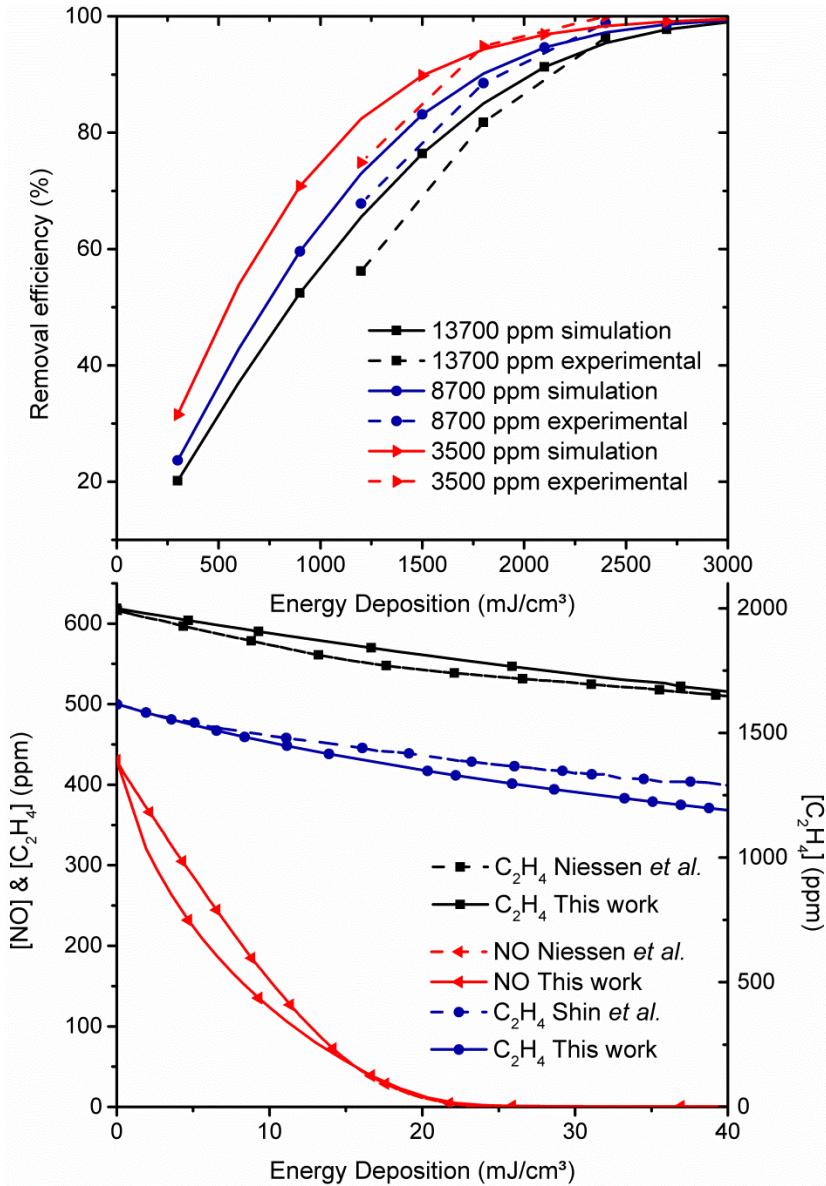


Figure 4-1: The top graph presents a comparison between the simulations and the experiments for the removal efficiency as a function of the specific energy density (SED) at 13700 ppm, 8700 ppm and 3500 ppm ethylene in dry air at a gas temperature of 300 K. The bottom graph presents a comparison of the ethylene and NO densities between our simulations and simulations adopted from literature in Niessen *et al.*^[34] and Shin *et al.*^[33], for the same conditions. The left y-axis is for the comparison with the data of Niessen *et al.*, whereas the comparison with the data of Shin *et al.* corresponds to the right y-axis.

To compare the results in terms of energy efficiency with data from literature, **Table 4-1** presents the amount of pollutant in ppm that can be converted for a SED of 1 mJ/cm³ for different pollutants, together with the inlet concentration, as adopted from literature. Ethylene has similar energy efficiencies as trichloroethylene; however, for aromatic molecules the energy efficiency is typically a factor of 10 lower. Indeed, benzene and toluene have a resonance system which makes the molecules much more stable compared with ethylene and trichloroethylene.

Table 4-1: A comparison of the energy efficiency, in ppm/(mJ/cm³), between different pollutants, as adopted from literature and our own work (for C₂H₄). The efficiency is calculated by dividing the converted concentration of the pollutant by the specific energy deposition.

Type of pollutant	Inlet concentration [ppm]	Efficiency [ppm/(mJ/cm ³)]	Reference
C ₂ H ₄	500-13700	3-5.5	This work
C ₂ HCl ₃	500	15-20	[12]
C ₆ H ₆	500-2700	0.25-0.9	[17]
C ₇ H ₈	150	0.5	[18]

4.3.2 Effect of concentration

In order to investigate the role of different species (i.e., radicals, metastables and electrons) in the initiation step of the destruction process, **Figure 4-2** presents the relative contributions of these species, integrated over time during the pulse and afterglow, for a mixture of dry air with 10, 50, 100, 500, 1000, 5000, 10000 ppm ethylene, at a SED of 1200 mJ/cm³. The most important metastables playing a role in the destruction of ethylene are the N₂(A³Σ⁺_u) species, whereas oxygen atoms are the most important radicals in the destruction process.

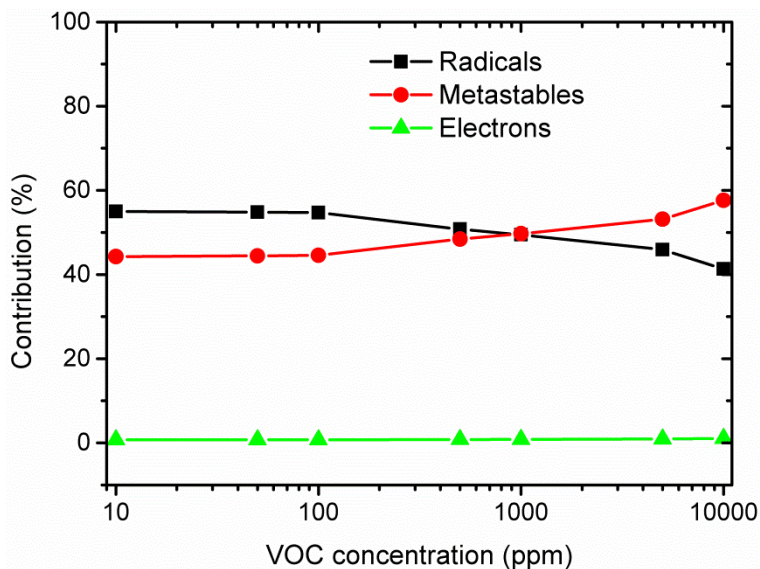


Figure 4-2: Calculated relative contributions of radicals, metastables and electrons to the destruction of ethylene, as a function of the ethylene concentration in dry air at a SED of 600 mJ/cm³.

The constant line for electrons indicates a very low contribution (below 1%), independent of the concentration. Unlike the electrons, the relative importance of metastable nitrogen $N_2(A^3\Sigma^+_u)$ and O atoms is influenced to some extent by the ethylene concentration. Below 100 ppm, a constant ratio between the metastables and the radicals is found, with the latter being slightly more important in the destruction process. Between 100 and 1000 ppm, a decrease in the relative contribution for the radicals and an increase for the metastables is observed. At around 1000 ppm, the radicals and metastables appear to contribute to nearly the same extent to the destruction of ethylene. Finally, above 1000 ppm, the relative contribution of the metastables further increases, whereas the radicals become gradually less important. This change in dominant destruction species upon increasing ethylene concentration suggests that the metastables, which have a shorter lifetime than the radicals, now have a larger chance of reacting with the ethylene molecules.

Further, it is clear from **Figure 4-2** that the electrons are not suitable for the direct destruction of ethylene. It should be realized, however, that electron impact dissociation reactions become more important for concentrated systems, which are found e.g., in the reforming of greenhouse gases^[19,20] (see **Chapters 6, 7 and 8** below).

Some authors also indicated that electrons could play a role in the destruction in an indirect way^[21,22]. For example, toluene could be ionized by electrons:



This ion can recombine with another electron to have a dissociative recombination:



This process could explain the destruction of some aromatics; however, in the case of ethylene this destruction mechanism is not observed.

4.3.3 Effect of specific energy deposition

Also the influence of SED on the initiation step was investigated, for a constant ethylene concentration of 500 ppm. The results shown in **Figure 4-3** indicate the radicals as the dominant species at low values of SED; however, they become clearly less important with increasing SED. At around 1200 mJ/cm³, the radicals and metastables appear to be equally important, and at still higher values of SED, the metastables become the dominant destruction species. The relative contribution of the electrons is

below 1%, even at these high values of SED, which indicates that direct destruction by electrons is not important for the destruction of ethylene, even with concentrations of several thousands of ppm. The reason for this will be discussed below.

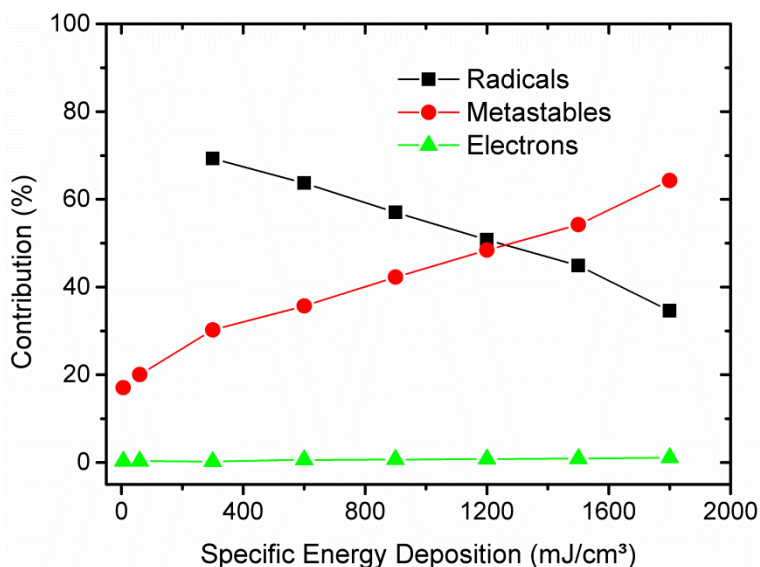


Figure 4-3: Calculated relative contribution of radicals, metastables and electrons to the destruction of ethylene, as a function of the SED in a dry air mixture containing 500 ppm ethylene.

By increasing the SED, more energy is introduced into the system, which is beneficial for the electron impact reactions. These reactions will produce more important destruction species, like O atoms and nitrogen metastables; the latter becoming more important with increasing energy. Above 1200 mJ/cm³, the production of metastables becomes dominant, so that more than half of the destruction is established by the metastables. Of course, at higher SED, the electrons will also be more energetic and in principle more capable for direct ethylene destruction. However, the metastables can transfer more energy to the ethylene molecules than the electrons, due to their higher mass.

4.3.4 Contribution of the important destruction reactions

In order to obtain additional information about the important destruction pathways, the relative contributions of the most important destruction reactions during the current pulse and the afterglow, for 100 ppm ethylene at a SED of 600 mJ/cm³, are plotted in **Figure 4-4**. These conditions are used because they are suitable for industrial application of low temperature plasmas, as a result of the low energy consumption and a corresponding simulated removal efficiency of 79%.

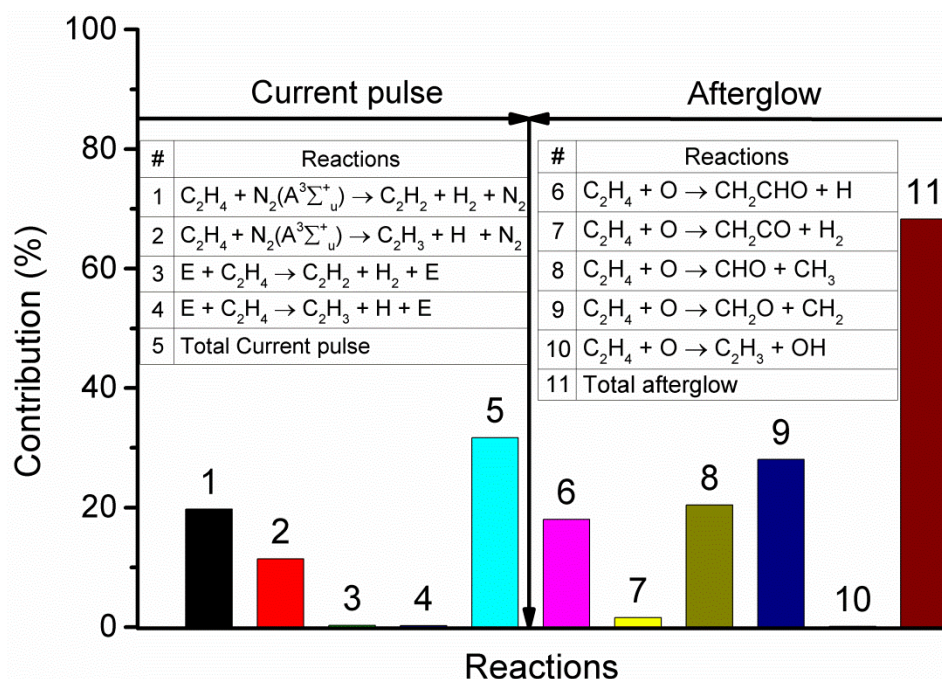
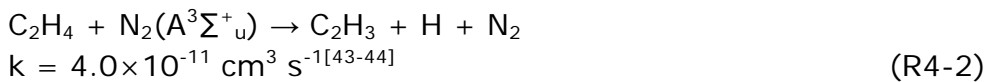
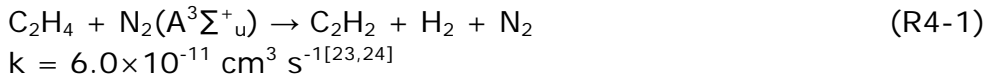


Figure 4-4: Calculated relative contributions of the most important destruction reactions during the current pulse and the afterglow region, together with the corresponding total values (i.e., relative contributions of total destruction either during the pulse or afterglow, i.e., no. 5 and 11, respectively), for an ethylene concentration of 100 ppm and a SED of 600 mJ/cm³.

As is clear from this figure, the metastables, or more precisely the metastable nitrogen $N_2(A^3\Sigma^+_u)$ species, with a maximum density of $1.6 \times 10^{16} \text{ cm}^{-3}$, are the dominant destruction species during the current pulse. The following reactions:

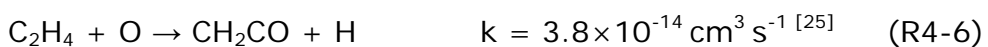
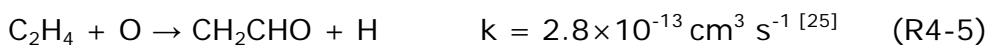


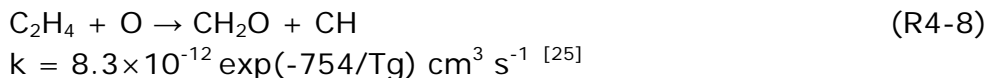
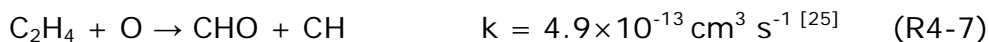
contribute together for 31 % to the direct destruction of ethylene. Reaction (R4-1) converts ethylene to acetylene, which is a more stable product than the vinyl radical formed by reaction (R4-2), and therefore reaction (R4-1) is slightly more important. The contribution of the electron impact dissociation reactions:



is less than 1%, as also indicated above.

The afterglow of the plasma is dominated by O atoms species which have a density of approximately $1 \times 10^{17} \text{ cm}^{-3}$. From the following reactions with O atoms:



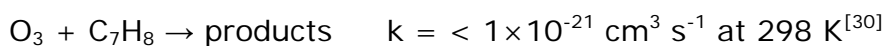
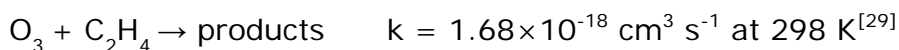


reaction (R4-8) is the most important destruction process, with a contribution of 28%. Also reactions (R4-5) and (R4-7) are quite important, with a contribution of 18% and 20%, respectively. Formaldehyde is a major product in the destruction of ethylene, not only because it is created in reaction (R4-8), but also because the products formed in reactions (R4-5), (R4-6), (R4-7), and (R4-9) will eventually react to formaldehyde. When looking at the complete destruction process, the afterglow is responsible for \pm 68% of the total destruction process, which is dominated by O atoms.

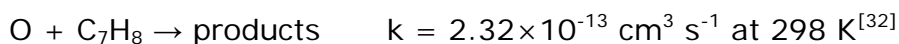
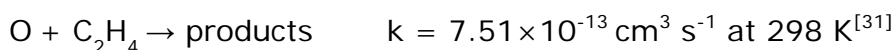
As indicated in the beginning of the chapter, a further increase of the relative contribution of O atoms might be expected when simulating multiple pulses, which can cause accumulation of certain radicals in each pulse and induce a further increase of their relative contribution. This destruction pathway is also indicated to be the most important one by other authors for different VOCs (i.e., trichloroethylene, acetaldehyde and formaldehyde)^[12,22,26].

Finally it is important to stress that other pathways, i.e., with ozone or hydroxyl radicals, which are also reported to be important in VOC destruction literature, are not found in our simulations, for the following reasons^[27,28].

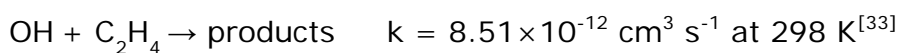
The reaction rate coefficients for the reactions of ozone with VOCs are rather small, as is illustrated here for ethylene and toluene:

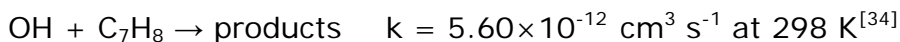


Indeed, the reaction rate coefficients for the corresponding reactions with O atoms are much higher:



However, not only the rate coefficients control the destruction rate of ethylene but also the density of the reacting species. Obviously, it is the product of rate coefficient and species densities which determines the rate. Although the maximum density of ozone ($7 \times 10^{16} \text{ cm}^{-3}$) is only slightly lower than the maximum density of O atoms ($2 \times 10^{17} \text{ cm}^{-3}$), the time-integrated absolute contribution, yields a value of 10^{10} cm^{-3} , which is significantly smaller than for O atoms, i.e., 10^{14} cm^{-3} , in our simulations with ethylene. Therefore, our simulations do not indicate ozone as one of the dominant species in the destruction process. On the other hand, the reactions with the hydroxyl radicals are characterized by a reaction rate coefficient that is even one order of magnitude higher than for O atoms, as illustrated below:





However, the density of the hydroxyl radicals was found to be at least two orders of magnitude lower in our simulations than the density of O atoms (i.e., in the order of 10^{15} cm^{-3} vs. 10^{17} cm^{-3}), at least in dry air. Therefore, the time-integrated absolute contribution yields a value of 10^9 cm^{-3} , which is significantly smaller than for O atoms, i.e. 10^{14} cm^{-3} .

4.4 Conclusion

It is demonstrated by means of modelling that direct electron impact dissociation reactions are negligible for the destruction of ethylene in the range of 10 – 10000 ppm and 0 – 3000 mJ/cm³. The radicals, especially O atoms, appear to be the dominant destruction species at low ethylene concentrations and low values of SED, whereas at high concentrations and high values of SED, the nitrogen metastables $\text{N}_2(\text{A}^3\Sigma^+_{\text{u}})$ are found to dominate the destruction process.

4.5 References

- [1] W.-J. Liang, J. Li, J.-X. Li, T. Zhu, Y.-Q. Jin, *J. Hazard. Mater.* **2010**, *175*, 1090–5.
- [2] H. Huang, D. Ye, D. Y. C. Leung, F. Feng, X. Guan, *J. Mol. Catal. A Chem.* **2011**, *336*, 87–93.
- [3] N. Blin-Simiand, F. Jorand, L. Magne, S. Pasquiers, C. Postel, J.-R. Vacher, *Plasma Chem. Plasma Process.* **2008**, *28*, 429–466.
- [4] A. S. Chiper, N. Blin-Simiand, M. Heninger, H. Mestdagh, P. Boissel, F. Jorand, J. Lemaire, J. Leprovost, S. Pasquiers, G. Popa, et al., *J. Phys. Chem. A* **2010**, *114*, 397–407.
- [5] Y. S. Mok, V. Demidyuk, J. C. Whitehead, *J. Phys. Chem. A* **2008**, *112*, 6586–6591.
- [6] I. Orlandini, U. Riedel, *J. Phys. D. Appl. Phys.* **2000**, *33*, 2467–2474.
- [7] M. J. Kushner, *J. Appl. Phys.* **1993**, *73*, 51–55.
- [8] C. Fitzsimmons, F. Ismail, J. C. Whitehead, J. J. Wilman, *J. Phys. Chem. A* **2000**, *104*, 6032–6038.
- [9] L. Magne, S. Pasquiers, N. Blin-Simiand, C. Postel, *J. Phys. D. Appl. Phys.* **2007**, *40*, 3112–3127.
- [10] M. Hübner, J. Röpcke, *J. Phys. Conf. Ser.* **2009**, *157*, 012004.
- [11] H. H. Shin, W. S. Yoon, *Plasma Chem. plasma Process.* **2003**, *23*, 681–704.
- [12] D. Evans, L. A. Rosocha, G. K. Anderson, J. J. Coogan, M. J. Kushner, *J. Appl. Phys.* **1993**, *74*, 5378.
- [13] W. Niessen, O. Wolf, R. Schruft, M. Neiger, *J. Phys. D. Appl. Phys.* **1998**, *31*, 542–550.
- [14] R. Dorai, M. J. Kushner, **2001**, *34*, 574–583.
- [15] R. Dorai, M. J. Kushner, *J. Appl. Phys.* **2000**, *88*, 3739–3747.
- [16] X. Tu, H. J. Gallon, M. V Twigg, P. A. Gorry, J. C. Whitehead, *J. Phys. D. Appl. Phys.* **2011**, *44*, 274007.
- [17] M. Cal, M. Schluep, *Environ. Prog.* **2001**, *20*, 151–156.
- [18] H.-H. Kim, A. Ogata, S. Futamura, *Appl. Catal. B Environ.* **2008**, *79*, 356–367.
- [19] C. De Bie, B. Verheyde, T. Martens, J. van Dijk, S. Paulussen, A. Bogaerts, *Plasma Process. Polym.* **2011**, *8*, 1033–1058.

- [20] H. Kohno, A. A. Berezin, M. Tamura, T. Yamamoto, A. Shibuya, S. Honda, *IEEE Trans. Ind. Appl.* **1998**, *34*, 953–966.
- [21] A. N. Trushkin, I. V. Kochetov, *Plasma Phys. Reports* **2012**, *38*, 407–431.
- [22] W. Liang, J. Li, J. Li, Y. Jin, *J. Hazard. Mater.* **2009**, *170*, 633–638.
- [23] H. Umemoto, *J. Chem. Phys.* **2007**, *127*, 014304.
- [24] N. Moreau, S. Pasquiers, N. Blin-Simiand, L. Magne, F. Jorand, C. Postel, J.-R. Vacher, *J. Phys. D. Appl. Phys.* **2010**, *43*, 285201.
- [25] D. L. Baulch, C. J. Cobos, R. A. Cox, C. Esser, P. Frank, T. Just, J. A. Kerr, M. J. Pilling, J. Troe, R. W. Walker, et al., *J. Phys. Chem. Ref. Data* **1992**, *21*, 411–734.
- [26] H. M. Lee, M. B. Chang, *Plasma Chem. Plasma Process.* **2001**, *21*, 329–343.
- [27] Y. Guo, X. Liao, J. He, W. Ou, D. Ye, *Catal. Today* **2010**, *153*, 176–183.
- [28] S. Schmid, M. C. Jecklin, R. Zenobi, *Chemosphere* **2010**, *79*, 124–30.
- [29] R. Atkinson, D. L. Baulch, R. A. Cox, J. N. Crowley, R. F. Hampson, R. G. Hynes, M. E. Jenkin, M. J. Rossi, J. Troe, *Atmos. Chem. Phys.* **2004**, *4*, 1461–1738.
- [30] D. H. Stedman, H. Niki, *Environ. Lett.* **1973**, *4*, 303–310.
- [31] D. Baulch, C. Cobos, R. Cox, P. Frank, G. Hayman, T. Just, J. Kerr, T. Murrells, M. Pilling, J. Troe, et al., *J. Phys. Chem. Ref. Data* **1994**, *23*, 847–1033.
- [32] J. T. Herron, R. E. Huie, *J. Phys. Chem. Ref. Data* **1973**, *2*, 467.
- [33] R. Atkinson, *Chem. Rev.* **1986**, *86*, 69–201.
- [34] B. J. Finlayson-Pitts, S. K. Hernandez, H. N. Berko, *J. Phys. Chem.* **1993**, *97*, 1172–1177.

Chapter 5:

Real time scale simulations for ethylene destruction in DBDs

In this chapter, the entire reaction pathway of ethylene destruction is investigated in detail, both in dry and humid air, and under more realistic conditions of consecutive pulses. This is an improvement of the model described in **Chapter 4**, where we only investigated the role of electrons on the initiation of the destruction path. In this chapter, the influence of the specific energy deposition on the removal efficiency and the selectivity towards CO and CO₂ is studied for different concentrations of ethylene. The model allows to identify the destruction pathway in dry and humid air. The latter is found to be mainly initiated by metastable N₂ molecules, but the further destruction steps are dominated by O atoms and OH radicals. At increasing air humidity the removal efficiency drops by ±15% (from 85% to 70%), but the selectivity towards CO and CO₂ stays more or less constant at 60% and 22%, respectively. Beside CO and CO₂, also acetylene, formaldehyde and water are identified as by-products of the destruction process, with concentrations of 1606 ppm, 15033 ppm and 185 ppm in humid air (with 20% RH), respectively. Finally, the by-products generated by the humid air discharge itself are investigated, which are the greenhouse gases O₃, N₂O and the toxic gas NO₂.

Aerts, R., Tu, X., Van Gaens, W., Whitehead, J. C., & Bogaerts, A. (2013). Gas purification by nonthermal plasma: a case study of ethylene. *Environmental Science & Technology*, 47(12), 6478–85. doi:10.1021/es400405c

5.1 Introduction

The numerous papers regarding modeling^[1–3] and experimental diagnostics^[4,5] indicate the degree of complexity in plasmas for environmental purposes. Both numerical and experimental results are necessary to fully understand the chemical mechanism in the destruction of ethylene. Previously published modeling work regarding VOCs^[6,7] (i.e. formaldehyde, trichloroethylene, ...) neglected the influence of chemical quenching reactions between metastable N_2 molecules and the hydrocarbon species. However, in the previous **Chapter 4** it is demonstrated that the contribution of N_2 metastables in the initiation step of C_2H_4 could not be neglected. Also Pasquiers and co-workers identified the important role of N_2 metastables in the destruction of different VOCs^[8,9]. Therefore, in the present chapter, the plasma chemistry is expanded to fully take into account the effect of metastable N_2 molecules in the destruction process of ethylene in humid air, in a DBD plasma.

In the previous chapter, the focus was on the role of electrons in the destruction path, for one pulse and afterglow, and it was found that they can be neglected. In the present chapter, the entire reaction pathway is investigated in detail, both in dry and humid air, and under more realistic conditions of consecutive pulses. The effect of humidity on the efficiency of the destruction process will also be evaluated and the important by-products will be identified as well. The latter is extremely important for environmental application of this technology.

5.2 Description of the model and the chemistry

5.2.1 Description of the chemical model

Also here we used the model described in **Chapter 3** developed by Kushner and co-workers. The temperature is chosen 50K higher than the experimental temperature of the gas flow, to take into account local overheating in the micro-discharges itself, which is reported to be around 50K^[10,11].

The chemistry set used in this model can be divided into two subsets. The first subset is for the background gas, i.e., humid air (21(1-x/100) %O₂, 79(1-x/100) %N₂ and x=%H₂O) and the second subset represents the hydrocarbon chemistry. The details of the humid air chemistry set are reported by Van Gaens et al.^[12] and a description of the initially dominant reactions in (humid) air can be found in the work of Kossyi and co-workers^[13]. The hydrocarbon set is based on the chemistry published by Snoeckx et al.^[14] and Aerts et. al.^[1], but it is extended with chemical reactions between N₂ metastable molecules and hydrocarbon species. In total the model contains 113 chemical species and 1639 reactions. More details can be found in **Appendix I**.

5.2.2 Description of the validation experiments

Also in this chapter, validation experiments were performed at the University of Manchester with the same reactor as described in the previous chapter (**Chapter 4**). The experimental setup used is a cylindrical DBD reactor consisting of two coaxial fused quartz tubes, both of which are covered by a stainless steel mesh electrode. A more detailed description of the reactor can be found in Tu et al.^[15], although in the present case no catalyst is placed

inside the reactor. The gap between both quartz tubes is 3 mm. The reactor volume is 11.4 cm³ and the experiments are carried out with a flow rate of 1 slm at 300 K, which corresponds to a residence time of 0.684 s. The molecules C₂-C₄ (representing various hydrocarbons with 2 till 4 C-atoms), CH₄, H₂, CO, CO₂ are analyzed by a two-channel micro-gas chromatograph (GC; Agilent 3000A) equipped with two thermal conductivity detectors (TCD) as described in Tu et. al.^[15]. The molecules NO₂ and N₂O are analyzed by on-line FTIR spectroscopy (Shimadzu 8300) with a long path IR cell (2.76 m). All the electrical signals are sampled by a four-channel digital oscilloscope (Agilent DSO6014A, 2 GHz). A LABVIEW control system is used for the online measurement of the discharge power by the area calculation of the Q-U Lissajous figure.

5.3 Results and discussion

5.3.1 Description of the power deposition

DBDs mostly operate in filamentary mode, which can be observed by the many short peaks in the electrical current waveform as shown in **Figure 5-1** (see also **Chapter 3**).

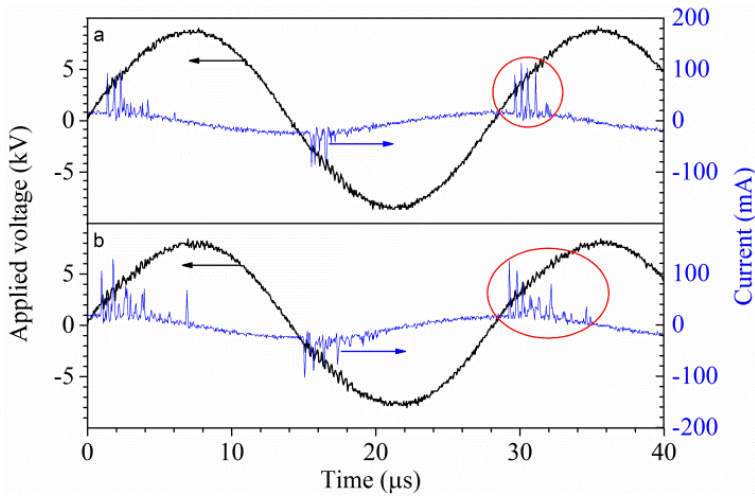


Figure 5-1: Measured voltage (left y-axis) and current (right y-axis) as a function of time, for a specific energy deposition (SED) of 1.2 J/cm^3 (a) and 2.4 J/cm^3 (b), in the case of 3500 ppm C_2H_4 in dry air. The red circles indicate that the number of microdischarge pulses increases as a function of SED (or power).

These filaments (streamers) are spread in volume and time, making it very difficult to model in a typical (continuum) plasma model. By using a zero-dimensional kinetic model, this problem can be overcome as follows (see also **Chapter 3**). The power deposition is defined as a pulse of 15 ns, which corresponds to the typical lifetime of such a filament^[16]. The maximum power deposition in this pulse is chosen to obtain typical values for electron temperature and electron density, as reported in literature^[16]. By simulating a number of these consecutive discharge pulses, the filamentary behavior of the DBD can be mimicked as explained in more detail in **Chapter 3**.

The exact number of filaments that a typical ethylene molecule will pass when flowing through the reactor is not known. Therefore, we have subdivided the total energy deposition in the experiment into a number of triangular pulses (filaments). The individual pulse energy and the number of pulses were adapted to

match the electron temperature adopted from literature and the experimentally obtained electron density, making sure that the total simulated energy deposition is the same as the total energy deposition in the experiment. If the obtained electron temperature and density have realistic values, the other plasma characteristics, including the densities of the other plasma species, are most probably also realistic (see also **Chapter 3**).

It should be mentioned that by increasing the specific energy deposition (SED) in the experiments the number of filaments visually increases, and as a result also the number of peaks in the current waveform becomes higher. **Figure 5-1** illustrates the increase in number of current pulses for a rise in SED from 1.2 to 2.4 J/cm³, for 3500 ppm ethylene in dry air.

In **Figure 5-2**, the values of electron density as obtained from the model and the experiment are plotted as a function of SED, together with the number of simulated discharge pulses through which the ethylene molecules will pass when flowing through the reactor. Note that the electron density obtained from the experiment is not measured directly, but is simply estimated from the electrical current density, as follows: $n_e = J / (E \mu_e)$, where J is the experimental current density, μ_e is the drift mobility for electrons, adopted from Nielsen et al.^[17], and E is the electric field, estimated from the ratio of breakdown voltage and gap^[15,18].

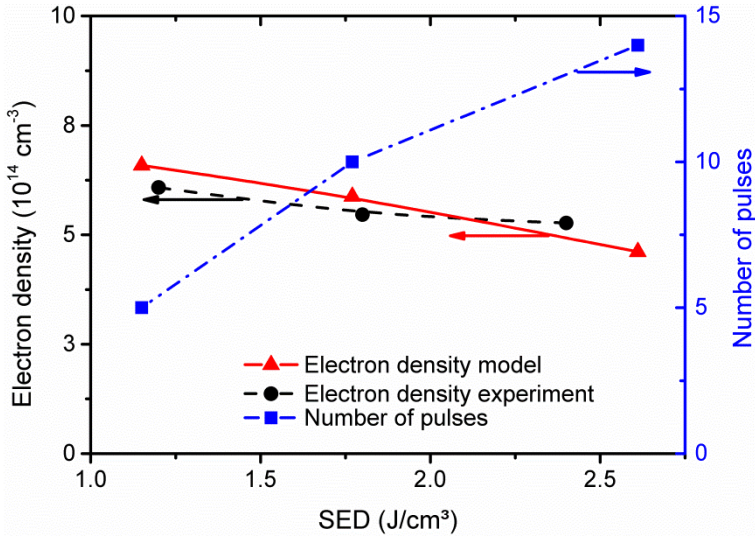


Figure 5-2: Electron density, both calculated from the model and estimated from the experiment, as a function of the specific energy deposition (SED) (left y-axis), as well as the total number of microdischarge pulses assumed in the simulations for a residence time of 0.684 s (right y-axis), for 3500 ppm C₂H₄ in dry air.

The figure shows that both the experimental and calculated electron density drop slightly upon increase of the SED (or the discharge power), and as a result, the number of pulses (filaments) should increase, to correspond to the rise in SED.

5.3.2 Effect of SED on the ethylene destruction process

In this section we will discuss the effect of the SED on the removal efficiency (RE) and on the selectivity of CO (S_{CO}) and CO₂ (S_{CO2}) production, which are defined as:

$$RE (\%) = \frac{C_2H_4_{inlet} - C_2H_4_{outlet}}{C_2H_4_{inlet}} \times 100\% \quad (E5-1)$$

$$S_{\text{CO}} (\%) = \frac{\text{moles of CO produced}}{2 \times \text{moles of C}_2\text{H}_4 \text{ converted}} \times 100\% \quad (\text{E5-2})$$

$$S_{\text{CO}_2} (\%) = \frac{\text{moles of CO}_2 \text{ produced}}{2 \times \text{moles of C}_2\text{H}_4 \text{ converted}} \times 100\% \quad (\text{E5-3})$$

The calculations and experiments are performed for 3500 ppm, 8700 ppm and 13700 ppm ethylene in dry air, in the range of discharge power from 20 to 40 W, corresponding to a SED between 1.2 and 2.4 J/cm³. **Figure 5-3** illustrates the calculated and measured RE, S_{CO} and S_{CO_2} for these three ethylene concentrations as a function of SED.

The RE increases with rising energy deposition, both in the experiments and in the simulations. This is attributed to the larger concentrations of “activating” air species (such as metastable N₂ molecules and O atoms; see below), which destroy the C₂H₄ molecules. It is also clear from **Figure 5-3 (a)** that the RE is the highest at low concentrations of C₂H₄, because the possibility that all C₂H₄ molecules can react with “activating” air species also increases. Nevertheless, at an SED of 2.5 J/cm³, the RE is almost 100% for all C₂H₄ concentrations. Note that the model predicted a somewhat lower RE for the 13700 ppm case compared to the experiment, but in general, the agreement is quite satisfactory. The removal efficiency was previously benchmarked with other VOCs^[1] (see also **Chapter 4**). However, it should be realized that ethylene is quite simple to destroy in a plasma compared to other (e.g., aromatic) VOCs, as can be seen from the high removal efficiencies close to 100% presented in literature for different discharge types^[19,20], for inlet concentrations ranging from 100 ppm till 3%.

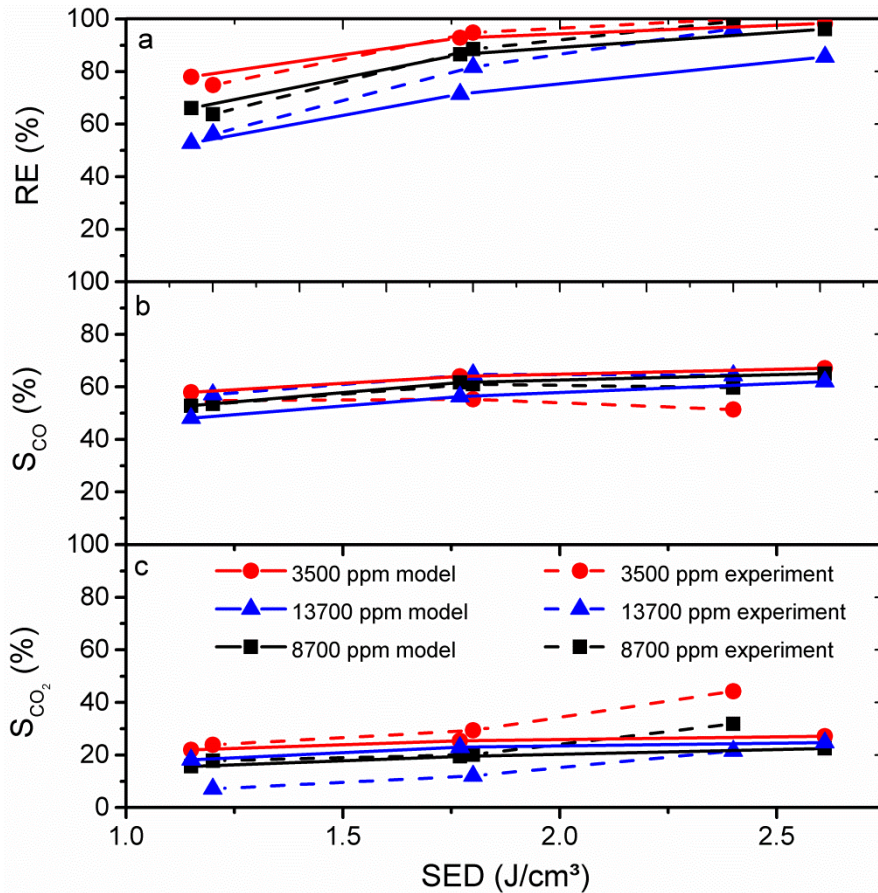


Figure 5-3: Comparison between calculated (solid lines) and measured (dashed lines) removal efficiency (RE) (a), and selectivities towards CO and CO₂, i.e., S_{CO} (b) and S_{CO_2} (c), at different concentrations of C₂H₄ in dry air, and as a function of the SED.

As is clear from **Figure 5-3(b,c)**, there is also a reasonable agreement between the model and experimental results for the CO and CO₂ selectivity. An increase in SED does not influence the CO selectivity to a large extent, which is more or less constant at ± 50 -60%. The selectivity towards CO₂ is in the order of 10-40%, increasing slightly upon higher SED, which is more apparent from the experiments than from the simulations (see **Figure 5-3(c)**). This can be explained by the increasing number of pulses upon rise of the SED, increasing the possibility to convert the by-

products into CO₂. The reason why the CO selectivity remains constant, is that it is more efficiently created from the by-products at higher SED, but at the same time, it is also more efficiently oxidized into CO₂, so that the net production of CO remains constant. Furthermore, for a lower concentration of ethylene, the CO selectivity drops slightly, whereas the CO₂ selectivity increases, indicating that the destruction process becomes "more clean". In general we can conclude that the destruction of C₂H₄ in a DBD is predicted by our model to be in reasonable agreement with the experiment, both for different C₂H₄ concentrations and different specific power depositions. Most of the C₂H₄ is converted to CO as can be seen from the selectivity towards CO ($\pm 60\%$). Moreover, at high values of SED and at low C₂H₄ concentrations, the selectivity towards CO₂ reaches $\pm 40\%$. In this case almost all C₂H₄ is converted into CO and CO₂. At lower values of SED and higher C₂H₄ concentrations, the selectivity towards CO₂ drops to $\pm 10-20\%$, indicating that some by-products are formed, as will be elaborated below.

5.3.3 Identification of the destruction pathway

As the calculated RE and selectivities of CO and CO₂ correspond well with the measured values, both in absolute values as well as the trends as a function of SED and C₂H₄ concentrations, the model can be used to elucidate the destruction pathway of C₂H₄ in a DBD in dry and humid air, which is illustrated in **Figure 5-4**.

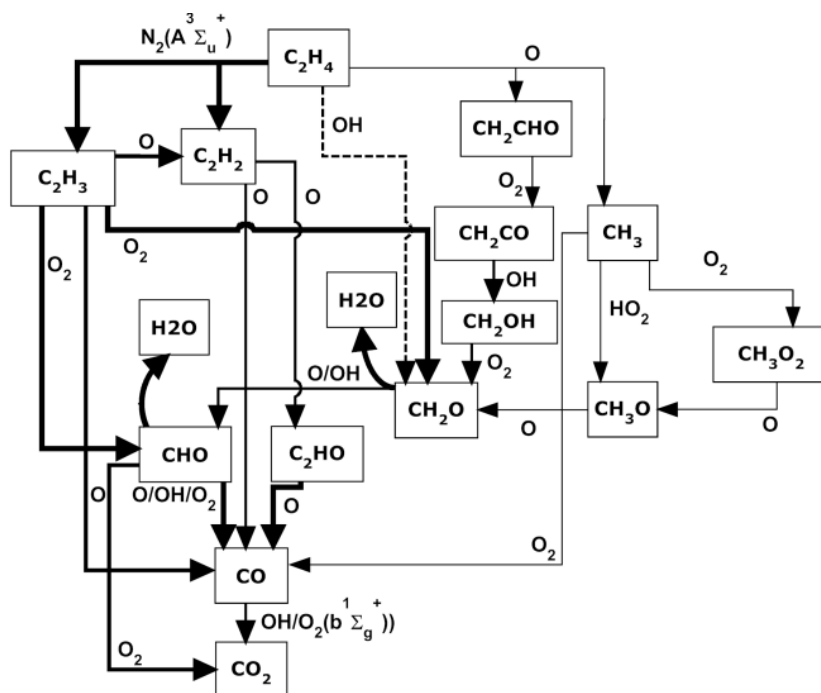


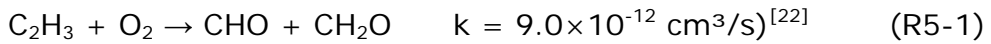
Figure 5-4: Ethylene destruction pathway in dry and humid air, as elucidated by the model. The thickness of the arrows indicates the importance of the various reaction paths. The pathway is more or less similar in both dry and humid air, except for some extra destruction path through OH radicals in humid air, as indicated by the dashed arrow in the figure.

The thickness of the arrows indicates the importance of the various reaction paths. Note that the latter might vary a bit, depending on the values used for some of the rate coefficients (cf. the deviations found for different literature values; see **Appendix I**). Nevertheless, in view of the good agreement between calculated and measured results, we are quite confident that this reaction pathway presents a realistic picture.

In general, both in dry and humid air, two main destruction mechanisms can be distinguished, i.e., upon collision with metastable N_2 molecules (especially $N_2(A^3\Sigma_u^+)$) and with O atoms,

but the first one appears to be most important, producing vinyl radicals (C_2H_3) and acetylene molecules (C_2H_2); see **Figure 5-4**. The fact that acetylene has a triple bond and a high ionization energy of 11.4 eV^[21] makes it very difficult to destroy, and as a result acetylene will be one of the by-products besides CO and CO₂ (see further). Nevertheless, it can also be further oxidized with O towards C_2HO , and finally towards CO and CO₂.

A more important oxidation path, especially in dry air, proceeds through the C_2H_3 radical, which will be oxidized to CHO radicals and formaldehyde (CH_2O):



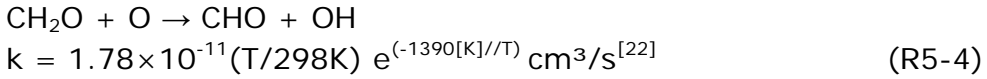
In addition, it can also react with O to CO and CH_3 , or to acetylene and OH:



Note that in **Figure 5-4**, only arrows are drawn towards CO and C_2H_2 , and not to CH_3 and OH, as the latter species are radicals which react further, whereas CO and C_2H_2 are obtained as by-products.

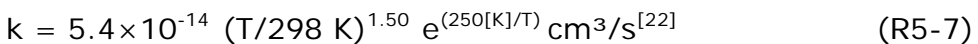
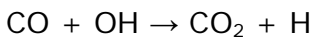
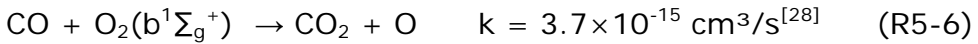
Hübner et al. also reported formaldehyde as one of the by-products in their experimental work on ethylene destruction^[24]. However, formaldehyde is also a VOC which can be destroyed in plasma^[9,25,26]. The latter is also observed in our model, where the formaldehyde concentration decreases for an increasing number of pulses. Indeed, most of the formaldehyde will be further

oxidized to CHO by O or OH, which have their highest density shortly after each pulse:



Reaction of CHO with O, O₂ or OH eventually leads to the formation of CO and CO₂, as is clear from **Figure 5-4**.

Finally, the oxidation process from CO to CO₂ can be assigned to the reaction with O₂(b¹Σ_g⁺) metastable molecules or OH radicals, the latter path being more important:



It should be noted that the paths presented in the right side of the figure contribute for only a few percent to the oxidation pathway, as indicated by the thinner arrows, and they are therefore not discussed in detail here. They become slightly more important in humid air.

The air humidity does not really influence the dominant reaction pathways, but it does affect the relative importance of the different reagents, i.e., OH, O and O₂. The higher OH density in

humid air introduces an extra reaction path (see dashed line in **Figure 5-4**), producing formaldehyde. The effect of the air humidity on the efficiency of the destruction process will be discussed in detail in the next section.

We can summarize the reaction pathway as follows:

- The initial destruction of ethylene in dry air is dominated by metastable N_2 molecules and to a lower extent by O atoms.
- The initial destruction of ethylene in humid air is similar as in dry air, but the OH radicals give rise to an extra destruction path.
- The further destruction path to CO and CO_2 in both dry and humid air is fully controlled by O atoms and OH radicals, and the contribution of the OH radicals increases with increasing humidity.

5.3.4 Effect of the air humidity on the ethylene destruction process

As mentioned in the previous section, an increase in air humidity does not influence the reaction pathway to a large extent, as most of the destruction is initiated by N_2 metastable molecules. **Figure 5-5** presents the effect of air humidity on the RE and on the selectivity towards CO and CO_2 , for an energy deposition of 1.8 J/cm^3 and 8700 ppm C_2H_4 in air. The calculations were performed for relative humidity between 0 and 99%, whereas the experiments could only be carried out until 20% humidity, but at least in this range the agreement between experiment and model is quite good.

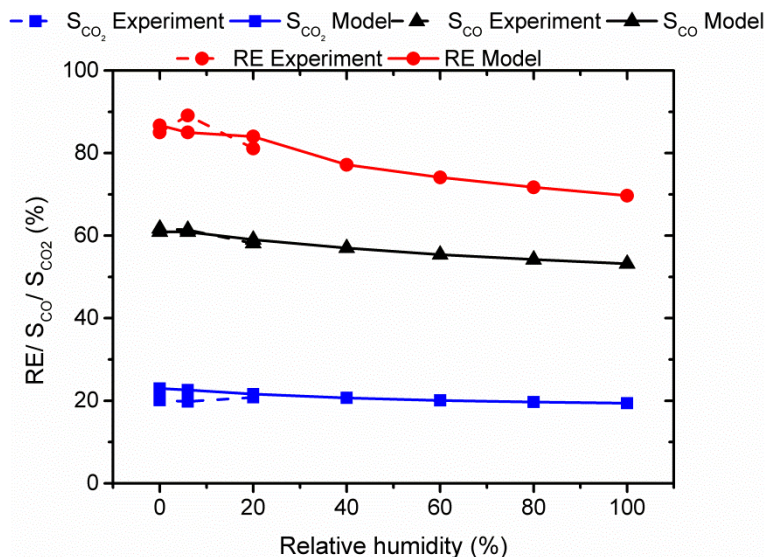


Figure 5-5: Comparison between calculated (solid lines) and measured (dashed lines) RE (red; circle), S_{CO} (black; triangle) and S_{CO₂} (blue; square), as a function of the relative air humidity, for an energy deposition of 1.8 J/cm³ at 8700 ppm C₂H₄ in air.

The calculations predict that the selectivity towards CO and CO₂ does not change significantly upon increasing humidity. However, the RE drops by about 15% when the humidity rises from 0 to 99%. This can be explained by the drop in densities of the O atoms and metastable N₂ molecules at the maximum of the pulse (i.e., from $8.8 \times 10^{16} \text{ cm}^{-3}$ to $4.8 \times 10^{16} \text{ cm}^{-3}$ for the O atoms, and from $6.8 \times 10^{16} \text{ cm}^{-3}$ to $4.1 \times 10^{16} \text{ cm}^{-3}$ for the metastable N₂ molecules). It should be mentioned that the humidity might influence the formation of other by-products (see below), but this effect will be minor, as the CO and CO₂ selectivities remain approximately constant.

Figure 5-6 illustrates the calculated densities (in ppm) of the most common by-products besides CO and CO₂ as a function of time, for 10 consecutive pulses (i.e., microdischarge filaments) with an interpulse time of $\pm 0.0684 \text{ s}$. Only the calculated

concentrations of the by-products could be obtained. Indeed, the C_2H_2 and C_2H_4 peaks could not be separated on the GC. However, a rough estimation by FTIR indicated ± 26 ppm C_2H_2 , which is somewhat lower than the calculated result (see **Figure 5-6** and below). CH_2O could not be detected on the GC or the FTIR, possibly because this species might be condensed after the plasma reactor. The results are shown for an energy deposition of 1.8 J/cm^3 and $8700 \text{ ppm } C_2H_4$, both in humid air with 20% relative humidity (RH) and in dry air.

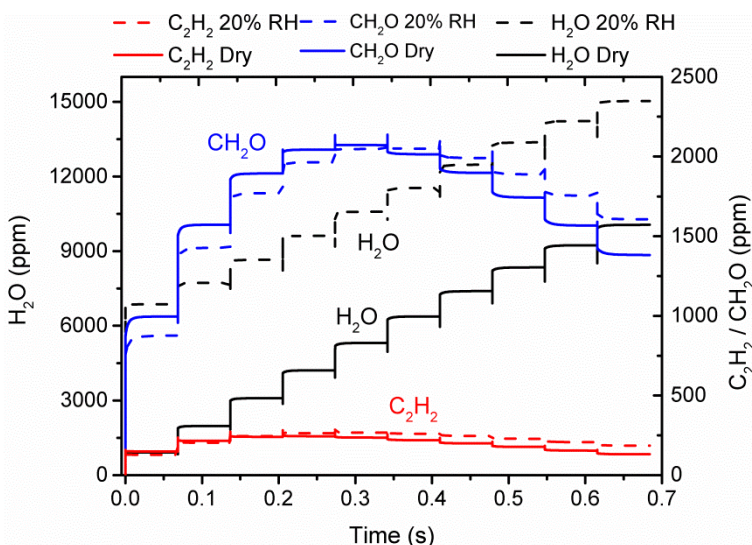


Figure 5-6: Calculated concentrations of H_2O (left axis), CH_2O and C_2H_2 (right axis), formed as by-products in C_2H_4 destruction, as a function of time during 10 consecutive microdischarge pulses, in the case of humid air with 20% RH (dashed lines) and dry air (solid lines), for a total energy deposition of 1.8 J/cm^3 at $8700 \text{ ppm } C_2H_4$ in air.

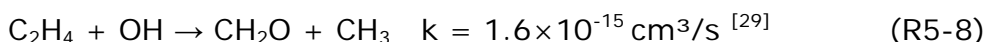
The concentrations of CH_2O , H_2O and C_2H_2 after the residence time of 0.684 s , i.e., when the gas flows out of the reactor, amount to 1606 ppm , 15033 ppm and 185 ppm , respectively in humid air (with 20% RH), and to 1382 ppm , 10057 ppm and 131 ppm , respectively in dry air. This corresponds to selectivities towards CH_2O and C_2H_2 of 11% and 3%, respectively, in the

humid air case (and slightly lower in dry air). At these conditions, the selectivities towards CO and CO₂ are calculated to be 60% and 22% (see **Figure 5-5**), so that the sum of these selectivities amounts to 96%; the remaining 4% going to methane, formic acid and ketene. Note that the selectivity towards H₂O is not included in these calculations, as the selectivities are obtained with respect to the C atoms in C₂H₄, and H₂O does not contain C atoms.

It is clear from **Figure 5-6** that the CH₂O, H₂O and C₂H₂ densities exhibit a rise (or a drop) at each pulse, whereas they remain more or less constant in the interpulse time. Furthermore, the H₂O density keeps on increasing for the consecutive pulses, whereas the CH₂O and C₂H₂ densities go over a maximum after the 5th pulse. The latter behavior can be explained because more chemically active species (i.e., O₃, O and N₂ metastable molecules) are available at this time to destroy CH₂O and C₂H₂. It is found that the C₂H₄ removal progresses as a function of time, and the densities of CH₂O and C₂H₂ become comparable to the C₂H₄ density, and at that point the chemically active species also yield the destruction of CH₂O and C₂H₂.

H₂O, on the other hand, will be consumed by electron impact dissociation and by vibrational excitation during each pulse, whereas after the pulse, it is produced again by decay of the vibrationally excited species and by reaction of OH radicals with hydrocarbon species (e.g., R5-5 above). However, an extra hydrogen source is necessary to explain the stepwise increasing H₂O density. The explanation can be found in the indirect production of H₂O by the destruction of ethylene and its by-products. The reactions between hydrocarbon species and O atoms will produce OH radicals (e.g., by R5-3) and those OH radicals will then react with hydrocarbon species in a second reaction (e.g., by R5-5).

In general, a higher humidity does not result in different by-products formed, but the concentration of formaldehyde increases by 224 ppm for a humidity of 20% compared to dry air. This difference is attributed to the higher density of OH radicals, which results in a new destruction path, as discussed above.



Note that the time-integrated rate of the reaction increases by one order of magnitude, i.e., from 10^{16} cm^{-3} to 10^{17} cm^{-3} , when the RH rises from 0% to 90%. However, this rate is still three orders of magnitude lower than the integrated rates of the reactions with metastable N_2 molecules, explaining why the effect of humidity is not significant. The effect of humidity on the C_2H_2 density is even smaller, and the minor drop in density can be assigned to the drop in metastable N_2 density, as most of the C_2H_2 production is caused by the N_2 metastable destruction of ethylene (see **Figure 5-4** above). Finally, the effect on the H_2O concentration is simply due to the extra water introduced in the humid air, but the H_2O production itself does not change, as is clear from **Figure 5-6**.

5.3.5 Production of O₃, NO₂, HNO₂, HNO₃ and N₂O

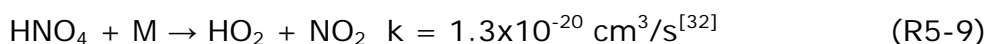
Not only hydrocarbon by-products are an issue in plasma destruction of VOCs, but also the production of O₃, NO₂, HNO₂, and N₂O in the carrier gas (air) must be considered. In **Table 5-1** the concentrations of produced O₃, NO₂, HNO₂ and N₂O species are listed, after treating 3500 ppm C₂H₄ in dry air with an energy deposition between 1.2 – 2.4 J/cm³.

Table 5-1: Calculated concentrations of O₃, NO₂, N₂O and HNO₂ formed as by-products in the destruction of 3500 ppm C₂H₄ in dry air, for different values of SED. The measured values of the NO₂ and N₂O concentrations are also indicated between brackets.

SED(J/cm ³)	Species			
	O ₃ (ppm)	NO ₂ (ppm)	N ₂ O (ppm)	HNO ₂ (ppm)
1.2	632	3 (165)	214 (52.5)	776
1.8	1089	6 (198)	287 (74)	996
2.4	3043	22 (225)	358 (77)	1249

DBDs are known as ozone producers since many years^[30]. It is, therefore, not unexpected that O₃ is also formed as a by-product in VOC destruction in air. As follows from **Table 5-1**, the created O₃ concentration is in the order of (several) 1000 ppm, hence the same order of magnitude as the C₂H₄ concentration to be destroyed. Moreover, it increases drastically with SED, which is directly related to the higher O atom density, producing more O₃ upon three-body recombination between molecular and O atoms^[31]. We could not detect any characteristic peak of O₃ on the FTIR, but we suspect that ozone is decomposed on the warm reactor walls and on the tubing to the FTIR. Secondly, it is also possible that we have reached the critical point of discharge poisoning by both working at higher power and heating of the electrodes^[16].

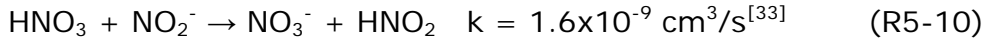
For the NO₂ and N₂O concentrations, both the calculated and measured values are listed. The calculated NO₂ concentration is 1-2 orders of magnitude lower than the measured values. This might be attributed to some missing reactions (or an error in some rate coefficients) in the NO_x plasma chemistry, which was of course not the main purpose of this chapter. However, it could also be an error in the experiment, due to the difference between the time of measurement and the residence time of the gas in the reactor. Indeed, the NO₂ concentration is still increasing at the end of our simulation, or in other words at the end of the reactor, therefore, it is likely that the actual NO₂ concentration would be higher at the place of measurement. The dissociation of HNO₄ can be found responsible for this production:



The calculated N₂O concentration is about a factor of 4 higher than the measured values, which is still reasonable, in view of the complex plasma chemistry. Moreover, in literature, the NO₂ concentration was typically reported to be lower than the N₂O concentration^[20,24], which corresponds to our modeling results. Another explanation for the different values could be temperature effects at the wall of the reactor, caused by Ohmic heating in the electrode, and therefore, the chemistry will locally be different from the bulk chemistry. Within this context we should stress that an experimental measurement of the O atoms concentration would provide us a more detailed validation.

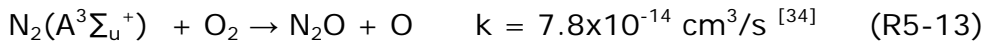
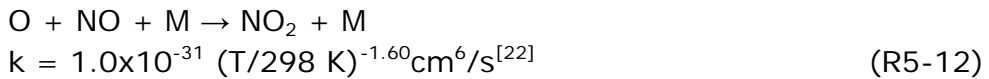
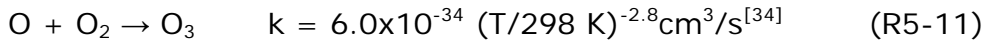
Furthermore, the model predicts the production of HNO₂ and small quantities of HNO₃, which is not directly expected in dry air, although water is produced during the destruction of ethylene. The destruction of water will then produce OH and HO₂ radicals which will react with NO or NO₂ producing HNO₂ and HNO₃. The

ratio between HNO_2 and HNO_3 will eventually be controlled by the reaction:



which explains why we calculated the largest density for HNO_2 and not for HNO_3 . We should, however, keep in mind that in this case the ratio between HNO_2 and HNO_3 is strongly dependent on the error on the rate coefficient. We were not able to detect any peaks of HNO_2 or HNO_3 on the FTIR, but it could be possible that they condense in the tubing to the FTIR, together with water.

Finally, similar as for O_3 , the NO_2 , N_2O and HNO_2 concentrations increase at higher SED, which can again be explained by the increasing density of O atoms and metastable N_2 species ($\text{N}_2(\text{A}^3\Sigma_u^+)$) in the discharge, giving rise to the following reactions:



Furthermore, an increase in the NO_2 density will then stimulate the production of HNO_2 and HNO_3 .

5.4 Conclusion

It can be concluded that the destruction of ethylene in a DBD goes side by side with the production of O_3 , NO_2 , HNO_2 , HNO_3 and N_2O , in concentrations which are not negligible to the C_2H_4 concentration to be destroyed. This should of course be avoided. In general, all end products of C_2H_4 destruction can be categorized as sources of photochemical smog (i.e., NO_2 , HNO_2 , CO and VOCs (e.g. formaldehyde)) or greenhouse gas emissions (i.e., O_3 , N_2O and CO_2 , where N_2O should be considered as the most harmful in this group, because of its global warming potential of 289 (based on 20 years)^[35]). We therefore believe that plasma technology can only be viable for VOC destruction purposes if combined with catalysis, i.e., so-called plasma catalysis, to minimize the outlet O_3 and NO_x concentrations, produced by the plasma itself^[36].

5.5 References

- [1] R. Aerts, X. Tu, C. De Bie, J. C. Whitehead, A. Bogaerts, *Plasma Process. Polym.* **2012**, *9*, 994–1000.
- [2] C. De Bie, B. Verheyde, T. Martens, J. van Dijk, S. Paulussen, A. Bogaerts, *Plasma Process. Polym.* **2011**, *8*, 1033–1058.
- [3] A. N. Trushkin, I. V. Kochetov, *Plasma Phys. Reports* **2012**, *38*, 407–431.
- [4] L. Magne, S. Pasquiers, N. Blin-Simiand, C. Postel, *J. Phys. D. Appl. Phys.* **2007**, *40*, 3112–3127.
- [5] X. Tu, J. C. Whitehead, *Appl. Catal. B Environ.* **2012**, *125*, 439–448.
- [6] G. Sathiamoorthy, S. Kalyana, W. C. Finney, R. J. Clark, B. R. Locke, *Ind. Eng. Chem. Res.* **1999**, *38*, 1844–1855.
- [7] D. Evans, L. A. Rosocha, G. K. Anderson, J. J. Coogan, M. J. Kushner, *J. Appl. Phys.* **1993**, *74*, 5378.
- [8] O. Koeta, N. Blin-Simiand, W. Faider, S. Pasquiers, a. Bary, F. Jorand, *Plasma Chem. Plasma Process.* **2012**, *32*, 991–1023.
- [9] N. Blin-Simiand, S. Pasquiers, F. Jorand, C. Postel, J.-R. Vacher, *J. Phys. D. Appl. Phys.* **2009**, *42*, 122003.
- [10] N. Jidenko, E. Bourgeois, J. Borra, *J. Phys. D. Appl. Phys.* **2010**, *43*, 295203.
- [11] O. Motret, C. Hibert, S. Pellerin, J. M. Pouvesle, *J. Phys. D. Appl. Phys.* **2000**, *33*, 1493–1498.
- [12] W. Van Gaens, A. Bogaerts, *J. Phys. D. Appl. Phys.* **2013**, *46*, 275201.
- [13] I. A. Kossyi, A. Yu Kostinsky, A. A. Matveyev, P. V. Silakov, *Plasma Sources Sci. Technol.* **1992**, *1*, 207–220.
- [14] R. Snoeckx, R. Aerts, X. Tu, A. Bogaerts, *J. Phys. Chem. C* **2013**, *117*, 4957–4970.
- [15] X. Tu, H. J. Gallon, M. V Twigg, P. A. Gorry, J. C. Whitehead, *J. Phys. D. Appl. Phys.* **2011**, *44*, 274007.
- [16] A. Fridman, *Plasma Chemistry*, Cambridge University Press, New York, **2008**.
- [17] R. Nielsen, N. Bradbury, *Phys. Rev.* **1937**, *51*, 69–75.
- [18] X. Tu, B. Verheyde, S. Corthals, S. Paulussen, B. F. Sels, *Phys. Plasmas* **2011**, *18*, 080702.

- [19] S. Chavadej, K. Saktrakool, P. Rangsunvigit, L. Lobban, T. Sreethawong, *Chem. Eng. J.* **2007**, *132*, 345–353.
- [20] A. M. Harling, D. J. Glover, J. C. Whitehead, K. Zhang, *Environ. Sci. Technol.* **2008**, *42*, 4546–50.
- [21] P. Plessis, P. Marmet, *Int. J. Mass Spectrom. Ion Process.* **1986**, *70*, 23–44.
- [22] D. L. Baulch, C. J. Cobos, R. A. Cox, C. Esser, P. Frank, T. Just, J. A. Kerr, M. J. Pilling, J. Troe, R. W. Walker, et al., *J. Phys. Chem. Ref. Data* **1992**, *21*, 411–734.
- [23] D. L. Baulch, *J. Phys. Chem. Ref. Data* **2005**, *34*, 757.
- [24] M. Hübner, J. Röpcke, *J. Phys. Conf. Ser.* **2009**, *157*, 012004.
- [25] M. J. Kushner, *J. Appl. Phys.* **1993**, *73*, 51–55.
- [26] W.-J. Liang, J. Li, J.-X. Li, T. Zhu, Y.-Q. Jin, *J. Hazard. Mater.* **2010**, *175*, 1090–5.
- [27] R. Atkinson, S. M. Aschmann, J. N. Pitts, *J. Phys. Chem.* **1988**, *92*, 3454–3457.
- [28] E. J. Dunlea, R. K. Talukdar, a R. Ravishankara, *J. Phys. Chem. A* **2005**, *109*, 3912–3920.
- [29] A.-M. Zhu, Q. Sun, J.-H. Niu, Y. Xu, Z.-M. Song, *Plasma Chem. Plasma Process.* **2005**, *25*, 371–386.
- [30] B. Eliasson, M. Hirth, U. Kogelschatz, *J. Phys. D. Appl. Phys.* **1987**, *20*, 1421–1437.
- [31] U. Kogelschatz, B. Eliasson, W. Egli, *Le J. Phys. IV* **1997**, *07*, C4–47–C4–66.
- [32] R. Atkinson, D. L. Baulch, R. A. Cox, J. N. Crowley, R. F. Hampson, R. G. Hynes, M. E. Jenkin, M. J. Rossi, J. Troe, *Atmos. Chem. Phys.* **2004**, *4*, 1461–1738.
- [33] H. D. O. Person J.C., *Radiat. Phys. Chem.* **1988**, *31*, 1–8.
- [34] R. Atkinson, D. L. Baulch, R. A. Cox, R. F. Hampson, J. A. Kerr, M. J. Rossi, J. Troe, *J. Phys. Chem. Ref. Data* **1997**, *26*, 1329–1499.
- [35] P. Forster, V. Ramaswamy, P. Artaxo, T. Berntsen, R. Betts, D. W. Fahey, J. Haywood, J. Lean, D. C. Lowe, G. Myhre, et al., in *Contrib. Work. Gr. I to Fourth Assess. Rep. Intergov. Panel Clim. Chang.*, Cambridge University Press, Cambridge (UK), **2007**.
- [36] M. Hussain, S. Bensaid, F. Geobaldo, G. Saracco, N. Russo, *Ind. Eng. Chem. Res.* **2011**, *50*, 2536–2543.

PART III:

STUDY OF

CO₂ SPLITTING

Chapter 6:

Single pulse simulations for CO₂ splitting in DBDs

In this chapter, the splitting of CO₂ in a pulsed plasma system, such as a DBD, is evaluated from a chemical point of view by means of numerical modeling. For this purpose, a chemical reaction set of CO₂ in a DBD is developed, including the vibrational states of CO₂, O₂ and CO. The simulated pulses are matched to the conditions of a filament (or microdischarge) and repeated with intervals of 1 microsecond. The influence of vibrationally excited CO₂, as well as other neutral species, ions and electrons on the CO₂ splitting is discussed. Our calculations predict that the electrons have the largest contribution to the CO₂ splitting at the conditions under study, by electron impact dissociation. The contribution of vibrationally excited CO₂ levels in the splitting of CO₂ is found to be 6.4%, when only considering one microdischarge pulse and its afterglow, but it can be much higher for consecutive discharge pulses, as is typical for a filamentary DBD, when the interpulse time is short enough and accumulation effects in the vibrationally excited CO₂ densities can occur.

Aerts, R., Martens, T., & Bogaerts, A. (2012). Influence of Vibrational States on CO₂ Splitting by Dielectric Barrier Discharges. *The Journal of Physical Chemistry C*, 116(44), 23257–23273. doi:10.1021/jp307525t

6.1 Introduction

In order to obtain a detailed description of the CO₂ splitting, a reaction set is constructed which contains the vibrational and electronic excitations of the CO₂, CO and O₂ molecules, because previous publications on pure CO₂ splitting by plasma showed that only these species were important^[1-4]. Previous studies which included these excited states usually only described the formation and quenching of these states but not their further role in the plasma chemistry^[5], while it is known that up to 97% of the discharge power for a low-temperature plasma can go to the vibrational excitation in a molecular plasma^[6,7] (see also section 2.3.2 in **Chapter 2**). Therefore, in the present chapter the influence of the vibrationally and electronically excited species on the ongoing chemistry is included. The experimental setup under study is a cylindrical DBD, inspired by the series of research performed at Moscow State University between 1960 and 1970^[8-16]. In these papers, a classic silent discharge for ozone production was applied for organic gas conversion^[17,18].

In the next section, the chemical reaction set will be presented. In the results section, first the influence of the electrons on the chemical splitting mechanism in CO₂ for a single power pulse will be investigated. Second, the vibrational chemistry for a single power pulse and its afterglow, as well as a series of pulses will be investigated. Third, the behavior of the various ions and neutral species, both for a single power pulse and a series of pulses will be studied, and finally, the contribution of the different species to the splitting of CO₂ will be evaluated.

6.2 Description of the model and the chemistry

The physical description of the model can be found in **Chapter 3**. For this reason, only the description of the chemistry is given here.

The species included in the model are presented in **Table 6-1**, and an overview of all chemical reactions considered in the model is given in the **Appendix II**. 8 neutral species (i.e., ground state molecules and radicals, related to CO₂ and O₂) are taken into account, as well as 11 different positive ions and 6 different negative ions. Moreover, several excited levels of CO₂, CO and O₂ are considered, as outlined in **Table 6-2**.

Table 6-1: Overview of the ground-state species included in the model.

Neutrals and radicals	Ions
CO ₂ , CO, C ₂ O	CO ₂ ⁺ , CO ₄ ⁺ , CO ⁺ , C ₂ O ₂ ⁺ , C ₂ O ₃ ⁺ , C ₂ O ₄ ⁺ , C ⁺ , C ₂ ⁺
C, C ₂	CO ₃ ⁻ , CO ₄ ⁻
O ₂ , O ₃ , O	O ₂ ⁺ , O ⁺ , O ₄ ⁺ O ⁻ , O ₂ ⁻ , O ₃ ⁻ , O ₄ ⁻

These levels have been grouped into effective levels, in order to limit the number of chemical reactions in the model. Indeed, the number of reactions can quickly increase if every excited species can react in a similar way as its ground state. This becomes more important in a later stage when time consumption becomes an issue, i.e., when this chemistry will be used to simulate full geometries in two- or three-dimensional models.

Table 6-2: Overview of excited species included in the model.

Ground state	Notation in the model	Described excited state(s)
CO ₂	CO ₂ v1	(010)
	CO ₂ v2	(100), (020)
	CO ₂ v3	(001)
	CO ₂ v4	(n00), (0n0)
	CO ₂ e1	CO ₂ (¹ Π _g)
	CO ₂ e2	CO ₂ (¹ Δ _u)
CO	COv1	sum of vibrations
	COe1	CO(A ³ Π)
	COe2	CO(A ¹ Π)
	COe3	CO(A ³ Σ), CO(D ³ Δ), CO(E ³ Σ), CO(B ³ Σ)
	COe4	CO(C ¹ Σ), CO(E ¹ Π), CO(B ¹ Σ), CO(I ¹ Σ), CO(D ¹ Δ)
O ₂	O ₂ v1	(n _v = 1, 2)
	O ₂ v2	(n _v = 3, 4)
	O ₂ v3	(n _v = 5, 6)
	O ₂ e1	O ₂ (a ¹ Δ) and O ₂ (b ¹ Σ)
	O ₂ e2	O ₂ (B ³ Σ) and higher triplets

After critical evaluation of the available cross sections of CO₂, CO and O₂, several groups of levels were defined (see **Table 6-2**)^[19–24]. The different vibrational levels of CO₂ have been grouped in four different levels, denoted as CO₂v1, CO₂v2, CO₂v3 and CO₂v4. CO₂v1 represents the first bending mode (010), CO₂v2 is the sum of the first symmetric stretch (100) and the second bending mode (020), CO₂v3 denotes the first asymmetric stretch mode (001) and finally, CO₂v4 represents the sum of the higher symmetric stretch (n00) and bending (0n0) modes. It should be clear that by combining these higher vibrational levels into one “effective” vibrational level, it is not possible to describe the VV transfers to higher vibrational levels, as mentioned by Fridman^[6,7]. However,

for high values of reduced electric field (i.e., higher than 100 Td) as is the case in DBDs, the VV transfers to higher levels will not be of such a great importance as for example in a microwave discharge, where most of the energy is transferred to the vibrationally excited states^[6,7]. Hence, although the CO₂ vibrational kinetics is in reality still much more complicated, we believe that this approximation is justified for the present study, and that the trends of the influence of vibrational levels can be qualitatively predicted for a DBD. The electronic excitation of CO₂ is described using two levels: i.e. CO₂ (¹Π_g) (denoted as CO₂e1) and CO₂ (¹Δ_u) (symbolized as CO₂e2).

For CO, all vibrational excitation is described using one mode, i.e., COv1, at a threshold of 1.01 eV. The electronic excitations have been grouped in four different levels. COe1 describes the excited level CO(A³Π), COe2 stands for the excited level CO(A¹Π), COe3 is the sum of the triplet levels CO(A³Σ), CO(D³Δ), CO(E³Σ) and CO(B³Σ) and finally, COe4 describes the sum of the singlet levels CO(C¹Σ), CO(E¹Π), CO(B¹Σ), CO(I¹Σ) and CO(D¹Δ).

O₂ is described using three vibrational states: O₂v1 denotes the first and second vibrational level. O₂v2 symbolizes the third and fourth vibrational level and O₂v3 stands for the fifth and sixth vibrational level. The electronic excitations are grouped into two states: O₂e1 groups the singlet states O₂(a¹Δ) and O₂(b¹Σ), while O₂e2 is the sum of O₂(B³Σ) and the higher triplet states.

These excited states have the same chemistry as their ground state levels (see below), except that the vibrationally excited states typically have a stimulated dissociation and the electronically excited states can have a stimulated ionization, i.e. the activation barriers of ionization and dissociation are lowered

as a consequence of the higher energy level of the excited reactants. Indeed, because the energy requirement to dissociate a vibrationally excited molecule is lower than for a ground state molecule, the threshold energy for the electron induced reactions is lowered with the same amount as the vibrational excitation energy.

The production of these vibrationally and electronically excited levels is by electron impact excitation, as outlined in **Appendix II**. Furthermore, we consider 3 types of loss processes for the vibrationally excited molecules. The first one is by electron impact reactions (see **Appendix II**), for which the corresponding cross section is shifted on the energy scale towards a lower energy. The second loss process is by VT and VV transfers with the ground state species CO₂, CO and O₂, for which the rate coefficients were adopted from literature and recalculated for a temperature of 400K^[25,26].

Finally, the third type of loss process is the interaction of heavy particles (i.e. ions and neutrals) with vibrationally excited states, which causes a bond break in the excited molecule. This process was taken into account by adopting the theory described by the Fridman-Macheret α -Model^[6,71]. This theory uses an Arrhenius expression for the reaction rate coefficient:

$$k_R(E_v, T_g) = k_{R0} \exp\left(-\frac{E_a - \alpha E_v}{T_g}\right) \theta(E_a - \alpha E_v) \quad (\text{E6-1})$$

In this equation E_a is the activation energy of an elementary chemical reaction and E_v is the vibrational energy. The coefficient α is the efficiency of the excitation energy use in overcoming the activation barrier, k_{R0} is the pre-exponential factor and $\theta(a-b)$ is

the so-called Heaviside function, which is zero when $b > a$ and it is 1 when $a \geq b$. The values for α were taken from Fridman and were only considered if there is a bond break in the vibrationally excited molecule^[6,7]. For exothermic reactions, $\alpha = 0.3$ was used, whereas for thermo-neutral reactions, $\alpha = 0.45$ is used and for one exothermic double exchange (i.e., reaction (74) of **Table A2 - 3** in the **Appendix II**) $\alpha = 0.2$ was used.

A similar procedure as described above is also used for the electronically excited species. The cross sections for electron induced ionizations are shifted on the energy scale to a lower energy with the same amount as the electronic excitation energy. For the interactions between heavy particles this effect is only considered for charge exchange reactions, because in such reaction ionization occurs in the electronically excited species. Classically, for such a reaction the collision cross section has a reverse proportionality with the square of the ionization potential and the reaction rate coefficient is proportional to the collision cross section^[10]. Therefore, the stimulation of charge exchange with electronically excited species was implemented as

$$k_R = k_{R0} \left((E_I)^2 / (E_I - E_E)^2 \right) \quad (\text{E6-2})$$

where k_{R0} is the original reaction rate coefficient, E_I is the ionization potential of the excited species and E_E is the electronic excitation threshold energy. Reaction 132 (see **Table A2 - 4** of the **Appendix II**) is a different type of reaction, but it is known that for this reaction the increase in reaction rate is also significant^[28]. Therefore, to describe this reaction with O₂e1 and O₂e2, we used the value $k = 3 \times 10^{-10} \text{ cm}^3 \text{ s}^{-1}$, as suggested by Kossyi and co-workers^[28]. Finally, the rate coefficients for the relaxation of the electronic excited states were estimated according to their expected lifetime and the report by Surzhikov^[26].

The resulting reaction chemistry consists of 42 chemical species (i.e., the species presented in **Table 6-1** and **Table 6-2**, as well as the electrons), who engage in 501 chemical reactions. The chemical reactions of the ground state species, together with the VV and VT transfers adopted from literature, are tabulated in Appendix II, as well as the corresponding rate coefficients and the references where these data are adopted from. As mentioned above, the same reactions are also included for the electronic and vibrationally excited species, but with modified rate coefficients, as explained above.

6.3 Results and discussion

6.3.1 Validation of the model

As our model is developed and applied here to study the plasma chemistry in one pulse (microdischarge) and afterglow, or five consecutive pulses in the microsecond time-scale (see below), comparison with experimental data to validate the model at this stage is extremely difficult. Therefore, initial validation of our model is performed by comparison with the validated modeling results from Cenian and co-workers^[29]. The research of Cenian et al. concerned a pure CO₂ discharge, operating at 30 torr and a temperature of 400 K, with an applied potential difference of 200 V between the electrodes and a current density of 7.5 A/cm², which leads to a power density of 1.5 kW/cm². To compare our model results with the work by Cenian, the same power density was implemented in our simulations. The fractional densities calculated by our model are plotted in **Figure 6-1**, together with the results from Cenian and co-workers^[29]. The calculated fractional CO and O₂ densities are nearly the same as found by Cenian. CO is calculated to be present for about 30% in the discharge and O₂ for about 17%. O₃ has a calculated fractional density of 0.05% in the discharge, which is slightly lower than the results of Cenian, while the calculated fractional density of the O

atoms (i.e., 0.02%) is somewhat higher. However, the obtained densities for O₃ and O are still in the same order of magnitude as the results obtained by Cenian. These differences are not unexpected since the chemical reaction set is considerably different. Nevertheless, the agreement for the densities of the most important species, i.e., CO and O₂, is very good, which provides us at least with some validation of our model.

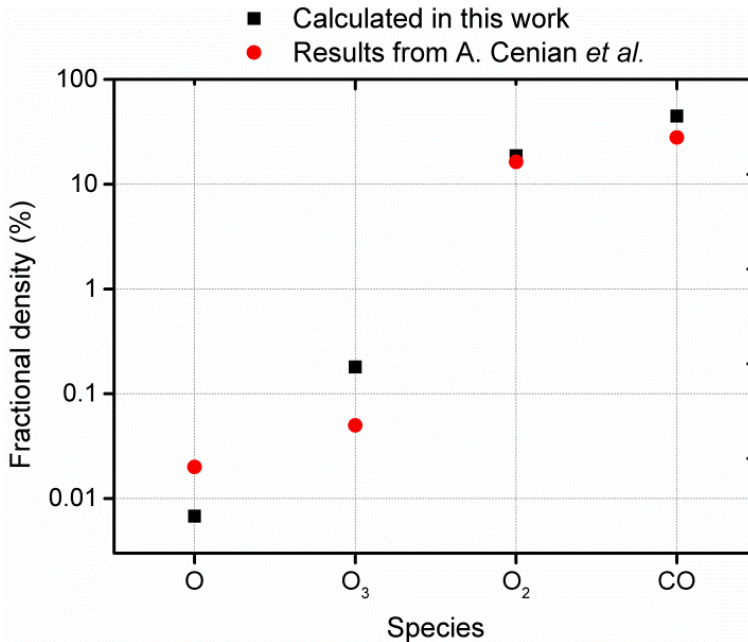


Figure 6-1: Calculated fractional densities of CO₂ conversion products, at 30 Torr, 400 K and a power input of 1.5 kW/cm², obtained in this work, in comparison with the results from Cenian and coworkers^[29].

6.3.2 Description of the power deposition in the model

As discussed in **Chapter 3** (section 3.1.2), we know that a typical voltage/current waveform of a DBD in a reactive gas shows nanosecond pulses which are repeated in the (sub-) microsecond scale^[30]. Therefore, for simplicity, we implemented a triangular 30 ns discharge pulse, every microsecond, based on the fact that in

one half period breakdown occurs which results in nanosecond fluctuations for a range of over a couple of microseconds^[30,31].

Figure 6-2 presents the calculated electron density and electron temperature, as well as the applied power, as a function of time for one pulse. In order to match the conditions of our pulse as close as possible to a single microdischarge, the power of the pulse was set to a maximum value of 8.0×10^7 W at 15 ns, which results in a calculated maximum electron temperature of 2.6 eV and a maximum electron density of 1.65×10^{15} cm⁻³, as shown in **Figure 6-2**. Indeed, these values of electron temperature and electron density match typical values reported in literature for microdischarges^[6,32]. As is clear from **Figure 6-2**, the largest change in densities takes place when the pulse reaches its maximum at 15 ns; therefore, the Boltzmann equation module will be called at the beginning and in the middle of every pulse. The calculation results presented below are all obtained for the pulse described above, with its corresponding electron temperature and electron density profiles shown in **Figure 6-2**, and for an initial CO₂ density of 1.8×10^{19} cm⁻³.

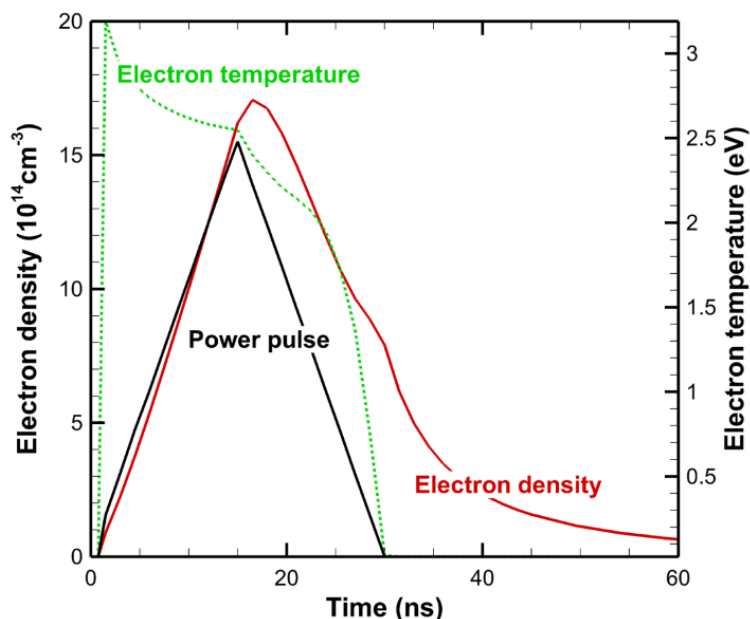


Figure 6-2: Calculated electron temperature (dashed green line; right y-axis) and electron density (solid red line; left y-axis) as a function of time during a single-pulse discharge and its afterglow. The applied power pulse is indicated by the solid black line (not shown on y-axis).

6.3.3 Energy transfer from electrons to different channels of CO₂ excitation, ionization and dissociation

Before looking in detail at the plasma chemistry of the CO₂ splitting, we wish to obtain first some insight in how the electron energy is transferred to different channels of excitation, ionization or dissociation of the CO₂ molecule. Indeed, the driving force behind plasma processing must be found in the electrons, which contribute in many electron impact reactions, especially for stable molecules as CO₂. To distinguish between the different energy loss processes of electrons, **Figure 6-3** illustrates the fractional energy transferred from electrons to different channels of CO₂ excitation, ionization and dissociation, as a function of the

reduced electric field (E/n) in a discharge. This plot is constructed based on the cross sections of the corresponding electron impact reactions, as a function of electron energy, which is calculated for the different values of E/n , shown in the x-axis.

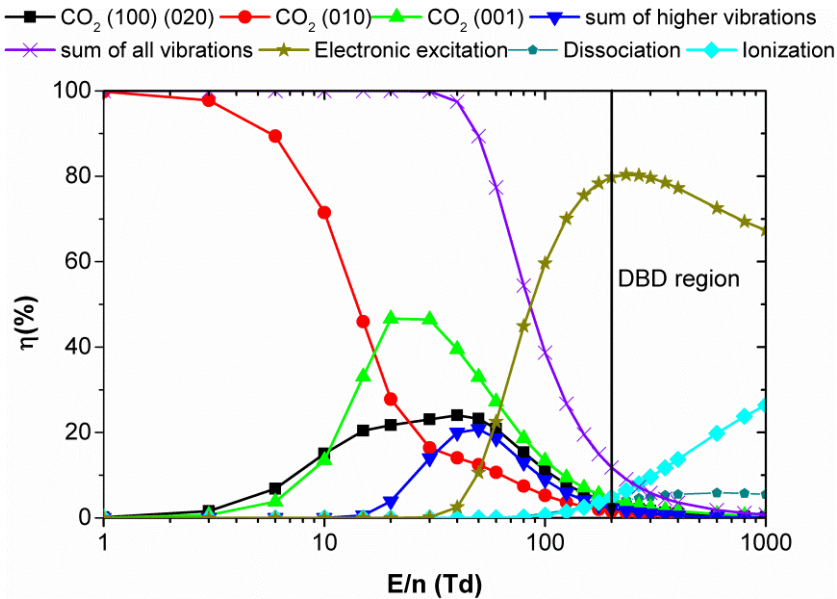


Figure 6-3: Fractions of electron energy transferred to different channels of excitation as well as ionization and dissociation of CO₂, as a function of the reduced electric field (E/n), as calculated from the corresponding cross sections of the electron impact reactions. The E/n region characteristic for DBDs is indicated by “DBD region”. The electron impact dissociation reaction of CO₂ through electron impact excitation, followed by dissociation, is mentioned in the figure as “dissociation”. The sum of electron impact electronic excitation reactions of CO₂ which form excited levels without dissociation are mentioned as “Electronic excitation”.

Fridman and coworkers stated that for gas discharges with an electron temperature around 1–2 eV, or a reduced electric field (E/n) of about 20–40 Td, up to 97% of the total non-thermal discharge energy can be transferred from plasma electrons to vibrational excitation of CO₂ molecules^[6,7,33]. This is indeed indicated by the calculated “sum of all vibrations” curve in **Figure**

6-3. A similar plot was also presented in the book of Fridman^[6]. However, the electron temperature in a DBD is about 2-3 eV. These values correspond to E/n values of about 200 Td or higher. This region is indicated as “DBD region” in the figure. It is clear that in this region at maximum only 12% of the energy is transferred to the vibrational states, whereas ~79% goes to electronic excited states, and ~ 4% and ~5% is transferred to dissociation and ionization of CO₂, respectively, with a further increasing contribution at rising E/n. This suggests that vibrationally excited states might not be so important for CO₂ splitting in a DBD as it would be in other types of discharges that are characterized by lower values of E/n, such as microwave discharges^[6,34]. Fridman indeed investigated different discharges for CO₂ splitting and concluded that higher pressures and lower values of reduced electric field make the vibrational excitation mechanism more favorable than the electronic excitation mechanism, explaining the higher energy efficiency of these type of discharges (e.g., microwave, gliding arc discharges)^[6,7,34–37]. In the next section, the role of the various plasma processes and plasma species, present in a DBD, on the actual dissociation of CO₂ will be elucidated.

6.3.4 Importance of electron impact reactions

The splitting upon electron impact with a CO₂ molecule can in general be considered as a one step process (i.e., reactions 3-8 of **Table A2 - 1** in **Appendix II**) or as a two-step process, where the CO₂ molecule is first vibrationally excited, followed by a dissociation reaction of the vibrationally excited molecule. **Figure 6-4** presents the formation rates of the electron impact reactions with CO₂ in the ground state and with the sum of all vibrationally excited states, for one discharge pulse of 30 ns and its afterglow.

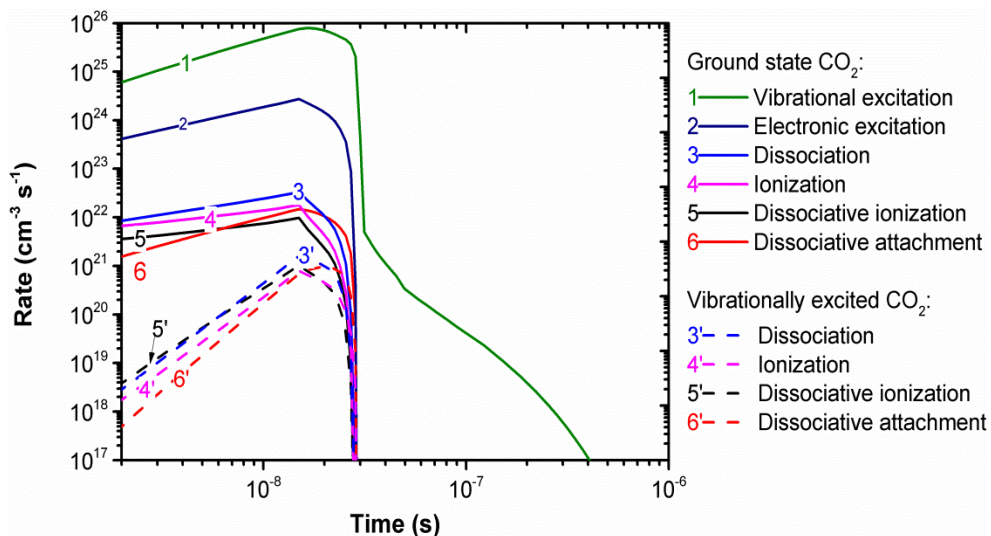


Figure 6-4: Rates of the different electron impact reactions with ground state CO₂ (solid lines) and vibrationally excited CO₂ (dashed lines) as a function of time during and after one discharge pulse of 30 ns.

The rates for vibrational excitation and electronic excitation from ground state CO₂ molecules are more or less two orders of magnitude higher than the other reaction rates for the ground state molecules (i.e., dissociation, ionization, dissociative ionization and attachment). Indeed, as was illustrated in **Figure 6-3**, most of the electron energy is transferred to the electronic excited states, and to a lower extent to the vibrational states. However, the threshold energy for vibrational excitation is significant lower (0.083 eV) compared to electronic excitation (7.000 eV), and this explains why the rate for vibrational excitation is still one order of magnitude higher than the rate for electronic excitation^[38]. Moreover, as a result of this low threshold energy, the rate for vibrational excitation decreases much more slowly in the afterglow, where the electron density and temperature are very low (see **Figure 6-2**). Indeed, CO₂ can be vibrationally excited even in the afterglow. The reason is that there are still high energy electrons, capable of electron impact vibrational excitation, present in the tail of the electron energy

distribution, even when the electron temperature reaches room temperature.

As mentioned above, **Figure 6-4** also depicts the rates for the electron impact reactions with vibrationally excited CO₂ molecules. It is clear that near the end of the discharge pulse these rates are only about one order of magnitude lower than the rates for the corresponding reactions from the ground state. This suggests that the density of the vibrationally excited CO₂ molecules is relatively close to the density of the ground state molecules. Moreover, the activation energy is lower compared to the same reaction with ground state CO₂, as already indicated above by the Fridman-Macheret α -Model^[6,7]. In the next section we will discuss in more detail the behavior of vibrationally excited CO₂ molecules, to elucidate whether they really play a role in the splitting process.

6.3.5 Behavior of vibrationally excited CO₂ molecules

In the previous section it became clear that vibrationally excited CO₂ molecules can be present in rather large amounts, because of the relatively low threshold for vibrational excitation, and as a result, electron impact reactions with vibrationally excited CO₂ molecules occur at a rate which is only one order of magnitude lower than the corresponding reactions with ground state CO₂ molecules. However, it is well possible that the vibrationally excited states return to the ground state by relaxation, without resulting in CO₂ splitting. To better understand the formation and the loss of vibrationally excited CO₂ molecules, and their role in the plasma, the densities of the various vibrational levels should be compared to the density of ground state CO₂. In **Figure 6-5(a)** the densities of the vibrationally excited levels taken into account in the model, as well as the ground state density of CO₂, are plotted as a function of time, for one discharge pulse of 30 ns

and its afterglow. The densities of the vibrationally excited CO₂ molecules are in the order of $1-8 \times 10^{17} \text{ cm}^{-3}$, which is about two orders of magnitude lower than the ground state CO₂ density ($\sim 1.8 \times 10^{19} \text{ cm}^{-3}$). This was already suggested in the previous section, as one of the explanations for the high rates for electron impact reactions with vibrationally excited CO₂. When comparing the different vibrational levels, it is clear that the lowest vibrational state (CO₂v1) has the highest density ($8 \times 10^{17} \text{ cm}^{-3}$ at the maximum), followed by CO₂v2, CO₂v3 and CO₂v4. This can be explained by the lowest threshold for vibrational excitation to the first vibrational state (CO₂v1) and by relaxation of the higher vibrational states to lower levels, controlled by VV transfers (see also below). These transfers cause an increase in the density of the lowest vibrational state after pulse termination, as is clear from **Figure 6-5(a)**, but at $2 \times 10^{-5} \text{ s}$, the density of this lowest vibrational state also starts to decrease. At this point, the density of ground state CO₂ starts to increase again. This suggests that indeed a lot of CO₂ is consumed by vibrational excitation, but eventually most of the vibrationally excited CO₂ molecules relax back to the ground state on a timescale of several 10s or 100s of microseconds. As a DBD consists of many discharge pulses spread in time and volume (see **Chapter 3**), this can eventually cause accumulation effects in the densities of some plasma species, if the interpulse time is shorter than the relaxation time of these species.

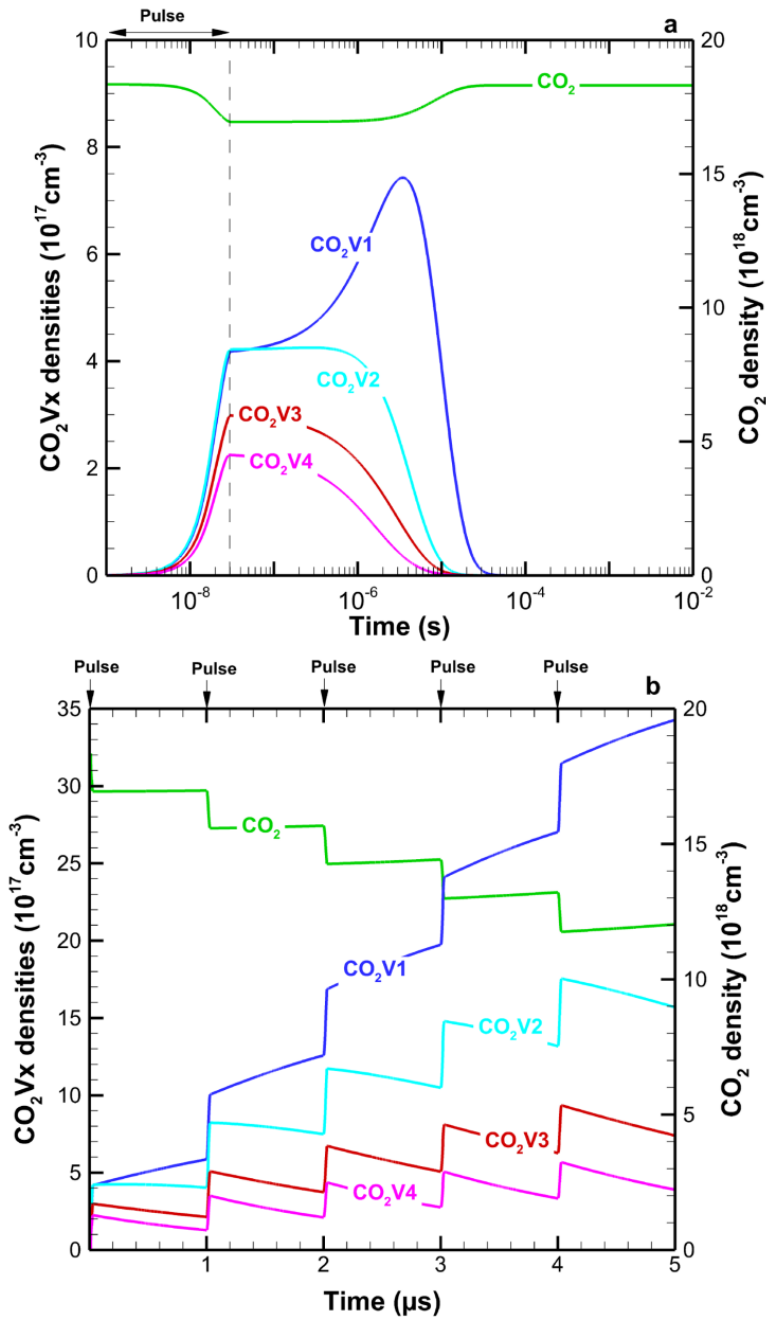


Figure 6-5: Densities of the vibrationaly excited CO₂ species (left y-axis) and the ground state CO₂ density (right y-axis), as a function of time, during and after one discharge pulse of 30 ns (a), as well as for five consecutive discharge pulses of 30 ns with an interpulse period of 1 μs (b).

To indicate such accumulation effects on the densities of vibrationally excited CO₂ molecules, **Figure 6-5(b)** presents the densities of the different CO₂ vibrational levels and the ground state as a function of time, for five consecutive discharge pulses with a length of 30 ns and an interpulse period of 1 μs. It is clear that the higher vibrational levels (i.e., CO₂v4 and CO₂v3) do not exhibit any significant accumulation effects, i.e., their density rises during the pulse, but it drops again in the afterglow to almost the same value when the next pulse starts. The lower vibrational levels, on the other hand, show considerable accumulation, especially CO₂v1. This can again be explained by the VV and VT transfers, leading to relaxation of the higher vibrational levels to the lower levels. The density of the CO₂ ground state molecules drops at each pulse, but stays more or less constant in the afterglow, or even slightly rises again, which is again attributed to relaxation from the vibrational levels. After five consecutive pulses, the CO₂ ground state density has slightly dropped from $1.7 \times 10^{19} \text{ cm}^{-3}$ to about $1.2 \times 10^{19} \text{ cm}^{-3}$, whereas the lowest vibrational level of CO₂ has increased nearly one order of magnitude, i.e., from $4 \times 10^{17} \text{ cm}^{-3}$ to $3.5 \times 10^{18} \text{ cm}^{-3}$, hence it becomes only a factor of 3 lower than the CO₂ ground state density. It should be stressed, however, that the time between two consecutive pulses (i.e., the interpulse time) is crucial for this accumulation effect.

In **Figure 6-6(a)** the net formation of vibrationally excited CO₂ (i.e., the sum of all levels), integrated from the net formation rates over the time of one (30 ns) pulse and its afterglow, is plotted for a wide range of afterglow times, or in other words, interpulse times, together with the so-called fall back ratio of vibrationally excited CO₂ (i.e., the fraction of vibrational CO₂ that has decayed back to the ground state) in **Figure 6-6(b)**. The figures indicate that for an interpulse time below 1 μs, a strong accumulation can be expected, as is clear from the high values of the time-integrated net formation and the almost negligible fall

back ratio. This was also obvious from **Figure 6-5(b)**. For an interpulse time between 1 μs and 10 μs , however, a fraction ranging from 2 to 72 % of the vibrationally excited CO₂ falls back to the ground state, and as a result the time-integrated net formation drops by a factor of ± 2 . This means that the accumulation effect on the vibrationally excited states becomes less important. If the interpulse time exceeds 10 μs , most of the vibrationally excited CO₂ molecules will decay back to the ground state before the next pulse starts, and the net formation drops by roughly 3 orders of magnitude. Hence, the accumulation effects for the vibrationally excited levels become negligible.

It should be realized that we do not exactly know the interpulse time between two filaments in a DBD, but it is likely that some molecules pass a couple of micro-discharges locally in a timeframe of 1 μs . If this is true, then this accumulation effect, and the role of vibrational levels, might be important, even in a DBD. More in general, it would be very interesting to utilize this accumulation effect to increase the efficiency of CO₂ splitting, by means of a pulsed power deposition system.

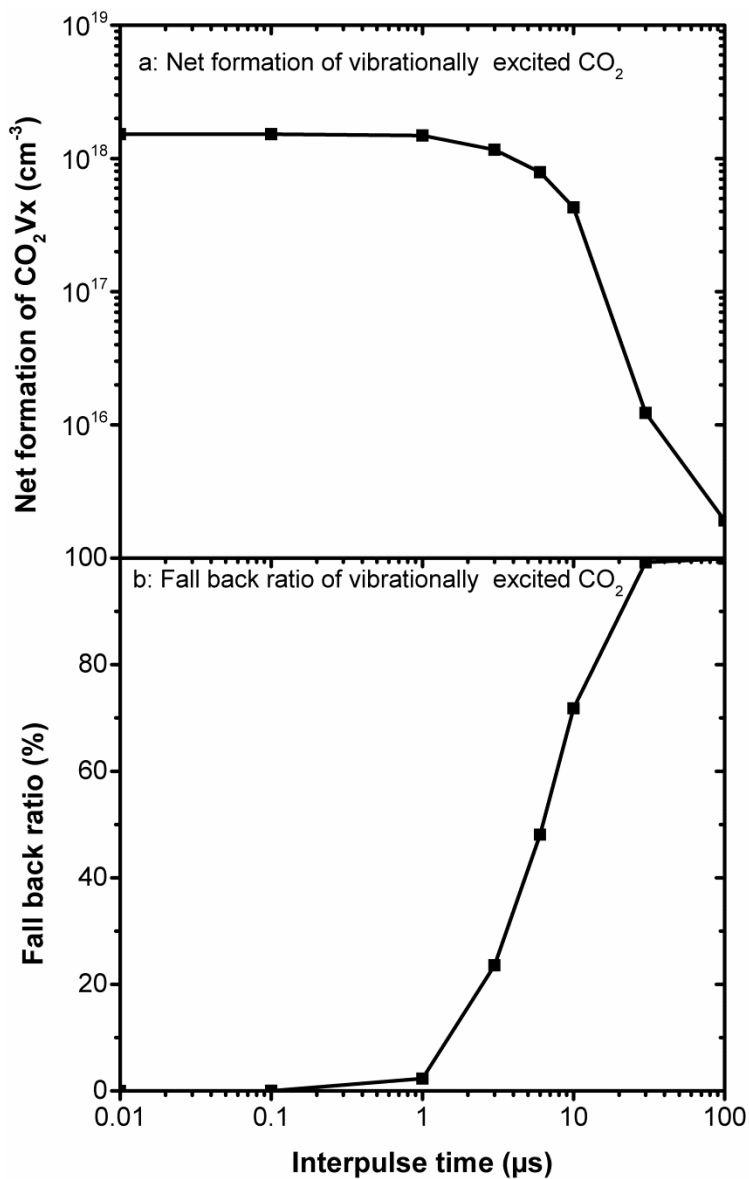


Figure 6-6: Net formation of vibrationally excited CO₂ (i.e., the sum of all levels) integrated over the time of one (30 ns) pulse and its afterglow (a), and fall back ratio of vibrationally excited CO₂ (i.e., the fraction of vibrational CO₂ that has decayed back to the ground state) (b), for a wide range of interpulse times.

6.3.6 Behavior of neutrals in the plasma

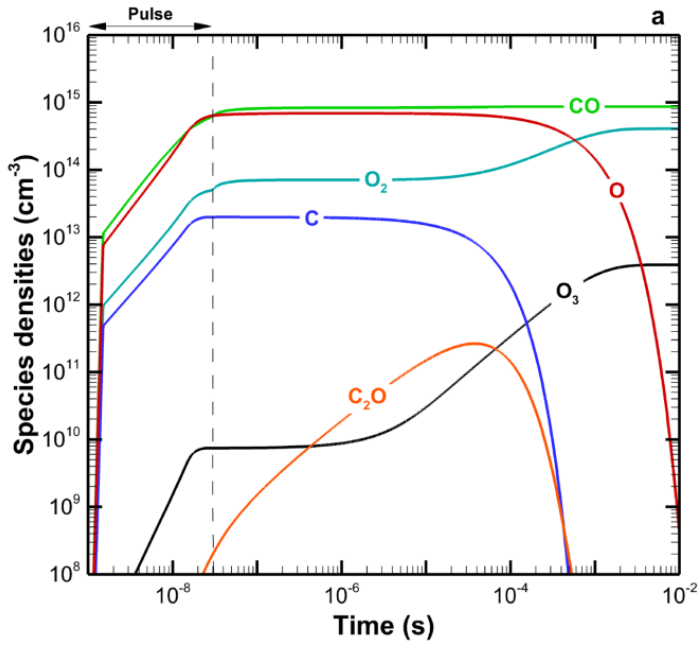
If we want to identify the dominant splitting pathways for CO₂, not only the role of the electrons and the vibrational species should be investigated but also the role of the neutral species and the ions. In **Figure 6-7(a)** and **7(b)** the densities of the most important neutral species formed in the CO₂ plasma, are plotted as a function of time, for one pulse of 30 ns and its afterglow (a), as well as for five consecutive pulses with an interpulse period of 1 μs (b). **Figure 6-7(a)** indicates CO, molecular oxygen and ozone as the main reaction products at the long time scale, although ozone is produced with a density at least two orders of magnitude lower than CO and oxygen. This explains why in literature CO and O₂ were only identified as reaction products^[2,30,39]. O atoms reach densities similar to CO (~1x10¹⁵ cm⁻³) during the pulse and in the afterglow until about 100 μs, but then it starts to drop very fast to negligible values, which causes the densities of molecular oxygen and ozone to increase. This increase is a consequence of the following three body reactions:



These reactions have maximum rates of 10¹⁷ cm⁻³ s⁻¹ and 10¹⁵ cm⁻³ s⁻¹, respectively, at around 30 ns.

Figure 6-7(a) also indicates other carbon containing species (i.e. C and C₂O) as reaction by-products with relatively high densities. As these species have the ability to oxidize in the presence of strong oxidizers (i.e. atomic and molecular oxygen) they eventually favor the production of CO, as well as CO₂ again

(reactions 70-73 of **Appendix II**), with a maximum rate at around $10^{16} \text{ cm}^{-3} \text{ s}^{-1}$, at 10 microseconds.



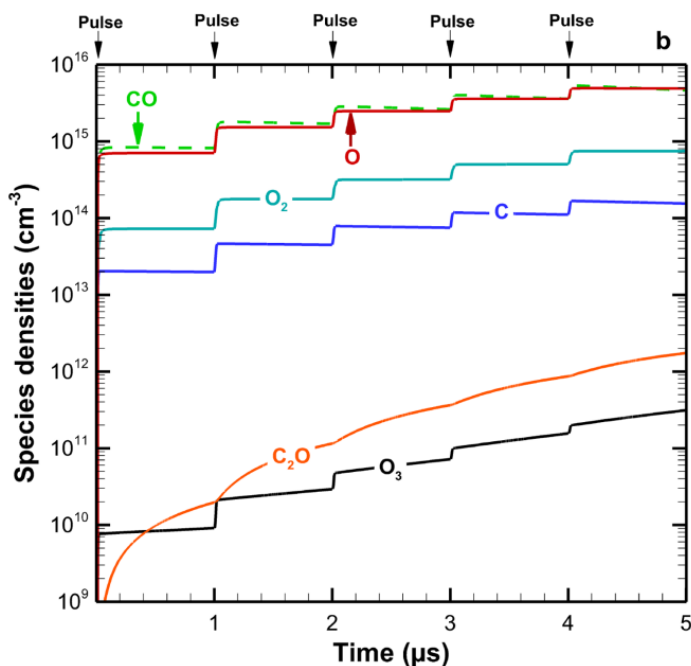


Figure 6-7: Densities of the important neutral species as a function of time, during and after one discharge pulse of 30 ns (a), as well as for five consecutive discharge pulses of 30 ns with an interpulse period of 1 μs (b).

Similar as in the previous section, the effect of accumulating neutral species is illustrated by simulating five consecutive pulses of 30 ns, with an interpulse period of 1 μs, as presented in **Figure 6-7(b)**. The neutral species indeed accumulate, as a result of their longer lifetime compared to excited species, i.e. for the conditions under study the lifetime was typically calculated to be lower than a few μs for the vibrationally excited CO₂ molecules (cf. **Figure 6-6(b)** above) vs >1 μs for the neutral species. The species with the highest densities accumulate stepwise by every nanosecond pulse, followed by a steady state or a small decrease in density during the afterglow. A more significant effect can be observed for C₂O and O₃, which are characterized by a more or less continuous increase, not only during the pulse but also during the afterglow. However, the density of C₂O will drop

dramatically at longer timescales, as was illustrated in **Figure 6-7(b)** for one pulse. This is not the case for ozone, which is quite stable at mild conditions (400K), with a dissociation rate coefficient of $1.603 \times 10^{-22} \text{ cm}^3 \text{ s}^{-1}$ (reaction 75 of **Appendix II**). As a consequence, the ozone density will always increase by accumulation even at longer interpulse periods above 1 microsecond.

6.3.7 Behavior of ions in the plasma

As illustrated in Section 6.3.3, a significant fraction of the electron energy is transferred to ionization at typical E/n values characteristic for a DBD. Therefore, **Figure 6-8(a)** presents the densities of the most important ions as a function of time, for the 30 ns pulse and its afterglow. Most small ions (i.e. C⁺, O⁺, O⁻, O₂⁺) recombine immediately after pulse termination, and hence their densities drop significantly to negligible values. The larger ions, such as CO₂⁺, CO⁺, C₂O₂⁺, C₂O₃⁺, C₂O₄⁺, recombine later at around 1 microsecond. Finally, some long living ions (i.e. CO₄⁻, CO₄⁺, CO₃⁻) are identified in our model, who recombine very slowly even after 1 millisecond. It should be mentioned, however, that although the ion chemistry used in this model is quite large, it is well possible that for these long living ions some loss mechanisms are not taken into account, as these ions are not so common and maybe not all their processes are known in literature. So it might be that the long lifetimes of these ions are somewhat overestimated. Nevertheless, this is not so important for the present study, as we will demonstrate below that the ions do not play a significant role in the CO₂ splitting mechanism.

Again, the densities of some ions can increase due to accumulation in consecutive pulses, as shown in **Figure 6-8(b)**, where the densities of the long-living ions are depicted for five consecutive pulses of 30 ns with an interpulse period of 1 μs. Note that the densities of the short-living ions are not plotted, as

they exhibit a peak during the pulse, but negligible values in between two pulses, as is clear from **Figure 6-8(a)**. Except for the CO₄⁻ ions, the density of the other long-living ions typically increases for each pulse, followed by a recombination period where the density decreases. No significant accumulation effect is observed for CO₄⁺ and CO₃⁻, and as a result, their density stays more or less constant in a pulsed power deposition system. The O₂⁻ density shows a somewhat different behavior: it increases with one order of magnitude during the pulse, and it drops by only half an order of magnitude in between two pulses, so that accumulation effects are apparent. However, their maximum density is still very low compared to the other ions illustrated in **Figure 6-8(b)**. Finally, the CO₄⁻ density is characterized by the opposite behavior: it decreases during each pulse (except for the first pulse), and increases during the interpulse period. This can be explained as follows. CO₄⁻ is mainly produced by the three body reaction between O₂⁻ and CO₂ (reaction 84 of **Appendix II**) and consumed by recombination with CO₂⁺ and C₂O₂⁺ (reactions 104 and 111) to form CO₂, CO and O₂. Hence, CO₄⁻ recombines during every pulse with these positive ions, until the pulse stops (and CO₂⁺ and C₂O₂⁺ decrease in density), and subsequently CO₄⁻ is only produced, from O₂⁻, which recombines more slowly than CO₂⁺ and C₂O₂⁺.

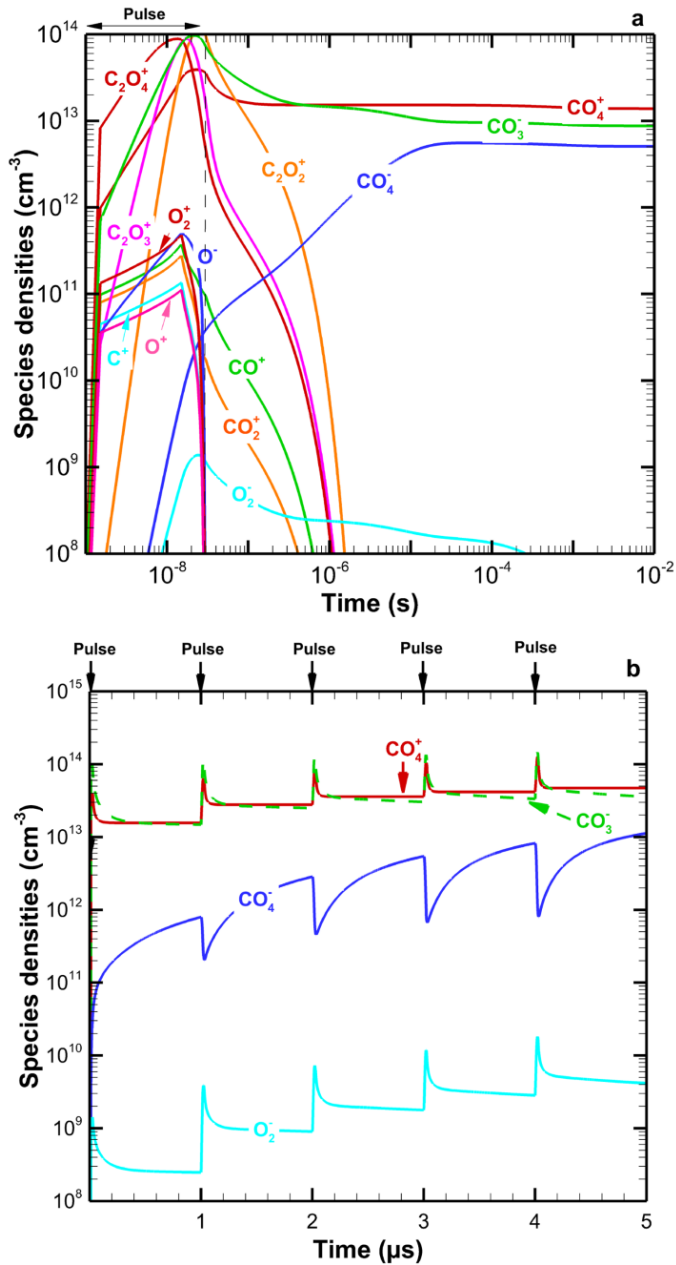


Figure 6-8: Densities of the ions as a function of time, during and after one discharge pulse of 30 ns (a), as well as for five consecutive discharge pulses of 30 ns with an interpulse period of 1 μs (b). Note that in (b) only those ions are shown that do not disappear immediately after pulse termination. The other ions are only characterized by a peak at each pulse, as can be derived from (a).

6.3.8 Contribution of the various plasma species to the CO₂ splitting

Up to this point only the densities of the vibrationally excited CO₂ molecules, the other neutral species and the ions were presented, but this does not yet give an answer to the question “which species and reactions contribute most to the CO₂ splitting?” Therefore, in **Figure 6-9(a)** and **6-9(b)** the rates of the reactions, involving ions and neutral species, contributing to the loss and production of CO₂, respectively, are plotted as a function of time during a 30 ns pulse and its afterglow. If we compare these rates with the rates of the electron impact reactions with CO₂ (**Figure 6-4**), it is clear that the electron impact vibrational and electronic excitation rates are 6 and 4 orders of magnitude higher than the rates of the highest ion-induced loss reactions of CO₂, and the electron impact dissociation, ionization, dissociative ionization and attachment rates are about 2 orders of magnitude higher. However, as already mentioned above, electron impact vibrational and electronic excitation do not necessary lead to the splitting of CO₂, because a considerable fraction of the excited states can relax back to the ground state of CO₂. The same applies to ionization, because the CO₂⁺ ions mostly recombine upon pulse termination, forming again CO₂ molecules. However, electron impact dissociation and dissociative ionization and attachment definitely give rise to splitting of the CO₂ molecules, and the rates of these reactions are also higher than the rates of the highest ion or neutral induced reactions, as is obvious from comparing **Figure 6-4** with **Figure 6-9(a)**. This tells us that electron impact reactions are mainly responsible for the CO₂ splitting, and that the contribution of ion and neutral reactions can be neglected, at least during the pulse.

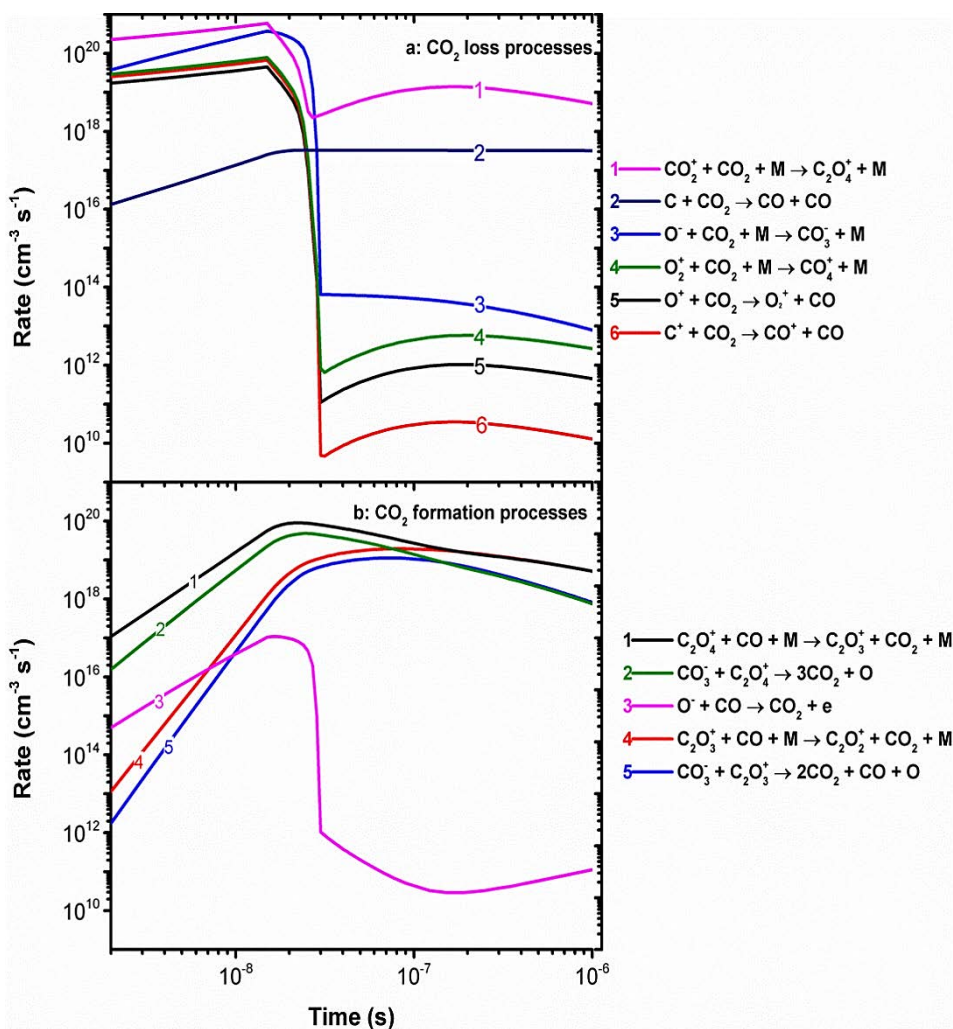


Figure 6-9: Rates for CO₂ loss (a) and formation (b) by the most important ion and neutral reactions, as a function of time during and after one discharge pulse of 30 ns.

Looking at the afterglow, the rates for the electron induced reactions drop significantly upon pulse termination, as illustrated in **Figure 6-4** above, but the same applies to the rates of most reactions involving ions, which also decrease over several orders of magnitude as a result of recombination processes (see curves 1, 3-6 in **Figure 6-9(a)**). This is not the case for the three-body

reaction with CO₂⁺ ions (curve 1 in **Figure 6-9(a)**), for which the CO₂ loss rate drops by two orders of magnitude at the end of the pulse, but remains more or less constant in the early afterglow, within a timeframe of 1 microsecond. However, after 1 microsecond, the CO₂ loss rate decreases very quickly (not shown, because out of scale), corresponding to the density profile of CO₂⁺ in **Figure 6-8(a)**. The neutrals do not contribute much to the loss of CO₂, except for the reaction between C and CO₂ producing two CO molecules (curve 2 in **Figure 6-9(a)**, and reaction 65 from **Appendix II**). Looking at the C atom density in **Figure 6-7(a)**, the CO₂ loss rate of this reaction is expected to remain constant in a timeframe up to 0.1 millisecond, followed by a fast decay afterwards.

To identify the actual net contribution of the various species to the loss of CO₂, the significant production reactions of CO₂ should also be accounted for. Their rates are also plotted as a function of time during the 30 ns pulse and its afterglow in **Figure 6-9(b)**. It is clear that most of the CO₂ production can be allocated to the same ions (namely C₂O₄⁺ and CO₃⁻) produced in the CO₂ loss processes by ions, except for C₂O₃⁺ and O⁻. Moreover, the sum of the rates for CO₂ formation and loss by ions have more or less the same magnitude and therefore the net contribution of ions to the CO₂ splitting will not be significant compared to the net contribution of the electron impact reactions. The formation of CO₂ by neutrals, on the other hand, is close to zero, meaning that their net contribution to the CO₂ splitting is determined only by their CO₂ loss rates. However, as illustrated in **Figure 6-9(a)**, this CO₂ loss rate is very low compared to the CO₂ loss rates of the ion reactions and certainly to the CO₂ loss rates of the electron impact reactions, so their contribution will also be negligible.

To further quantify the role of the various species and reactions to the CO₂ splitting, the time integrated contributions of the various

processes are presented in **Table 6-3**, for the 30 ns pulse, an afterglow of 0.1 s, and the sum of both. It is clear that most of the CO₂ molecules are lost by vibrational excitation (cf. the high values of their time-integrated rates, presented in **Table 6-3**). However, keeping in mind that most of these excited species might return to the ground state when the afterglow is long enough (see above), we will focus on the electron impact reactions which cause a direct dissociation (or ionization, or dissociative ionization or attachment) of CO₂.

Table 6-3: Overview of the time-integrated net rates of the different reaction types contributing to the loss of ground state CO₂, during a pulse of 30 ns, an afterglow of 0.1 s, and the sum of both, as well as the net overall contributions (in %) for the actual dissociation of the CO₂ ground state molecules.^a

Reactions	Pulse (cm ⁻³)	Afterglow (cm ⁻³)	Pulse + afterglow (cm ⁻³)	Overall contribution to CO ₂ splitting (%)
EI vibrational excitation	1.5 × 10 ¹⁸	3.8 × 10 ¹⁴	1.5 × 10 ¹⁸	
EI electronic excitation	3.9 × 10 ¹⁶		3.9 × 10 ¹⁶	
EI dissociation	4.8 × 10 ¹⁴		4.8 × 10 ¹⁴	(52%)
EI ionization	2.6 × 10 ¹⁴		2.6 × 10 ¹⁴	(29%)
EI dissociative ionization	1.4 × 10 ¹⁴		1.4 × 10 ¹⁴	(16%)
EI dissociative attachment	2.2 × 10 ¹⁴		2.2 × 10 ¹⁴	(23%)
Ion reactions	-1.2 × 10 ¹⁴	-8.5 × 10 ¹³	-2.0 × 10 ¹⁴	(-22%)
Neutral reactions	7.4 × 10 ⁹	1.9 × 10 ¹³	1.9 × 10 ¹³	(2%)

^aThe time-integrated vibrational and electronic excitation rates are also listed, to illustrate the dominant role of these processes in the plasma, but they do not (directly) contribute to the CO₂ splitting, and are therefore not included in the calculation of the overall contributions presented in the last column. (EI means electron impact)

As can be seen in **Table 6-3**, the pulse period has obviously the highest contribution to the loss of CO₂, in spite of its short time-scale, and this is almost exclusively due to the electron impact reactions (i.e. dissociation, ionization, dissociative ionization and

attachment). Indeed, the contribution of the neutral reactions is several orders of magnitude lower, and the ion induced reactions cause even a net formation of CO₂, as also reported by Indarto et al.^[4] In the afterglow, the electron impact reactions do not contribute to the CO₂ splitting, because of too low values for the electron density and temperature. In contrast, the contribution of the neutrals increases by almost four orders of magnitude ($\sim 10^9$ vs $\sim 10^{13}$ cm⁻³), which is mainly attributed to the long time-scale of the afterglow assumed here. Nevertheless, this contribution is still significantly lower than the electron contributions during the pulse. Again, the ions contribute only to the net formation of CO₂ in the afterglow.

The overall (i.e., sum of pulse and afterglow) net contribution to the loss of CO₂ can be completely assigned to electron impact reactions, especially to electron impact dissociation (with a contribution of 52%). Electron impact ionization and dissociative ionization also contribute for 29% and 16%, respectively, but this is partly compensated by the “negative contribution” (-22%) of the ion reactions. Indeed, the ions formed by electron impact (dissociative) ionization, or by further charge exchange reactions of the formed ions, will mostly recombine again, i.e., they contribute again to the formation of CO₂, so that the net contribution of ionization (including dissociative ionization) should be interpreted as around 23%. The same value of 23% was also found to be the contribution of dissociative attachment. Finally, the neutrals contribute only by 2%, in case of such a long afterglow (0.1s), but if the afterglow will be shorter, as is well possible in a filamentary DBD, the contribution of neutrals to the CO₂ splitting will become negligible. In fact, the contribution of the neutrals can be fully allocated to one reaction, i.e. $C + CO_2 \rightarrow 2 CO$ (see **Figure 6-9**).

As we want to elucidate the role of vibrationally excited CO₂ molecules, the same calculation as for **Table 6-3** was carried out

to obtain **Table 6-4**, which represents the different reactions taking place with the sum of all vibrationally excited CO₂ molecules, and their corresponding time integrated contributions during the pulse, the afterglow and the sum of both. The first line of **Table 6-4** indicates the time-integrated relaxation rate by VV and VT transfers to the CO₂ ground state. It is clear that the overall integrated rate of these relaxation processes (i.e., during pulse + afterglow) is exactly the same as the integrated rate of vibrational excitation of CO₂ (i.e., $1.5 \times 10^{18} \text{ cm}^{-3}$), meaning that all vibrationally excited CO₂ molecules return back to the ground state without contributing to the CO₂ splitting, at least when assuming such a long afterglow. It is, however, important to stress that if the afterglow is shorter, this is not the case, as was elaborated above. In any case, these relaxation processes obviously do not contribute to the CO₂ splitting, and are therefore not included in our calculation of the relative contributions in the last column of **Table 6-4**.

Table 6-4: Overview of the time-integrated net rates of the different reaction types contributing to the loss of vibrationally excited CO₂, during a pulse of 30 ns, an afterglow of 0.1s, and the sum of both, as well as the net overall contributions (in %) for the actual dissociation of the vibrationally excited CO₂ molecules.^a

Reactions	Pulse (cm ⁻³)	Afterglow (cm ⁻³)	Pulse + afterglow (cm ⁻³)	Overall contribution to CO ₂ splitting (%)
Relaxation	1.1 × 10 ¹⁵	1.5 × 10 ¹⁸	1.5 × 10 ¹⁸	
EI dissociation	1.2 × 10 ¹³		1.2 × 10 ¹³	(19%)
EI ionization	5.1 × 10 ¹²		5.1 × 10 ¹²	(8%)
EI dissociative ionization	2.2 × 10 ¹²		2.2 × 10 ¹²	(4%)
EI dissociative attachment	7.0 × 10 ¹²		7.0 × 10 ¹²	(11%)
Ion reactions	3.0 × 10 ¹³	6.7 × 10 ¹²	3.6 × 10 ¹³	(57%)
Neutral reactions	2.1 × 10 ⁹	8.4 × 10 ¹¹	8.4 × 10 ¹¹	(1%)

^aThe time-integrated (VV and VT) relaxation rate is also listed, to illustrate the importance of this process, but it does obviously not contribute to the CO₂ splitting, and is therefore not included in the calculation of the overall contributions presented in the last column. (EI means electron impact)

Looking closer to the processes which can cause dissociation of the vibrationally excited CO₂ molecules during the pulse, the electron impact reaction rates are at least one order of magnitude lower than the same reactions with ground state CO₂. Indeed the rate coefficients of the reactions with vibrationally excited CO₂ molecules are larger than for the same reactions with ground state CO₂, but their densities are at least 2 orders of magnitude lower (see above). As far as the ion reactions are concerned, in contrast with ground state CO₂, the ion reactions with vibrationally excited CO₂ contribute quite significantly to the net loss, with an overall contribution of 57%, followed by electron impact dissociation (19%) and dissociative attachment (11%). Ionization and dissociative ionization of vibrationally excited CO₂ contribute for only 8 and 4%, respectively, which is lower than their contribution for ground state CO₂. This can be explained by their high threshold energy (i.e., 13.3 eV), which is still clearly

higher than the energy of the vibrational levels (i.e., ~ 1 eV), so that the advantage of a lower threshold for ionization from the vibrational levels is limited. Indeed, the electronically excited states are more suitable for stimulating ionization than the vibrationally excited states (see section 6.2).

Finally, to distinguish between the actual contribution of the vibrationally excited levels and of the ground state to the CO₂ splitting, we need to compare the sum of the net contributions of ground state CO₂ with the sum of the net contributions of vibrationally excited CO₂, both integrated during the pulse and the afterglow. Integrated over pulse and afterglow, the total loss of CO₂ from ground state molecules amounts to 9.2×10^{14} cm⁻³, whereas the total loss of CO₂ from the vibrational levels is 6.3×10^{13} cm⁻³. This means that the majority (i.e., 94%) of the CO₂ splitting occurs by reactions with ground state CO₂ and only 6% by reactions with vibrationally excited CO₂. It should be realized, however, that these estimations are performed for one pulse and a long afterglow, and that the actual contribution of vibrationally excited CO₂ could be (much) higher in a DBD, attributed to accumulation effects due to consecutive pulses, depending on the interpulse period between successive filaments, as discussed in detail above.

Eventually the influence of vibrationally excited CO₂ molecules can be summarized as follows:

- 1) Vibrationally excited CO₂ molecules have a high density compared to the other CO₂ splitting species in the plasma.
- 2) The influence of accumulation can play a role for the lower vibrational states and must be considered in DBDs, which consist of successive pulses (filaments).

- 3) The activation energy of the reactions with vibrationally excited CO₂ is lower compared to the same reactions with ground state CO₂.
- 4) The vibrationally excited CO₂ molecules will, however, eventually relax back to the ground state, if the afterglow (i.e., interpulse period) is long enough, so that their net contribution to the CO₂ splitting is estimated to be limited to 6 %.
- 5) This contribution can, however, be much larger if the interpulse period between successive filaments is shorter, so that accumulation effects become important.

6.4 Conclusions

The plasma chemistry in a DBD operating in pure CO₂, including the role of vibrationally excited levels is investigated, and the important species and reactions playing a role in the CO₂ splitting are identified. It should, however, be pointed out that the vibrational excitation of CO and O₂ could also play an important role in the plasma, especially in long time scale simulations where the CO and O₂ densities will build up. The effect of these vibrational levels is not yet taken into account in the present model. Also, the vibrational kinetics for CO₂ might in reality be more complex, because higher vibrational levels might be important, although we expect this to be limited in a DBD plasma. When applying the model to a microwave plasma or a gliding arc plasma, the vibrational kinetics scheme should be extended to the higher vibrational levels. Such a study was recently performed within our group PLASMANT^[40].

The densities and rates of the important reactions of the different plasma species (i.e. electrons, vibrationally excited CO₂ molecules, various neutrals and ions) were plotted as a function of time during one pulse and afterglow, as well as for five

consecutive pulses with an interpulse period of 1 μ s, to mimic the filamentary behavior of a DBD. The production rates of vibrationally and electronic excited CO₂ were found to be at least 2 orders of magnitude higher than the other electron impact reaction rates, i.e., dissociation, ionization, dissociative ionization and attachment. As a result, the densities of the vibrationally excited species were found to be only two orders of magnitude lower than the ground state CO₂ density, during the pulse.

We have also pointed out the effect of accumulation on the density of vibrationally excited CO₂. The accumulation was found to be significant at interpulse times below 1 microsecond, but at an interpulse time between 1 and 10 microseconds the vibrationally excited CO₂ molecules start to fall back to the ground state, and above an interpulse time of 10 microseconds most of the vibrationally excited CO₂ molecules have decayed back into the ground state. The interpulse time between two filaments is not exactly known in a DBD, but our results indicate that it could be possible that locally the density of vibrationally excited CO₂ molecules, and hence their role in the CO₂ splitting, increases as a result of accumulation due to successive filaments.

The neutrals of interest were found to be molecular oxygen and CO, which are also reported in literature as the dominant end products^[2,3,30]. The role of neutrals in the CO₂ splitting was, however, not found significant, although O atoms seem to play a vital role in the formation of molecular oxygen and ozone. The role of the ions in the plasma was also investigated and short living ions which are formed and lost during the 30 nanosecond pulse, as well as long living ions which have a significant density even in the millisecond range were identified.

The findings of this chapter regarding the net contribution of the different plasma species and reactions to the dissociation of CO₂ can be summarized as follows:

- 1) The splitting of ground state CO₂ is dominated by electron impact reactions, and predominantly by electron impact dissociation. Electron impact ionization is also important, but is compensated by the fact that a large fraction of the formed ions will eventually recombine, resulting again in the formation of CO₂.
- 2) The splitting of vibrationally excited CO₂ is mainly dominated by ion reactions, followed by electron impact dissociation.
- 3) 94% of the CO₂ splitting is achieved from the ground state whereas 6% occurs from the vibrationally excited states. This contribution is, however, calculated for one pulse and a long afterglow. If the interpulse period between two successive filaments is shorter, accumulation effects can occur for the vibrationally excited molecules, and consequently, their role can be (much) higher.

6.5 References

- [1] H. Matsumoto, S. Tanabe, K. Okitsu, Y. Hayashi, S. L. Suib, *Bull. Chem. Soc. Jpn.* **1999**, *72*, 2567–2571.
- [2] L. F. Spencer, A. D. Gallimore, *Plasma Chem. Plasma Process.* **2010**, *31*, 79–89.
- [3] A. Indarto, J. Choi, H. Lee, H. K. Song, *Environ. Eng. Sci.* **2006**, *23*, 1033–1043.
- [4] A. Indarto, D. R. Yang, J.-W. Choi, H. Lee, H. K. Song, *J. Hazard. Mater.* **2007**, *146*, 309–15.
- [5] H. Hokazono, M. Obara, K. Midorikawa, H. Tashiro, *J. Appl. Phys.* **1991**, *69*, 6850.
- [6] A. Fridman, *Plasma Chemistry*, Cambridge University Press, New York, **2008**.
- [7] A. A. Fridman, V. D. Rusanov, *Pure Appl. Chem.* **1994**, *66*, 1267–1278.
- [8] G. M. Semiokhin, I. A., Andreev, Y. P., and Panchenkov, *Russ. J. Phys. Ch.* **1964**, *38*, 1126–1128.
- [9] V. V. Andreev, Y. P., Semiokhin, I. A., Panchenkov, G. M., and Baraev, *Russ. J. Phys. Ch.* **1964**, *38*, 431–434.
- [10] Y. P. Semiokhin, I. A. and Andreev, *Russ. J. Phys. Ch.* **1966**, *40*, 1279–1282.
- [11] I. F. Luk'yanov, V. B., Emel'yanov, Y. M., and Aleksandrova, *Russ. J. Phys. Ch.* **1967**, *41*, 86–90.
- [12] V. V. Luk'yanov, V. B., Emel'yanov, Y. M., and Kovalenko, *Russ. J. Phys. Ch.* **1967**, *41*, 1081–1083.
- [13] V. B. Luk'yanov, *Russ. J. Phys. Ch.* **1967**, *41*, 1083–1085.
- [14] V. G. Luk'yanov, V. B., Nesmeyanov, A. N., and Bachinin, *Russ. J. Phys. Ch.* **1967**, *41*, 1438–1441.
- [15] V. B. Luk'yanov, *Russ. J. Phys. Ch.* **1967**, *41*, 1536–1537.
- [16] V. I. Luk'yanov, V. B., Simonov, E. F., and Golovanov, *Russ. J. Phys. Ch.* **1969**, *43*, 640–645.
- [17] W. Siemens, *Ann. der Phys. und Chemie* **1857**, *178*, 66–122.
- [18] B. Eliasson, U. Kogelschatz, *IEEE Trans. Plasma Sci.* **1991**, *19*, 309–323.
- [19] J. J. Lowke, A. Phelps, B. W. Irwin, *J. Appl. Phys.* **1973**, *44*, 4664.
- [20] T. G. Beuthe, J.-S. Chang, *Jpn. J. Appl. Phys.* **1997**, *36*, 4997–5002.

- [21] A. Jain, D. Norcross, *Phys. Rev. A* **1992**, 45, 1644–1656.
- [22] W. Liu, G. A. Victor, *Astrophys. J.* **1994**, 435, 909.
- [23] A. V Phelps, *Tabulations of Collision Cross Sections and Calculated Transport and Reaction Coefficients for Electron Collisions with O₂ Technical Report*, **1985**.
- [24] G. Govinda Raju, *Gaseous Electronics*, CRC Press, **2005**.
- [25] N. G. R. Blauer Jay A., *A Survey of Vibrational Relaxation Rate Data for Processes Important to CO₂-N₂-H₂O Infrared Plume Radiation*, Irvine, **1973**.
- [26] Sergey T. Surzhikov, *Non-Equilibrium Gas Dynamics – From Physical Models to Hypersonic Flights*, Moscow, **2009**.
- [27] A. Chirokov, A. Gutsol, A. Fridman, *Pure Appl. Chem.* **2005**, 77, 487–495.
- [28] I. A. Kossyi, A. Yu Kostinsky, A. A. Matveyev, P. V. Silakov, *Plasma Sources Sci. Technol.* **1992**, 1, 207–220.
- [29] A. Cenian, A. Chernukho, V. Borodin, G. Śliwiński, *Contrib. to Plasma Phys.* **1994**, 34, 25–37.
- [30] S. Paulussen, B. Verheyde, X. Tu, C. De Bie, T. Martens, D. Petrovic, A. Bogaerts, B. Sels, *Plasma Sources Sci. Technol.* **2010**, 19, 034015.
- [31] X. Tu, H. J. Gallon, M. V Twigg, P. A. Gorry, J. C. Whitehead, *J. Phys. D. Appl. Phys.* **2011**, 44, 274007.
- [32] U. Kogelschatz, *Plasma Chem. Plasma Process.* **2003**, 23, 1–16.
- [33] D. I. Slovetsky, PhD Dissertation, Kinetics and Mechanisms of Physical and Chemical Processes in Non-Equilibrium Plasma-Chemical Systems, USSR Academy of Sciences, **1979**.
- [34] A. Gutsol, A. Rabinovich, A. Fridman, *J. Phys. D. Appl. Phys.* **2011**, 44, 274001.
- [35] A. Rabinovich, T. Nunnally, F. Alexander, G. Alexander, *Non-Equilibrium Gliding Arc Plasma System for CO₂ Dissociation*, **2012**, US 2012/0090985 A1.
- [36] S. Y. Savinov, H. Lee, H. K. Song, B.-K. Na, *Korean J. Chem. Eng.* **2002**, 19, 564–566.
- [37] T. Nunnally, K. Gutsol, A. Rabinovich, A. Fridman, A. Gutsol, A. Kemoun, *J. Phys. D. Appl. Phys.* **2011**, 44, 274009.
- [38] B. Bulos, A. Phelps, *Phys. Rev. A* **1976**, 14, 615–629.
- [39] J. Amouroux, S. Cavadias, a Doubla, *IOP Conf. Ser. Mater. Sci. Eng.* **2011**, 19, 012005.

- [40] T. Kozák, A. Bogaerts, *Plasma Sources Sci. Technol.* **2014**, 23, 045004.

Chapter 7:

Real time scale simulations and experimental study for CO₂ splitting in DBDs

In this chapter, we extend the model presented in previous chapter, to run real time scale simulations. Furthermore, we perform experiments to study the CO₂ splitting in a DBD plasma for a wide range of parameters. The frequency and dielectric material do not affect the CO₂ conversion and energy efficiency, but the discharge gap can have a considerable effect. The specific energy input has the most important effect on the CO₂ conversion and energy efficiency. The plasma chemistry model for CO₂ splitting shows reasonable agreement with the experimental conversion and energy efficiency. This model is used to elucidate the critical reactions that are mostly responsible for the CO₂ conversion. Finally, the results are benchmarked with other CO₂ splitting techniques, and the limitations as well as the benefits and future possibilities are identified in terms of modifications of DBD plasmas for greenhouse gas conversion in general.

Aerts, R., Somers, W., & Bogaerts, A. (2014). CO₂ splitting in a dielectric barrier discharge plasma: A combined experimental and computational study. Submitted to ChemSusChem

7.1 Introduction

In spite of the growing interest in CO₂ conversion into value-added chemicals by means of plasma technology, systematic investigations for the optimum operating conditions have not yet been carried out. Nevertheless, such a systematic investigation is highly needed, before the technology is ready for practical applications. In the present chapter, this will be performed for the case of pure CO₂ splitting into CO and O₂.

Some scattered results on CO₂ splitting have been reported already for specific operating conditions^[1–3]. Paulussen et al.^[1] investigated the effect of flow rate, applied power, frequency and temperature and reported a maximum conversion of 30% at a flow rate of 0.05 l/min, a power density of 15 W/cm³ and a frequency of 60 kHz. Yu et al.^[2] found that adding a dielectric packing results in a rise of the conversion with 8% up to 22.5%, at a plasma power of 35.3 W and a flow rate of 40 ml/min. Tagawa et al.^[3] proposed a hybrid reactor, i.e., a DBD plasma on the surface of a solid oxide electrolyser cell (SOEC) but they didn't study the DBD without the SOEC in detail.

Some results are also reported for a mixture of CO₂ with an inert gas, e.g. Ar and N₂^[4–10]. Wang et al.^[4] investigated the effect of electrode material and concluded that a Cu electrode has the largest reactivity towards CO₂ decomposition. New ceramic dielectric barriers were developed by Li et al.^[6–9] and Wang et al.^[10], and gave rise to an increase of the conversion. Zheng et al.^[5] studied the effect of voltage and CO₂ concentration, and found that a high voltage and a low CO₂ concentration gave rise to a lower energy efficiency.

Therefore, we strongly believe that a more systematic study is required to improve the performance and also to put a benchmark for other (plasma) technologies. The process envisaged is the following (see also **Chapter 2**, section 2.3.2):



$$\Delta H_{\text{R}} = 279.8 \text{ kJ/mol} = 2.9 \text{ eV/molec (at 300 K)}$$

This reaction is highly endothermic, so the energy efficiency of the process is a critical issue. However, plasmas can be beneficial for this purpose, compared to other (classical) technologies, because it is well known that the vibrational levels of CO₂ can be efficiently populated in a plasma, and this forms an attractive, energy-efficient route for the dissociation of CO₂, as explained in detail by Fridman^[11] as well as in **Chapter 2 and Chapter 6**.

In this chapter, experiments will be carried out, varying the applied frequency, power, gas flow rate, dielectric material and discharge gap, focusing on the CO₂ conversion and energy efficiency. Moreover, computer simulations will be also performed, in order to elucidate the underlying mechanisms of the CO₂ splitting process. Finally, the results will be benchmarked with other CO₂ splitting techniques, and the limitations and future possibilities for CO₂ splitting by DBD plasmas will be identified.

7.2 Description of the chemistry and the experiments

7.2.1 Description of the chemical model

The physical description of the model can again be found in **Chapter 3**, and the plasma chemistry is the same as in **Chapter 6**.

In the present chapter, the model is applied to exactly the same residence times as obtained in the experiments, i.e., in the order of 1-60 s. This means that up to 2000 consecutive pulses (of 60 ns) are simulated, with interpulse time of 0.03 s, to mimic the filamentary character of the DBD, i.e., the gas molecules pass through a large number of microdischarge filaments on their way through the reactor. Note that the pulse duration is chosen to be 60 ns instead of 30 ns, because this will reduce the total number pulses required for the same SEI, and thus it reduces the calculation time. Finally, as the actual plasma volume (i.e., sum of the filament volumes) is much smaller than the total volume of the plasma reactor (see **Chapter 3**, section 3.1.2), the deposited energy was chosen a factor 7 higher (see section 7.3.2).

Finally, a reduced chemistry set is also developed, by comparing the calculation results with the full set, in the entire range of conditions investigated here, as will be explained below. This reduced set can be very useful for more time-consuming 2D or 3D plasma models of CO₂ splitting.

7.2.2 Description of the validation experiments

The plasma reactor is a tubular DBD reactor, consisting of a dielectric tube and two concentric cylindrical electrodes. A more detailed description can be found in **Chapter 3**. The feed and product gases are analyzed by a three-channel compact-gas chromatograph (CGC) (Interscience), equipped with two thermal conductivity detectors (TCD) and a flame ionization detector (FID) (see also **Chapter 3**).

The conversion of CO₂ is calculated from the peak areas measured in the gas chromatograms (where CO_{2,inlet} is measured without plasma):

$$X_{CO_2}(\%) = \left(\frac{CO_{2,inlet} - CO_{2,outlet}}{CO_{2,inlet}} \right) * 100\% \quad (E7-1)$$

The oxygen-based selectivities of CO and O₂ are calculated as:

$$S_{CO}(\%) = 0.5 * \frac{CO_{outlet}}{CO_{2,inlet} - CO_{2,outlet}} * 100\% \quad (E7-2)$$

$$S_{O_2}(\%) = \frac{O_{2,outlet}}{CO_{2,inlet} - CO_{2,outlet}} * 100\% \quad (E7-3)$$

In order to calculate the energy cost and energy efficiency of the process, the specific energy input (SEI) in the plasma from the power and the gas flow rate is defined:

$$SEI \left(\frac{J}{cm^3} \right) = SEI \left(\frac{kJ}{l} \right) = \frac{Power (kW)}{Flow rate \left(\frac{l}{min} \right)} * 60 \left(\frac{s}{min} \right) \quad (E7-4)$$

The energy cost to produce 1 mole of CO is then calculated as:

$$E_{CO} \left(\frac{kJ}{mol} \right) = SEI \left(\frac{kJ}{l} \right) * \left[\frac{molar volume \left(\frac{l}{mol} \right) * 100\%}{X_{CO_2}(\%)} \right] \quad (E7-5)$$

And finally, the energy efficiency (η) is calculated as:

$$\eta(\%) = \frac{\Delta H_R \left(\frac{kJ}{mol} \right)}{E_{CO} \left(\frac{kJ}{mol} \right)} * 100\% \quad (E7-6)$$

where the value of the reaction enthalpy (ΔH_R) is 279.8 kJ/mol (see Introduction).

7.3 Results and Discussion

7.3.1 Experimental parameter screening

In this section the experimental results will be discussed for the influence of various operating parameters, i.e., frequency, kind of dielectric, discharge gap, electrical power and gas flow rate, on the CO₂ conversion and energy efficiency of the process. Note that also the effect of these parameters on the selectivities of the formed products was investigated, i.e., CO and O₂, but no influence was observed. The CO and O₂ selectivities were always around 50%, for all conditions investigated. This is like expected, as the underlying chemistry of CO₂ splitting is very simple, i.e., it is determined by the reaction: $\text{CO}_2 \rightarrow \text{CO} + \frac{1}{2} \text{O}_2$. Some traces of O₃ can be formed (see reaction scheme and calculated number densities in section 7.3.2 below), but this could not be detected in our GC analysis.

Effect of the frequency

The frequency (varied in the range between 6 and 75 kHz at a constant flow rate and plasma power) was found to have a negligible influence on the conversion and energy efficiency. However, the plasma appears more filamentary at high frequency (75 kHz) compared to low frequency (6 kHz), as is illustrated in **Figure 7-1**. Therefore, in this study a fixed frequency of 23.5 kHz was applied, which is the energetically optimal resonance frequency of the power generator used.

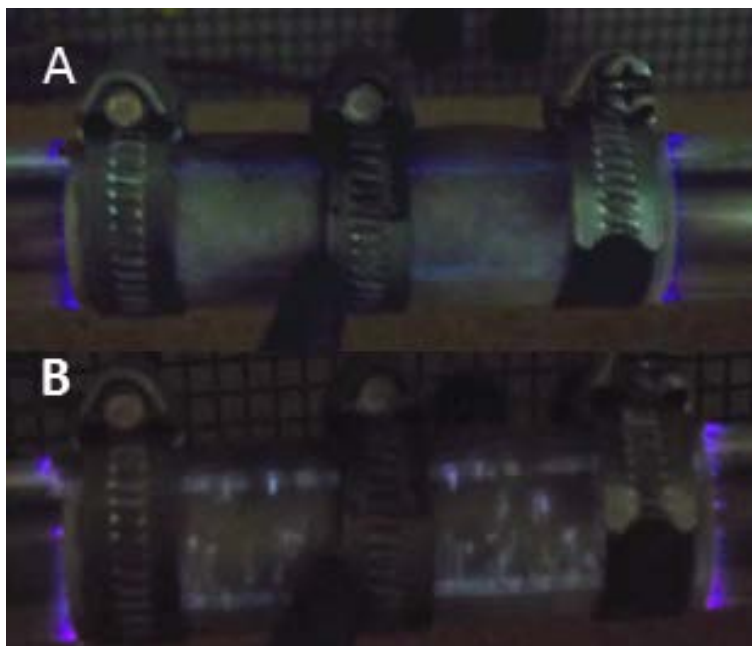


Figure 7-1: Pictures of the DBD plasma at a frequency of 6 kHz (A) and 75 kHz (B), illustrating the difference in filamentary character.

Effect of the dielectrics

Several experiments were performed, for different discharge gaps and a wide range of operating conditions, comparing quartz and alumina (99.7% Al₂O₃, Ceratec) as dielectrics, but no significant difference in the performance of the CO₂ splitting was observed. **Figure 7-2** presents the conversion and energy efficiency for both dielectrics, as a function of SEI, for a discharge gap of 1.8mm. The SEI is defined here by changing the gas flow rate between 10 and 500 ml/min, while keeping the applied power constant at 80W. This results in a plasma power of 35W ± 3W for quartz and 39W ± 1W for alumina. The conversion increases with SEI, as expected, and reaches values up to 35% at the highest values of SEI investigated (around 225 J/cm³, which corresponds in this case, i.e., for a power of 39W ± 1W, to a gas flow rate of 10 ml/min, or a quite long gas residence time of 44s). The energy

efficiency, on the other hand, drops upon higher SEI, which is also like expected (see the formulas in section 7.2.2 above). When reaching a conversion of 35%, the energy efficiency is only 2%. A higher energy efficiency of 8% could be reached at an SEI of 25 J/cm³, but this corresponds to a very low conversion of only a few %. Hence, there is a clear trade-off between conversion and energy efficiency. Depending on the targeted application and the boundary conditions (e.g., use of sustainable electricity), the one or the other can thus be optimized or a compromise between both can be sought.

Although virtually no difference was observed between quartz and alumina dielectrics on the conversion and energy efficiency (except for some minor differences in the lower region of the SEI, i.e., below 100 J/cm³), the use of alumina instead of quartz has some advantages in terms of fabrication, and it is more resistant against arc formation and high temperature (melting point of 2054 °C vs. 1470 °C for quartz)^[12]. It is worth to mention that in literature some more sophisticated dielectrics, like Ca_{0.8}Sr_{0.2}TiO₃^[10] and Ca_{0.7}Sr_{0.3}TiO₃ with 0.5 wt.% Li₂Si₂O₅^[6,7], were reported to enhance the CO₂ conversion and/or energy efficiency, because they increase the density of the filaments in the plasma. A more thorough discussion about this effect will be made in section 7.3.4.

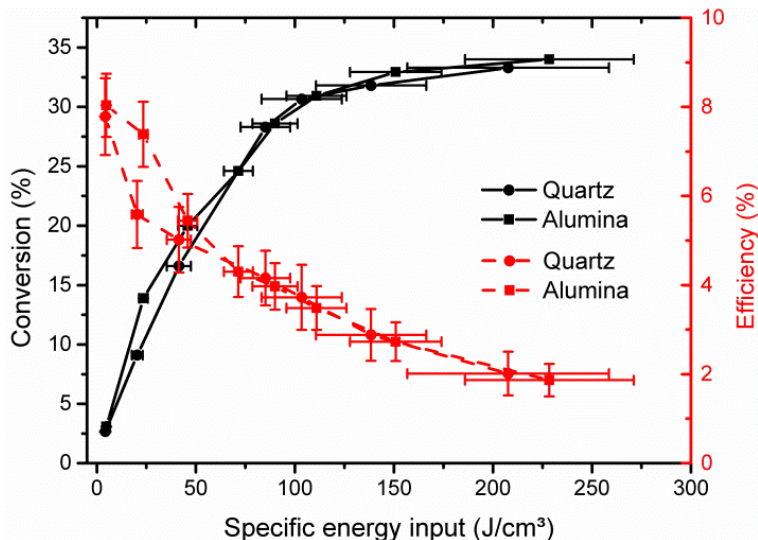


Figure 7-2: Effect of the dielectric on the conversion (black curves, left axis) and energy efficiency (red curves, right axis), as a function of the SEI. The calculation of the error bars is based on the uncertainties of the power, the flow rate and the GC measurements. The error bars of the conversion in the y-direction are smaller than 1% and therefore not visible.

Effect of the discharge gap

The influence of the discharge gap on the conversion and energy efficiency is presented as a function of the SEI in **Figure 7-3**. Here a quartz dielectric is used, because it is transparent and thus allows visible observation. The SEI is again varied by adjusting the gas flow rate in the range between 10 and 500 ml/min, at a constant plasma power of $35\text{W} \pm 3\text{W}$.

The gaps of 1.8 mm and 2.3 mm yield roughly the same conversion and energy efficiency, but the gap of 3.3 mm results in a clear drop in conversion and hence also in the energy efficiency. A larger gap of 4.5 mm was also tested but the discharge was only ignited at the sharp edges of the foil electrode and thus no stable volume discharge was established. Note that

for a fixed SEI (and hence gas flow rate and power) the residence time will be longer, and the power density will be lower, for the larger discharge gaps, due to the larger volume (i.e., the reactor volume is 7.4 cm³, 9.2 cm³, and 12.3 cm³, for the gaps of 1.8, 2.3 and 3.3 mm). Indeed, for instance at a SEI of 100 J/cm³, the residence times will be 22.1, 27.4 and 36.8, while the power densities will be 4.7, 3.7 and 3.2, in the gaps of 1.8 mm, 2.3 mm and 3.3 mm, respectively. It appears that this longer residence time and lower power density compensate each other for the gaps of 1.8 and 2.3 mm, but for the 3.3 mm gap, the lower power density seems dominant.

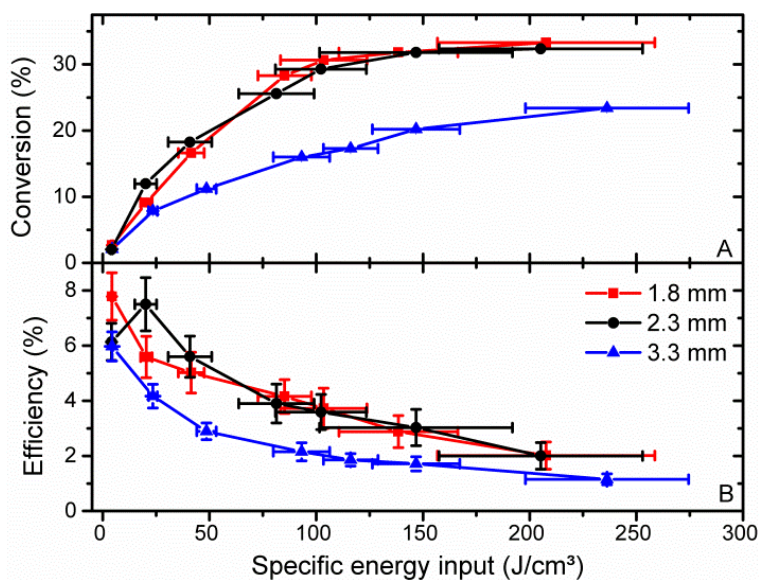


Figure 7-3: Effect of the discharge gap on the conversion (Figure A) and energy efficiency (Figure B), as a function of the SEI . The calculation of the error bars is based on the uncertainties of the power, the flow rate and the GC measurements. The error-bars of the conversion in the y-direction are smaller than 1% and therefore not visible.

Therefore, a more detailed analysis of the effect of the discharge gap is made by looking at the Lissajous plots (see also **Chapter 3**), presented in **Figure 7-4**. Note that the total surface area is

the same, as the latter is determined by the plasma power ($\pm 35\text{W}$), but nevertheless, there are distinct differences in the three Lissajous plots. Indeed, as the gap increases, a larger applied voltage is necessary to maintain the discharge (i.e., 13, 14 and 15 kV_{pp} for the gaps of 1.8, 2.3 and 3.3 mm, respectively). Moreover, as the plasma power is the same, this increase in applied voltage is compensated by a drop in peak-to-peak charge.

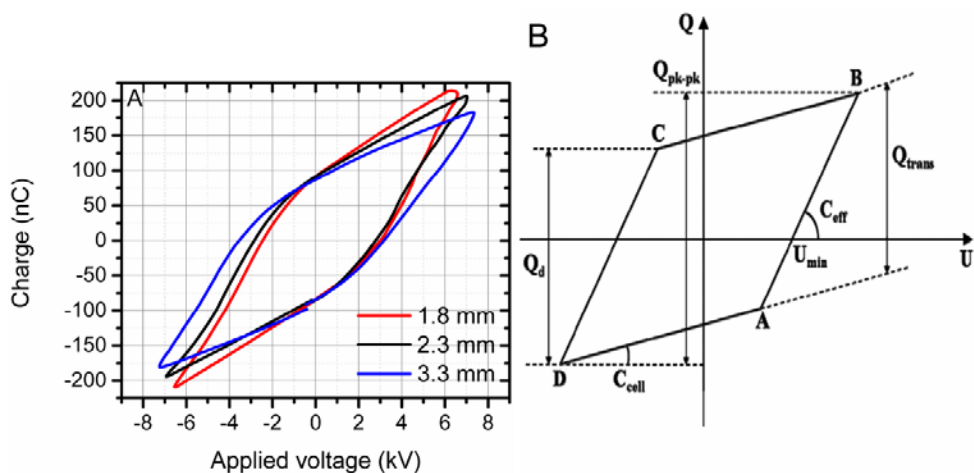


Figure 7-4: Lissajous plots for the three different discharge gaps, at a plasma power of $\pm 35\text{ W}$, with a quartz dielectric (A), and schematic diagram of the Lissajous plot, explaining all the quantities that can be deduced from it (see text) (B).

The difference in applied voltage and charges for the three discharge gaps is, however, gradual, and the same for the gaps of 1.8, 2.3 and 3.3 mm, and therefore it cannot explain why virtually no difference in conversion and energy efficiency was observed between 1.8 and 2.3 mm, whereas the difference was quite striking for the 3.3 mm gap. Therefore, to fully understand the effect of the gap on the conversion, the capacitance for the dielectric (C_d) and the gap (C_g), as well as the capacitance of the reactor without plasma (C_{cell}) and the effective capacitance during the plasma-on stage (C_{eff}) are calculated^[13].

$$C_d = \frac{2\pi\epsilon_0\epsilon_d L}{\ln(r_{\text{outer}}/r_{\text{inner}})} \quad (\text{E7-7})$$

$$C_g = \frac{2\pi\epsilon_0\epsilon_g L}{\ln(r_{\text{inner}}/r_{\text{rod}})} \quad (\text{E7-8})$$

$$C_{\text{cell}} = \frac{1}{C_d} + \frac{1}{C_g} \quad (\text{E7-9})$$

In these formulas $\epsilon_0 = 8.854 \times 10^{-12} \text{ Fm}^{-1}$ is the permittivity of vacuum, $\epsilon_g = 1.000922$ is the relative permittivity of CO₂ and $\epsilon_d = 3.8$ for quartz^[13,14]. Furthermore, L is the length of the plasma (90 mm; see above), r_{inner} and r_{outer} are the inner and outer radii of the dielectric tube (i.e., constant in the three cases) and r_{rod} is the radius of the high voltage electrode (rod), which is varied as 5, 6 and 6.5 mm (see above). This results in a constant C_d of 67 pF, whereas C_g varies from 21 pF for the smallest gap (1.8 mm) to 16 pF for the gap of 2.3 mm, and 10 pF for the largest gap of 3.3 mm.

These values should be compared with the slopes of lines AB and CD from the Lissajous plots of **Figure 7-4**, which represent the effective capacitance C_{eff} during the discharge-on phase, when the gas breakdown occurs in the gap and the plasma is ignited. The slope of these lines should be equal to C_d for a fully bridged gap^[15]. In our case, C_{eff} is determined to be 56 pF for the gaps of 1.8 and 2.3 mm, and 40 pF for the gap of 3.3 mm. This is clearly lower than the capacitance of the dielectric quartz tube ($C_d = 67$ pF; see above), especially for the largest gap, indicating that the discharge gap is not fully bridged. Tu et al. indeed reported that C_{eff} depends on the spatial distribution of the discharge across the gap over a half-period of the applied voltage^[16]. Hence, it can be concluded that the total plasma volume (i.e., the volume occupied

by the streamers) is much smaller than the total volume of the plasma reactor, especially for the largest gap.

This reduced formation of streamers is clearly visible in the electric current waveforms, illustrated in **Figure 7-5**. Comparing the waveforms of the 1.8 and 2.3 mm gaps tells us that the absolute values of the current are somewhat lower in the 2.3 mm gap, which is correlated with the slightly lower peak-to-peak charges, illustrated in the Lissajous plots. This trend is also continued, and even more striking, for the gap of 3.3 mm, but on top of that, the streamer frequency is clearly reduced, compared to the gaps of 1.8 and 2.3 mm.

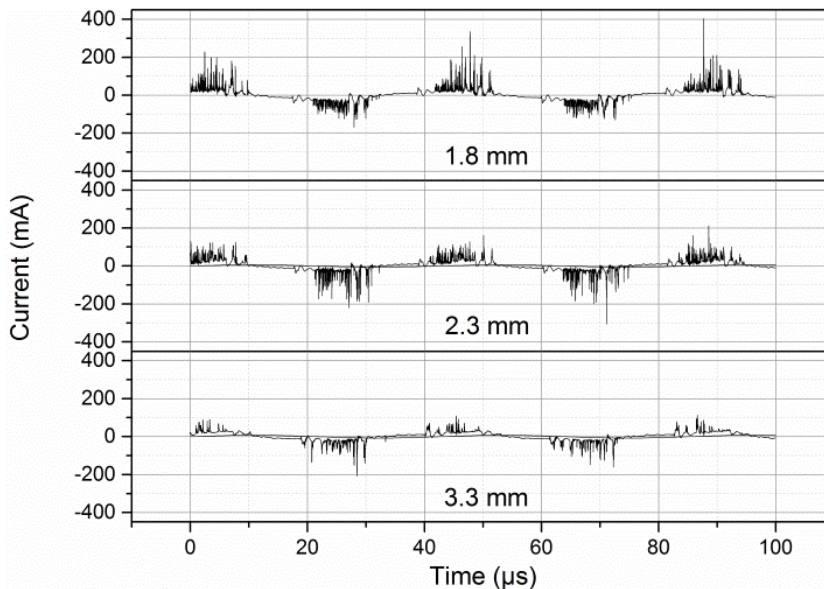


Figure 7-5: Comparison of the electric current waveforms for the three different discharge gaps at a plasma power of ± 35 W, with a quartz dielectric, illustrating the reduced streamer formation for the gap of 3.3 mm.

To conclude, the gaps of 1.8 and 2.3 mm yield more or less the same CO₂ conversion and energy efficiency, because they exhibit

the same streamer behavior. On the other hand, the larger gap of 3.3 mm results in a clearly lower CO₂ conversion and energy efficiency (cf. **Figure 7-3** above), as less streamers are formed for a fixed SEI, giving rise to a lower effective plasma volume, and therefore a reduced possibility for CO₂ conversion. Moreover, the streamers seem to have lower peak currents, which corresponds to a drop in the electron density, due to the following relation:

$$n_e = \frac{J}{E \mu_e e} \quad (\text{E7-10})$$

where J is the current density, E the electric field and μ_e the electron mobility. Consequently, the lower electron density results in a lower CO₂ conversion, because of the drop in electron impact reaction rates^[17]. Finally, an increasing gap distance gives rise to a reduced electric field strength (E/N), and this results in a drop in the average electron energy in the discharge. This lower electron energy (or reduced electric field) will affect the fraction of energy transferred to the various types of collisions^[17,18]. Nevertheless, as the gap of 3.3 mm clearly shows a lower conversion and energy efficiency than the gaps of 1.8 and 2.3 mm, it can be concluded that the reduced streamer density in the 3.3 mm gap is more important in determining the lower conversion and energy efficiency than the latter two effects.

Effect of the electric power and gas flow rate

As indicated by the formula in Section 7.2.2 above, the SEI in the plasma system is defined by both the gas flow rate and the plasma power. In literature, the SEI is often used as a major determining factor for the conversion and energy efficiency, and therefore, the conversion and energy efficiency are often plotted

as a function of SEI^[19–22]. However, it is observed that the same values of SEI, but defined by different combinations of plasma power and gas flow rate, can result in a different conversion. Therefore, in this section the influence of gas flow rate (or residence time) and plasma power on the CO₂ conversion and energy efficiency separately is investigated. To our knowledge, such a separate study is never published before.

In **Figure 7-6** the conversion and energy efficiency are plotted vs SEI, for different values of residence time (or gas flow rate) at fixed plasma power (red curve), and for different values of plasma power, at fixed gas flow rates (blue and black curves). The figure clearly indicates that these two parameters affect the SEI, and therefore the CO₂ conversion and energy efficiency, in a different way. In all cases, the conversion first increases with SEI, but then saturates to a maximum value, which appears to be different in the different cases. A low plasma power (40 W) with a low gas flow rate (of 10 ml/min, corresponding to a long residence time of 44 s) gives rise to a maximum conversion (see red curve). The same SEI can also be obtained with a higher plasma power and higher gas flow rate (or shorter residence time), and this obviously results in a lower maximum conversion, as is clear from the black and blue curves. Hence, the flow rate (or gas residence time) seems to have a more pronounced effect on the conversion than the plasma power. The same effect is visible for the energy efficiency, but it is less pronounced. To our knowledge, this effect has not yet been reported before. It suggests that by a proper tuning of plasma power versus gas flow rate, the conversion and energy efficiency at a certain SEI can be increased, which is very promising. However, this effect is only observed for high values of SEI (above 100 J/cm³), which unfortunately gives rise to a low energy efficiency.

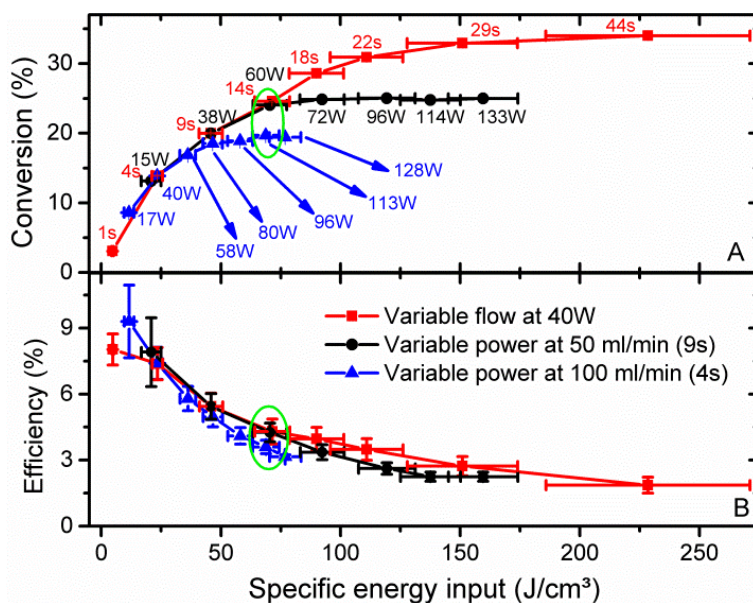


Figure 7-6: Effect of the gas flow rate (or residence time) and plasma power on the conversion (Figure A) and energy efficiency (Figure B), plotted as a function of the SEI, using alumina dielectrics. The corresponding values of plasma power, resulting in certain SEI values at the fixed gas flow rates of 50 and 100 ml/min (black and blue curves), as well as the corresponding values of the residence time, resulting in certain SEI values at a fixed plasma power of ± 40 W (red curve), are also shown in Figure A. The calculation of the error bars is based on the uncertainties of the power, the flow rate and the GC measurements. For the sake of clarity, the error bars are only presented for the energy efficiency. The green circle in Figure A indicates the conditions plotted in Figure 8 below.

To compare the three cases presented in **Figure 7-6** from the electrical point of view, the current and voltage waveforms for three distinct combinations of plasma power and gas flow rate, resulting in nearly the same SEI of 70 J/cm^3 , are shown in **Figure 7-7**. More streamers are observed and especially higher current values in the case of a high power and high flow rate (upper panel) than in the case of a low power and low flow rate (lower panel), which is quite logical. Nevertheless, the first condition gives rise to a lower conversion. This indicates that the longer residence time, which arises from the lower gas flow rate (lower

panel), has a more pronounced effect on the conversion (and hence energy efficiency) than the higher power (and thus higher current and higher streamer intensity). Indeed, a longer residence time means that the CO₂ molecules can stay longer within the streamers, and this seems more important for the conversion than the higher streamer intensity (or electron density), for the same SEI .

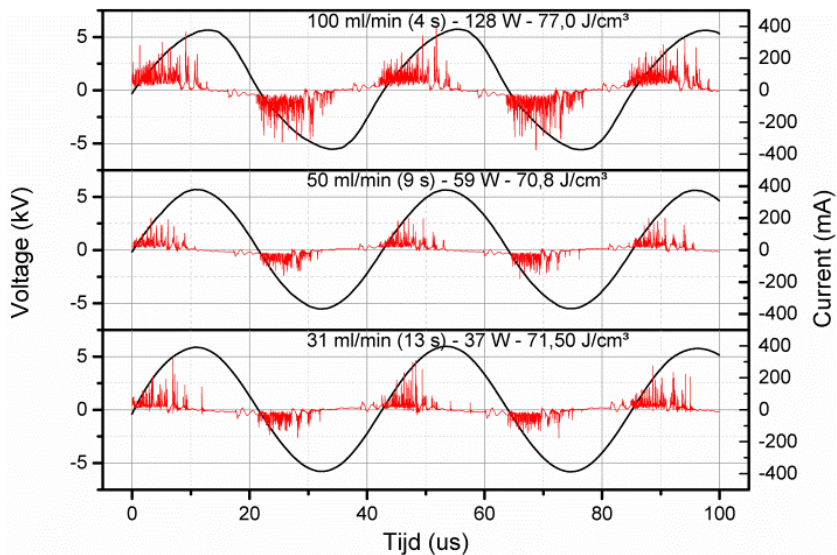


Figure 7-7: Comparison of the voltage and electric current waveforms for three different combinations of plasma power and gas flow rate (or residence time), yielding a similar SEI (cf. the green circle indicated in Figure 7 above).

7.3.2 Modelling the plasma chemistry of CO₂ splitting

In this section the model presented in previous chapter is extended to longer residence times, by simulating a large number of consecutive pulses (i.e., microdischarge filaments or streamers) at a frequency of 34.4 Hz (see above), until a given residence time is reached. As indicated in Section 7.3.1 above, the effective volume occupied by the sum of all individual micro-

discharges is much smaller than the total plasma reactor volume. Therefore, the power density used as input in the model, from which the SEI is calculated, is multiplied by a factor 7, to account for this. Note that the exact value of the effective plasma volume occupied by the streamers is not known, so this factor 7 is chosen somewhat arbitrarily, because it yields reasonable agreement between the calculated and measured values for the CO₂ conversion (see below). Nevertheless, even if this factor can be considered as a kind of fitting parameter, it does have a physical meaning, as demonstrated by Motret et al.^[23,24], and even if the quantitative calculation results might be dependent on this factor, the qualitative trends predicted by the model can still be validated in this way, and the validated model can then subsequently be used to elucidate the underlying plasma chemistry. The latter will be illustrated in this section, based on a reduced plasma chemistry, which still describes the essential processes for the CO₂ conversion, and which will also be very useful for the development of time-consuming 2D or 3D plasma chemistry models.

Validation of the model

Figure 7-8 illustrates the comparison of the calculated conversion with measured values for different powers and gas flow rates (cf. **Figure 7-6** above), as a function of SEI. A very good agreement is reached for SEI values up to 100 J/cm³. Above 100 J/cm³ the model does not show saturation, like in the experiments, but the experimental data also yield different degrees of saturation, depending on the combination of power and gas flow rate, as explained in detail in section 7.3.1 above. On the other hand, the energy efficiency at these high SEI values is very low (see section 7.3.1 above), and the residence time becomes quite long, so these conditions are probably not attractive anyway. Therefore, one may conclude that the agreement between model and experiments is reasonable, at

least in the SEI region of most practical interest. Furthermore, it was checked in the previous chapter that the calculated electron density and temperature in the model are in the correct order of magnitude, compared with literature data. Hence, one may conclude that the model is sufficiently realistic to be used for elucidating the underlying chemical pathways of CO₂ splitting.

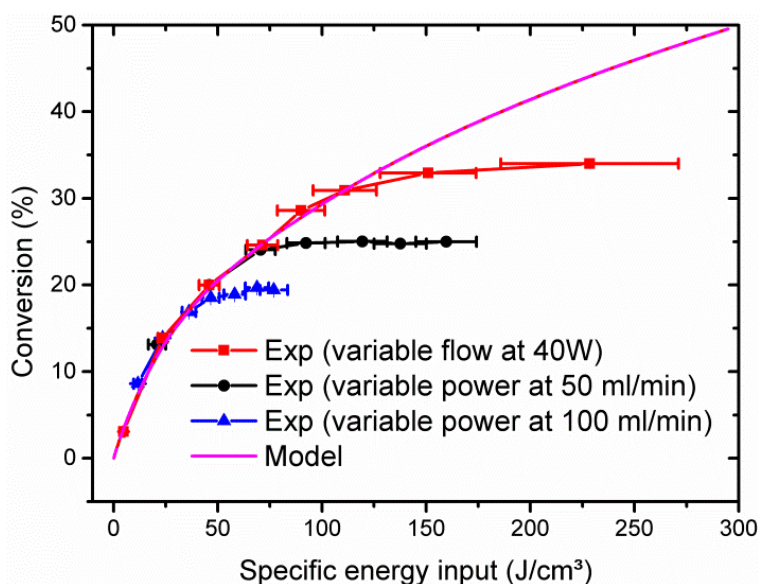


Figure 7-8: Comparison of the calculated and measured values for the conversion, as a function of the SEI. Note that the power density, and hence the SEI, used in the model is multiplied by a factor 7, to account for the lower volume occupied by the streamers (see text). The calculation of the error bars is based on the uncertainties of the power, the flow rate and the GC measurements. The error-bars in the y-direction are smaller than 1% and therefore not visible.

Reduced chemistry set for CO₂ splitting

As mentioned in **Chapter 6**, the complete model contains 42 species which interact with each other in 501 chemical reactions. This will be prohibitively long for 2D and 3D plasma models. Therefore, this chemistry set has been reduced, based on the

most important production and loss processes of our full model, so that it only includes the most critical plasma species and reactions for the CO₂ splitting (see below).

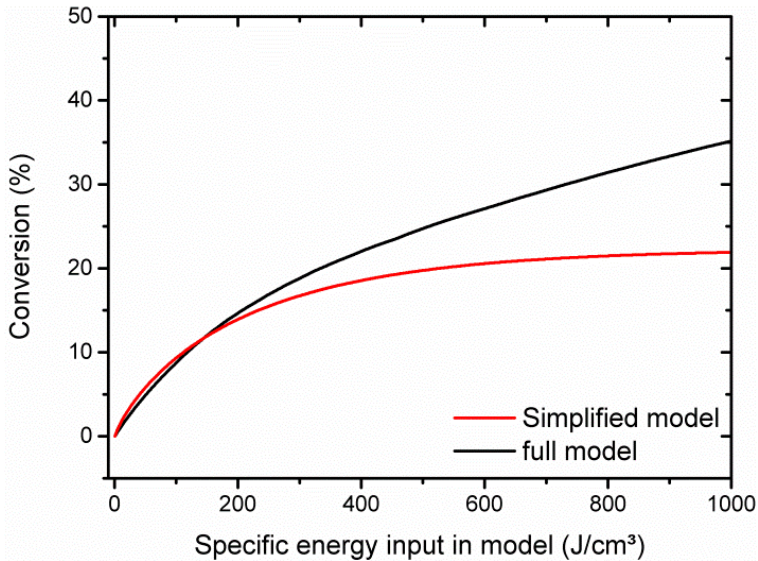


Figure 7-9: Comparison of the conversion, calculated with the simplified model and the full model from Chapter 0, as a function of SEI in the model.

A good agreement is reached in the lower range of the SEI, yielding a limited conversion of CO₂ (i.e., up to 15%), for the reasons discussed below. When the conversion rises above 15%, the chemistry becomes more complex due to the higher concentrations of CO and O₂. To obtain a good correlation in the higher SEI range, too many reactions have to be included again, so that there is no significant speed-up, compared with the full model. Therefore, for higher conversions, the use of the full chemistry set is recommended.

Only 9 different species are included in this reduced model, i.e., CO₂, CO, O, O₂ and O₃ as neutral species, and CO₂⁺, O₂⁻, O⁻ and

the electrons as charged species. Indeed, the vibrationally or electronically excited levels of the molecules are not included as separate species. Although vibrationally excited CO₂ molecules play a critical role in the CO₂ splitting in microwave or gliding arc plasmas^[11,25], their contribution in DBD plasmas is of minor importance^[11,17,25]. On the other hand, these excited species play a role in the consumption of the electron energy. To compensate for this, some dummy reactions with no change in chemical species, which account for the energy loss in the electron energy equation, were included.

The only electron impact ionization process included in the reduced model is the ionization of CO₂ to CO₂⁺ (reaction 1 in **Table 7-1**), as this reaction was found to be much more important than dissociative ionization of CO₂^[17]. Moreover, the ionization processes of CO and O₂ are also less important, as long as the conversion is not too high. This will of course limit the validity of the reduced model to low conversions (i.e., up to 15%; see **Figure 7-9** above), but including these ionization processes will increase the number of species and reactions. Hence, this shows the trade-off between complexity (or calculation time) and validity of the model. Furthermore, charge transfer processes between ions are not considered either, as the role of ions to the actual splitting of CO₂ is almost negligible^[17]. The only reactions of the CO₂⁺ ions included are recombination with electrons and with O₂⁻ ions (reactions 11, 12 in **Table 7-1**).

Table 7-1: Reactions included in the reduced chemistry model, as well as the corresponding rate coefficients and the references where these data are adopted from. The rate coefficients are in units of cm³ s⁻¹ for the two-body reactions, and in cm⁶ s⁻¹ for the three-body reactions.

	Reaction	Rate coefficient	Ref.
1	$e^- + CO_2 \rightarrow CO_2^+ + 2 e^-$	5.4×10^{-11}	a [17]
2	$e^- + CO_2 \rightarrow CO + O + e^-$	5.8×10^{-11}	a [17]
3	$e^- + CO_2 \rightarrow CO + O^-$	7.0×10^{-12}	a [17]
4	$e^- + O_3 \rightarrow O + O_2 + e^-$	2.0×10^{-9}	a [17]
5	$e^- + O_2 \rightarrow O + O + e^-$	2.0×10^{-9}	a [17]
6	$e^- + O_2 \rightarrow O + O^-$	4.0×10^{-11}	a [17]
7	$e^- + O_2 + M \rightarrow O_2^- + M$	3.0×10^{-30}	a [17]
8	$O^- + CO \rightarrow CO_2 + e^-$	5.5×10^{-10}	[26]
9	$O^- + O_2 \rightarrow O_3 + e^-$	1.0×10^{-12}	[27]
10	$O^- + O_3 \rightarrow O_2 + O_2 + e^-$	3.0×10^{-10}	[28]
11	$e^- + CO_2^+ \rightarrow CO + O$	6.5×10^{-7}	[29]
12	$O_2^- + CO_2^+ \rightarrow CO + O_2 + O$	6.0×10^{-7}	[30]
13	$O + O + M \rightarrow O_2 + M$	$5.2 \times 10^{-35} \exp(900/T[K])$	[31]
14	$O + O_2 + M \rightarrow O_3 + M$	$4.5 \times 10^{-34} (T[K]/298)^{-2.70}$	[32]
15	$O + O_3 \rightarrow O_2 + O_2$	$8.0 \times 10^{-12} \exp(-17.13/T[K])$	[32]
16	$O + CO + M \rightarrow CO_2 + M$	$1.7 \times 10^{-33} \exp(-1510 [K]/T)$	[33]
17	$O_3 + M \rightarrow O_2 + O + M$	$4.1 \times 10^{-10} \exp(-11430/T[K])$	[26]

^aRate coefficient calculated by an online Boltzmann solver in the model, at initialization conditions of pure CO₂.

Three electron impact dissociation reactions are incorporated, i.e., for CO₂, O₃ and O₂ (reactions 2, 4, 5 in **Table 7-1**). The dissociation of CO can be neglected because it requires 1069.2 kJ/mol, while the dissociation of CO₂ requires 529.8 kJ/mol^[5]; due to this energy difference the total rate of CO dissociation, as calculated by the full model, is much lower than the rate of CO₂ dissociation, especially for lower conversions (below 15%). Furthermore, three electron attachment processes are considered, i.e., dissociative attachment to CO₂ and O₂, as well as (three-body) attachment to O₂, producing O⁻ or O₂⁻ ions, respectively (reactions 3, 6, 7 in **Table 7-1**). As only a limited number of reactions are included for these negative ions in the

simplified model, this is another reason why the model should not be used for conversions above 15%. On the other hand, the electron attachment reactions with O₂ are essential, even in this reduced chemistry set, as they are faster than the one with CO₂ and they will induce a drop in electron density, resulting in a flattening in the CO₂ conversion upon rising SEI, which is also observed experimentally (see above), because less electrons will be available for direct splitting of CO₂. Furthermore, three electron detachment reactions are included, i.e., by O⁻ upon collision with CO, O₂ and O₃ (reactions 8-10). The O₂⁻ ions, on the other hand, are neutralized by recombination with CO₂⁺ ions (reaction 12; see above).

Finally, some chemical reactions between the neutral species are incorporated (reactions 13-17). The O atoms recombine almost completely to O₂ by reaction 13, although some O atoms give rise to the production of O₃ as well, predominantly by reaction 14. Moreover, some O atoms can recombine with CO to produce CO₂ (reaction 16), especially at high conversions and a long residence time. Indeed, this reaction will become important if the density of O atoms is high enough. In addition, a rise in the supplied energy will also increase the rate of this reaction, e.g., when a large fraction of O atoms is in excited levels or at higher gas temperature^[11]. That is the reason why in thermal (or warm) plasmas used for CO₂ splitting, the gas needs to be quenched (cooled) rapidly to prevent the backward reaction (i.e., recombination of CO and O, to form CO₂ again) to occur^[11]. At the conditions under study, the gas is near room temperature, and therefore, this reaction will be less important, at least for not too long residence times (see below). Hence, once the CO molecules are formed, they will be rather stable in the plasma. On the other hand, a certain balance in our model between O₃ and O₂ is observed, determined by reactions 13-15, 17. It should be mentioned, however, that especially the rate constants for the three-body reactions adopted from literature show a variation

between different publications and thus the exact O₃/O₂ ratio obtained by the model is subject to uncertainties. Experimental measurements of the O₃ density would give vital information to understand the balance between O₂ and O₃ in the splitting of CO₂. However, O₃ could not be detected with the current GC setup.

The reactions included in the reduced model, as well as the corresponding rate coefficients and the references where these data are adopted from are listed in **Table 7-1**, and a schematic diagram of the reaction scheme is presented in **Figure 7-10**.

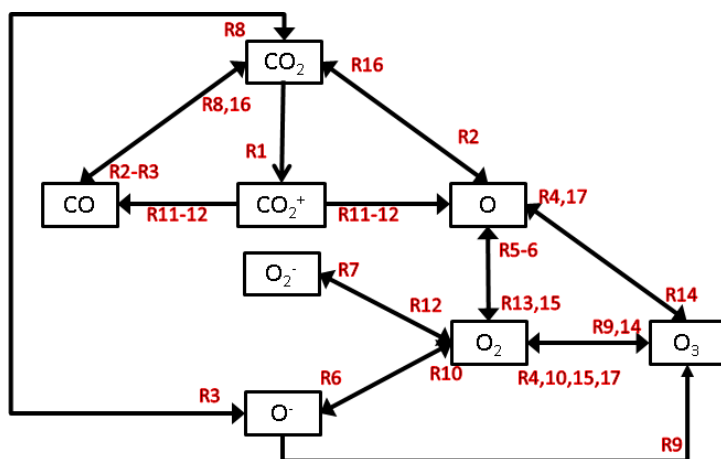


Figure 7-10: Reaction scheme, illustrating the chemistry of CO₂ splitting and further reactions, as predicted by the reduced model.

It is clear from **Figure 7-10** that the actual splitting of CO₂ is quite straightforward. The most important reactions for CO₂ splitting are electron impact dissociation (to form CO and O atoms (R2)), electron impact ionization (to form CO₂⁺ ions (R1), which will further dissociatively recombine with electrons or O₂⁻ ions into CO and O and/or O₂ (R11, R12)), and electron dissociative attachment (to form CO and O⁻ ions (R3)). These three mechanisms contribute typically for 50%, 38% and 12% to the CO₂ splitting. As mentioned above, the CO molecules are relatively stable and will only react further at longer residence

times or higher O densities; they can recombine with O⁻ ions (electron detachment of O⁻ (R8)) or O atoms (R16) to form again CO₂. At a residence time of 1 s, both processes are more or less equally important, but their total rate is a factor 5 lower than the total rate of CO production from CO₂. However, for a residence time of 40s the total rate is only a factor 1.2 lower, indicating that the backward process then becomes indeed important. Furthermore, the recombination with O atoms then contributes for 80% while the recombination with O⁻ ions only contributes for 20%. Hence, two major phenomena which cause the flattening of the conversion at long residence times or high values of the SEI can be distinguished. The first one is the drop in the electron density due to electron attachment with oxygen. The second one is the increasing contribution of the backward reaction, i.e. the recombination of O atoms with CO to form again CO₂.

At shorter residence times, however, the O atoms will almost immediately recombine into O₂ or O₃, as mentioned above (R13, R14), and there are several other reactions between O, O₂ and O₃ as well (sometimes also involving the negative ions; i.e., R4-R7, R9, R10, R15, R17). Therefore, most freedom to influence the splitting process can be found in the balance of O/O₂/O₃. Moreover, introducing H-containing gases, like H₂ or CH₄, can further control the production of O₂ by consumption of O atoms^[34].

To conclude, the selectivity towards CO will always be close to 50%, whereas the selectivity towards O₂ was predicted in the model to be between 45 and 50%, depending on the O₃ production (and keeping in mind the uncertainties in the three-body rate coefficients, as mentioned above). The question is whether O₂ or O₃ would be the most valuable product. Based on the chemical reactivity, O₃ is more favorable, but due to its high reactivity, the storage of O₃ is not straightforward and therefore

an on-site production would be beneficial when O₃ is intended to be produced for bleaching or oxidizing purposes^[35].

Finally, the calculated number densities of the molecules included in the model are plotted as a function of residence time in **Figure 7-11(A)**, for a SEI of 129 J/cm³. It is clear that the CO₂ density gradually drops, while being converted into CO and O₂, and some fraction of O₃. The densities of the other species included in the model (i.e., the O atoms and the various ions) are negligible at these long time-scales; however, their densities are plotted, together with the molecule densities, as a function of time during 5 consecutive microdischarge pulses (mimicking the filaments in the DBD reactor) in **Figure 7-11(B)**, for the same SEI value.

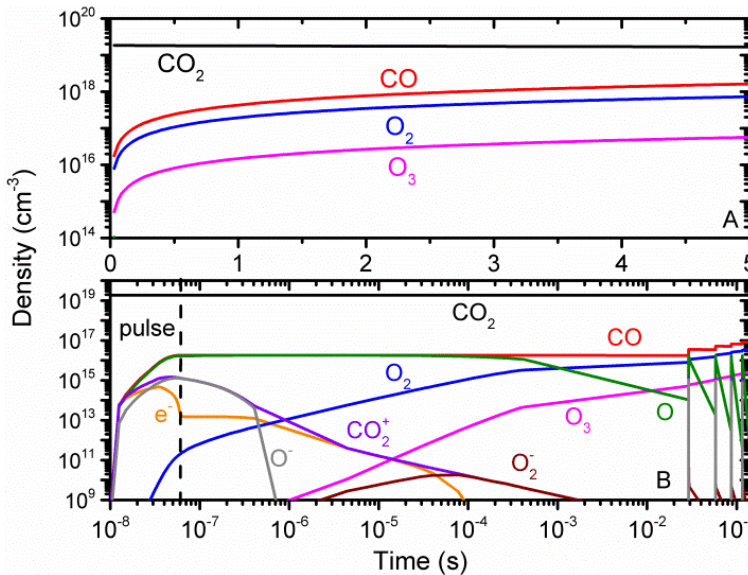


Figure 7-11: Calculated molecule densities as a function of residence time (A), and densities of all plasma species included in the simplified model, as a function of time during 5 consecutive microdischarge filaments (B), for a SEI of 129 J/cm³.

Note that a logarithmic x-axis is used, to clearly illustrate the temporal behavior of the ions during and after one pulse. It is

clear that the densities of CO, O₂ and O₃ increase (more or less) stepwise at each pulse, while the CO₂ density slightly drops. The densities of the O atoms, the various ions and the electrons rise during each pulse, but they decay again before the next pulse is reached. The decay time is the longest for the O atoms, whereas the electrons and the various negative ions become completely negligible, long before the next pulse starts.

7.3.3 Theoretical energy cost versus actual energy cost

In the performed experiments, the conversion was at maximum around 35%, but this was reached at a high SEI above 200 J/cm³, and therefore it corresponds to a low energy efficiency of only 2%. A maximum energy efficiency of 8% could be obtained at low SEI (~ 25 J/cm³), but at the expense of the conversion, which was only a few % in this case. An important remark is that the energy efficiency reported in this work, as well as in literature (see section 7.3.4 below), is calculated with respect to the plasma power. Therefore, one should refer to it as the “energy efficiency of the plasma” or the “theoretical energy efficiency”. Indeed, the plasma power is typically around 50% lower than the applied electrical power in a DBD reactor, due to losses in the high voltage power source and the cables (reflection, heating, zero load power requirements,...). As a consequence, the actual energy efficiency of the process will still be lower, or vice versa, the actual energy cost will be higher.

Figure 7-12 shows a comparison of the energy cost and the energy efficiency, as calculated from the electrical power and the plasma power, as a function of the SEI. It is clear that the actual energy cost, calculated from the electrical power, is at least 50% higher (see black dashed line) and therefore, the actual energy efficiency (red dashed line) is also at least 50% lower, compared

to the theoretical energy cost and energy efficiency (black and red solid lines).

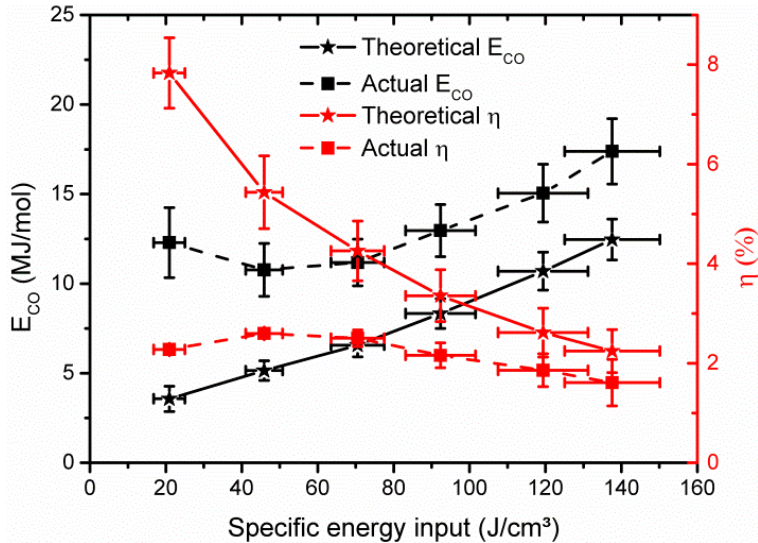


Figure 7-12: Energy cost (black curves; left axis) and energy efficiency (red curves; right axis), as calculated from the electrical power (“actual”; dashed lines) and from the plasma power (“theoretical”; solid lines), as a function of the SEI, using alumina dielectrics and a constant flow rate of 50ml/min.

At higher values of the SEI, the difference between actual and theoretical energy cost and energy efficiency is somewhat lower than at low SEI values. This can be explained by the zero load power of the power source, which is $\pm 40\text{W}$ in our experiments, independent of the applied power. Hence, the power loss at higher applied power is thus relatively smaller than at lower applied power.

In the present chapter, the work is focused on the energy efficiency of the plasma process itself, like is typically done in plasma studies in literature. Nevertheless, the total electrical power consumption must be kept in mind, especially when

different plasma sources are compared, and certainly also when benchmarking with other CO₂ conversion technologies.

7.3.4 Feasibility of CO₂ splitting by DBDs, and benchmarking with other techniques

The purpose of this study is to identify the possibilities and drawbacks of CO₂ splitting by DBDs, by investigating the effect of various operating conditions. It is found that a proper tuning of power versus gas flow rate can increase the conversion and energy efficiency at a certain SEI, but this is only observed for high values of SEI (above 100 J/cm³), which yields a low energy efficiency anyway. Reducing the discharge gap can enhance the filament formation, and therefore the conversion and energy efficiency, but this enhancement was only observed for larger gaps. Changing the dielectrics from quartz to alumina did not show any effects on the conversion and energy efficiency, although more sophisticated dielectric materials did show drastic changes, as reported in literature^[6-10] (see below).

To benchmark the obtained results of this work, a comparison is made in **Table 7-2** with some studies published for CO₂ splitting by several types of plasmas, as well as with classical thermal splitting. Note that it is only possible to compare with other studies for pure CO₂ splitting, as other gas mixtures (e.g., with inert gases) affect the conversion and energy efficiency^[4-9,36,37], and we don't want to draw the wrong conclusions. The table focuses on the maximum conversion, the energy efficiency (if this could be calculated from the literature data) and the gas flow rate. The latter is also relevant because it gives an idea about the scalability and industrial applicability of the process. Indeed, a high conversion at a very low flow rate and long residence time is not of interest for industrial applications.

Table 7-2: Benchmark of our results, in terms of maximum conversion, energy efficiency and the corresponding gas flow rates in both cases, with data from literature for other plasma types and classical thermal splitting, all carried out at atmospheric pressure.

	Max. conversion (%)	Flow rate (l/min)	Max. energy efficiency (%)	Flow rate (l/min)
Our work	35	0.01	8	0.5
DBD^[1]	30	0.05	-	-
DBD^[2]	12.5	0.04	3.5	0.04
Microwave plasma^[38]	45	1	20	16
Gliding arc plasma^[21]	9	14	43	27
Gliding arc plasma^[43]	18	0.8	-	-
Thermal splitting^[39]	22	0.02	(1400°C-1800°C)	-

Detailed, systematic studies for CO₂ splitting in a pure CO₂ mixture, presenting values for both conversion and energy efficiency in a DBD, appear to be very scarce in literature. The most detailed study up to now was presented by Paulussen et al.^[1] and Yu et al.^[2]. Paulussen et al.^[1] found a maximum conversion of 30% at a flow rate of 0.05 l/min, a power density of 15 W/cm³ and a frequency of 60 kHz. However, they did not report the plasma power or the energy efficiency. Yu et al.^[2] reported a maximum conversion of 12.5% at a constant flow rate of 40 ml/min, hence somewhat lower than our results. Their maximum energy efficiency was around 3.5%, which is also somewhat lower than in our case. However, it should be pointed out that the reactor used in their work had a very large gap (4 mm) to study the effect of a packing material. Therefore, these results should be compared with our results for a gap of 3.3 mm (see **Figure 7-3** above), showing a maximum conversion of 25% and a maximum energy efficiency of 6%.

A microwave discharge seems very promising for CO₂ splitting^[11,25,38,40-42]. In the 1970s, Fridman and coworkers reported energy efficiencies up to 80-90%, when operating in the

supersonic flow regime, with a flow rate in the order of 5-50 ml/min and a static pressure between 0.02 and 0.05 atm^[11]. The highest energy efficiency reported recently, for similar conditions, was around 60%^[42]. Note, however, that these results were obtained at reduced pressure (0.2 bar), which is not so practical for high-throughput processing of exhaust gases, and it will increase the total energy cost, as higher pressures are required for gas storage. Furthermore, it was also reported^[21,38,40] that increasing the pressure can lead to a significant drop in the energy efficiency. Therefore, in this benchmarking, microwave results obtained at atmospheric pressure are compared, which allows a more fair comparison for industrial purposes. At a pressure of 1 atm, Spencer et al.^[38] reported a conversion of 45% at a flow rate of 1 l/min, and an energy efficiency of 20% at a flow rate of 16 l/min, for a microwave discharge, which is still much better than obtained for a DBD.

Another very promising discharge type for CO₂ splitting is a gliding arc plasma, where high flow rates are possible at atmospheric conditions, together with high energy efficiency and reasonable conversion^[21,43]. Nunally et al.^[21] reported conversions of 2-9% for a SEI variation from 0.1 to 1.0 eV/molecule and flow rate input variation in the range of 14-40 l/min. Furthermore, a maximum energy efficiency of 43 % was reached at a flow rate of 27 l/min. Indarto et al.^[43] obtained conversions of 15-18% at a flow rate of 0.8 to 2.4 l/min, but they did not report the energy efficiency as defined by Fridman^[11]. However, they compared the power efficiency with a DBD and found that the power efficiency increased with a factor of 3 compared to the DBD described in Wang et al.^[4]

The plasma-based CO₂ splitting can also be compared with classical thermal splitting in membrane reactors. In this case, high temperatures of 1400-1800 °C need to be used.^[44] This illustrates the advantages of plasma technology, because it can

circumvent the difficult thermodynamics of this reaction. Indeed, a high temperature is not needed, because the electrons are heated by the electric power, and they induce the chemical reactions, while the gas itself can remain at or near room temperature. On the other hand, processing at high temperature can also have benefits, when coupling the thermal process with a secondary process. For instance, Jin et al.^[45] proposed the coupling of CO₂ splitting and partial oxidation of methane in a membrane reactor, in such a way that the O₂ produced in the splitting diffuses to the second reactor for the partial oxidation process. This method allows the transfer of thermal energy to the membrane and to the partial oxidation process. Although this process still suffers from problems like instability of the membrane, sealing and pressure drop, it shows promising results. If the stability of such membranes can be improved, new possibilities can be found, e.g., in the coupling of a plasma reactor with a partial oxidation reactor, especially for gliding arc and microwave discharges, as they operate at a higher temperature.

Finally, we also looked at photo- and electro-catalytic processes, but it was impossible to compare them with plasma technology, in terms of conversion and energy efficiency. We believe that also here a combination of different processes, like the thermochemical cycle based on Zn/ZnO^[46,47] or the photochemical reduction of CO₂^[48] might give rise to the most valuable process.

Hence, it can be concluded that a DBD reactor can split CO₂ at relatively high conversion, when using a low flow rate, but the energy efficiency is still too low for commercial applications. Indeed, when the electric energy for the CO₂ splitting would originate from fossil fuels, an energy efficiency of 52% would be needed to make sure that not more electric energy is consumed for this process than the electricity produced from the fossil fuel combustion, or in other words, that not more CO₂ is produced in

the electricity production than can be split by the plasma process^[49].

It should be noted, however, that all the DBD data reported in **Table 7-2**, are for simple DBD reactors with a pure CO₂ gas flow, like applied in our study. However, there is still considerable room for improvement for the DBD technology, as already demonstrated in literature^[2-4,6-10]. Indeed, **Figure 7-13** presents an overview of different modifications applied to DBD reactors, reported in literature, showing both the absolute values of the conversion and energy efficiency reached, as well as the relative changes compared to their standard setup without the modification or with a less efficient modification. Because it is difficult to compare the absolute values of conversion and energy efficiency adopted from literature (due to the different operating conditions and geometries, which are not always thoroughly described), one should mainly focus on the relative changes as a result of these reactor modifications. Note that the relative changes for conversion and energy efficiency were calculated for the conditions of the highest conversion and maximum energy efficiency, respectively.

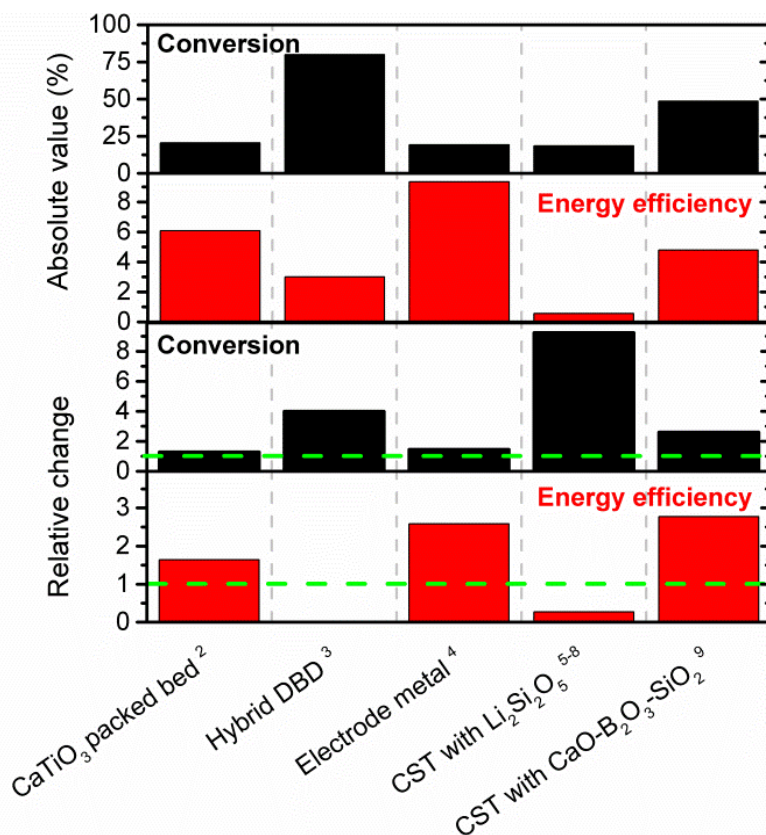


Figure 7-13: Modifications to a simple DBD reactor, as reported in literature, yielding a higher CO₂ conversion and energy efficiency. Both the reported maximum values of conversion and energy efficiency are plotted, as well as the relative changes compared to the same setup without the modification. See text for more explanation. The dashed green line indicates no change compared to the standard setup.

A packed bed DBD configuration with spherical pellets was proposed by Yu et al.^[2]. The authors used silica gel, quartz, γ -Al₂O₃, α -Al₂O₃ and CaTiO₃ as packing material and found that the maximum conversion (i.e., 20.5%) was reached for CaTiO₃, which was a factor 1.3 higher than for a non-packed DBD. Furthermore, the highest energy efficiency of 6% was obtained for CaTiO₃, which was reported at least a factor 1.6 higher than for the non-packed DBD at the same conditions. This packing effect was

attributed to the enhancement of the electron energy, thus facilitating the electron impact dissociation of CO₂. Also the morphology and the acid–base properties of the packing material were found to affect the conversion. Furthermore, the presence of heterogeneous reactions on the packing surface was also identified and could facilitate the conversion. It is worth to mention that introducing a dielectric packing in a DBD reactor was also demonstrated to enhance the energy efficiency for VOC remediation^[50–53], so we indeed believe that a packed bed DBD reactor has great potential for CO₂ splitting as well.

Tagawa et al.^[3] proposed a hybrid reactor, i.e., a DBD plasma on the surface of a solid oxide electrolyser cell (SOEC), which allows the in-situ exclusion of O₂ during the CO₂ splitting. A maximum energy efficiency of 3% was reported, but we were not able to deduce the relative change of this parameter in their work. Moreover, an increase with a factor 4 was observed for the conversion, up to a maximum value of 80% compared to the DBD discharge only. Indeed, a high O₂ concentration has a suppressing effect on the CO₂ conversion due to its high electronegativity, thereby trapping the electrons, so that they are not available for electron impact dissociation anymore. Moreover, the oxygen will also be partially present as O atoms, which can react with CO to produce CO₂ (see section 7.3.2 above). Therefore, it is logical that the in-situ exclusion of O₂ has a beneficial effect on the CO₂ conversion.

Wang et al.^[4] investigated the effect of different metals used as high voltage electrode in a DBD reactor for a mixture of 4% CO₂ in helium. The advantage of using different metals as central electrode is that the conductivity of the electrode changes. They obtained a relative order of Cu≈Au>Rh>Fe≈Pd≈Pt for the reactivity toward CO₂ decomposition, which is the same order as for the electrical conductivity. A maximum conversion of 19.4% was reported for a Cu electrode, while the conversions for Au, Rh,

Pt, Fe and Pd were 19.2%, 15.3% 14.2%, 13.2% and 12.9%, respectively. Note again that one should not focus too much on these absolute values, as they were obtained for other conditions (e.g., in a mixture with helium). However, the relative changes are very interesting. Indeed, the Cu and Au electrodes yielded a relative increase in the conversion of a factor 1.5, compared to a Fe (stainless steel) or Pd electrode. Furthermore, a maximum energy efficiency of 9.3% was reported for the Au electrode, which was almost three times higher than the energy efficiency for the Rh electrode at the same conditions. Furthermore, it should be pointed out that the plasma power varies between the electrodes and therefore the energy efficiency is the highest for Au and not for Cu. The maximum energy efficiencies for the Cu, Fe, Pd, Pt and Rh electrodes were 8.5%, 6.7%, 5.9% and 5.6% and 3.6%, respectively.

Li et al.^[6-9] investigated the influence of Ca_{0.8}Sr_{0.2}TiO₃ (CST) with 0.5 wt% Li₂Si₂O₅ as dielectric barrier, in a mixture of 10% CO₂ in N₂. They found an improvement of the conversion by a factor 9 up to 18.5% at the same electrical power, compared to silica glass as dielectric barrier. However, if the plasma power is taken into account to calculate the theoretical energy efficiency, a drop of the energy efficiency by a factor 0.3 was found, compared to silica glass. The authors concluded that for the same electrical power a much higher plasma power was deposited in the plasma by changing the dielectric barrier, so the actual energy efficiency is in this case closer to the theoretical energy efficiency, which was, however, only 0.6% at its maximum.

In a similar work performed by Wang et al.^[10] the performance of a CST ceramic dielectric barrier with glass addition on the conversion of CO₂ was investigated. The authors produced CST ceramic barriers with addition of CaO–B₂O₃–SiO₂ (CBS) glass in the range between 0.5 and 5.0 wt%, to enhance the dielectric properties and the microstructures of the ceramics. The

experiments were performed in a mixture of 10% CO₂ in N₂. The addition of 5.0 wt% CBS resulted in a rise of the conversion with a factor 2.6 up to 49%, compared to 0.5 wt% CBS. Furthermore, the energy efficiency almost tripled at 5.0 wt% CBS compared to 0.5 wt% CBS, resulting in a maximum of 5%. The authors claimed that a higher amount of CBS leads to a drop in the total surface resistance and a rise in the capacitance of the grain boundaries, which results in a higher CO₂ conversion and a higher energy efficiency. In addition, they also found that the grain boundaries on the dielectric barrier surface serve as charge trapping sites, so that a more homogenous discharge is created.

In summary, although the absolute energy efficiencies reported in these papers are modest, the relative increase in the energy efficiencies due to these modifications, compared to a standard setup or other modifications, is quite promising. Therefore, a combination of the proposed modifications with the proper tuning of the operating parameters might lead to even higher energy efficiencies and possibly could make a DBD reactor competitive with the other plasma systems listed in **Table 7-2**.

On the other hand, it is important to realize that more and more electric energy is nowadays originating from sustainable energy sources, and this trend will definitely continue in the coming years. In that case, the energy efficiency requirements of the plasma conversion will be somewhat less strict. Moreover, sustainable energy sources often suffer from peak currents (e.g., on sunny or windy days), when the electricity is in principle “for free”. A DBD plasma can then be very useful for peak shaving, as it is very flexible and can be very easily switched on and off, so that it will be extremely suitable for temporal energy storage.

In general, in terms of practical use, a DBD has some benefits compared to the other plasma types (microwave and gliding arc),

because its construction is very simple, robust and allows an easy scale-up, as was already demonstrated 150 years ago for the commercial application of O₃ production^[11,35]. Moreover, it is reported in literature that by combining a DBD with a catalyst, in so-called plasma catalysis^[54–56], the selectivity of the process can be steered towards the desired products. This is not really an issue for pure CO₂ splitting, but it is very promising when adding a co-reagent (e.g., methane or water), to produce value-added compounds, such as syngas, methanol, formaldehyde and formic acid^[18,54,57].

7.4 Conclusions

The effect of various operating conditions on the conversion and energy efficiency of CO₂ splitting in a DBD plasma reactor were investigated in detail. The applied frequency and the kind of dielectric (quartz or alumina) seem to have no effect on the conversion and energy efficiency. The discharge gap can have a significant effect when it gives rise to a different streamer behavior. This was indeed observed for the gap of 3.3 mm, compared to the gaps of 1.8 and 2.3 mm, as visualized by the Lissajous plots and the current waveforms. Indeed, the 3.3 mm gap results in less streamer formation, so that the effective plasma (streamer) volume, which can contribute to the CO₂ conversion, is much smaller than the actual reactor plasma volume, resulting in a significantly lower CO₂ conversion and energy efficiency, for the same SEI.

The SEI obviously is most dominant in determining the conversion and energy efficiency. The conversion clearly increases, while the energy efficiency decreases, with rising SEI, which is logical. The SEI itself is determined by both the plasma power and the gas flow rate. It is observed that the gas flow rate, and hence the residence time, has the most important effect on the conversion

and energy efficiency. The power also has some effect, but it is less significant. Indeed, a higher power with higher gas flow rate gives rise to more intense streamers, but the residence time is lower, and the latter seems more important as it determines the time that the CO₂ molecules stay within the streamers and can be subject to conversion. Therefore, a lower power with lower gas flow rate results in a higher conversion and energy efficiency than a higher power with higher gas flow rate, at the same fixed SEI. This can be of interest, because it means that a proper tuning of power versus gas flow rate can increase the conversion and energy efficiency at a certain SEI. However, this behavior was observed only for high values of SEI (above 100 J/cm³), which unfortunately yield a low energy efficiency. The effect of the various parameters on the conversion and energy efficiency is summarized in **Table 7-3**.

Table 7-3: Summary of the experimental parameter screening, illustrating their effect on the CO₂ conversion and energy efficiency.

Parameter	Effect on conversion	Effect on energy efficiency
Lower gas flow rate/higher residence time	↑↑	↓↓
Higher power	↑	↓
Larger gap (when streamer formation ↓)	↓	↓
Higher frequency	-	-
Dielectric (alumina/quartz)	-	-

The highest CO₂ conversion was found to be around 35%, and was obtained at a high SEI (above 200 J/cm³), and thus it corresponds to a low energy efficiency of only 2%. On the other hand, the highest energy efficiency, i.e., 8%, was obtained at low SEI (~ 25 J/cm³), but at the expense of the conversion, which was only a few % in this case. The selectivities of the formed products (i.e., CO and O₂) were also measured, but they were always found to be around 50%, for all conditions investigated.

Besides the experimental results, also modeling results were presented for the CO₂ splitting, and reasonable agreement was obtained between the calculated and measured conversions and energy efficiencies as a function of SEI, when the power density (and hence the SEI) in the model was multiplied with a factor 7, to account for the smaller volume occupied by the streamers, compared to the total plasma reactor volume.

As the model shows good correlation with the experimental trends, it can be used to elucidate the most important chemical reactions for the CO₂ splitting. For this purpose, the chemistry set of our complete model has been reduced to a simpler model with only 9 species and 17 reactions, to better identify the critical reactions. It was found that the CO₂ splitting is mainly dictated by electron impact dissociation (to form CO and O atoms), electron impact ionization (to form CO₂⁺ ions, which will subsequently recombine with electrons or O₂⁻ ions into CO and O or O₂), and electron dissociative attachment (to form CO and O⁻ ions). The CO molecules can recombine with O⁻ ions or O atoms to form again CO₂, but these reactions are only important at high oxygen densities or high conversions (i.e. long residence time). The O atoms can, however, easily recombine into O₂ by a three-body reaction, although a fraction also recombines into O₃. Furthermore, there are also several other reactions between O, O₂ and O₃. Therefore, most freedom to influence the splitting process can be found in the balance of O/O₂/O₃.

Finally, the experimental results for the CO₂ splitting in a DBD were compared with literature data for several types of plasma reactors, as well as with classical thermal CO₂ splitting, to benchmark the obtained results. It can be concluded that a DBD reactor can provide reasonable conversions, but the energy efficiency is still too low for commercial applications, at least when using electricity from fossil fuel combustion. However, in literature, several modifications to a standard DBD reactor have

been reported already. A summary of these reactor modifications from literature is presented, illustrating that they might indeed improve the energy efficiency, as well as the conversion.

Furthermore, when using electricity from sustainable energy sources, the energy efficiency might be somewhat less critical. In this respect, we believe that a DBD plasma can even become very useful in the future, for energy storage of peak currents, as it can be easily switched on and off.

Finally, a DBD reactor is also very promising when combined with catalysis. Indeed, when introducing a catalytic packing in a DBD reactor, the selectivity of the process (in case of a co-reagent like methane or water) can be tuned, which has also great promise for the selective production of value-added chemicals.

7.5 References

- [1] S. Paulussen, B. Verheyde, X. Tu, C. De Bie, T. Martens, D. Petrovic, A. Bogaerts, B. Sels, *Plasma Sources Sci. Technol.* **2010**, *19*, 034015.
- [2] Q. Yu, M. Kong, T. Liu, J. Fei, X. Zheng, *Plasma Chem. Plasma Process.* **2011**, *32*, 153–163.
- [3] Y. Tagawa, S. Mori, M. Suzuki, I. Yamanaka, T. Obara, J. Ryu, Y. Kato, *Kagaku Kogaku Ronbushu* **2011**, *37*, 114–119.
- [4] J. Wang, G. Xia, A. Huang, S. L. Suib, Y. Hayashi, H. Matsumoto, **1999**, *159*, 152–159.
- [5] G. Zheng, J. Jiang, Y. Wu, R. Zhang, H. Hou, *Plasma Chem. Plasma Process.* **2003**, *23*, 59–68.
- [6] R. Li, Q. Tang, S. Yin, T. Sato, *J. Phys. D. Appl. Phys.* **2007**, *40*, 5187–5191.
- [7] R. Li, Q. Tang, S. Yin, T. Sato, *Fuel Process. Technol.* **2006**, *87*, 617–622.
- [8] R. Li, Q. Tang, S. Yin, T. Sato, *Appl. Phys. Lett.* **2007**, *90*, 131502.
- [9] R. Li, *Solid State Ionics* **2004**, *172*, 235–238.
- [10] S. Wang, Y. Zhang, X. Liu, X. Wang, *Plasma Chem. Plasma Process.* **2012**, *32*, 979–989.
- [11] A. Fridman, *Plasma Chemistry*, Cambridge University Press, New York, **2008**.
- [12] D. R. Lide, W. M. M. Haynes, G. Baysinger, L. I. Berger, D. L. Roth, D. Zwillinger, M. Frenkel, R. N. Goldberg, *J. Am. Chem. Soc.* **2009**, *131*, 12862–12862.
- [13] R. Valdivia-Barrientos, J. Pacheco-Sotelo, M. Pacheco-Pacheco, J. S. Benítez-Read, R. López-Callejas, *Plasma Sources Sci. Technol.* **2006**, *15*, 237–245.
- [14] K. F. Young, H. P. R. Frederikse, *J. Phys. Chem. Ref. Data* **1973**, *2*, 313.
- [15] K. Francke, R. Rudolph, H. Miessner, *Plasma Chem. Plasma Process.* **2003**, *23*, 47–57.
- [16] X. Tu, H. J. Gallon, M. V Twigg, P. A. Gorry, J. C. Whitehead, *J. Phys. D. Appl. Phys.* **2011**, *44*, 274007.
- [17] R. Aerts, T. Martens, A. Bogaerts, *J. Phys. Chem. C* **2012**, *116*, 23257–23273.
- [18] D. Larkin, *Catal. Today* **2001**, *71*, 199–210.

- [19] A. A. Khassin, B. L. Pietruszka, M. Heintze, V. N. Parmon, *React. Kinet. Catal. Lett.* **2004**, *82*, 111–119.
- [20] Q. Wang, B.-H. Yan, Y. Jin, Y. Cheng, *Plasma Chem. Plasma Process.* **2009**, *29*, 217–228.
- [21] T. Nunnally, K. Gutsol, A. Rabinovich, A. Fridman, A. Gutsol, A. Kemoun, *J. Phys. D. Appl. Phys.* **2011**, *44*, 274009.
- [22] A. Gutsol, A. Rabinovich, A. Fridman, *J. Phys. D. Appl. Phys.* **2011**, *44*, 274001.
- [23] O. Motret, C. Hibert, S. Pellerin, J. M. Pouvesle, *J. Phys. D. Appl. Phys.* **2000**, *33*, 1493–1498.
- [24] O. Motret, S. Pellerin, M. Nikravech, *Plasma Chem. Plasma Process.* **1997**, *17*, 393–407.
- [25] T. Kozák, A. Bogaerts, *Plasma Sources Sci. Technol.* **2014**, *23*, 045004.
- [26] T. G. Beuthe, J.-S. Chang, *Jpn. J. Appl. Phys.* **1997**, *36*, 4997–5002.
- [27] A. Cenian, A. Chernukho, V. Borodin, *Contrib. to Plasma Phys.* **1995**, *35*, 273–296.
- [28] A. A. Ionin, I. V Kochetov, A. P. Napartovich, N. N. Yuryshev, *J. Phys. D. Appl. Phys.* **2007**, *40*, R25–R61.
- [29] H. Hokazono, H. Fujimoto, *J. Appl. Phys.* **1987**, *62*, 1585.
- [30] H. Hokazono, M. Obara, K. Midorikawa, H. Tashiro, *J. Appl. Phys.* **1991**, *69*, 6850.
- [31] S. Hadj-Ziane, B. Held, P. Pignolet, R. Peyrous, C. Coste, *J. Phys. D. Appl. Phys.* **1992**, *25*, 677–685.
- [32] A. Cenian, A. Chernukho, V. Borodin, G. Śliwiński, *Contrib. to Plasma Phys.* **1994**, *34*, 25–37.
- [33] W. Tsang, R. F. Hampson, *J. Phys. Chem. Ref. Data* **1986**, *15*, 1087–1279.
- [34] R. Aerts, R. Snoeckx, A. Bogaerts, *Plasma Process. Polym.* **2014**, n/a–n/a.
- [35] B. Eliasson, M. Hirth, U. Kogelschatz, *J. Phys. D. Appl. Phys.* **1987**, *20*, 1421–1437.
- [36] N. R. Pinhao, A. Janeco, J. B. Branco, *Plasma Chem. Plasma Process.* **2011**, *31*, 427–439.
- [37] M. Ramakers, I. Michielsen, R. Aerts, V. Meynen, A. Bogaerts, **n.d.**, unpublished work.
- [38] L. F. Spencer, A. D. Gallimore, *Plasma Sources Sci. Technol.* **2013**, *22*, 015019.
- [39] Y. Nigara, B. Cales, *Bull. Chem. Soc. Jpn.* **1986**, *59*, 1997–2002.

- [40] A. Vesel, M. Mozetic, A. Drenik, M. Balat-Pichelin, *Chem. Phys.* **2011**, *382*, 127–131.
- [41] A. Gutsol, A. Rabinovich, A. Fridman, *J. Phys. D. Appl. Phys.* **2011**, *44*, 274001.
- [42] A. P. H. Goede, W. A. Bongers, M. G. Graswinckel, R. M. C. van de Sanden, L. Martina, K. Jochen, A. Schulz, W. Mathias, *3rd Eur. Energy Conf. Budapest* **2013**.
- [43] A. Indarto, D. R. Yang, J.-W. Choi, H. Lee, H. K. Song, *J. Hazard. Mater.* **2007**, *146*, 309–15.
- [44] S. Rayne, *Nat. Preced.* **2008**, DOI: 10.1038/npre.2008.1741.1.
- [45] W. Jin, C. Zhang, P. Zhang, Y. Fan, N. Xu, **2006**, *52*, 0–5.
- [46] M. E. Gálvez, P. G. Loutzenhiser, I. Hischer, A. Steinfeld, *Energy & Fuels* **2008**, *22*, 3544–3550.
- [47] P. G. Loutzenhiser, M. E. Gálvez, I. Hischer, A. Stamatiou, A. Frei, A. Steinfeld, *Energy & Fuels* **2009**, *23*, 2832–2839.
- [48] R. D. Richardson, E. J. Holland, B. K. Carpenter, *Nat. Chem.* **2011**, *3*, 301–3.
- [49] L. F. Spencer, A. D. Gallimore, *Plasma Chem. Plasma Process.* **2010**, *31*, 79–89.
- [50] H. L. Chen, H. M. Lee, S. H. Chen, *Ind. Eng. Chem. Res.* **2008**, *47*, 2122–2130.
- [51] G. Horvath, N. J. Mason, L. Polachova, M. Zahoran, L. Moravsky, S. Matejcik, *Plasma Chem. Plasma Process.* **2010**, *30*, 565–577.
- [52] A. Ogata, K. Mizuno, S. Kushiyama, T. Yamamoto, **1998**, *18*, 363–373.
- [53] H.-X. Ding, A.-M. Zhu, X.-F. Yang, C.-H. Li, Y. Xu, *J. Phys. D. Appl. Phys.* **2005**, *38*, 4160–4167.
- [54] X. Tu, J. C. Whitehead, *Appl. Catal. B Environ.* **2012**, *125*, 439–448.
- [55] K. Francke, *Catal. Today* **2000**, *59*, 411–416.
- [56] H. Chen, H. Lee, S. Chen, Y. Chao, M. Chang, *Appl. Catal. B Environ.* **2008**, *85*, 1–9.
- [57] T. Nozaki, K. Okazaki, *J. Japan Pet. Inst.* **2011**, *54*, 146–158.

Chapter 8:

In-situ chemical trapping of oxygen in CO₂ splitting

In this chapter, we present the in-situ chemical trapping of oxygen, produced in CO₂ splitting, by means of modeling and experimental validation. Indeed, a crucial step in the plasma splitting of CO₂ is the separation of the conversion products, and this is not straightforward, especially for separating O₂ from CO₂ and CO. In this chapter the trapping of O atoms by adding a hydrogen source, which enhances the chemical conversion into water, is demonstrated. The experimental and modelling results show that by adding 3% of H₂ and 2% of CH₄ most of the oxygen can be trapped at a CO₂ conversion of $\pm 2.5\%$. The identified products formed by the addition of CH₄ or H₂ are mainly H₂O and in the case of CH₄ also H₂. Adding a hydrogen source (H₂ or CH₄) thus leads to the removal of O₂, leaving behind a gas mixture that can be more easily separated.

Aerts, R., Snoeckx, R., & Bogaerts, A. (2014). In-Situ Chemical Trapping of Oxygen in the Splitting of Carbon Dioxide by Plasma. *Plasma Processes and Polymers*, in press doi:10.1002/ppap.201400091

8.1 Introduction

In previous chapters (**Chapter 6 and Chapter 7**), we have shown that CO₂ can be split in O₂ and CO with reasonable conversions and energy efficiencies. However, besides the conversion of the CO₂ inside the plasma, another critical issue is the separation of the CO₂/O₂/CO gas mixture after the splitting, which is not straightforward, especially for the separation of the CO-O₂ mixture^[1]. Commonly used techniques such as centrifugation, distillation and absorption are difficult and most certainly not energy efficient, due to the small difference in molar mass of CO and O₂. Electrolytic membranes, which have a conductivity towards oxygen, have been proposed in literature, but they require high temperatures, again lowering the overall energy efficiency if low temperature plasmas are used^[1]. A simpler, and probably more energy-efficient way of separation is the conversion of O₂ into other molecules, which can be more easily separated from CO.

In this chapter, the in-situ chemical trapping of O₂ by the conversion of CO₂ with admixtures of H₂ or CH₄ into H₂O, will be demonstrated, by computer simulations and experimental validation. This trapping of the oxygen by a chemical step is as far as we know never investigated or published, although the removal of H₂O from feedstock gases (i.e., drying) is already a widely investigated technology^[2]. As mentioned above, no energy efficient technology exists at this moment to separate the mixture of CO/CO₂ and O₂. However, after the chemical trapping, a more conventional separation of the gas mixture CO/CO₂ can be performed with existing membrane technology^[3,4]. Note that this addition of CH₄ is not the same as the already existing dry reforming of methane (DRM) since in DRM it is the purpose to generate syngas (a mixture of CO and H₂) which can then be further processed by Fischer-Tropsch synthesis. In this work, on

the other hand, we are looking for a way to deal with the problem of gas separation (i.e., CO, O₂, CO₂), inherent to plasma based CO₂ splitting, by trapping the atomic O into H₂O. For this reason we first investigated the effect of adding small amounts (1-5%) of H₂ to the mixture, and subsequently also CH₄, since the latter has advantages regarding cost, availability and safety over H₂. We realize that it would be even better to add green and sustainable hydrogen sources; nevertheless we first need to understand the mechanism by simple case study molecules, like H₂ and CH₄.

CO₂ splitting by plasmas is dominated by electron impact dissociation^[5]:



This reaction produces free O atoms which will recombine to O₂. This means that the key step for the chemical trapping of O₂ is to convert the O atoms into other chemicals with a higher rate than the three-body recombination to O₂ ($k = 1.05 \times 10^{-33} \text{ cm}^6/\text{s}$ at 300K; with any gas molecule as third body)^[5]. A feasible trapping route could be the production of OH radicals through the three-body recombination of O and H atoms, which is indeed clearly faster at equal concentrations of O and H atoms (i.e., $k = 4.33 \times 10^{-32} \text{ cm}^6/\text{s}$ at 300K)^[6].

We investigate this O₂ trapping in the same DBD plasma as in **Chapter 7** (see detailed description in **Chapter 3**), by means of a kinetic model, supported with experiments.

8.2 Description of the model and the chemistry

8.2.1 Description of the chemical model

Also here, the physical model described in chapter 3 developed by Kushner and co-workers was used. The chemistry contains 62 plasma species and 520 reactions, as listed in Snoeckx et. al.^[7]. The model is applied to a DBD plasma, consisting of a large number of microdischarge filaments. The latter are accounted for in the model by assuming the power deposition to occur in consecutive triangular pulses of 60 ns with a maximum power density of 5.0×10^5 W/cm³. The pulse repetition frequency is 667 s⁻¹. A gas residence time of 0.74 s, i.e. was simulated, the same as in the experiment (see next section), so this corresponds to 491 consecutive pulses. The total energy deposition is 4.2 kJ/l, like in the experiment (see next section), and results in a CO₂ conversion of $\pm 2.4\%$ when H₂ or CH₄ is added, compared to 2.7% when pure CO₂ is converted. More details about this power deposition and the model in general can be found in **Chapter 3** and in refs^[5,8].

8.2.2 Description of the validation experiments

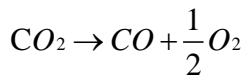
The plasma reactor is the concentric DBD, presented in **Chapter 3**, with an Al₂O₃ dielectric, a length of 9 cm and a discharge gap of 3 mm, resulting in a volume of 12.3 cm³. The total gas flow rate and electric power inserted in the plasma are kept constant at 1000 ml/min and 100 W, which corresponds to a residence time of 0.74 s and a total energy deposition of 4.2 kJ/l, i.e., exactly the same as assumed in the model. The gas composition after plasma treatment is measured with a three-channel compact GC (Interscience), equipped with two thermal conductivity

detectors (TCD) and a flame ionization detector (FID). More details about the experimental set-up can be found in **Chapter 3**.

8.3 Results and discussion

Two different H-sources are investigated in the modelling part of this work. First, H₂ is added to CO₂, with a fraction between 0.1% and 5%. The O₂ trapping is identified by calculating the O-based selectivity of the different products as a function of the H₂ fraction.

The formulas used in the following discussion are based on the total reaction of CO₂ splitting as described in literature^[9]:



$$\text{Conversion (\%)} = \frac{CO_{2 \text{ inlet}} - CO_{2 \text{ outlet}}}{CO_{2 \text{ inlet}}} \times 100\% \quad (\text{E8-1})$$

$$\text{O based CO selectivity (\%)} = \frac{CO_{\text{outlet}}}{2(CO_{2 \text{ inlet}} - CO_{2 \text{ outlet}})} \times 100\% \quad (\text{E8-2})$$

$$\text{O based O}_2 \text{ selectivity (\%)} = \frac{O_{2 \text{ outlet}}}{CO_{2 \text{ inlet}} - CO_{2 \text{ outlet}}} \times 100\% \quad (\text{E8-3})$$

8.3.1 Modelling the oxygen trapping upon addition of H₂ and CH₄

The model predicts that in pure CO₂ only CO and O₂ are formed, with O-based selectivities of 50%, as is clear from **Figure 8-1**, but as soon as H₂ is added, the selectivity of O₂ drops significantly, and all the O₂ is replaced by H₂O at a H₂ fraction of 3%.

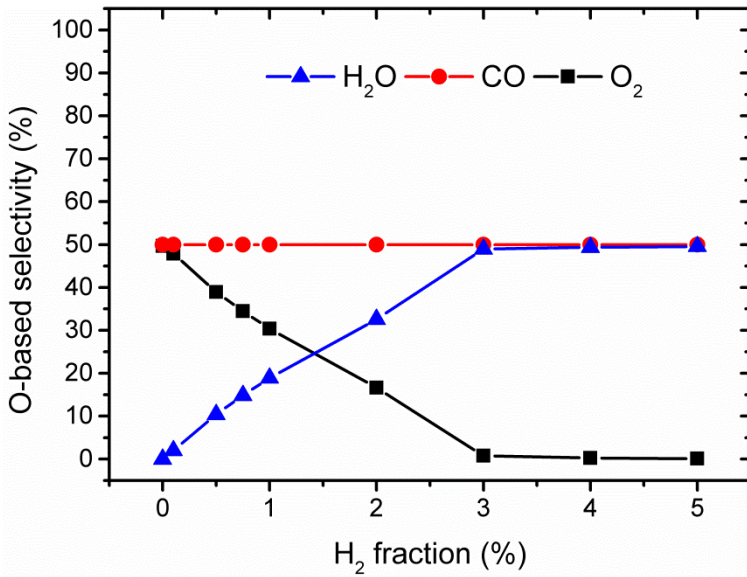


Figure 8-1: Calculated O-based selectivity of the reaction products as a function of H₂ fraction added to the CO₂ plasma.

The mechanism behind this trapping is indeed the faster three-body recombination of O and H into OH radicals, which subsequently react further into H₂O:



Another possible H-source is CH₄, which is not only cheaper than H₂, but it also has 4 instead of 2 H-atoms available for O₂ trapping. **Figure 8-2** demonstrates that water is again the most important trapping product, and that the O₂ is completely trapped at 2% CH₄ added to the CO₂ plasma.

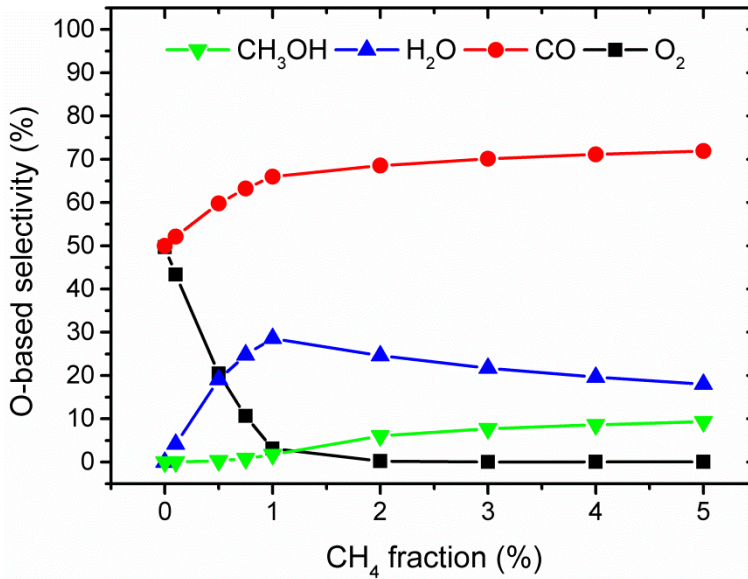
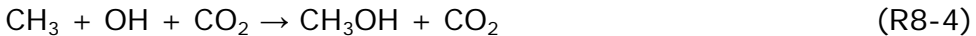


Figure 8-2: Calculated O-based selectivity of the reaction products, as a function of CH₄ fraction added to the CO₂ plasma.

The maximum O-based selectivity towards H₂O is found around 1% of CH₄. A further increase in the CH₄ fraction results in the formation of methanol, which is mainly produced by:



It is also clear from **Figure 8-2** that the CO selectivity rises above 50% upon addition of CH₄, indicating that part of the O atoms are converted into CO due to the presence of an extra carbon source (coming from CH₄ and its derivatives):





The calculated concentrations of the gas components after plasma treatment are plotted in **Figure 8-3**, for different fractions of H₂ and CH₄ added to CO₂, as well as for pure CO₂. The remaining fraction (up to 100%) is unconverted CO₂.

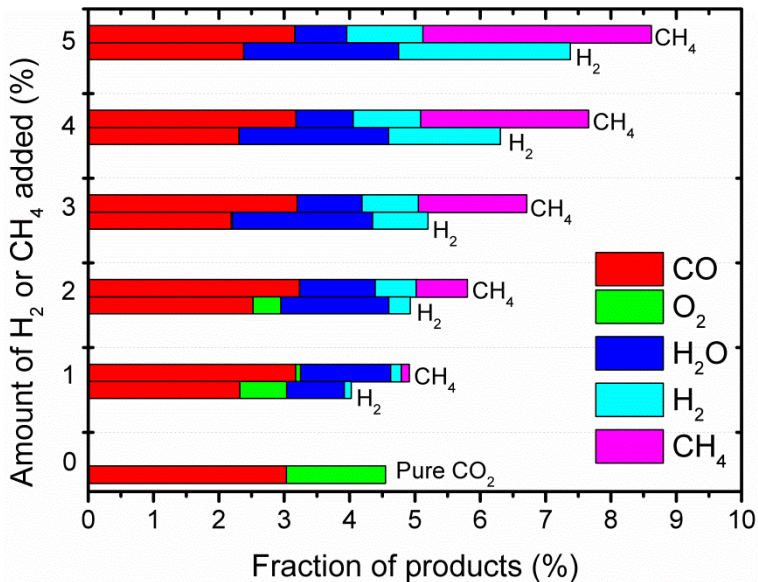


Figure 8-3: Calculated fractions of the various components in the gas mixture after plasma treatment, for pure CO₂ and for different fractions of H₂ and CH₄ added to the CO₂ plasma. Note that the remaining fraction (up to 100%) corresponds to unreacted CO₂.

It is clear that the O₂ can be completely trapped when adding 2% CH₄ or 3% H₂ at a conversion of ±2.5%, as also demonstrated in **Figure 8-1** and **Figure 8-2**. Furthermore, the fraction (or yield) of CO slightly drops when adding H₂, because not all the energy put into the plasma can be used for CO₂ splitting and some energy is now also consumed by the H source.

In other words, the selectivity of CO remains 50% (see above), but the CO₂ conversion slightly drops, resulting in a somewhat lower yield of CO. In the case of CH₄ addition, however, the CO yield remains constant, because the lower CO₂ conversion is compensated by the extra C-source, yielding a CO selectivity above 50%, as explained above. Finally, one can deduce from **Figure 8-3** that by using 3% H₂ (or more) a clean gas mixture is created with only CO, H₂O and unconverted H₂ and CO₂. The separation of this mixture is relatively simple and/or part of it can be used directly as syngas. When CH₄ is used in small concentrations (i.e., 1%) a similar gas mixture can be reached, with only tiny fractions of O₂ and CH₄ left, but with a lower H₂/CO ratio in the syngas, as CH₄ is both a H and C source.

At higher CH₄ concentration (> 2%) the O₂ is completely trapped, but a larger fraction of unconverted CH₄ remains, whereas the fractions of H₂O, H₂ and CO remain almost unchanged, so we believe that the process should be tuned in such a way that the CH₄ is completely converted, to facilitate the mixture separation.

8.3.2 Experimental proof for oxygen trapping upon CH₄ addition

In order to validate these model predictions, experiments for various additions of CH₄ in CO₂ were performed, for the same energy deposition and gas residence time in the plasma as in the simulations, i.e., 3.7 kJ/l and 0.74 s, and we identified the H₂O, O₂, H₂ and CO production by gas chromatography (GC). The relative concentrations (normalized to its highest area) of each component are plotted against the CH₄ fraction in **Figure 8-4**. The reason why we opted for this approach rather than a quantitative one is closely related to an inherent problem of plasma experiments. During the plasma process the gas expands (or contracts), meaning that an external calibration of the components will induce an error on the measured concentration,

depending of the actual gas composition^[10] (see also **Chapter 3**). Hence, considering this calibration problem, and taking into account that all the products detected by the thermal conductivity detector (TCD) have a linear response, a non-quantitative comparison is more reliable.

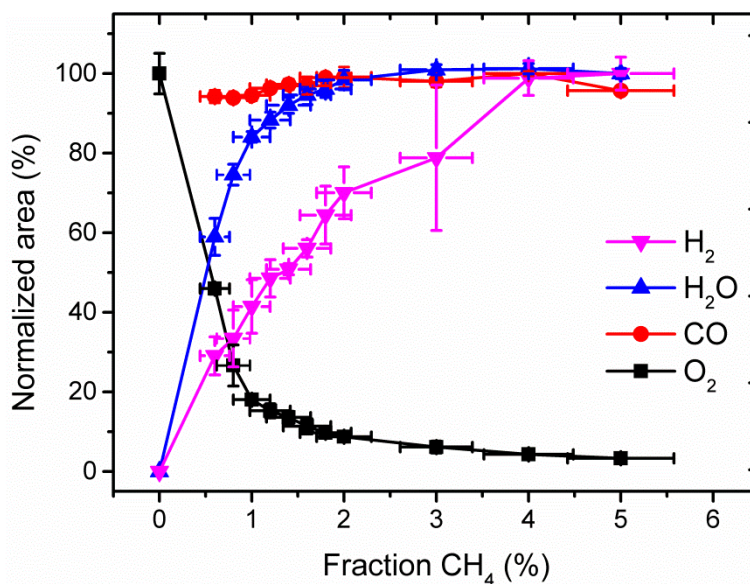


Figure 8-4: Measured normalized area of each product obtained by GC analysis, after plasma treatment of CO₂ with various admixtures of CH₄. Note: the 0% CH₄ point for CO is not displayed, since a split-peak method was used for the calibration of the CO and CH₄ peaks. Furthermore, we were not able to measure the CH₃OH concentration in our setup.

Although the validation is only qualitative, a good correlation with the calculation results is found. It is indeed clear that the O₂ concentration drops significantly upon CH₄ addition, and that the trapping is almost complete at 2% CH₄, which is very similar to the model predictions in **Figure 8-2** and **Figure 8-3**. Furthermore, the production of water reaches its maximum at 2% CH₄. Further increasing the CH₄ fraction will enhance the production of different oxygenated chemicals (cf. **Figure 8-2**), which are indeed observed as trace elements in the flame

ionization detector (FID), but with too low concentrations to be shown in this figure (see also below). The normalized area of CO remains almost constant upon CH₄ addition, similar to the calculation results (see reason explained above). Finally, the rising production of H₂ is also observed in the simulations (see **Figure 8-3**).

8.3.3 Liquids produced: Study of the carbon balance based on the calculations

The trace elements that might be formed in the experiments where CH₄ is added as trapping agent could have an influence on the downstream processing after the chemical trapping. Although we have investigated the formation of condensing products by placing a cold trap after our reactor, not enough liquid sample could be collected to perform a proper analysis. Also heating of the tubing between the reactor and the GC did not increase the traces shown on the FID detector. However, to identify those species observed on the FID detector, a carbon balance is made based on our model calculations, and the calculated fractions of the various species are shown in **Figure 8-5**. The fractions in the carbon balance are calculated by the following equation:

$$\text{Fractions in the carbon balance (\%)} = n \times \frac{C_n H_m O_x \text{ outlet}}{CO_{2 \text{ inlet}} + CH_{4 \text{ inlet}}} \times 100\% \quad (\text{E8-4})$$

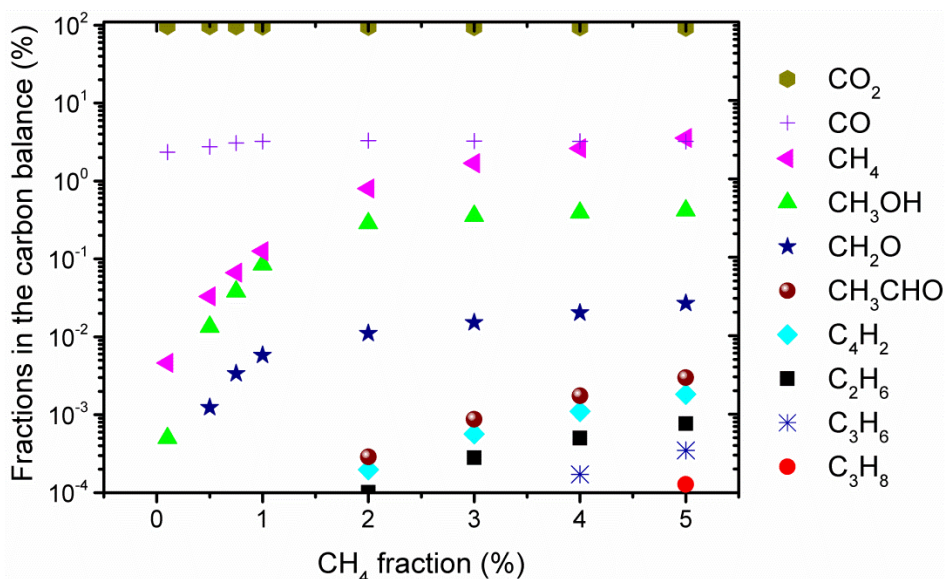


Figure 8-5: Calculated fractions in the carbon balance of the various components in the gas mixture after plasma treatment, as obtained from the model, for pure CO₂ and for different fractions of CH₄ added to the CO₂ plasma.

The largest fractions in the carbon balance are of course given by the unconverted CO₂, which has a fraction between 92.8% and 97.6%, and the unconverted CH₄, which fraction increases from 0.005% to 3.6% (see **Figure 8-5**). As far as the formed products are concerned, the largest fractions are given by CO and methanol. The CO fraction remains constant at about 3% upon CH₄ addition, while the methanol fraction increases with increasing CH₄ addition, until a fraction of 0.3% is reached at 2% CH₄, after which also the methanol level remains constant. The same trend can be found for formaldehyde, although its fraction in the carbon balance is more than one order of magnitude lower, with a maximum value of 0.01%. Furthermore, the addition of 2% CH₄ also gives rise to the formation of acetaldehyde with a maximum fraction of 0.003%, as well as some unsaturated hydrocarbons (such as butadiene and propene) and saturated hydrocarbons (such as ethane and propane), all with fractions below 0.001%.

The analysis of the carbon balance indicates that the production of alkanes and alkenes can be minimized as long as oxygen is available. This means that only controlled amounts of CH₄ should be added, in relation with the produced O₂, as discussed below (see conclusion).

Hence, the most likely produced liquids will be water, formaldehyde and methanol. The latter two are quite volatile products, having boiling points below 100°C (-19.3 °C for CH₂O and 64.2 for CH₃OH) ^[11], making separation together with water possible. Moreover, the mixture of formaldehyde, methanol and water is a well-known and studied mixture in the production of formaldehyde by the Formox process and could be distilled or directly used as feedstock in the process itself^[12]. Furthermore, it is stated that even in dry reforming the dominant liquid product is H₂O, with some traces of hydrocarbons, although this is highly dependent on the CH₄/CO₂ ratio^[13].

Finally, by adding H₂, no CH_x radicals are produced, making it unlikely that hydrocarbons will be formed during the trapping process. Indeed, our calculations show that in case of H₂ addition, the highest hydrocarbon fraction in the carbon balance is formaldehyde, with a fraction below 0.001%.

8.3.4 Energy-efficiency study of the chemical trapping of O₂

In this section the energy cost of the proposed method of adding either H₂ or CH₄ for O₂ trapping is estimated and compared to the energy cost of the splitting without any addition of a hydrogen source. The energy cost of producing 1 mole of CO by splitting CO₂ into CO and O₂ can be calculated as follows:

$$E_{CO} \left(\frac{kJ}{mol} \right) = SED_{CO_2} \left(\frac{kJ}{l} \right) * \left[\frac{\text{molar volume} \left(\frac{l}{mol} \right) * 100\%}{X_{CO_2} (\%)} \right] \quad (E8-5)$$

Where SED (kJ/l) is defined as:

$$SED \left(\frac{kJ}{l} \right) = \frac{\text{Power (kW)}}{\text{Flowrate} \left(\frac{l}{min} \right)} * 60 \left(\frac{s}{min} \right) \quad (E8-6)$$

Note that these formulas apply both to pure CO₂ splitting and to CO₂ splitting in the case of H₂ addition. However, the formula for calculating the energy cost for producing 1 mole of CO in the case of adding CH₄ is slightly different:

$$E_{CO} \left(\frac{kJ}{mol} \right) = \text{molar volume} \left(\frac{l}{mol} \right) * \left(\left(SED_{CO_2} \left(\frac{kJ}{l} \right) * \left[\frac{1}{X_{CO_2} (\%)} \right] \right) + \left(SED_{CH_4} \left(\frac{kJ}{l} \right) * \left[\frac{1}{X_{CH_4} (\%)} \right] \right) \right) * 100\% \quad (E8-7)$$

Indeed, in this case, not only CO₂ but also CH₄ can be converted into CO.

The CO₂ conversion, and the values for SED_{CO₂} and SED_{CH₄} in the case of pure CO₂ splitting, as well as when adding 3% of H₂ and 2% of CH₄ are shown in **Table 8-1**, together with the calculated energy cost for producing 1 mole of CO in the three cases. The small drop in SED_{CO₂} can be explained because the total SED is constant (at constant total flow rate; see eq. above), but a few % is now consumed by H₂ or CH₄, respectively, so that the

remaining part that can be used for CO₂ conversion is slightly lower than 100%.

Table 8-1: Calculated values of CO₂ conversion, specific energy deposition for CO₂ conversion (SED_{CO2}) and CH₄ conversion (SED_{CH4}) as well as the energy cost for producing 1 mole of CO (E_{CO}) in the case of pure CO₂ splitting, as well as when adding 3% H₂ or 2% CH₄ as trapping gases.

	Conversion (%)	SED _{CO2} (kJ/l)	SED _{CH4} (kJ/l)	E _{CO} (kJ/mol)
Pure CO ₂ splitting	2.7	4.2	-	34.2
97 % CO ₂ + 3% H ₂	2.3	4.0	-	39.9
98% CO ₂ + 2% CH ₄	2.4	4.1	0.1	37.5

The table shows that the energy cost of pure CO₂ splitting is 34.2 kJ/mol, for an SED of 4.2 kJ/l and a conversion of 2.7 % (see table 1). Adding 3% of H₂ for the complete removal of O₂ causes an increase of the energy cost by ±6 kJ/mol. Indeed, the CO₂ conversion decreases in this case to 2.3%, which induces an increase of the energy cost to 39.9 kJ/mol. Similarly, when adding 2% of CH₄ for the complete removal of O₂, the conversion decreases to 2.4%, and this yields a total energy cost of 37.5 kJ/mol, i.e. an increase of ±3 kJ/mol. Hence, the addition of a trapping gas (CH₄ or H₂) will lead to a small reduction of the CO₂ conversion, as a part of the plasma power will be consumed by the trapping gas. Consequently, this slightly lower CO₂ conversion results in a slightly higher energy cost for CO production.

Now this energy cost for CO production within the plasma will be compared with the energy requirements for the gas separation of the exit gas stream. Indeed, this will most probably be the most energy expensive part, and that is the reason why we propose here an alternative method, at least for the separation of O₂, which is considered to be not straightforward, as the existing membrane technology to separate CO/CO₂/O₂ is still under development^[21,25–27]. For this reason, we cannot yet put an

absolute number on the energy cost for separating the CO/CO₂/O₂ gas mixture. However, we expect that this energy cost will be higher than for the separation of the CO₂/CO gas mixture, i.e., without O₂, for which technology is already available^[3,4,15], and for which we can at least make an estimate, based on energy costs for a reference gas mixture CO₂/N₂^[10,19]. Indeed, we expect that the separation costs will be similar^[16], or will give at least an indication. **Table 8-2** shows the energy cost (again in kJ/mol) of different methods for separating CO₂ from a binary mixture of CO₂/N₂, together with the obtained purity of the CO₂, based on the work of Brunetti et al.^[4].

Table 8-2: Energy cost of different CO₂ separation systems, as well as the obtained CO₂ purity^[4].

	Membrane technology	Absorption with MEA	Cryogenic separation
Energy cost (kJ/mol)	22 - 264	176 - 264	264 - 440
CO ₂ purity (%)	80 - 95	> 95	99.99

It is clear that the cost of the membrane separation technology (22-264 kJ/mol) is in the same order of magnitude, or up to a factor of 7.7 higher than the production cost of 1 mole of CO (i.e., 34-40 kJ/mol; cf. **Table 8-1** above), at least in the case of a DBD reactor. Indeed, in the case of a microwave or gliding arc plasma, it can be expected that the energy cost for CO production within the plasma will be up to a factor 6 lower^[9,17], so that the separation cost by membrane technology will be even higher in relative terms. Furthermore, the cost of absorption with monoethanolamine (MEA) and cryogenic distillation is even higher, i.e., around 176 – 264 kJ/mol and 264 – 440 kJ/mol, respectively (see **Table 8-2**), so this cost is clearly higher than the cost for CO production within the plasma. On the other hand, with the current membrane separation technology, the purity of the CO₂ is less compared to the absorption with MEA and especially compared to cryogenic separation (see **Table 8-2**). Hence, we can conclude that a tradeoff exists between the energy

cost (which is the lowest for membrane technology) and the purity of the obtained CO₂ when separated from the CO (which is the highest for cryogenic separation).

To really estimate the effect of the chemical trapping of O₂ on the energy cost of the downstream separation, one should also compare the energy cost of separating a CO₂/CO mixture with the cost of separating a CO₂/CO/O₂ mixture. However, as mentioned above, the membrane technology for the latter separation is not yet fully developed, and therefore, it is too preliminary to put a number on this energy cost. Currently, this technology operates at temperatures above 700°C^[14,18–20], so it is expected that the energy cost will be higher than for separating the CO₂/CO mixture by membrane technology, where the operation temperature is closer to room temperature. Furthermore, to our knowledge, the only commercially existing technology at this moment to separate a CO/CO/O₂ mixture with a high purity is cryogenic separation^[4], which typically has higher energy costs than membrane technology (see **Table 8-2**). Hence, it is expected that the energy cost for separating the CO₂/CO/O₂ mixture will be certainly higher than for separating the CO₂/CO mixture, which is already higher than (or in the best case comparable to) the energy cost of producing 1 mole of CO within the plasma, even when adding a trapping gas (cf. **Table 8-2** and **Table 8-2** above). Therefore, based on these estimates and considerations, it can be expected that this chemical method of O₂ trapping will be an energy efficient alternative to gas separation methods.

8.4 Conclusion

To conclude, the possibility to chemically trap O₂ during the plasma splitting of CO₂ by the addition of H₂ or CH₄ is demonstrated by a combination of modelling and experiments. The addition of a few % of either H₂ or CH₄ seems enough to trap

the O₂ completely, and produce H₂O instead. It should however, be pointed out that in our case, the CO₂ conversion was only a few %, and at higher conversion also more H₂/CH₄ would be needed to trap the O₂. However, to prevent that dry reforming occurs at high conversions, resulting in the formation of hydrocarbons, the addition of CH₄ should be controlled as a function of the residence time, so that the kinetics favor water production instead of dry reforming. The concept of adding a small amount of reactants is already proven in the production of fine chemicals by plasma, favoring the production of one type of molecule^[21]. One possible way to accomplish this is by using a recycle stream, in such a way that the outlet stream is dried (H₂O is removed) and the CO₂/CO mixture is separated, so that the separated non-converted CO₂ can be re-mixed with a fresh inlet stream containing a hydrogen source. A second possibility would be to use a couple of DBD reactors in series, in such a way that after each reactor the gas is dried (H₂O is removed), leaving only CO and CO₂ as outlet stream. A small amount of hydrogen source could then be added before each individual reactor, and at the end of the reactor series a gas will be produced without O₂ and with a high conversion towards CO.

In the case of CH₄ addition, also H₂ is formed. If the two admixtures are compared, CH₄ is probably the better choice since it requires smaller fractions for O₂ trapping, and it is less expensive compared to H₂. It should be pointed out that the purpose of this research was to identify a chemical removal mechanism by OH radicals. Although we only investigated H₂ and CH₄, in principle, more green and sustainable sources for OH or H could also be used (for example glycerol)^[22] to make this approach probably more interesting and cost efficient. Moreover Tagawa et. al.^[23] showed that by removing O₂ from the plasma, the CO₂ conversion increased up to 40%. Hence, their results obtained with a hybrid reactor existing of a Solid Oxide Electrolyser Cell and a DBD indicate that separation of O₂ not only

solves a downstream problem (further processing) but gives also rise to a higher conversion.

To conclude, it is clear that the trapping of O₂ during the CO₂ splitting can be accomplished by a simply chemical step, making the separation of end-products possible with the existing membrane technology for CO₂ separation.

8.5 References

- [1] V. Givotov, A. Fridman, M. Krotov, E. Krasheninnikov, B. Patrushev, V. Rusanov, G. Sholin, *Int. J. Hydrogen Energy* **1981**, *6*, 441–449.
- [2] Tadeusz Kudra and Arun S. Mujumdar, *Advanced Drying Technologies, Second Edition*, Taylor & Francis Inc, Boca Roca, **2009**.
- [3] Y. Liu, E. Hu, E. a. Khan, Z. Lai, *J. Memb. Sci.* **2010**, *353*, 36–40.
- [4] A. Brunetti, F. Scura, G. Barbieri, E. Drioli, *J. Memb. Sci.* **2010**, *359*, 115–125.
- [5] R. Aerts, T. Martens, A. Bogaerts, *J. Phys. Chem. C* **2012**, *116*, 23257–23273.
- [6] W. Tsang, R. F. Hampson, *J. Phys. Chem. Ref. Data* **1986**, *15*, 1087–1279.
- [7] R. Snoeckx, R. Aerts, X. Tu, A. Bogaerts, *J. Phys. Chem. C* **2013**, *117*, 4957–4970.
- [8] R. Snoeckx, M. Setareh, R. Aerts, P. Simon, A. Maghari, A. Bogaerts, *Int. J. Hydrogen Energy* **2013**, *38*, 16098–16120.
- [9] A. Indarto, D. R. Yang, J.-W. Choi, H. Lee, H. K. Song, *J. Hazard. Mater.* **2007**, *146*, 309–15.
- [10] N. R. Pinhao, A. Janeco, J. B. Branco, *Plasma Chem. Plasma Process.* **2011**, *31*, 427–439.
- [11] D. R. Lide, W. M. M. Haynes, G. Baysinger, L. I. Berger, D. L. Roth, D. Zwillinger, M. Frenkel, R. N. Goldberg, *J. Am. Chem. Soc.* **2009**, *131*, 12862–12862.
- [12] G. Wiesgickl, H. P. Beck, G. Emig, *Appl. Catal.* **1990**, *59*, L1–L7.
- [13] H. J. Gallon, X. Tu, J. C. Whitehead, *Plasma Process. Polym.* **2012**, *9*, 90–97.
- [14] S. Rayne, *Nat. Preced.* **2008**, DOI: 10.1038/npre.2008.1741.1.
- [15] P. Bernardo, E. Drioli, G. Golemme, *Ind. Eng. Chem. Res.* **2009**, *48*, 4638–4663.
- [16] R. Bounaceur, N. Lape, D. Roizard, C. Vallieres, E. Favre, *Energy* **2006**, *31*, 2556–2570.
- [17] L. F. Spencer, A. D. Gallimore, *Plasma Sources Sci. Technol.* **2013**, *22*, 015019.
- [18] B. He, K. Zhang, Y. Ling, J. Xu, L. Zhao, *J. Memb. Sci.* **2014**, *464*, 55–60.

- [19] J. Yi, T. E. Weirich, M. Schroeder, *J. Memb. Sci.* **2013**, 437, 49–56.
- [20] W. Chen, C. Chen, H. J. M. Bouwmeester, A. Nijmeijer, L. Winnubst, *J. Memb. Sci.* **2014**, 463, 166–172.
- [21] Z. Zhang, X. Gong, S. Zhang, H. Yang, Y. Shi, C. Yang, X. Zhang, X. Xiong, X. Fang, Z. Ouyang, *Sci. Rep.* **2013**, 3, 3481.
- [22] X. Zhu, T. Hoang, L. L. Lobban, R. G. Mallinson, *Chem. Commun.* **2009**, 2908–10.
- [23] Y. Tagawa, S. Mori, M. Suzuki, I. Yamanaka, T. Obara, J. Ryu, Y. Kato, *Kagaku Kogaku Ronbushu* **2011**, 37, 114–119.

Chapter 9:

General conclusions and critical assessment

The purpose of this dissertation was to obtain chemical information by modelling for the environmental applications of DBDs. These discharges can destroy VOCs with high conversions; moreover, they can also convert chemically stable greenhouse gases into “useful” chemicals. However, the energy consumption is currently still much too high to be a competitive industrial product. Nevertheless, there are some commercial examples available for gas cleaning, more specifically for indoor gas cleaning by companies such as Plasmaclean (www.plasmaclean.com), AEROX (www.aeroinjector.com) and AXIAIR (www.axiair.nl).

Besides the large energy consumption, it must be clear that the chemical complexity of plasmas does make selective gas processing difficult. For instance, in the case of VOC destruction, many by-products will be produced by intermediate reactions but also by the background gas (O_3 , NO_x ,...). These problems should be investigated in depth before a safe and environmentally acceptable product can be delivered to the industry. Although a lot of work still has to be done, I strongly believe that a working combination of plasma and a specially designed catalyst could solve many of these problems. At this moment, the actual mechanism of plasma catalysis is not really understood, although some promising results are reported in literature. It will be important to understand the interaction between plasma and a

catalyst surface, not only for plasma catalysis but also for the plasma treatment of existing catalysts. We already obtained some first promising results in collaboration with LADCA (Laboratory of Adsorption and Catalysis at UA), which definitely show that plasmas can induce reactions on a catalyst surface.

To conclude, plasmas can induce chemical reactions which are almost impossible in classical thermochemistry. However due to their complexity the step to industrialization will also be much larger.

Summary

Air pollution has become a major global concern which affects all inhabitants of our precious earth. Nowadays it is fact that our climate is changing and the sea level is rising. Moreover, we are facing an energy crisis because all our fossil fuel resources will sooner or later be running empty. It is clear that drastic measures are needed to keep our planet as it is today for generations to come. One of these measures is the 20-20-20 targets imposed by the European Commission, which stimulates the research for environmental energy applications.

In this dissertation two environmental applications of plasma technology are discussed. The first one is the abatement of flue gases, and more specifically the destruction of volatile organic compounds (VOCs). The second one is the conversion of CO₂ into valuable chemicals. Both of these applications suffer from a large energy cost under classical (thermodynamic) conditions, due to the chemical stability of these molecules.

Plasma technology is quite promising to overcome these thermodynamic barriers. Plasmas allow reactions at different time-scales with different species, such as electrons, ions, radicals, molecules and excited species, creating new chemical pathways. Indeed, in a plasma the applied electrical energy is directly transferred to the electrons, which activate the gas by ionization, excitation and dissociation, hence creating reactive species (ions, excited species, radicals), that can further easily undergo other chemical reactions. Especially gas discharges, which are low temperature plasmas, show promising results in the destruction of pollutants at mild conditions. A common type of gas discharge is the dielectric barrier discharge (DBD) which has been successfully

scaled up for industrial ozone generation and is widely investigated in the field of environmental applications.

The complexity of DBDs creates difficulties for experimental diagnostics and therefore numerical studies can help to improve our understanding of the ongoing processes. A chemical kinetics model developed by M. Kushner and co-workers combined with experiments was used in this PhD dissertation to obtain insight in the ongoing plasma chemistry for two different environmental applications. The model and the experimental setup are briefly discussed in **Chapter 3**.

The first environmental application is studied in **PART II (Chapter 4 and Chapter 5)** and covers the destruction of VOCs. In **Chapter 4** the initiation step of the destruction of VOCs by low temperature plasmas is investigated. This step is known to be determined by electrons, radicals and metastable species. In this chapter a kinetic model is presented for the destruction of ethylene in low temperature plasmas, which allows estimating the relative importance of all plasma species and their related reactions. Both the ethylene concentration and the specific energy deposition have a major impact on the relative importance of O atoms and the metastable nitrogen species $N_2(A^3\Sigma^+_u)$ in the destruction process. The obtained results show that the direct destruction by electron impact reactions is negligible in the initiating step. Furthermore, they show that the influence of metastable nitrogen is quite significant.

In **Chapter 5** the entire reaction pathway of ethylene is investigated in detail, both in dry and humid air, and under more realistic conditions of consecutive pulses. This is an improvement of the model described in **Chapter 4**, where we only investigated the role of electrons in the initiation of the destruction path. The influence of the specific energy deposition on the removal

efficiency and the selectivity towards CO and CO₂ is studied for different concentrations of ethylene at real residence times. The model allows to identify the destruction pathway in both dry and humid air. The destruction is found to be mainly initiated by metastable N₂ molecules as also indicated in **Chapter 4**, but the following destruction steps are dominated by O atoms and OH radicals. At increasing air humidity the removal efficiency drops by ±15%, but the selectivity towards CO and CO₂ stays more or less constant at 60% and 22%, respectively. Beside CO and CO₂, also acetylene, formaldehyde and water were identified as by-products of the destruction process, with concentrations of 1606 ppm, 15033 ppm and 185 ppm in humid air (with 20% RH), respectively. Finally, the by-products generated by the humid air discharge itself are investigated, which are the greenhouse gases O₃, N₂O and the toxic gas NO₂.

Part III (Chapter 6, Chapter 7 and Chapter 8) covers the second environmental application under study in this dissertation, namely the splitting of CO₂. First, the role of vibrationally excited CO₂ is investigated in **Chapter 6**. In this chapter, the splitting of CO₂ in a pulsed plasma system, such as a DBD, is evaluated from a chemical point of view by means of numerical modeling. For this purpose, a chemical reaction set of CO₂ in an atmospheric pressure plasma is developed, including the vibrational states of CO₂, O₂ and CO. The simulated pulses are matched to the conditions of a microdischarge and repeated with intervals of 1 microsecond. The calculations predict that the electrons have the largest contribution to the CO₂ splitting at the conditions under study, by electron impact dissociation. The contribution of vibrationally excited CO₂ levels in the splitting of CO₂ is found to be 6.4%, when only considering one microdischarge pulse and its afterglow. However, it can be much larger for consecutive discharge pulses, as is typical for a filamentary DBD, when the interpulse time is short enough and accumulation effects in the vibrationally excited CO₂ densities can occur.

In **Chapter 7**, the model of **Chapter 6** is extended to real time scale simulations, and a combined experimental and numerical study is performed to evaluate the splitting of CO₂. Experiments to study the splitting in the same DBD plasma in a wide range of parameters are performed. The frequency and dielectric material do not affect the CO₂ conversion and energy efficiency, but the discharge gap can have a considerable effect. The specific energy input has the most important effect on the CO₂ conversion and energy efficiency. Moreover, the plasma chemistry model for CO₂ splitting, explained in previous chapter, shows reasonable agreement with the experimental conversion and energy efficiency. This model is used to elucidate the critical reaction pathway that is mostly responsible for the CO₂ conversion. Finally, the results are also benchmarked with other CO₂ splitting techniques, and the limitations as well as the benefits and future possibilities are identified in terms of modifications of DBD plasmas for greenhouse gas conversion in general.

Finally, **Chapter 8** deals with a major drawback of CO₂ splitting, i.e. the separation of the conversion products. In this chapter the trapping of O atoms by adding a hydrogen source, which enhances the chemical conversion into water, is demonstrated. The experimental and modelling results show that by adding 3% of H₂ and 2% of CH₄ most of the oxygen can be trapped at a CO₂ conversion of $\pm 2.5\%$. The identified products formed by the addition of CH₄ or H₂ are mainly H₂O and in the case of CH₄ also H₂. Adding a hydrogen source (H₂ or CH₄) thus leads to the removal of O₂, leaving behind a gas mixture that can be more easily separated.

The PhD dissertation ends with a short conclusion in **Chapter 9** about the use of plasmas for environmental applications.

Samenvatting

Luchtverontreiniging is uitgegroeid tot één van de grootste problemen op onze aarde. Men kan nu met zekerheid zeggen dat ons klimaat verandert en de zeespiegel stijgt. Verder dreigt er in de toekomst een energiecrisis als gevolg van een tekort aan fossiele brandstoffen. Het is duidelijk dat drastische maatregelen nodig zijn om onze planeet leefbaar te houden voor de volgende generaties. Eén van deze maatregelen zijn de 20-20-20 doelstellingen opgelegd door de Europese Commissie, die het onderzoek voor milieu en energie gerelateerde toepassingen stimuleert.

In dit proefschrift worden twee milieu-toepassingen van plasmatechnologie onderzocht. De eerste is de behandeling van rookgassen, en meer specifiek de afbraak van vluchtige organische stoffen (VOS). De tweede is de omzetting van CO₂ in waardevolle chemicaliën. Beide toepassingen hebben te kampen met hoge energiekosten onder klassieke (thermodynamische) voorwaarden, vanwege de chemische stabiliteit van de moleculen.

Plasmatechnologie is een veelbelovende technologie om deze thermodynamische barrières te overwinnen. In plasma's treden reacties op met verschillende tijdschalen tussen verschillende soorten deeltjes, zoals elektronen, ionen, radicalen, moleculen en geëxciteerde deeltjes, waardoor nieuwe chemische routes mogelijk worden. In een plasma wordt immers de aangelegde elektrische energie direct overgedragen aan de elektronen, die het gas kunnen activeren door ionisatie, excitatie en dissociatie, waarbij reactieve deeltjes (ionen, geëxciteerde deeltjes, radicalen) gevormd worden, die verder gemakkelijk andere chemische reacties kunnen ondergaan. Voornamelijk lage

temperatuur plasma's, ook gasontladingen genoemd, tonen veelbelovende resultaten voor de afbraak van verontreinigende stoffen bij milde omstandigheden. Een veel voorkomend type van een gasontlading is de diëlektrische barrière ontlading (DBD) die met succes is opgeschaald voor de industriële productie van ozon. Bovendien wordt deze gasontlading vaak gebruikt voor onderzoek naar milieu-toepassingen.

De chemische complexiteit van gasontladingen maakt experimentele diagnostiek moeilijk en daarom worden in dit werk numerieke studies gebruikt om de onderliggende processen beter te kunnen begrijpen. Meer specifiek trachten we door de combinatie van een chemisch kinetisch model en experimenten inzicht te krijgen in de plasmachemie van gasontladingen gebruikt voor milieutoepassingen. In **hoofdstuk 3** worden het model en de experimentele opstelling kort besproken.

De eerste milieu-applicatie wordt bestudeerd in **deel II (hoofdstukken 4 en 5)** en heeft betrekking tot de afbraak van VOS.

In **hoofdstuk 4** wordt de initiatie stap van de afbraak van VOS bij lage temperatuur plasma's onderzocht. Deze stap wordt voornamelijk bepaald door elektronen, radicalen en metastabiele deeltjes. Hierbij wordt een kinetisch model gebruikt om het relatieve belang van alle plasmadeeltjes en hun bijbehorende reacties te onderzoeken voor de afbraak van ethyleen. Zowel de ethyleenconcentratie als de specifieke energie depositie hebben een grote invloed op het relatieve belang van atomaire zuurstof en het metastabiele stikstofdeeltje $N_2(A^3\Sigma^+_u)$ voor het afbraakproces. Verder tonen de resultaten aan dat de directe afbraak door elektron impact reacties verwaarloosbaar is.

In **hoofdstuk 5** wordt de afbraak van ethyleen in een DBD in meer detail onderzocht door de combinatie van een kinetisch model en experimenten, voor meer reële omstandigheden van repeterende pulsen. Dit is een verbetering van de studie in **hoofdstuk 4** waar enkel de initiatie van de afbraak bestudeerd werd. De invloed van de specifieke energie depositie op de verwijderingsefficiëntie en de selectiviteit voor CO en CO₂ worden bestudeerd bij verschillende concentraties van ethyleen en bij reële verblijftijden. Het model maakt het mogelijk om het afbraakmechanisme in droge en vochtige lucht te identificeren. Dit mechanisme wordt hoofdzakelijk geïnitieerd door metastabiele N₂ moleculen, zoals ook aangegeven in **hoofdstuk 4**. Echter, de verdere afbraak wordt gedomineerd door O-atomen en OH-radicalen. Het verhogen van de luchtvochtigheid zorgt voor een daling van de verwijderingsefficiëntie met ± 15%, waarbij de selectiviteit voor CO en CO₂ min of meer constant blijft, bij respectievelijk 60% en 22%. Naast CO en CO₂ worden ook acetyleen, formaldehyde en water geïdentificeerd als bijproducten van het afbraakproces, met respectievelijk een concentratie van 1606 ppm, 15033 ppm en 185 ppm in vochtige lucht (met 20% RV). Tenslotte wordt er ook gekeken naar de bijproducten die door de ontlading (in lucht) zelf worden gevormd. Deze producten zijn hoofdzakelijk de broeikasgassen O₃, N₂O en het giftige gas NO₂.

Deel III (hoofdstukken 6, 7 en 8) handelt over een tweede milieu-applicatie, namelijk de conversie van broeikasgassen naar waardevolle feedstocks voor de chemische industrie.

In **hoofdstuk 6** wordt de invloed van vibrationeel geëxciteerd CO₂ bestudeerd in een gepulst plasma systeem, zoals een DBD. Voor deze studie werd een reactieset ontwikkeld voor CO₂ in atmosferische plasma's met de geëxciteerde toestanden van CO₂, O₂ en CO, zodat deze kan worden gebruikt in een kinetisch model. De gesimuleerde pulsen werden vergeleken met de typische condities van een micro-ontlading en werden herhaald

binnen een interval van één microseconde. De berekeningen voorspellen dat de grootste bijdrage tot de splitsing van CO₂ kan worden toegewezen aan de elektronen door elektron impact reacties. Echter, de bijdrage van vibrationeel geëxciteerd CO₂ tot de splitsing van CO₂ bedraagt slechts 6.4% voor één puls en zijn nagloei. Deze bijdrage kan echter wel toenemen als meerdere pulsen kort na elkaar worden beschouwd, zodat de vibrationeel geëxciteerde deeltjes kunnen accumuleren tot een hogere dichtheid.

In **hoofdstuk 7** wordt het model van vorig hoofdstuk uitgebreid naar lange tijdsschaal simulaties en wordt een gecombineerde experimentele en numerieke studie voorgesteld over de splitsing van CO₂ in een DBD. Er wordt een experimentele parameterstudie uitgevoerd met een zelfgebouwde DBD reactor. De frequentie en het diëlektrische materiaal tonen weinig invloed op de CO₂ conversie en de energie-efficiëntie, maar de afstand tussen beide elektroden (of de ontladingsruimte) toont een aanzienlijk effect. De specifieke energie depositie heeft het meest uitgesproken effect op de CO₂ conversie en energie-efficiëntie en is dus de meest kritische parameter. Het plasma chemisch model voor CO₂ splitsing, beschreven in **hoofdstuk 6**, vertoont een redelijke overeenkomst met de experimentele conversie en energie-efficiëntie. Dit model kan worden gebruikt om het reactiemechanisme voor CO₂ splitsing te identificeren bij verschillende condities. Ten slotte worden de resultaten ook vergeleken met andere technieken voor CO₂ splitsing waarbij de beperkingen, de voordelen en toekomstige mogelijkheden worden geïdentificeerd.

In **hoofdstuk 8** wordt de scheiding van de eindproducten van CO₂ splitsing besproken. Deze scheiding gebeurt door het chemisch opvangen van atomair zuurstof met behulp van een waterstofbron zodat water kan worden gevormd. De experimentele en berekende resultaten tonen aan dat door

toevoeging van 3% H₂ of 2% CH₄ bij een conversie ±2.5% het merendeel van de zuurstof kan worden opgeslagen. Door deze toevoeging wordt voornamelijk H₂O gevormd maar ook H₂ in het geval van CH₄. De toevoeging van een waterstofbron zorgt dus voor de verwijdering van O₂ zodat de eindproducten makkelijker kunnen worden gescheiden.

Tot slot wordt in **hoofdstuk 9** een korte algemene conclusie gegeven over het gebruik van plasma's voor milieu gerelateerde toepassingen.

List of publications

- Aerts, R., Somers, W., & Bogaerts, A. (2014). CO₂ splitting in a dielectric barrier discharge plasma: A combined experimental and computational study. Submitted to ChemSusChem
- Aerts, R., Snoeckx, R., & Bogaerts, A. (2014). In-Situ Chemical Trapping of Oxygen in the Splitting of Carbon Dioxide by Plasma. *Plasma Processes and Polymers*, in press. doi:10.1002/ppap.201400091
- Aerts, R., Tu, X., Van Gaens, W., Whitehead, J. C., & Bogaerts, A. (2013). Gas purification by nonthermal plasma: a case study of ethylene. *Environmental Science & Technology*, 47(12), 6478–85. doi:10.1021/es400405c
- Aerts, R., Martens, T., & Bogaerts, A. (2012). Influence of Vibrational States on CO₂ Splitting by Dielectric Barrier Discharges. *The Journal of Physical Chemistry C*, 116(44), 23257–23273. doi:10.1021/jp307525t
- Aerts, R., Tu, X., De Bie, C., Whitehead, J. C., & Bogaerts, A. (2012). An Investigation into the Dominant Reactions for Ethylene Destruction in Non-Thermal Atmospheric Plasmas. *Plasma Processes and Polymers*, 9(10), 994–1000. doi:10.1002/ppap.201100168
- Vandenbroucke, A., Aerts, R., Van Gaens, W., De Geyter, N., Leys C., Morent, R., & Bogaerts, A. (2014). Modeling and experimental study of trichloroethylene abatement with a negative direct current corona discharge. *Plasma Chemistry and Plasma Processing*, in press. doi: 10.1007/s11090-014-9584-7

- Snoeckx, R., Aerts, R., Tu, X., & Bogaerts, A. (2013). Plasma-Based Dry Reforming: A Computational Study Ranging From Nanoseconds to Seconds Timescale. *The Journal of Physical Chemistry C*, 117, 4957–4970. doi: 10.1021/jp311912b
- Snoeckx, R., Setareh, M., Aerts, R., Simon, P., Maghari, A., & Bogaerts, A. (2013). Influence of N₂ concentration in a CH₄/N₂ dielectric barrier discharge used for CH₄ conversion into H₂. *International Journal of Hydrogen Energy*, 38(36), 16098–16120. doi: 10.1016/j.ijhydene.2013.09.136

List of conference contributions

- R. Aerts, W. Somers and A. Bogaerts, "Modelling of the pure CO₂ splitting in a dielectric barrier discharge", **Talk** at the "9th International Symposium on Non-Thermal/Thermal Plasma Pollution Control Technology & Sustainable Energy" (ISNTP), Dalian, China, 16-20 June 2014
- R. Aerts and A. Bogaerts, "Kinetic modelling of pure CO₂ splitting in plasmas", **Invited talk** at the Workshop of the Solvay Institutes: "Plasmas for Environmental Applications", Brussels, Belgium, 31 March – 2 April 2014
- Passive contribution: Carbon Dioxide utilization summit, Essen, Germany, 30-31 October 2013
- R. Aerts, T. Martens and A. Bogaerts, "CO₂ Utilization by dielectric barrier discharges", **Talk** at the "International Symposium on Plasma Chemistry" (ISPC), Cairns, Australia, 4-9 August 2013
- R. Aerts, T. Martens and A. Bogaerts, "Modelling of the pure CO₂ splitting in a dielectric barrier discharge", **Talk** at the "8th International Symposium on Non-Thermal/Thermal Plasma Pollution Control Technology & Sustainable Energy" (ISNTP), Camaret, France, 25-29 June 2012
- R. Aerts, T. Martens and A. Bogaerts, "Kinetic modelling of pure CO₂ splitting in plasmas", **Invited talk** at the VITO ISUP congress, Bruges, Belgium, 7-9 May 2012
- R. Aerts, T. Martens and A. Bogaerts, "Dry reforming of CH₄ in dielectric barrier discharge plasma reactors", **Talk** at the

"KVCV Chemcys Conference", Blankenberge, Belgium, 1-2 March 2012

Passive contribution: Symposium Plasma Assisted Catalysis: Recent Advances and Perspectives, Antwerpen, Belgium, 28 November 2011

R. Aerts and A. Bogaerts, "An investigation into the dominant reactions for ethylene destruction in non-thermal atmospheric plasmas", **Talk** at the "Conference on Advanced Oxidation Technology", San Diego, US, 7-10 November 2011

R. Aerts, C. De Bie and A. Bogaerts, "Valorization of CO₂ and CH₄ by means of low temperature plasmas, **Poster** presentation on the "Colloquium on Chemical Reaction Engineering, Munich", Germany, 10-11 October 20; **Rewarded with Best Poster Award.**

R. Aerts, X. Tu and A. Bogaerts, "An investigation of the ethylene destruction mechanism in a dielectric barrier discharge reactor", **Poster** presentation at the "International Symposium on Plasma Chemistry" (ISPC), Philadelphia, US, 24-29 July 2011

Appendix I

Reactions used in Chapters 4 and 5 to describe ethylene destruction in a dry or humid air plasma, with their corresponding rate coefficients or cross sections, and the references where these data were adopted from.

Table A1- 1: Reactions occurring in the dry or humid air chemistry in Chapter 4.

#	Reaction	Rate coefficient ^a / Cross section	Ref.
1	$e^- + O \rightarrow O + e^-$	$\sigma(E)$	[1]
2	$e^- + O \rightarrow O^+ + e^- + e^-$	$\sigma(E)$	[1]
3	$e^- + O_2 \rightarrow O^- + O$	$\sigma(E)$	[1]
4	$e^- + O_2 \rightarrow O_2(A^1\Delta_g) + e^-$	$\sigma(E)$	[1]
5	$e^- + O_2 \rightarrow O + O + e^-$	$\sigma(E)$	[1]
6	$e^- + O_2 \rightarrow O(^1D) + O + e^-$	$\sigma(E)$	[1]
7	$e^- + O_2 \rightarrow O_2^+ + e^- + e^-$	$\sigma(E)$	[1]
8	$e^- + O_2 \rightarrow O(^1D) + O + e^-$	$\sigma(E)$	[1]
9	$e^- + O_2 \rightarrow O^+ + O + e^- + e^-$	$\sigma(E)$	[1]
10	$e^- + O_2(A^1\Delta_g) \rightarrow O^- + O$	$\sigma(E)$	[1]
11	$e^- + O_2(A^1\Delta_g) \rightarrow O_2 + e^-$	$\sigma(E)$	[1]
12	$e^- + O_2(A^1\Delta_g) \rightarrow O + O + e^-$	$\sigma(E)$	[1]
13	$e^- + O_2(A^1\Delta_g) \rightarrow O(^1D) + O + e^-$	$\sigma(E)$	[1]
14	$e^- + O_2(A^1\Delta_g) \rightarrow O^+ + O + e^- + e^-$	$\sigma(E)$	[1]
15	$e^- + O_2(B^1\Sigma_g^+) \rightarrow O^- + O$	$\sigma(E)$	[1]
16	$e^- + O_2(B^1\Sigma_g^+) \rightarrow O_2 + e^-$	$\sigma(E)$	[1]
17	$e^- + O_2(B^1\Sigma_g^+) \rightarrow O_2(A^1\Delta_g) + e^-$	$\sigma(E)$	[1]
18	$e^- + O_2(B^1\Sigma_g^+) \rightarrow O_2(V) + e^-$	$\sigma(E)$	[1]
19	$e^- + O_2(B^1\Sigma_g^+) \rightarrow O + O + e^-$	$\sigma(E)$	[1]
20	$e^- + O_2(B^1\Sigma_g^+) \rightarrow O(^1D) + O + e^-$	$\sigma(E)$	[2]
21	$e^- + O_2(B^1\Sigma_g^+) \rightarrow O^+ + O + e^- + e^-$	$\sigma(E)$	[2]

22	$e^- + O_2^+ \rightarrow O_2$	2.0×10^{-7}	[3]
23	$e^- + e^- + O_2^+ \rightarrow O + O(^1D)$	$6.87 \times 10^{-9} (Te)^{-0.7}$	[3]
24	$e^- + O_2^+ \rightarrow e + O_2^+$	$\sigma(E)$	EST
25	$e^- + O_2^+ \rightarrow O + O$	$\sigma(E)$	EST
26	$e^- + O_2(V) \rightarrow O^- + O$	$\sigma(E)$	EST
27	$e^- + O_2(V) \rightarrow O_2 + e^-$	$\sigma(E)$	EST
28	$e^- + O_2(V) \rightarrow O_2(A^1\Delta_g) + e^-$	$\sigma(E)$	EST
29	$e^- + O_2(V) \rightarrow O_2(R) + e^-$	$\sigma(E)$	EST
30	$e^- + O_2(V) \rightarrow O + O + e^-$	$\sigma(E)$	EST
31	$e^- + O_2(V) \rightarrow O(^1D) + O + e^-$	$\sigma(E)$	EST
32	$e^- + O_2(V) \rightarrow O^+ + O + e^- + e^-$	$\sigma(E)$	EST
33	$e^- + O_3 \rightarrow O^- + O_2$	$\sigma(E)$	[4]
34	$e^- + O_3 \rightarrow O_2^- + O$	$\sigma(E)$	[4]
35	$e^- + N \rightarrow N(^2D) + e^-$	$\sigma(E)$	[5]
36	$e^- + N \rightarrow N^+ + e^- + e$	$\sigma(E)$	[5]
37	$e^- + N_2 \rightarrow N_2 + e^-$	$\sigma(E)$	[6]
38	$e^- + N_2 \rightarrow N_2(A_3\Sigma_u^+) + e^-$	$\sigma(E)$	[6]
39	$e^- + N_2 \rightarrow N_2(R) + e^-$	$\sigma(E)$	[6]
40	$e^- + N_2 \rightarrow N + N + e^-$	$\sigma(E)$	[6]
41	$e^- + N_2 \rightarrow N_2^+ + e^- + e^-$	$\sigma(E)$	[6]
42	$e^- + N_2(V) \rightarrow N_2 + e^-$	$\sigma(E)$	[6]
43	$e^- + N_2(V) \rightarrow N(^2D) + e^-$	$\sigma(E)$	[6]
44	$e^- + N_2(V) \rightarrow N_2^+ + e^- + e^-$	$\sigma(E)$	[6]
45	$O + O^- \rightarrow O_2 + e^-$	$2.00 \times 10^{-10} (T/300)^{0.5}$	[7]
46	$O + O_2(B^1\Sigma_g^+) \rightarrow O_2 + O(^1D)$	$3.39 \times 10^{-11} \exp(-4201/T)$	[3]
47	$O + O_3 \rightarrow O_2 + O_2$	$8.00 \times 10^{-12} \exp(-2060/T)$	[2]
48	$O + O_3^- \rightarrow O_2^- + O_2$	$4.50 \times 10^{-12} (T/300)^{0.5}$	[7]
49	$O^- + O_2(A^1\Delta_g) \rightarrow O_3 + e^-$	2.20×10^{-11}	[8]
50	$O^- + O_2(A^1\Delta_g) \rightarrow O_2^- + O$	1.10×10^{-11}	[8]
51	$O^- + O_2^+ \rightarrow O + O_2$	$1.50 \times 10^{-7} (T/300)^{-0.5}$	[8]
52	$O^- + O_2^+ \rightarrow O + O + O$	$2.00 \times 10^{-7} (T/300)^{-0.5}$	[9]
53	$O^- + O_2^+ + O_2 \rightarrow O_3 + O_2$	$2.00 \times 10^{-25} (T/300)^{-2.5}$	[9]
54	$O^- + O_2 \rightarrow O + O_2 + e^-$	5.00×10^{-15}	[9]
55	$O^- + O_3 \rightarrow O_2 + O_2 + e^-$	$3.01 \times 10^{-10} (T/300)^{0.5}$	[7]
56	$O^- + O_3 \rightarrow O_3^- + O$	$1.99 \times 10^{-10} (T/300)^{0.5}$	[7]
57	$O^- + O_3 \rightarrow O_2^- + O_2$	$1.02 \times 10^{-11} (T/300)^{0.5}$	[7]
58	$O(^1D) + O_2 \rightarrow O + O_2$	$0.48 \times 10^{-11} \exp(67/T)$	[2]

59	$O(^1D) + O_2 \rightarrow O + O_2(A^1\Delta_g)$	$0.16 \times 10^{-11} \exp(67/T)$	[2]
60	$O(^1D) + O_2 \rightarrow O + O_2(B^1\Sigma^+_g)$	$2.56 \times 10^{-11} \exp(67/T)$	[2]
61	$O(^1D) + O_3 \rightarrow O_2 + O_2$	1.20×10^{-10}	[1]
62	$O(^1D) + O_3 \rightarrow O_2 + O + O$	1.20×10^{-11}	[1]
63	$O(^1D) + O_3 \rightarrow O_2 + O_2(A^1\Delta_g)$	1.50×10^{-12}	[10]
64	$O(^1D) + O_3 \rightarrow O_2 + O_2(B^1\Sigma^+_g)$	7.20×10^{-12}	[11]
65	$O_2 + O_2(A^1\Delta_g) \rightarrow O_2 + O_2$	$3.00 \times 10^{-18} \exp(-200/T)$	[2]
66	$O_2 + O_2(A^1\Delta_g) \rightarrow O_2 + O_2$	$4.00 \times 10^{-17} \exp(-200/T)$	[2]
67	$O_2 + O_3 \rightarrow O_2 + O + O_2$	2.29×10^{-26}	[12]
68	$O_2(A^1\Delta_g) + O_2(A^1\Delta_g) \rightarrow O_2(B^1\Sigma^+_g) + O_2$	$0.90 \times 10^{-16} \exp(-560/T)$	[13]
69	$O_2(A^1\Delta_g) + O_2^- \rightarrow e^- + O_2 + O_2$	$2.00 \times 10^{-10} (T/300)^{0.5}$	[7]
70	$O_2(A^1\Delta_g) + O_3 \rightarrow O_2 + O_2 + O$	$5.20 \times 10^{-11} \exp(-2840/T)$	EST
71	$O_2(B^1\Sigma^+_g) + O_3 \rightarrow O_2 + O_2 + O$	2.20×10^{-11}	[13]
72	$O_2(B^1\Sigma^+_g) + O_3 \rightarrow O_2(A^1\Delta_g) + O_3$	2.20×10^{-11}	[13]
73	$O_2(B^1\Sigma^+_g) + O_3 \rightarrow O_2 + O_3$	2.20×10^{-11}	[13]
74	$O_2^+ + O_3^- \rightarrow O_3 + O_2$	2.00×10^{-7}	[9]
75	$O_2^+ + O_3^- \rightarrow O_3 + O + O$	1.00×10^{-7}	[9]
76	$O_2^- + O_3 \rightarrow O_3^- + O_2$	$6.00 \times 10^{-10} \exp(4201/T)$	[7]
77	$O_3 + M \rightarrow O_2 + O + M$	$1.56 \times 10^{-9} \exp(-11490/T)$	EST
78	$O + O_2 + O_3 \rightarrow O_3 + O_3$	1.52×10^{-33}	[12]
79	$O + O_2 + M \rightarrow O_3 + M$	$6.90 \times 10^{-34} (T/300)^{-1.25}$	[14]
80	$O^- + O_2^+ + M \rightarrow O + O_2 + M$	$2.00 \times 10^{-25} (T/300)^{-2.5}$	[9]
81	$O_2 + O_2 \rightarrow O_3 + O$	$1.11 \times 10^{-11} \exp(-24950/T)$	[15]
82	$O_2 + O_2^+ \rightarrow O_2 + O_2^+$	$1.00 \times 10^{-09} (T/300)^{0.5}$	[8]
83	$O_2^- + O_2^+ \rightarrow O_2 + O_2$	2.00×10^{-7}	[8]
84	$O_2^- + O_2^+ \rightarrow O_2 + O + O$	1.00×10^{-7}	[9]
85	$O_2^- + O_2(A^1\Delta_g) \rightarrow e^- + O_2 + O_2$	$2.00 \times 10^{-10} (T/300)^{0.5}$	[7]
86	$O_2^- + O_3 \rightarrow O_3^- + O_2$	$6.00 \times 10^{-10} (T/300)^{0.5}$	[7]
87	$N + N_2(A^3\Sigma_u^+) \rightarrow N_2 + N(^2D)$	4.50×10^{-11}	[16]
88	$N(^2D) + N_2 \rightarrow N_2 + N$	2.40×10^{-14}	[2]
89	$N_2 + N_2(A^3\Sigma_u^+) \rightarrow N_2 + N_2$	1.90×10^{-13}	[8]
90	$N + N + M \rightarrow N_2 + M$	3.90×10^{-33}	[17]
91	$O + NO + N_2 \rightarrow NO_2 + N_2$	$9.90 \times 10^{-32} (T/300)^{-1.6}$	[18]
92	$O + NO_2 \rightarrow NO + O_2$	$6.50 \times 10^{-12} \exp(120/T)$	[18]
93	$O + NO_2 + M \rightarrow NO_3 + M$	$9.00 \times 10^{-32} (T/300)^{-2.0}$	[18]
94	$O + NO_3 \rightarrow O_2 + NO_2$	1.00×10^{-11}	[17]
95	$O(^1D) + N_2 \rightarrow O + N_2$	$1.80 \times 10^{-11} \exp(-107/T)$	[18]
96	$O(^1D) + NO \rightarrow O_2 + N$	8.50×10^{-11}	[10]
97	$O(^1D) + N_2O \rightarrow NO + NO$	6.70×10^{-11}	[10]
98	$O(^1D) + N_2O \rightarrow O_2 + N_2$	4.40×10^{-11}	[19]
99	$O^+ + O^- + M \rightarrow O_2 + M$	$3.00 \times 10^{-6} (T/300)^{-0.5}$	EST
100	$O^- + NO^+ \rightarrow NO + O$	$3.00 \times 10^{-6} (T/300)^{-0.5}$	EST

101	$O^- + NO_2^+ \rightarrow NO_2 + O$	$3.00 \times 10^{-6} (T/300)^{-0.5}$	[20]
102	$O_2 + N \rightarrow NO + O$	$4.40 \times 10^{-12} \exp(-3220/T)$	[18]
103	$O_2 + N(^2D) \rightarrow NO + O$	6.80×10^{-12}	[17]
104	$O_2 + N^+ \rightarrow NO^+ + O$	2.60×10^{-10}	[17]
105	$O_2 + N^+ \rightarrow O_2^+ + N$	3.10×10^{-10}	[17]
106	$O_2 + N^+ \rightarrow O^+ + NO$	3.60×10^{-11}	[17]
107	$O_2 + N_2(A^3\Sigma_u^+) \rightarrow O + O + N_2$	1.50×10^{-12}	[21]
108	$O_2 + N_2(A^3\Sigma_u^+) \rightarrow O_2 + N_2$	2.80×10^{-11}	[21]
109	$O_2 + N_2^+ \rightarrow O_2^+ + N_2$	5.10×10^{-11}	[17]
110	$O_2(A^1\Delta_g) + N \rightarrow NO + O$	$2.10 \times 10^{-11} \exp(-600/T)$	[13]
111	$O_2(A^1\Delta_g) + N_2 \rightarrow N_2 + O_2$	1.40×10^{-19}	[8]
112	$O_2(A^1\Delta_g) + NO \rightarrow NO + O_2$	2.50×10^{-11}	[3]
113	$O_2(B^1\Sigma_g^+) + N_2 \rightarrow O_2(A^1\Delta_g) + N_2$	$4.90 \times 10^{-15} \exp(-253/T)$	[13]
114	$O_2^+ + N_2 \rightarrow NO^+ + NO$	1.00×10^{-17}	[17]
115	$O_2^+ + N \rightarrow NO^+ + O$	1.20×10^{-10}	[17]
116	$O_2^+ + NO \rightarrow NO^+ + O_2$	4.40×10^{-10}	[17]
117	$O_2^+ + NO_2 \rightarrow NO_2^+ + O_2$	6.60×10^{-10}	[17]
118	$O_2^+ + NO_2 \rightarrow NO^+ + O_3$	1.00×10^{-11}	[17]
119	$O_2^+ + NO_2^- \rightarrow O_2 + NO_2$	$2.00 \times 10^{-6} (T/300)^{-0.5}$	[17]
120	$O_2^+ + NO_3^- \rightarrow O_2 + NO_3$	$2.00 \times 10^{-6} (T/300)^{-0.5}$	[20]
121	$O_2^+ + N_2O_5 \rightarrow O_2 + NO_2^+ + NO_3$	8.80×10^{-10}	[20]
122	$O_2^- + NO_2 \rightarrow NO_2^- + O_2$	7.00×10^{-10}	[17]
123	$O_3 + N \rightarrow NO + O_2$	$5.00 \times 10^{-16} \exp(4201/T)$	[17]
124	$O_3 + NO \rightarrow NO_2 + O_2$	$2.00 \times 10^{-12} \exp(-1400/T)$	[10]
125	$O_3 + NO_2 \rightarrow NO_3 + O_2$	$1.20 \times 10^{-13} \exp(-2450/T)$	[18]
126	$N + NO \rightarrow N_2 + O$	3.10×10^{-11}	[17]
127	$N + NO_2 \rightarrow N_2O + O$	2.40×10^{-12}	[17]
128	$N + NO_2 \rightarrow NO + NO$	6.00×10^{-13}	[17]
129	$N_2(A^3\Sigma_u^+) + N_2O \rightarrow N_2 + N_2 + O$	1.40×10^{-11}	[21]
130	$O + N + M \rightarrow NO + M$	$5.46 \times 10^{-33} \exp(155/T)$	[22]
131	$O + O_2 + NO \rightarrow NO_2 + O_2$	$8.48 \times 10^{-32} (T/300)^{-1.8}$	[18]
132	$NO + NO_3 \rightarrow NO_2 + NO_2$	$1.60 \times 10^{-11} \exp(150/T)$	[18]
133	$NO^+ + NO_2^- \rightarrow NO + NO_2$	$3.00 \times 10^{-6} (T/300)^{0.5}$	[17]
134	$NO^+ + NO_3^- \rightarrow NO + NO_3$	$3.00 \times 10^{-6} (T/300)^{0.5}$	[17]
135	$NO_2 + NO_2 + N_2 \rightarrow N_2O_4 + N_2$	$1.40 \times 10^{-23} (T/300)^{-3.8}$	[23]
136	$NO_2 + NO_3 + M \rightarrow N_2O_5 + M$	$2.70 \times 10^{-30} (T/300)^{-3.4}$	[18]
137	$e^- + H \rightarrow H(^1) + e^-$	$\sigma(E)$	EST
138	$e^- + H \rightarrow H^+ + e + e$	$\sigma(E)$	[24]
139	$e^- + H^+ \rightarrow H$	$\sigma(E)$	EST
140	$e^- + H_2 \rightarrow H_2(^1\Delta_g^+) + e^-$	$\sigma(E)$	[25]
141	$e^- + H_2 \rightarrow H_2(V) + e^-$	$\sigma(E)$	[25]

142	$e^- + H_2 \rightarrow H_2(R) + e^-$	$\sigma(E)$	[25]
143	$e^- + H_2 \rightarrow H + H + e^-$	$\sigma(E)$	[25]
144	$e^- + H_2 \rightarrow H(^1) + H + e^-$	$\sigma(E)$	[25]
145	$e^- + H_2 \rightarrow H_2^+ + e + e^-$	$\sigma(E)$	[25]
146	$e^- + H_2O \rightarrow H^- + OH$	$\sigma(E)$	[26]
147	$e^- + H_2O \rightarrow OH + H + e^-$	$\sigma(E)$	[26]
148	$e^- + H_2O \rightarrow O + H + H + e^-$	$\sigma(E)$	[26]
149	$e^- + H_2O \rightarrow H_2O^+ + e^- + e^-$	$\sigma(E)$	[27]
150	$e^- + NH \rightarrow NH^+ + e^- + e^-$	$\sigma(E)$	[28]
151	$e^- + NH_2 \rightarrow NH + H + e^-$	$\sigma(E)$	[28]
152	$e^- + NH_2 \rightarrow NH_2^+ + e^- + e^-$	$\sigma(E)$	[28]
153	$e^- + NH_2 \rightarrow NH^+ + H + e^- + e^-$	$\sigma(E)$	[28]
154	$e^- + NH_3 \rightarrow H^- + NH_2$	$\sigma(E)$	[28]
155	$e^- + NH_3 \rightarrow NH_2 + H + e^-$	$\sigma(E)$	[28]
156	$e^- + NH_3 \rightarrow NH_2^+ + H + e^- + e^-$	$\sigma(E)$	[28]
157	$e^- + NH^+ \rightarrow N + H$	$\sigma(E)$	EST
158	$e^- + NH_2^+ \rightarrow NH + H$	$\sigma(E)$	EST
159	$e^- + NH_3^+ \rightarrow NH_2 + H$	$\sigma(E)$	EST
160	$H + O_2 \rightarrow OH + O$	$4.75 \times 10^{-5} (T/300)^{-0.9} \exp(-8750/T)$	[17]
161	$H + O_3 \rightarrow OH + O_2$	$1.40 \times 10^{-10} \exp(-480/T)$	[10]
162	$H + OH \rightarrow O + H_2$	$5.21 \times 10^{-11} (T/300)^{0.67} \exp(-518/T)$	[29]
163	$H + HO_2 \rightarrow OH + OH$	$2.80 \times 10^{-10} \exp(-440/T)$	[17]
164	$H + HO_2 \rightarrow H_2O + O$	9.40×10^{-13}	[17]
165	$H + HO_2 \rightarrow H_2 + O_2$	$1.10 \times 10^{-10} \exp(-1070/T)$	[10]
166	$H + H_2O_2 \rightarrow H_2O + OH$	$4.00 \times 10^{-11} \exp(-2000/T)$	[30]
167	$H + H_2O_2 \rightarrow HO_2 + H_2$	5.15×10^{-15}	[31]
168	$H + OH + M \rightarrow H_2O + M$	4.30×10^{-31}	[17]
169	$H + NO + M \rightarrow HNO + M$	3.40×10^{-32}	[17]
170	$H_2 + O \rightarrow OH + H$	$1.60 \times 10^{-11} \exp(-4570/T)$	[17]
171	$H_2 + O(^1D) \rightarrow OH + H$	1.10×10^{-10}	[17]
172	$H_2 + OH \rightarrow H_2O + H$	$7.70 \times 10^{-12} \exp(-2100/T)$	[2]
173	$H_2^+ + H^- \rightarrow H + H_2$	3.00×10^{-6}	[32]
174	$H_2^+ + O^- \rightarrow O + H_2$	$3.00 \times 10^{-6} (T/300)^{-0.5}$	[32]
175	$H^- + O^+ + M \rightarrow OH + M$	$3.00 \times 10^{-6} (T/300)^{-0.5}$	EST
176	$H^- + N_2^+ \rightarrow H + N_2$	$3.00 \times 10^{-6} (T/300)^{-0.5}$	EST
177	$H^- + H_2O^+ \rightarrow H + H_2O$	$3.00 \times 10^{-6} (T/300)^{-0.5}$	[32]

178	$\text{H}^- + \text{H}_3\text{O}^+ \rightarrow \text{H}_2 + \text{H}_2\text{O}$	$3.00 \times 10^{-6} (\text{T}/300)^{-0.5}$	EST
179	$\text{H}^- + \text{NH}_3^+ \rightarrow \text{H} + \text{NH}_3$	$3.00 \times 10^{-6} (\text{T}/300)^{-0.5}$	EST
180	$\text{H}^- + \text{NH}_4^+ \rightarrow \text{H}_2 + \text{NH}_3$	$3.00 \times 10^{-6} (\text{T}/300)^{-0.5}$	EST
181	$\text{H}^- + \text{NO}^+ + \text{M} \rightarrow \text{HNO} + \text{M}$	$1.20 \times 10^{-25} (\text{T}/300)^{-0.5}$	EST
182	$\text{H}^- + \text{NO}_2^+ + \text{M} \rightarrow \text{HNO}_2 + \text{M}$	$1.20 \times 10^{-25} (\text{T}/300)^{-0.5}$	EST
183	$\text{H}^- + \text{N}^+ + \text{M} \rightarrow \text{NH} + \text{M}$	$1.20 \times 10^{-25} (\text{T}/300)^{-0.5}$	EST
184	$\text{H}^- + \text{N}_2^+ \rightarrow \text{H} + \text{N} + \text{N}$	$3.00 \times 10^{-6} (\text{T}/300)^{-0.5}$	EST
185	$\text{OH} + \text{HO}_2 \rightarrow \text{O}_2 + \text{H}_2\text{O}$	8.47×10^{-12}	[19]
186	$\text{OH} + \text{OH} \rightarrow \text{O} + \text{H}_2\text{O}$	$1.03 \times 10^{-12} (\text{T}/300)^{1.40} \exp(200/\text{T})$	[2]
187	$\text{OH} + \text{O} \rightarrow \text{H} + \text{O}_2$	$2.30 \times 10^{-11} \exp(110/\text{T})$	[2]
188	$\text{OH} + \text{O}_3 \rightarrow \text{HO}_2 + \text{O}_2$	$1.91 \times 10^{-12} \exp(-1000/\text{T})$	[17]
189	$\text{OH} + \text{N} \rightarrow \text{NO} + \text{H}$	$3.80 \times 10^{-11} \exp(85/\text{T})$	[18]
190	$\text{OH} + \text{M} \rightarrow \text{O} + \text{H} + \text{M}$	$4.00 \times 10^{-9} \exp(-50000/\text{T})$	[18]
191	$\text{OH} + \text{H}_2\text{O}_2 \rightarrow \text{H}_2\text{O} + \text{HO}_2$	$2.90 \times 10^{-12} \exp(-160/\text{T})$	[17]
192	$\text{OH} + \text{NH}_3 \rightarrow \text{NH}_2 + \text{H}_2\text{O}$	$3.50 \times 10^{-12} \exp(-925/\text{T})$	[17]
193	$\text{OH} + \text{NO}_3 \rightarrow \text{HO}_2 + \text{NO}_2$	2.60×10^{-11}	[33]
194	$\text{OH} + \text{N}_2\text{O} \rightarrow \text{HNO} + \text{NO}$	3.80×10^{-17}	[17]
195	$\text{OH} + \text{HNO} \rightarrow \text{H}_2\text{O} + \text{NO}$	$9.76 \times 10^{-13} (\text{T}/300)^{1.88} \exp(481/\text{T})$	[10]
196	$\text{OH} + \text{HNO}_2 \rightarrow \text{NO}_2 + \text{H}_2\text{O}$	1.80×10^{-11}	[18]
197	$\text{OH} + \text{HNO}_3 \rightarrow \text{NO}_3 + \text{H}_2\text{O}$	$1.50 \times 10^{-14} \exp(650/\text{T})$	[17]
198	$\text{OH} + \text{O} + \text{M} \rightarrow \text{HO}_2 + \text{M}$	2.76×10^{-31}	[10]
199	$\text{OH} + \text{NO} + \text{M} \rightarrow \text{HNO}_2 + \text{M}$	$7.40 \times 10^{-31} (\text{T}/300)^{-2.4}$	[18]
200	$\text{OH} + \text{OH} + \text{O}_2 \rightarrow \text{H}_2\text{O}_2 + \text{O}_2$	$6.90 \times 10^{-31} (\text{T}/300)^{-0.8}$	[18]
201	$\text{OH} + \text{NO}_2 + \text{O}_2 \rightarrow \text{HNO}_3 + \text{O}_2$	$2.60 \times 10^{-30} (\text{T}/300)^{-2.9}$	[34]
202	$\text{H}_2\text{O} + \text{O}(^1\text{D}) \rightarrow \text{O} + \text{H}_2\text{O}$	1.20×10^{-11}	[17]
203	$\text{H}_2\text{O} + \text{O}(^1\text{D}) \rightarrow \text{OH} + \text{OH}$	2.20×10^{-10}	[17]
204	$\text{H}_2\text{O} + \text{N}_2^+ \rightarrow \text{H}_2\text{O}^+ + \text{N}_2$	2.00×10^{-9}	EST
205	$\text{H}_2\text{O} + \text{H}_2\text{O}^+ \rightarrow \text{H}_3\text{O}^+ + \text{OH}$	1.70×10^{-9}	[17]
206	$\text{H}_2\text{O} + \text{N}_2\text{O}_5 \rightarrow \text{HNO}_3 + \text{HNO}_3$	5.00×10^{-21}	[17]
207	$\text{H}_2\text{O} + \text{O}(^1\text{D}) \rightarrow \text{H}_2 + \text{O}_2$	2.30×10^{-12}	[17]
208	$\text{H}_2\text{O}^+ + \text{O}_2 \rightarrow \text{O}_2^+ + \text{H}_2\text{O}$	4.30×10^{-10}	[17]
209	$\text{H}_3\text{O}^+ + \text{O}^- \rightarrow \text{OH} + \text{H}_2\text{O}$	$3.00 \times 10^{-6} (\text{T}/300)^{-0.5}$	EST
210	$\text{HO}_2 + \text{HO}_2 \rightarrow \text{H}_2\text{O}_2 + \text{O}_2$	$3.63 \times 10^{-12} \exp(200/\text{T})$	[33]
211	$\text{HO}_2 + \text{O} \rightarrow \text{OH} + \text{O}_2$	$2.90 \times 10^{-11} \exp(200/\text{T})$	[18]
212	$\text{HO}_2 + \text{O}_3 \rightarrow \text{OH} + \text{O}_2 + \text{O}_2$	$1.40 \times 10^{-14} \exp(-600/\text{T})$	[17]
213	$\text{HO}_2 + \text{NO} \rightarrow \text{HNO} + \text{O}_2$	$9.00 \times 10^{-19} \exp(2819/\text{T})$	[10]
214	$\text{HO}_2 + \text{NO}_3 \rightarrow \text{OH} + \text{NO}_2 + \text{O}_2$	3.60×10^{-11}	[33]
215	$\text{HO}_2 + \text{NO}_3 \rightarrow \text{HNO}_3 + \text{O}_2$	9.20×10^{-12}	[33]
216	$\text{HO}_2 + \text{NO} + \text{M} \rightarrow \text{HNO}_3 + \text{M}$	5.60×10^{-33}	[10]
217	$\text{NH} + \text{O}_2 \rightarrow \text{HNO} + \text{O}$	2.30×10^{-13}	[17]
218	$\text{NH} + \text{NO} \rightarrow \text{N}_2 + \text{OH}$	4.50×10^{-11}	[10]

219	$\text{NH}_2 + \text{H}_2 \rightarrow \text{NH}_3 + \text{H}$	$5.98 \times 10^{-12} \exp(-2290/T)$	[30]
220	$\text{NH}_2 + \text{O} \rightarrow \text{H}_2 + \text{NO}$	8.30×10^{-12}	[10]
221	$\text{NH}_2 + \text{O} \rightarrow \text{NH} + \text{OH}$	1.20×10^{-11}	[18]
222	$\text{NH}_2 + \text{O} \rightarrow \text{HNO} + \text{H}$	7.60×10^{-11}	[34]
223	$\text{NH}_2 + \text{NO} \rightarrow \text{N}_2 + \text{H}_2\text{O}$	$1.60 \times 10^{-11} (T/300)^{-1.5}$	[18]
224	$\text{NH}_2 + \text{NO}_2 \rightarrow \text{N}_2\text{O} + \text{H}_2\text{O}$	1.90×10^{-11}	[17]
225	$\text{NH}_3 + \text{O}(^1\text{D}) \rightarrow \text{NH}_2 + \text{OH}$	2.50×10^{-10}	[17]
226	$\text{NH}_3 + \text{N}(^2\text{D}) \rightarrow \text{NH} + \text{NH}_2$	5.00×10^{-11}	[17]
227	$\text{NH}_3 + \text{O}_2^+ \rightarrow \text{NH}_3^+ + \text{O}_2$	$1.60 \times 10^{-9} (T/300)^{-2.2}$	[17]
228	$\text{NH}_3 + \text{H}_3\text{O}^+ \rightarrow \text{NH}_4^+ + \text{H}_2\text{O}$	2.50×10^{-9}	[17]
229	$\text{NH}_3^+ + \text{O}^- \rightarrow \text{O} + \text{NH}_3$	$3.00 \times 10^{-6} (T/300)^{-0.5}$	EST
230	$\text{NH}_4^+ + \text{O}^- \rightarrow \text{OH} + \text{NH}_3$	$3.00 \times 10^{-6} (T/300)^{-0.5}$	EST
231	$\text{H}_2\text{O}_2 + \text{O} \rightarrow \text{OH} + \text{HO}_2$	$1.40 \times 10^{-12} \exp(-2000/T)$	[2]
232	$\text{HNO} + \text{O} \rightarrow \text{OH} + \text{NO}$	1.82×10^{-11}	[10]
233	$\text{HNO} + \text{O}_2 \rightarrow \text{NO} + \text{HO}_2$	$5.25 \times 10^{-12} \exp(-1510/T)$	[10]
234	$\text{HNO}_3 + \text{NO}_2^- \rightarrow \text{NO}_3^- + \text{HNO}_2$	1.60×10^{-9}	[17]
235	$e^- + \text{O}^+ + \text{M} \rightarrow \text{O} + \text{M}$	1.00×10^{-26}	[3]
236	$e^- + \text{NO}^+ \rightarrow \text{N} + \text{O}$	$4.00 \times 10^{-7} (300/\text{Te})^{1.5}$	[13]
237	$e^- + \text{NO}^+ \rightarrow \text{N}(^2\text{D}) + \text{O}$	$3.00 \times 10^{-7} (300/\text{Te})^{1.0}$	[13]
238	$e^- + e^- + \text{NO}^+ \rightarrow e^- + \text{NO}$	$1.00 \times 10^{-29} (300/\text{Te})^{1.5}$	[13]
239	$e^- + \text{NO}^+ + \text{M} \rightarrow \text{NO} + \text{M}$	$6.00 \times 10^{-27} (300/\text{Te})^{1.5}$	[13]
240	$e^- + \text{OH} \rightarrow e^- + \text{O} + \text{H}$	$2.08 \times 10^{-7} (\text{Te})^{-0.76} \exp(-6.9/\text{Te})$	[35]

^a Rate coefficients have units of $\text{cm}^3 \text{s}^{-1}$ unless stated otherwise. Te is the electron temperature in eV, T is the gas temperature in K and activation energies have equivalent units of K. (EST: Means estimated values)

The reaction set for ethylene destruction in dry or humid air is based on the chemistry set of C. De Bie^[36]. In the following table, only the modifications with respect to that chemistry set are shown.

Table A1- 2: Reactions for ethylene destruction in dry or humid air: Modifications to the reaction set adopted from C. De Bie^[36]

#	Reaction	Rate coefficient	Ref.
241	$\text{C}_2\text{H}_4 + \text{NO}_3 \rightarrow \text{HNO}_3 + \text{C}_2\text{H}_3$	2.10×10^{-16}	[18]
242	$\text{C}_2\text{H}_4 + \text{N} \rightarrow \text{HCN} + \text{CH}_3$	2.46×10^{-12}	[37]
243	$\text{C}_2\text{H}_4 + \text{N}_2(\text{A}^3\Sigma_u^+) \rightarrow \text{C}_2\text{H}_2 + \text{H}_2 + \text{N}_2$	5.27×10^{-11}	EST/ [38]
244	$\text{C}_2\text{H}_4 + \text{N}_2(\text{A}^3\Sigma_u^+) \rightarrow \text{C}_2\text{H}_3 + \text{H} + \text{N}_2$	4.43×10^{-11}	EST/ [38]
245	$\text{C}_2\text{H}_3 + \text{NO} \rightarrow \text{HCN} + \text{CH}_2\text{O}$	8.78×10^{-12}	[39]

246	$C_2H_2 + N_2(A^3\Sigma_u^+) \rightarrow C_2 + H_2 + N_2$	7.00×10^{-11}	EST/ [40]
247	$C_2H_2 + N_2(A^3\Sigma_u^+) \rightarrow C_2H + H + N_2$	7.00×10^{-11}	EST/ [40]
248	$CH_4 + NO_3 \rightarrow CH_3 + HNO_3$	1.00×10^{-18}	[19]
249	$CH + NO \rightarrow CO + NH$	2.51×10^{-10}	[41]
250	$CH + NO \rightarrow HCN + O$	1.33×10^{-11}	[42]
251	$CH + NO \rightarrow CN + OH$	1.40×10^{-10}	[41]
252	$CH_3O + NO \rightarrow CH_2O + HNO$	1.18×10^{-8} $(T/300)^{-0.7}$	[43]
253	$CH_3O_2 + NO \rightarrow NO_2 + CH_3O$	$2.80 \times 10^{-12} \exp$ $(285/T)$	[43]

^a Rate coefficients have units of $cm^3 s^{-1}$ unless stated otherwise. Te is the electron temperature in eV, T is the gas temperature in K and activation energies have equivalent units of K. (EST: Means estimated values)

- [1] A. V Phelps, *Tabulations of Collision Cross Sections and Calculated Transport and Reaction Coefficients for Electron Collisions with O₂ Technical Report*, **1985**.
- [2] R. Atkinson, D. L. Baulch, R. A. Cox, R. F. Hampson, J. A. Kerr, M. J. Rossi, J. Troe, *J. Phys. Chem. Ref. Data* **1997**, *26*, 1329–1499.
- [3] A. Bogaerts, *Spectrochim. Acta Part B At. Spectrosc.* **2009**, *64*, 1266–1279.
- [4] S. Matejcek, A. Kiendler, P. Cicman, J. Skalny, P. Stampfli, E. Illenberger, Y. Chu, A. Stamatovic, T. D. Märk, *Plasma Sources Sci. Technol.* **1997**, *6*, 140–146.
- [5] S. Geltman, *J. Quant. Spectrosc. Radiat. Transf.* **1973**, *13*, 601–613.
- [6] C.-M. Chan, *Polymer Surface Modification and Characterization*, Hanser Gardner Publications, **1993**.
- [7] M. Hamden, *Rapid Commun. Mass Spectrom.* **1989**, *3*, 244.
- [8] J. Herron, D. Green, *Plasma Chem. Plasma Process.* **2001**, *21*.
- [9] A. Kanka, *Vacuum* **2002**, *67*, 415–420.
- [10] Y. Mirokin, G. Mallard, *The NIST Chemical Kinetics Database*, **1998**.
- [11] G. Senn, J. Skalny, A. Stamatovic, N. Mason, P. Scheier, T. Märk, *Phys. Rev. Lett.* **1999**, *82*, 5028–5031.
- [12] S. Hadj-Ziane, B. Held, P. Pignolet, R. Peyrous, C. Coste, *J. Phys. D. Appl. Phys.* **1992**, *25*, 677–685.
- [13] I. A. Kossyi, A. Yu Kostinsky, A. A. Matveyev, P. V. Silakov, *Plasma Sources Sci. Technol.* **1992**, *1*, 207–220.
- [14] K. Tachibana, *Phys. Rev. A* **1986**, *34*, 1007–1015.
- [15] S. W. Benson, A. E. Axworthy, *J. Chem. Phys.* **1957**, *26*, 1718–1726.
- [16] J. T. Herron, *J. Phys. Chem. Ref. Data* **1999**, *28*, 1453.
- [17] H. D. O. Person J.C., *Radiat. Phys. Chem.* **1988**, *31*, 1–8.
- [18] W. Tsang, R. F. Hampson, *J. Phys. Chem. Ref. Data* **1986**, *15*, 1087–1279.
- [19] R. Atkinson, D. L. Baulch, R. A. Cox, J. N. Crowley, R. F. Hampson, R. G. Hynes, M. E. Jenkin, M. J. Rossi, J. Troe, *Atmos. Chem. Phys.* **2004**, *4*, 1461–1738.
- [20] F. Poncin-Epaillard, B. Chevet, J.-C. Brosse, *J. Adhes. Sci. Technol.* **1994**, *8*, 455–468.

- [21] S. Mukkavilli, C. K. Lee, K. Varghese, L. L. Tavlarides, *IEEE Trans. Plasma Sci.* **1988**, *16*, 652–660.
- [22] D. Baulch, C. Cobos, R. Cox, P. Frank, G. Hayman, T. Just, J. Kerr, T. Murrells, M. Pilling, J. Troe, et al., *J. Phys. Chem. Ref. Data* **1994**, *23*, 847–1033.
- [23] S. Razumovskii, *Eur. Polym. J.* **1971**, *7*, 275–285.
- [24] H. Tawara, T. Kato, *At. Data Nucl. Data Tables* **1987**, *36*, 167–353.
- [25] M. Hayashi, *Le J. Phys. Colloq.* **1979**, *40*, C7–45–C7–46.
- [26] M. Hayashi, in *Springer-Verlag* (Ed.: A.C. and S.T. L.C. Pitchford, B.V. McKoy), New-York, **1987**, p. 1.
- [27] M. Hayashi, in *Meet. 4th Int. Swarm Semin. Inelast. Electron-Molecular Collis. Symp.*, **1985**, p. 345.
- [28] M. Hayashi, in *None Equilib. Process. Partial. Ioniz. Gases* (Ed.: M. Capitelli AND J. Norman Bardsley), Plenum, New-York, **n.d.**, pp. 333–340.
- [29] J. L. Pack, R. E. Voshall, A. V. Phelps, L. E. Kline, *J. Appl. Phys.* **1992**, *71*, 5363–5371.
- [30] D. J. Carlsson, D. M. Wiles, *Polym. Rev.* **1976**, *14*, 65–106.
- [31] D. L. Baulch, C. J. Cobos, R. A. Cox, C. Esser, P. Frank, T. Just, J. A. Kerr, M. J. Pilling, J. Troe, R. W. Walker, et al., *J. Phys. Chem. Ref. Data* **1992**, *21*, 411–734.
- [32] R. E. Olson, *J. Chem. Phys.* **1970**, *53*, 3391–3397.
- [33] A. Mellouki, G. Le Bras, G. Poulet, *J. Phys. Chem.* **1988**, *92*, 2229–2234.
- [34] J.-C. Loison, S. Sanglar, E. Villenave, *Rev. Sci. Instrum.* **2005**, *76*, 053105.
- [35] D. X. Liu, P. Bruggeman, F. Iza, M. Z. Rong, M. G. Kong, *Plasma Sources Sci. Technol.* **2010**, *19*, 025018.
- [36] C. De Bie, B. Verheyde, T. Martens, J. van Dijk, S. Paulussen, A. Bogaerts, *Plasma Process. Polym.* **2011**, *8*, 1033–1058.
- [37] R. Atkinson, S. M. Aschmann, J. N. Pitts, *J. Phys. Chem.* **1988**, *92*, 3454–3457.
- [38] H. Umemoto, *J. Chem. Phys.* **2007**, *127*, 014304.
- [39] F. Striebel, L. E. Jusinski, A. Fahr, J. B. Halpern, S. J. Klippenstein, C. A. Taatjes, *Phys. Chem. Chem. Phys.* **2004**, *6*, 2216–2223.
- [40] I. Nadler, S. Rosenwaks, *J. Chem. Phys.* **1985**, *83*, 3932–3940.
- [41] H. Geiger, P. Wiesen, K. H. Becker, *Phys. Chem. Chem. Phys.* **1999**, *1*, 5601–5606.
- [42] A. Bergeat, T. Calvo, N. Daugey, J.-C. Loison, G. Dorthe, *J. Phys. Chem. A* **1998**, *102*, 8124–8130.
- [43] R. Atkinson, D. L. Baulch, R. A. Cox, R. F. Hampson, J. A. Kerr, M. J. Rossi, J. Troe, *J. Phys. Chem. Ref. Data* **1999**, *28*, 191–393.

Table A1- 3: Reactions between the metastable N₂ molecules and hydrocarbon species, with their corresponding rate coefficients adopted from literature. The fourth column indicates the standard deviations (in %) between the values adopted in this work, and other rate coefficients found in literature. We evaluated the different rate coefficients by comparison with our experimental results and we used the ones which resulted in the best match.

#	Reaction	Rate coefficient (cm ³ s ⁻¹)	Ref.	Standard Deviation (%)
1	CO ₂ + N ₂ (A ³ Σ _u ⁺) → O + CO + N ₂	1.54 × 10 ⁻¹²	[1,2]	138
2	C ₂ H ₄ + N ₂ (A ³ Σ _u ⁺) → C ₂ H ₂ + H ₂ + N ₂	5.50 × 10 ⁻¹¹	[1,3,4] J	53
3	C ₂ H ₄ + N ₂ (A ³ Σ _u ⁺) → C ₂ H ₃ + H + N ₂	5.50 × 10 ⁻¹¹	[1,3,4] J	56
4	C ₂ H ₄ + N ₂ (a ¹ Σ _u ⁻) → C ₂ H ₂ + H ₂ + N ₂	2.00 × 10 ⁻¹⁰	[3]	47
5	C ₂ H ₄ + N ₂ (a ¹ Σ _u ⁻) → C ₂ H ₃ + H + N ₂	2.00 × 10 ⁻¹⁰	[3]	47
6	C ₂ H ₂ + N ₂ (A ³ Σ _u ⁺) → C ₂ H + H + N ₂	2.00 × 10 ⁻¹⁰	[4,5]	68
7	C ₂ H ₂ + N ₂ (a ¹ Σ _u ⁻) → C ₂ H + H + N ₂	3.00 × 10 ⁻¹⁰	[5]	-
8	HCN + N ₂ (A ³ Σ _u ⁺) → H + CN + N ₂	2.00 × 10 ⁻¹⁰	[1]	-
9	CH ₂ CO + N ₂ (A ³ Σ _u ⁺) → CH ₂ + CO + N ₂	6.50 × 10 ⁻¹⁴	[1]	-
10	CH ₃ CHO + N ₂ (A ³ Σ _u ⁺) → CH ₃ + CHO + N ₂	1.60 × 10 ⁻¹¹	[1]	-
11	CH ₃ CHO + N ₂ (A ³ Σ _u ⁺) → CH ₄ + CO + N ₂	1.60 × 10 ⁻¹¹	[1]	-
12	CH ₃ CHO + N ₂ (A ³ Σ _u ⁺) → CH ₂ CO + H ₂ + N ₂	1.60 × 10 ⁻¹¹	[1]	-
13	CH ₃ CHO + N ₂ (A ³ Σ _u ⁺) → CH ₃ CO + H + N ₂	2.00 × 10 ⁻¹²	[1]	-

- [1] O. Koeta, N. Blin-Simiand, W. Faider, S. Pasquiers, a. Bary, F. Jorand, *Plasma Chem. Plasma Process.* **2012**, *32*, 991–1023.
- [2] J. T. Herron, *J. Phys. Chem. Ref. Data* **1999**, *28*, 1453.
- [3] L. Magne, S. Pasquiers, K. Gadonna, P. Jeanney, N. Blin-Simiand, F. Jorand, C. Postel, *J. Phys. D. Appl. Phys.* **2009**, *42*, 165203.
- [4] H. Umemoto, *J. Chem. Phys.* **2007**, *127*, 014304.
- [5] N. Moreau, S. Pasquiers, N. Blin-Simiand, L. Magne, F. Jorand, C. Postel, J.-R. Vacher, *J. Phys. D. Appl. Phys.* **2010**, *43*, 285201.

Appendix II

Reactions used in Chapters 6 and 7 to describe CO₂ splitting, with their corresponding rate coefficients or cross sections, and the references where these data were adopted from.

Table A2 - 1: Overview of the electron impact reactions included in the model.^a

No.	Reaction	Reaction type	Rate coeff.	Ref.
(1)	$e^- + \text{CO}_2 \rightarrow e^- + \text{CO}_2$	Momentum transfer	$f(\sigma)$	[1]
(2)	$e^- + \text{CO}_2 \rightarrow e^- + e^- + \text{CO}_2^+$	Ionisation	$f(\sigma)$	[1,2]
(3)	$e^- + \text{CO}_2 \rightarrow e^- + e^- + \text{CO}^+ + \text{O}$	Dissociative ionisation	$f(\sigma)$	[1,2]
(4)	$e^- + \text{CO}_2 \rightarrow e^- + e^- + \text{C}^+ + \text{O}_2$	Dissociative ionisation	$f(\sigma)$	[1,2]
(5)	$e^- + \text{CO}_2 \rightarrow e^- + e^- + \text{O}^+ + \text{CO}$	Dissociative ionisation	$f(\sigma)$	[1,2]
(6)	$e^- + \text{CO}_2 \rightarrow e^- + e^- + \text{O}_2^+ + \text{C}$	Dissociative ionisation	$f(\sigma)$	[1,2]
(7)	$e^- + \text{CO}_2 \rightarrow \text{O}^- + \text{CO}$	Electron attachment	$f(\sigma)$	[1]
(8)	$e^- + \text{CO}_2 \rightarrow e^- + \text{CO} + \text{O}$	Dissociation	$f(\sigma)$	[1]
(9)	$e^- + \text{CO}_2 \rightarrow e^- + \text{CO}_2 \text{ v1}$	Vibrational excitation	$f(\sigma)$	[1]
(10)	$e^- + \text{CO}_2 \rightarrow e^- + \text{CO}_2 \text{ v2}$	Vibrational excitation	$f(\sigma)$	[1]
(11)	$e^- + \text{CO}_2 \rightarrow e^- + \text{CO}_2 \text{ v3}$	Vibrational excitation	$f(\sigma)$	[1]
(12)	$e^- + \text{CO}_2 \rightarrow e^- + \text{CO}_2 \text{ v4}$	Vibrational excitation	$f(\sigma)$	[1]
(13)	$e^- + \text{CO}_2 \rightarrow e^- + \text{CO}_2 \text{ e1}$	Electronic excitation	$f(\sigma)$	[1]
(14)	$e^- + \text{CO}_2 \rightarrow e^- + \text{CO}_2 \text{ e2}$	Electronic excitation	$f(\sigma)$	[1]
(15)	$e^- + \text{CO} \rightarrow e^- + \text{CO}$	Momentum transfer	$f(\sigma)$	[3]
(16)	$e^- + \text{CO} \rightarrow e^- + e^- + \text{CO}^+$	Ionisation	$f(\sigma)$	[4]
(17)	$e^- + \text{CO} \rightarrow e^- + e^- + \text{C}^+ + \text{O}$	Dissociative ionisation	$f(\sigma)$	[4]

(18)	$e^- + CO \rightarrow e^- + e^- + C + O^+$	Dissociative ionisation	$f(\sigma)$	[4]
(19)	$e^- + CO \rightarrow O^- + C$	Electron attachment	$f(\sigma)$	[4]
(20)	$e^- + CO \rightarrow e^- + C + O$	Dissociation	$f(\sigma)$	[4]
(21)	$e^- + CO \rightarrow e^- + COv1$	Vibrational excitation	$f(\sigma)$	[4]
(22)	$e^- + CO \rightarrow e^- + COe1$	Electronic excitation	$f(\sigma)$	[4]
(23)	$e^- + CO \rightarrow e^- + COe2$	Electronic excitation	$f(\sigma)$	[4]
(24)	$e^- + CO \rightarrow e^- + COe3$	Electronic excitation	$f(\sigma)$	[4]
(25)	$e^- + CO \rightarrow e^- + COe4$	Electronic excitation	$f(\sigma)$	[4]
(26)	$e^- + C \rightarrow e^- + C$	Momentum transfer	$f(\sigma)$	[5]
(27)	$e^- + C \rightarrow e^- + e^- + C^+$	Dissociative ionisation	$f(\sigma)$	[5]
(28)	$e^- + C_2 \rightarrow e^- + C_2$	Momentum transfer	$f(\sigma)$	[6]
(29)	$e^- + C_2 \rightarrow e^- + C + C$	Dissociation	$f(\sigma)$	[6]
(30)	$e^- + C_2 \rightarrow e^- + e^- + C_2^+$	Ionisation	$f(\sigma)$	[6]
31)	$e^- + O_2 \rightarrow e^- + O_2$	Momentum transfer	$f(\sigma)$	[7]
(32)	$e^- + O_2 \rightarrow e^- + O + O$	Dissociation	$f(\sigma)$	[7]
(33)	$e^- + O_2 \rightarrow e^- + e^- + O_2^+$	Ionisation	$f(\sigma)$	[7]
(34)	$e^- + O_2 \rightarrow e^- + e^- + O + O^+$	Dissociative ionisation	$f(\sigma)$	[8]
(35)	$e^- + O_2 \rightarrow O^- + O$	Dissociation	$f(\sigma)$	[7]
(36)	$e^- + O_2 \rightarrow e^- + O_2 v1$	Vibrational excitation	$f(\sigma)$	[7]
(37)	$e^- + O_2 \rightarrow e^- + O_2 v2$	Vibrational excitation	$f(\sigma)$	[7]
(38)	$e^- + O_2 \rightarrow e^- + O_2 v3$	Vibrational excitation	$f(\sigma)$	[7]
(39)	$e^- + O_2 \rightarrow e^- + O_2 e1$	Electronic excitation	$f(\sigma)$	[7]
(40)	$e^- + O_2 \rightarrow e^- + O_2 e2$	Electronic excitation	$f(\sigma)$	[7]
(41)	$e^- + O_3 \rightarrow e^- + O_3$	Momentum transfer	$f(\sigma)$	[9]
(42)	$e^- + O_3 \rightarrow e^- + O_2 + O$	Dissociation	$f(\sigma)$	[10]
(43)	$e^- + O_3 \rightarrow e^- + e^- + O_2^+ + O$	Dissociative ionisation	$f(\sigma)$	[10]
(44)	$e^- + O_3 \rightarrow e^- + O^+ + O^- + O$	Dissociative	$f(\sigma)$	[10]

(45)	$e^- + O_3 \rightarrow O^- + O_2$	ionisation Electron attachment	$f(\sigma)$	[11]
(46)	$e^- + O_3 \rightarrow O + O_2^-$	Electron attachment	$f(\sigma)$	[11]
(47)	$e^- + O \rightarrow e^- + O$	Momentum transfer	$f(\sigma)$	[12]
(48)	$e^- + O \rightarrow e^- + e^- + O^+$	Ionisation	$f(\sigma)$	[13]

^aNote: The electron impact dissociation reaction of CO₂ (i.e., reaction 8) proceeds through electron impact excitation, followed by dissociation. The electron impact electronic excitation reactions of CO₂ (i.e., reactions 13 and 14), on the other hand, form excited levels which decay back to the ground state, without dissociation. The same is true for the electron impact dissociation and electronic excitations of CO (reaction 20 and reactions 22-25, respectively) and O₂ (reaction 32 and reactions 39-40, respectively).

Table A2 - 2: Overview of the electron-ion recombinations and electron attachment reactions included in the model.

No.	Reaction	Rate coefficient	Reference
(49)	$e^- + CO_2^+ \rightarrow CO + O$	$2 \times 10^{-5} \times Tg^{-1} \times Te(eV)^{-0.5} cm^3 s^{-1}$	[14]
(50)	$e^- + CO_2^+ \rightarrow C + O_2$	$3.939 \times 10^{-7} \times Te(eV)^{-0.4} cm^3 s^{-1}$	[2]
(51)	$e^- + CO_4^+ \rightarrow CO_2 + O_2$	$1.608 \times 10^{-7} \times Te(eV)^{-0.5} cm^3 s^{-1}$	[2]
(52)	$e^- + CO^+ \rightarrow C + O$	$3.683 \times 10^{-8} \times Te(eV)^{-0.55} cm^3 s^{-1}$	[4]
(53)	$e^- + C_2O_2^+ \rightarrow CO + CO$	$4.0 \times 10^{-7} \times Te(eV)^{-0.34} cm^3 s^{-1}$	[15]
(54)	$e^- + C_2O_3^+ \rightarrow CO_2 + CO$	$5.4 \times 10^{-8} \times Te(eV)^{-0.7} cm^3 s^{-1}$	[15]
(55)	$e^- + C_2O_4^+ \rightarrow CO_2 + CO$	$2.0 \times 10^{-5} \times Tg^{-1} \times Te^{-0.5} cm^3 s^{-1}$	[15]
(56)	$e^- + C_2^+ \rightarrow C + C$	$1.79 \times 10^{-8} \times Te(eV)^{-0.5} cm^3 s^{-1}$	[15]
(57)	$e^- + O_2 + M \rightarrow O_2^- + M$	$3 \times 10^{-30} cm^6 s^{-1}$	[16]
(58)	$e^- + O_3 + M \rightarrow O_3^- + M$	$5 \times 10^{-31} \times Te(eV)^{-0.5} cm^6 s^{-1}$	[15]
(59)	$e^- + O + M \rightarrow O^- + M$	$10^{-31} cm^6 s^{-1}$	[16]
(60)	$e^- + O_2^+ + M \rightarrow O_2 + M$	$10^{-26} cm^6 s^{-1}$	[17]
(61)	$e^- + O_2^+ \rightarrow O + O$	$6 \times 10^{-7} \times Tg(K)^{-0.5} \times Te(eV)^{-0.5} cm^3 s^{-1}$	[14]
(62)	$e^- + O^+ + M \rightarrow O + M$	$10^{-26} cm^6 s^{-1}$	[17]
(63)	$e^- + O_4^+ \rightarrow O_2 + O_2$	$2.251 \times 10^{-7} \times Te(eV)^{-0.5} cm^3 s^{-1}$	[18]

Table A2 - 3: Overview of the neutral reactions included in the model.

No.	Reaction	Rate coefficient	Ref.
(64)	$O + CO_2 \rightarrow CO + O_2$	$2.8 \times 10^{-11} \times \exp(-26500/Tg(K)) \text{ cm}^3 \text{ s}^{-1}$	[2]
(65)	$C + CO_2 \rightarrow CO + CO$	$1.0 \times 10^{-15} \text{ cm}^3 \text{ s}^{-1}$	[15]
(66)	$O + CO + M \rightarrow CO_2 + M$	$8.2 \times 10^{-34} \times \exp(-1510/Tg(K))$	[16]
(67)	$O_2 + CO \rightarrow CO_2 + O$	$4.2 \times 10^{-12} \times \exp[-24000/Tg(K)] \text{ cm}^3 \text{ s}^{-1}$	[2]
(68)	$O_3 + CO \rightarrow CO_2 + O_2$	$4.0 \times 10^{-25} \text{ cm}^3 \text{ s}^{-1}$	[2]
(69)	$C + CO + M \rightarrow C_2O + M$	6.5×10^{-32}	[16]
(70)	$O_2 + C \rightarrow CO + O$	$3.0 \times 10^{-11} \text{ cm}^3 \text{ s}^{-1}$	[16]
(71)	$O + C + M \rightarrow CO + M$	$2.136 \times 10^{-29} \times (Tg(K)/300)^{-3.08} \times \exp(2114/Tg(K)) \text{ cm}^6 \text{ s}^{-1}$	[2]
(72)	$O + C_2O \rightarrow CO + CO$	$5.0 \times 10^{-11} \text{ cm}^3 \text{ s}^{-1}$	[15]
(73)	$O_2 + C_2O \rightarrow CO_2 + CO$	$3.3 \times 10^{-13} \text{ cm}^3 \text{ s}^{-1}$	[16]
(74)	$O + O_3 \rightarrow O_2 + O_2$	$3.1e-14 \times Tg(K)^{0.75} \times \exp[-1575/Tg(K)] \text{ cm}^3 \text{ s}^{-1}$	[16]
(75)	$O_3 + M \rightarrow O_2 + O + M$	$4.1175 \times 10^{-10} \times \exp(-11430/Tg(K)) \text{ cm}^3 \text{ s}^{-1}$	[2]
(76)	$O + O_2 + M \rightarrow O_3 + M$	$1.81 \times 10^{-33} \times (Tg(K)/300)^{-1.2}$	[16]
(77)	$O + O + M \rightarrow O_2 + M$	$1.27 \times 10^{-32} \times (Tg(K)/300)^{-1} \times \exp(-170/Tg(K)) \text{ cm}^6 \text{ s}^{-1}$	[19]

Table A2 - 4: Overview of ion-neutral and ion-ion reactions included in the model.

No.	Reaction	Rate coefficient	Ref.
(78)	$O_2^+ + CO_2 + M \rightarrow CO_4^+ + M$	$2.3 \times 10^{-29} \text{ cm}^6 \text{ s}^{-1}$	[2]
(79)	$O^+ + CO_2 \rightarrow O_2^+ + CO$	$9.4 \times 10^{-10} \text{ cm}^3 \text{ s}^{-1}$	[2]
(80)	$O^+ + CO_2 \rightarrow CO_2^+ + O$	$4.5 \times 10^{-10} \text{ cm}^3 \text{ s}^{-1}$	[2]
(81)	$C^+ + CO_2 \rightarrow CO^+ + CO$	$1.1 \times 10^{-9} \text{ cm}^3 \text{ s}^{-1}$	[20]
(82)	$CO^+ + CO_2 \rightarrow CO_2^+ + CO$	$1.0 \times 10^{-9} \text{ cm}^3 \text{ s}^{-1}$	[20]
(83)	$O^- + CO_2 + M \rightarrow CO_3^- + M$	$9.0 \times 10^{-29} \text{ cm}^6 \text{ s}^{-1}$	[14]

(84)	$O_2^- + CO_2 + M \rightarrow CO_4^- + M$	$1.0 \times 10^{-29} \text{ cm}^6 \text{ s}^{-1}$	[14]
(85)	$O_3^- + CO_2 \rightarrow O_2 + CO_3^-$	$5.5 \times 10^{-10} \text{ cm}^3 \text{ s}^{-1}$	[16]
(86)	$O_4^- + CO_2 \rightarrow CO_4^- + O_2$	$4.8 \times 10^{-10} \text{ cm}^3 \text{ s}^{-1}$	[15]
(87)	$CO_2^+ + CO_2 + M \rightarrow C_2O_4^+ + M$	$3.0 \times 10^{-28} \text{ cm}^6 \text{ s}^{-1}$	[15]
(88)	$O^+ + CO \rightarrow CO^+ + O$	$4.9 \times 10^{-12} \times (Tg/300)^{0.5} \times \exp[-4580/Tg] \text{ cm}^3 \text{ s}^{-1}$	[20]
(89)	$O^- + CO \rightarrow CO_2 + e^-$	$5.5 \times 10^{-10} \text{ cm}^3 \text{ s}^{-1}$	[2]
(90)	$CO_3^- + CO \rightarrow 2CO_2 + e^-$	$5 \times 10^{-13} \text{ cm}^3 \text{ s}^{-1}$	[14]
(91)	$C_2O_3^+ + CO \rightarrow CO_2 + C_2O_2^+$	$1.1 \times 10^{-9} \text{ cm}^3 \text{ s}^{-1}$	[15]
(92)	$C_2O_4^+ + CO \rightarrow C_2O_3^+ + CO_2$	$9.0 \times 10^{-10} \text{ cm}^3 \text{ s}^{-1}$	[15]
(93)	$C_2O_3^+ + CO + M \rightarrow C_2O_2^+ + CO_2 + M$	$2.6 \times 10^{-26} \text{ cm}^6 \text{ s}^{-1}$	[15]
(94)	$C_2O_4^+ + CO + M \rightarrow C_2O_3^+ + CO_2 + M$	$4.2 \times 10^{-26} \text{ cm}^6 \text{ s}^{-1}$	[15]
(95)	$C^+ + CO \rightarrow CO^+ + C$	$5.0 \times 10^{-13} \text{ cm}^3 \text{ s}^{-1}$	[2]
(96)	$CO^+ + C \rightarrow CO + C^+$	$1.1 \times 10^{-10} \text{ cm}^3 \text{ s}^{-1}$	[20]
(97)	$O_2^+ + C \rightarrow CO^+ + O$	$5.2 \times 10^{-11} \text{ cm}^3 \text{ s}^{-1}$	[20]
(98)	$O_2^+ + C \rightarrow C^+ + O_2$	$5.2 \times 10^{-11} \text{ cm}^3 \text{ s}^{-1}$	[20]
(99)	$C_2^+ + C \rightarrow C_2 + C^+$	$1.1 \times 10^{-10} \text{ cm}^3 \text{ s}^{-1}$	[20]
(100)	$O + CO_2^+ \rightarrow O_2^+ + CO$	$1.64 \times 10^{-10} \text{ cm}^3 \text{ s}^{-1}$	[20]
(101)	$O + CO_2^+ \rightarrow O^+ + CO_2$	$9.62 \times 10^{-11} \text{ cm}^3 \text{ s}^{-1}$	[20]
(102)	$O_2 + CO_2^+ \rightarrow O_2^+ + CO_2$	$5.3 \times 10^{-11} \text{ cm}^3 \text{ s}^{-1}$	[20]
(103)	$CO_3^- + CO_2^+ \rightarrow 2CO_2 + O$	$5 \times 10^{-7} \text{ cm}^3 \text{ s}^{-1}$	[14]
(104)	$CO_4^- + CO_2^+ \rightarrow 2CO_2 + O_2$	$5 \times 10^{-7} \text{ cm}^3 \text{ s}^{-1}$	[14]
(105)	$O_2^- + CO_2^+ \rightarrow CO + O_2 + O$	$6 \times 10^{-7} \text{ cm}^3 \text{ s}^{-1}$	[14]
(106)	$O + CO^+ \rightarrow CO + O^+$	$1.4 \times 10^{-10} \text{ cm}^3 \text{ s}^{-1}$	[20]
(107)	$O_2 + CO^+ \rightarrow O_2^+ + CO$	$1.2 \times 10^{-10} \text{ cm}^3 \text{ s}^{-1}$	[20]
(108)	$O_2 + C_2O_2^+ \rightarrow CO + CO + O_2^+$	$5.0 \times 10^{-12} \text{ cm}^3 \text{ s}^{-1}$	[15]
(109)	$C_2O_2^+ + M \rightarrow CO^+ + CO + M$	$1.0 \times 10^{-12} \text{ cm}^3 \text{ s}^{-1}$	[15]
(110)	$CO_3^- + C_2O_2^+ \rightarrow CO_2 + 2CO + O$	$5.0 \times 10^{-7} \text{ cm}^3 \text{ s}^{-1}$	[15]

(111)	$\text{CO}_4^- + \text{C}_2\text{O}_2^+ \rightarrow \text{CO}_2 + 2\text{CO} + \text{O}_2$	$5.0 \times 10^{-7} \text{ cm}^3 \text{ s}^{-1}$	[15]
(112)	$\text{O}_2^- + \text{C}_2\text{O}_2^+ \rightarrow 2\text{CO} + \text{O}_2$	$6.0 \times 10^{-7} \text{ cm}^3 \text{ s}^{-1}$	[15]
(113)	$\text{CO}_3^- + \text{C}_2\text{O}_3^+ \rightarrow 2\text{CO}_2 + \text{CO} + \text{O}$	$5.0 \times 10^{-7} \text{ cm}^3 \text{ s}^{-1}$	[15]
(114)	$\text{CO}_4^- + \text{C}_2\text{O}_3^+ \rightarrow 2\text{CO}_2 + \text{CO} + \text{O}_2$	$5.0 \times 10^{-7} \text{ cm}^3 \text{ s}^{-1}$	[15]
(115)	$\text{O}_2^- + \text{C}_2\text{O}_3^+ \rightarrow \text{CO}_2 + \text{CO} + \text{O}_2$	$6.0 \times 10^{-7} \text{ cm}^3 \text{ s}^{-1}$	[15]
(116)	$\text{C}_2\text{O}_4^+ + \text{M} \rightarrow \text{CO}_2^+ + \text{CO}_2 + \text{M}$	$1.0 \times 10^{-14} \text{ cm}^3 \text{ s}^{-1}$	[15]
(117)	$\text{CO}_3^- + \text{C}_2\text{O}_4^+ \rightarrow 3\text{CO}_2 + \text{O}$	$5.0 \times 10^{-7} \text{ cm}^3 \text{ s}^{-1}$	[15]
(118)	$\text{CO}_4^- + \text{C}_2\text{O}_4^+ \rightarrow 3\text{CO}_2 + \text{O}_2$	$5.0 \times 10^{-7} \text{ cm}^3 \text{ s}^{-1}$	[15]
(119)	$\text{O}_2^- + \text{C}_2\text{O}_4^+ \rightarrow 2\text{CO}_2 + \text{O}_2$	$6.0 \times 10^{-7} \text{ cm}^3 \text{ s}^{-1}$	[15]
(120)	$\text{O}_2^+ + \text{CO}_3^- \rightarrow \text{CO}_2 + \text{O}_2 + \text{O}$	$3 \times 10^{-7} \text{ cm}^3 \text{ s}^{-1}$	[14]
(121)	$\text{O} + \text{CO}_3^- \rightarrow \text{CO}_2 + \text{O}_2^-$	$8 \times 10^{-11} \text{ cm}^3 \text{ s}^{-1}$	[14]
(122)	$\text{O}_2^+ + \text{CO}_4^- \rightarrow \text{CO}_2 + \text{O}_2 + \text{O}_2$	$3 \times 10^{-7} \text{ cm}^3 \text{ s}^{-1}$	[14]
(123)	$\text{O} + \text{CO}_4^- \rightarrow \text{CO}_3^- + \text{O}_2$	$1.1 \times 10^{-10} \text{ cm}^3 \text{ s}^{-1}$	[2]
(124)	$\text{O} + \text{CO}_4^- \rightarrow \text{CO}_2 + \text{O}_2 + \text{O}^-$	$1.4 \times 10^{-11} \text{ cm}^3 \text{ s}^{-1}$	[2]
(125)	$\text{O} + \text{CO}_4^- \rightarrow \text{CO}_2 + \text{O}_3^-$	$1.4 \times 10^{-11} \text{ cm}^3 \text{ s}^{-1}$	[2]
(126)	$\text{O}_3 + \text{CO}_4^- \rightarrow \text{CO}_2 + \text{O}_3^- + \text{O}_2$	$1.3 \times 10^{-10} \text{ cm}^3 \text{ s}^{-1}$	[15]
(127)	$\text{O}_2 + \text{C}^+ \rightarrow \text{CO} + \text{O}^+$	$6.2 \times 10^{-10} \text{ cm}^3 \text{ s}^{-1}$	[20]
(128)	$\text{O}_2 + \text{C}^+ \rightarrow \text{CO}^+ + \text{O}$	$3.8 \times 10^{-10} \text{ cm}^3 \text{ s}^{-1}$	[2]
(129)	$\text{O}^+ + \text{O}_2 \rightarrow \text{O}_2^+ + \text{O}$	$1.9\text{e-}11 \times (\text{Tg}(\text{K})/300)^{-0.5} \text{ cm}^3 \text{ s}^{-1}$	[2]
(130)	$\text{O}_2^+ + \text{O}_2 + \text{M} \rightarrow \text{O}_4^+ + \text{M}$	$2.4 \times 10^{-30} \text{ cm}^6 \text{ s}^{-1}$	[18]
(131)	$\text{O}_2^- + \text{O}_2 + \text{M} \rightarrow \text{O}_4^- + \text{M}$	$3.5 \times 10^{-31} \text{ cm}^6 \text{ s}^{-1}$	[18]
(132)	$\text{O}^- + \text{O}_2 \rightarrow \text{O}_3 + \text{e}^-$	$1 \times 10^{-12} \text{ cm}^3 \text{ s}^{-1}$	[15]
(133)	$\text{O}^- + \text{O}_2 + \text{M} \rightarrow \text{O}_3^- + \text{M}$	$3.0 \times 10^{-28} \times (\text{Tg}(\text{K})/300)^{-1} \text{ cm}^6 \text{ s}^{-1}$	[15]
(134)	$\text{O}^- + \text{O}_3 \rightarrow \text{O}_3^- + \text{O}$	$8 \times 10^{-10} \text{ cm}^3 \text{ s}^{-1}$	[15]
(135)	$\text{O}^- + \text{O}_3 \rightarrow \text{O}_2 + \text{O}_2 + \text{e}^-$	$3.0 \times 10^{-10} \text{ cm}^3 \text{ s}^{-1}$	[21]
(136)	$\text{O}_2^- + \text{O}_3 \rightarrow \text{O}_3^- + \text{O}_2$	$4.0 \times 10^{-10} \text{ cm}^3 \text{ s}^{-1}$	[17]
(137)	$\text{O}_3^- + \text{O}_3 \rightarrow \text{O}_2 + \text{O}_2 + \text{O}_2 + \text{e}^-$	$3.0 \times 10^{-10} \text{ cm}^3 \text{ s}^{-1}$	[15]
(138)	$\text{O}^+ + \text{O}_3 \rightarrow \text{O}_2^+ + \text{O}_2$	$1.0 \times 10^{-10} \text{ cm}^3 \text{ s}^{-1}$	[18]

(139)	$O^+ + O + M \rightarrow O_2^+ + M$	$1.0 \times 10^{-29} \text{ cm}^6 \text{ s}^{-1}$	[17]
(140)	$O^- + O \rightarrow O_2 + e^-$	$2.3 \times 10^{-10} \text{ cm}^3 \text{ s}^{-1}$	[22]
(141)	$O_2^- + O \rightarrow O_2 + O^-$	$3.3 \times 10^{-10} \text{ cm}^3 \text{ s}^{-1}$	[17]
(142)	$O_2^- + O \rightarrow O_3 + e^-$	$3.3 \times 10^{-10} \text{ cm}^3 \text{ s}^{-1}$	[22]
(143)	$O_3^- + O \rightarrow O_3 + O^-$	$1.0 \times 10^{-13} \text{ cm}^3 \text{ s}^{-1}$	[21]
(144)	$O_3^- + O \rightarrow O_2 + O_2 + e^-$	$1.0 \times 10^{-13} \text{ cm}^3 \text{ s}^{-1}$	[15]
(145)	$O_3^- + O \rightarrow O_2^- + O_2$	$2.5 \times 10^{-10} \text{ cm}^3 \text{ s}^{-1}$	[15]
(146)	$O_4^- + O \rightarrow O_3^- + O_2$	$4.0 \times 10^{-10} \text{ cm}^3 \text{ s}^{-1}$	[18]
(147)	$O_4^- + O \rightarrow O^- + O_2 + O_2$	$3.0 \times 10^{-10} \text{ cm}^3 \text{ s}^{-1}$	[18]
(148)	$O_4^+ + O \rightarrow O_2^+ + O_3$	$3.0 \times 10^{-10} \text{ cm}^3 \text{ s}^{-1}$	[18]
(149)	$O^+ + O_2^- + M \rightarrow O_3 + M$	$2.0 \times 10^{-25} \text{ cm}^6 \text{ s}^{-1}$	[17]
(150)	$O^+ + O_2^- \rightarrow O + O_2$	$2.7 \times 10^{-7} \text{ cm}^3 \text{ s}^{-1}$	[22]
(151)	$O_2^+ + O_2^- \rightarrow O_2 + O_2$	$2.0 \times 10^{-7} \text{ cm}^3 \text{ s}^{-1}$	[22]
(152)	$O_2^+ + O_2^- \rightarrow O_2 + O + O$	$4.2 \times 10^{-7} \text{ cm}^3 \text{ s}^{-1}$	[14]
(153)	$O_2^+ + O_2^- + M \rightarrow O_2 + O_2 + M$	$2.0 \times 10^{-25} \text{ cm}^6 \text{ s}^{-1}$	[17]
(154)	$O_2^- + O_2 \rightarrow O_2 + O_2 + e^-$	$2.18 \times 10^{-18} \text{ cm}^3 \text{ s}^{-1}$	[17]
(155)	$O_2^- + M \rightarrow O_2 + M + e^-$	$2.7 \times 10^{-10} \times$ $(Tg(K)/300)^{0.5} \times \exp(-$ $5590/Tg(K)) \text{ cm}^3 \text{ s}^{-1}$	[2]
(156)	$O_2^+ + O_3^- \rightarrow O_2 + O_3$	$2.0 \times 10^{-7} \text{ cm}^3 \text{ s}^{-1}$	[17]
(157)	$O_2^+ + O_3^- \rightarrow O + O + O_3$	$1.0 \times 10^{-7} \text{ cm}^3 \text{ s}^{-1}$	[17]
(158)	$O^+ + O_3^- \rightarrow O_3 + O$	$1.0 \times 10^{-7} \text{ cm}^3 \text{ s}^{-1}$	[17]
(159)	$O_2 + O_3^- \rightarrow O_2 + O_3 + e^-$	$2.3 \times 10^{-11} \text{ cm}^3 \text{ s}^{-1}$	[17]
(160)	$O_3^- + M \rightarrow O_3 + e^-$	$2.3 \times 10^{-11} \text{ cm}^3 \text{ s}^{-1}$	[2]
(161)	$O^+ + O^- \rightarrow O + O$	$4.0 \times 10^{-8} \text{ cm}^3 \text{ s}^{-1}$	[22]
(162)	$O^+ + O^- + M \rightarrow O_2 + M$	$2.0 \times 10^{-25} \text{ cm}^6 \text{ s}^{-1}$	[17]
(163)	$O_2^+ + O^- \rightarrow O_2 + O$	$1.0 \times 10^{-7} \text{ cm}^3 \text{ s}^{-1}$	[14]
(164)	$O_2^+ + O^- \rightarrow O + O + O$	$2.6 \times 10^{-8} \text{ cm}^3 \text{ s}^{-1}$	[22]
(165)	$O_2^+ + O^- + M \rightarrow O_3 + M$	$2.0 \times 10^{-25} \text{ cm}^6 \text{ s}^{-1}$	[17]

(166)	$M + O^- \rightarrow O + M + e^-$	$4 \times 10^{-12} \text{ cm}^3 \text{ s}^{-1}$	[15]
(167)	$M + O_4^- \rightarrow O_2^- + O_2 + M$	$3.08 \times 10^{-12} \text{ cm}^3 \text{ s}^{-1}$	[21]
(168)	$O_4^+ + M \rightarrow O_2^+ + O_2 + M$	$1.73 \times 10^{-13} \text{ cm}^3 \text{ s}^{-1}$	[18]

Table A2 - 5: Overview of the vibrational relaxation processes upon collision with ground state molecules, included in the model, yielding transformation to a higher or lower vibrational level (i.e., V-V relaxations) or to the ground state (i.e., V-T relaxations) (EST means estimated).

No.	Reaction	Rate coefficient	Ref.
(169)	$CO_2 v1 + CO_2 \rightarrow CO_2 + CO_2$	$1.07 \times 10^{-14} \text{ cm}^3 \text{ s}^{-1}$	[23]
(170)	$CO_2 v1 + CO \rightarrow CO_2 + CO$	$7.48 \times 10^{-15} \text{ cm}^3 \text{ s}^{-1}$	[23]
(171)	$CO_2 v1 + O_2 \rightarrow CO_2 + O_2$	$7.48 \times 10^{-15} \text{ cm}^3 \text{ s}^{-1}$	[23]
(172)	$CO_2 v2 + CO_2 \rightarrow CO_2 + CO_2$	$9.00 \times 10^{-18} \text{ cm}^3 \text{ s}^{-1}$	[23]
(173)	$CO_2 v2 + CO \rightarrow CO_2 + CO$	$2.79 \times 10^{-17} \text{ cm}^3 \text{ s}^{-1}$	[23]
(174)	$CO_2 v2 + O_2 \rightarrow CO_2 + O_2$	$2.79 \times 10^{-17} \text{ cm}^3 \text{ s}^{-1}$	[23]
(175)	$CO_2 v2 + CO_2 \rightarrow CO_2 v1 + CO_2$	$2.90 \times 10^{-14} \text{ cm}^3 \text{ s}^{-1}$	[23]
(176)	$CO_2 v2 + CO \rightarrow CO_2 v1 + CO$	$2.03 \times 10^{-14} \text{ cm}^3 \text{ s}^{-1}$	[23]
(177)	$CO_2 v2 + O_2 \rightarrow CO_2 v1 + O_2$	$2.03 \times 10^{-14} \text{ cm}^3 \text{ s}^{-1}$	[23]
(178)	$CO_2 v3 + CO_2 \rightarrow CO_2 v2 + CO_2$	$7.72 \times 10^{-16} \text{ cm}^3 \text{ s}^{-1}$	[23]
(179)	$CO_2 v3 + CO \rightarrow CO_2 v2 + CO$	$2.32 \times 10^{-16} \text{ cm}^3 \text{ s}^{-1}$	[23]
(180)	$CO_2 v3 + O_2 \rightarrow CO_2 v2 + O_2$	$3.09 \times 10^{-16} \text{ cm}^3 \text{ s}^{-1}$	[23]
(181)	$CO_2 v3 + CO_2 \rightarrow CO_2 v4 + CO_2$	$6.05 \times 10^{-15} \text{ cm}^3 \text{ s}^{-1}$	[23]
(182)	$CO_2 v3 + CO \rightarrow CO_2 v4 + CO$	$1.81 \times 10^{-15} \text{ cm}^3 \text{ s}^{-1}$	[23]
(183)	$CO_2 v3 + O_2 \rightarrow CO_2 v4 + O_2$	$2.42 \times 10^{-15} \text{ cm}^3 \text{ s}^{-1}$	[23]
(184)	$CO_2 v3 + CO_2 \rightarrow CO_2 v1 + CO_2 v2$	$2.42 \times 10^{-15} \text{ cm}^3 \text{ s}^{-1}$	[23]
(185)	$CO_2 v3 + CO_2 \rightarrow CO_2 v1 + CO_2$	$1.70 \times 10^{-18} \text{ cm}^3 \text{ s}^{-1}$	[23]
(186)	$CO_2 v3 + CO \rightarrow CO_2 v1 + CO$	$5.10 \times 10^{-19} \text{ cm}^3 \text{ s}^{-1}$	[23]
(187)	$CO_2 v3 + O_2 \rightarrow CO_2 v1 + O_2$	$6.80 \times 10^{-19} \text{ cm}^3 \text{ s}^{-1}$	[23]
(188)	$CO_2 v4 + CO_2 \rightarrow CO_2 v2 + CO_2$	$4.33 \times 10^{-14} \text{ cm}^3 \text{ s}^{-1}$	[23]
(189)	$CO_2 v4 + CO \rightarrow CO_2 v2 + CO$	$3.03 \times 10^{-14} \text{ cm}^3 \text{ s}^{-1}$	[23]

(190)	$\text{CO}_2 \text{ v4} + \text{O}_2 \rightarrow \text{CO}_2 \text{ v2} + \text{O}_2$	$3.03 \times 10^{-14} \text{ cm}^3 \text{ s}^{-1}$	[23]
(191)	$\text{CO}_2 \text{ v4} + \text{CO}_2 \rightarrow \text{CO}_2 \text{ v1} + \text{CO}_2$	$9.08 \times 10^{-18} \text{ cm}^3 \text{ s}^{-1}$	[23]
(192)	$\text{CO}_2 \text{ v4} + \text{CO} \rightarrow \text{CO}_2 \text{ v1} + \text{CO}$	$6.18 \times 10^{-15} \text{ cm}^3 \text{ s}^{-1}$	[23]
(193)	$\text{CO}_2 \text{ v4} + \text{O}_2 \rightarrow \text{CO}_2 \text{ v1} + \text{O}_2$	$6.18 \times 10^{-15} \text{ cm}^3 \text{ s}^{-1}$	[23]
(194)	$\text{COv1} + \text{CO}_2 \rightarrow \text{CO} + \text{CO}_2$	$1.34 \times 10^{-23} \text{ cm}^3 \text{ s}^{-1}$	[23]
(195)	$\text{COv1} + \text{CO} \rightarrow \text{CO} + \text{CO}$	$1.34 \times 10^{-23} \text{ cm}^3 \text{ s}^{-1}$	[23]
(196)	$\text{COv1} + \text{O}_2 \rightarrow \text{CO} + \text{O}_2$	$4.78 \times 10^{-24} \text{ cm}^3 \text{ s}^{-1}$	[23]
(197)	$\text{O}_2 \text{ v1} + \text{CO}_2 \rightarrow \text{O}_2 + \text{CO}_2$	$7.55 \times 10^{-23} \text{ cm}^3 \text{ s}^{-1}$	[23]
(198)	$\text{O}_2 \text{ v1} + \text{CO} \rightarrow \text{O}_2 + \text{CO}$	$2.52 \times 10^{-23} \text{ cm}^3 \text{ s}^{-1}$	[23]
(199)	$\text{O}_2 \text{ v1} + \text{O}_2 \rightarrow \text{O}_2 + \text{O}_2$	$2.52 \times 10^{-23} \text{ cm}^3 \text{ s}^{-1}$	[23]
(200)	$\text{O}_2 \text{ v2} + \text{CO}_2 \rightarrow \text{O}_2 + \text{CO}_2$	$7.55 \times 10^{-23} \text{ cm}^3 \text{ s}^{-1}$	EST [24]
(201)	$\text{O}_2 \text{ v2} + \text{CO} \rightarrow \text{O}_2 + \text{CO}$	$2.52 \times 10^{-23} \text{ cm}^3 \text{ s}^{-1}$	EST [24]
(202)	$\text{O}_2 \text{ v2} + \text{O}_2 \rightarrow \text{O}_2 + \text{O}_2$	$2.52 \times 10^{-23} \text{ cm}^3 \text{ s}^{-1}$	EST [24]
(203)	$\text{O}_2 \text{ v3} + \text{CO}_2 \rightarrow \text{O}_2 + \text{CO}_2$	$7.55 \times 10^{-23} \text{ cm}^3 \text{ s}^{-1}$	EST [24]
(204)	$\text{O}_2 \text{ v3} + \text{CO} \rightarrow \text{O}_2 + \text{CO}$	$2.52 \times 10^{-23} \text{ cm}^3 \text{ s}^{-1}$	EST [24]
(205)	$\text{O}_2 \text{ v3} + \text{O}_2 \rightarrow \text{O}_2 + \text{O}_2$	$2.52 \times 10^{-23} \text{ cm}^3 \text{ s}^{-1}$	EST [24]

- [1] J. J. Lowke, A. Phelps, B. W. Irwin, *J. Appl. Phys.* **1973**, *44*, 4664.
 [2] T. G. Beuthe, J.-S. Chang, *Jpn. J. Appl. Phys.* **1997**, *36*, 4997–5002.
 [3] A. Jain, D. Norcross, *Phys. Rev. A* **1992**, *45*, 1644–1656.
 [4] W. Liu, G. A. Victor, *Astrophys. J.* **1994**, *435*, 909.
 [5] R. K. Janev, D. Reiter, *ChemInform* **2003**, *34*, DOI 10.1002/chin.200325274.
 [6] T. Janev, R. K., Wang, J. G., Murakami, I., and Kato, *Cross Sections and Rate Coefficients for Electron-Impact Ionization of Hydrocarbon Molecules Research Report*, Tokio, Japan, **2001**.
 [7] A. V Phelps, *Tabulations of Collision Cross Sections and Calculated Transport and Reaction Coefficients for Electron Collisions with O2 Technical Report*, **1985**.
 [8] E. Krishnakumar, S. K. Srivastava, *Int. J. Mass Spectrom. Ion Process.* **1992**, *113*, 1–12.
 [9] K. A. Publishers, *Technology* **2001**, *74*, 71–77.
 [10] Eliasson, B. and Kogelschatz, U., *Basic Data for Modelling of Electrical Discharges in Gases: Oxygen Research Report*, **1986**.

-
- [11] S. Matejcik, A. Kiendler, P. Cicman, J. Skalny, P. Stampfli, E. Illenberger, Y. Chu, A. Stamatovic, T. D. Märk, *Plasma Sources Sci. Technol.* **1997**, *6*, 140–146.
- [12] Y. Itikawa, A. Ichimura, *J. Phys. Chem. Ref. Data* **1990**, *19*, 637.
- [13] R. R. Laher, F. R. Gilmore, *J. Phys. Chem. Ref. Data* **1990**, *19*, 277.
- [14] H. Hokazono, H. Fujimoto, *J. Appl. Phys.* **1987**, *62*, 1585.
- [15] A. Cenian, A. Chernukho, V. Borodin, *Contrib. to Plasma Phys.* **1995**, *35*, 273–296.
- [16] A. Cenian, A. Chernukho, V. Borodin, G. Śliwiński, *Contrib. to Plasma Phys.* **1994**, *34*, 25–37.
- [17] B. Eliasson, M. Hirth, U. Kogelschatz, *J. Phys. D. Appl. Phys.* **1987**, *20*, 1421–1437.
- [18] I. A. Kossyi, A. Yu Kostinsky, A. A. Matveyev, P. V. Silakov, *Plasma Sources Sci. Technol.* **1992**, *1*, 207–220.
- [19] S. Hadj-Ziane, B. Held, P. Pignolet, R. Peyrous, C. Coste, *J. Phys. D. Appl. Phys.* **1992**, *25*, 677–685.
- [20] J. Woodall, M. Agúndez, A. J. Markwick-Kemper, T. J. Millar, *Astron. Astrophys.* **2007**, *466*, 1197–1204.
- [21] A. A. Ionin, I. V Kochetov, A. P. Napartovich, N. N. Yuryshev, *J. Phys. D. Appl. Phys.* **2007**, *40*, R25–R61.
- [22] J. T. Gudmundsson, E. G. Thorsteinsson, *Plasma Sources Sci. Technol.* **2007**, *16*, 399–412.
- [23] N. G. R. Blauer Jay A., *A Survey of Vibrational Relaxation Rate Data for Processes Important to CO₂-N₂-H₂O Infrared Plume Radiation*, Irvine, **1973**.
- [24] Sergey T. Surzhikov, *Non-Equilibrium Gas Dynamics – From Physical Models to Hypersonic Flights*, Moscow, **2009**.